TECHNICAL UNIVERSITY OF CRETE

SCHOOL OF PRODUCTION ENGINEERING & MANAGEMENT

Study of matter behaviour dynamics governed by the interaction with laser pulses and external strong currents

By

Evaggelos N. Kaselouris

A dissertation submitted in partial fulfilment of the
requirements for the degree of
Doctor of Philosophy (PhD)

Chania, September 2016

TECHNICAL UNIVERSITY OF CRETE

SCHOOL OF PRODUCTION ENGINEERING & MANAGEMENT

Study of matter behaviour dynamics governed by the interaction with laser pulses and external strong currents

By

Evaggelos N. Kaselouris

Advisory Committee

Dr. Ioannis K. Nikolos (Supervisor)
Associate Professor
Technical University of Crete
School of Production Engineering & Management

Dr. Michael Tatarakis (Co-supervisor)
Professor
Technological Educational Institute of Crete
Department of Electronic Engineering/Centre for Plasma Physics and Lasers

Dr. Nektarios A. Papadogiannis (Co-supervisor)
Professor
Technological Educational Institute of Crete
Department of Music Technology & Acoustics Engineering/Centre for Plasma Physics and Lasers

Thesis Examination Committee

Dr. Georgios E. Stavroulakis
Professor
Technical University of Crete
School of Production Engineering & Management

Dr. Anargyros I. Delis
Associate Professor
Technical University of Crete
School of Production Engineering & Management

Dr. Yiannis Tsompanakis
Associate Professor
Technical University of Crete
School of Environmental Engineering

Dr. Vasilios Dimitriou
Assistant Professor
Technological Educational Institute of Crete
Department of Natural Resources & Environmental Engineering/Centre for Plasma Physics and Lasers

"Intentionally left blank"

In memory of my Dad

Abstract

This thesis studies the physical phenomena that occur during the deposition of energy in matter and consists of two parts. In the first part, the nanosecond pulsed laser irradiation of thin metal films-substrate systems is investigated for thermoelastic, melting and ablation regimes, using the finite element method (FEM). The numerical simulations are compared and validated with experimental results, obtained by dynamic imaging interferometry and white-light tomographic interferometry. In the second part, the sequential stages of explosion of a Z-pinch copper wire from solid to plasma formation and its plasma expansion are investigated using multiphysics coupled numerical simulations, validated by experimental results obtained by interferometry, shadowgraphy, schlieren and diffraction imaging techniques.

In more details, for the first part coupled thermal-structural, transient models based on FEM are developed to give a comprehensive spatiotemporal numerical solution of the physical phenomena occurring in laser matter interactions. Temperature dependent material properties of metal coatings deposited on glass substrates are used for the simulations. Initially, a 2D axisymmetric model is developed to study the generation and propagation of laser generated ultrasounds, for laser fluences below the melting threshold of metallic film-substrates. Afterwards, a 3D quarter-symmetric FEM model is developed and used for all regimes of interest. The developed FEM modeling provides a simultaneous analysis of the thermal and structural parameters, as defined by the solution of the heat conduction and wave propagation equations. The wave equation determines the displacements of the target imposed by the laser energy deposition, while the heat conduction equation predicts the temperature distribution induced by absorption of the laser pulse in the target. The 3D model computes the phase changes of matter by taking into account the latent heats of melting and vaporization, depending on the laser fluence. Ablation is simulated by the ‘killing’ of the elements that exceed the boiling temperature and are subsequently deactivated. The attenuation of the laser irradiance at the target surface due to plasma absorption is also taken into account. With regard to loading conditions, a heat source term is used, representing the laser energy absorbed by the sample and described by a Gaussian distribution in time and space. The Lagrangian mesh is locally adaptive, depending on the simulation needs. Moreover, the elastic and plastic behaviour of thin films is being investigated by taking into account stress-strains temperature-dependent curves of

different materials until fracture into the 3D model. Furthermore, the finite element model was further extended to simulate the presence of surface and solid volume defects (gaps) and their subsequent influence on the generation and propagation of ultrasonic waves (surface acoustic waves).

For the second part that concerns the matter behaviour dynamics, governed by the interaction with external strong currents, a 3D coupled mechanical/thermal FEM model, simulating the initial stages of explosion of a Z-pinch metallic copper wire, was initially developed. The model conveyed a simultaneous analysis of the thermal and structural parameters, as defined by the solution of the heat conduction and mechanical motion equations. The mechanical equation determines the displacements of the wire imposed by an alternative nanosecond pulsed current while the heat equation predicts the temperature distribution. The source term of the heat generation rate is the Joule heating term and is used as loading condition, while the pulsed imposed current is provided from experiments.

In order to investigate the crucial physical phenomena that take place in the initial stages of wire explosion, a 3D electromagnetic-thermal-structural hydrodynamic FEM model is developed. Large volumetric deformation is considered by taking into account the material's hydrodynamic behavior via equations of state (Gruneisen and multiphase tabular) and the elastoplastic behavior is also considered by a flow stress constitutive model (Johnson-Cook). A Lagrangian transient analysis has been carried out. The loading condition of the simulation is a nanosecond pulsed alternative current, which is provided from experiments. The sequential stages of explosion of a Z-pinch copper wire from solid to plasma formation and its plasma expansion are investigated. The expansion of the exploded material is being investigated with a magnetohydrodynamic code that uses as initial condition the density distribution and radius instabilities from the above aforementioned 3D FEM model.

Keywords: Multiphysics Numerical Simulation, Coupled Physical Fields, Finite Element Method, Laser Matter Interaction, Exploding Wires, Phase Change, Plasma, Magnetohydrodynamics

Περίληψη

Η παρούσα διατριβή μελετάει τα φυσικά φαινόμενα που λαμβάνουν χώρα κατά την εναπόθεση ενέργειας στην ύλη και αποτελείται από δύο μέρη στα οποία παρουσιάζονται δύο διαφορετικοί μηχανισμοί εναπόθεσης. Αναφορικά με τη δυναμική συμπεριφορά της ύλης όταν αλληλεπιδρά με παλμούς λέιζερ, η ακτινοβόληση λεπτών μεταλλικών φιλμ-υποστρωμάτων από παλμικό λέιζερ διάρκειας νανοδευτερολέπτων ερευνάται για την θερμοελαστική περιοχή, την περιοχή τήξης και την περιοχή φωτοαποδόμησης χρησιμοποιώντας τη μέθοδο των πεπερασμένων στοιχείων (ΜΠΣ). Οι αριθμητικές προσομοιώσεις συγκρίνονται και επικυρώνονται με τα πειραματικά αποτελέσματα που προκύπτουν από την τεχνική δυναμικής συμβολομετρίας απεικόνισης. Αναφορικά με τη δυναμική συμπεριφορά της ύλης όταν αλληλεπιδρά με εξωτερικά ισχυρά ρεύματα, τα διαδοχικά στάδια της έκρηξης ενός χάλκινου σύρματος Z-pinch από στερεά κατάσταση ως τη δημιουργία πλάσματος καθώς και η εξάπλωση του πλάσματος διερευνώνται αναπτύσσοντας multiphysics αριθμητικές προσομοιώσεις συζευγμένων πεδιών οι οποίες επικυρώνονται από πειραματικά αποτελέσματα που λαμβάνονται από οπτικές τεχνικές απεικόνισης (συμβολομετρία, σκιαγράφηση, Schlieren, απεικόνιση περίθλασης Fraunhofer).

Αναλυτικότερα για το πρώτο μέρος, αναπτύσσεται συζευγμένο θερμικό-μηχανικό μοντέλο δυναμικά μεταβαλλόμενο στο χρόνο που βασίζεται στη ΜΠΣ με σκοπό να δώσει μια ολοκληρωμένη χωροχρονική αριθμητική επίλυση των φυσικών φαινομένων που συμβαίνουν κατά τη διάρκεια της αλληλεπίδραση ύλης με λέιζερ. Για τις προσομοιώσεις λαμβάνονται υπόψη θερμοκρασιακά εξαρτώμενες ιδιότητες υλικών, των μεταλλικών επικαλύψεων που εναποτίθενται σε γυάλινα υποστρώματα. Αρχικά, αναπτύχθηκε δισδιάστατο 2D αξονοσυμμετρικό μοντέλο με σκοπό να μελετηθεί η δημιουργία και διάδοση υπερήχων που παράγονται για πυκνότητες ροής ακτινοβολίας λέιζερ κάτω από το όριο τήξης του μεταλλικού φιλμ-υποστρώματος. Στη συνέχεια τρισδιάστατο 3D τέταρτο-συμμετρικό μοντέλο πεπερασμένων στοιχείων αναπτύχθηκε για όλες τις περιοχές ενδιαφέροντος (θερμοελαστική, τήξης, φωτοαποδόμησης/πλάσματος). Η αναπτυχθείσα μεθοδολογία παρέχει μια ταυτόχρονη ανάλυση των θερμικών και μηχανικών παραμέτρων όπως ορίζεται από την επίλυση των εξισώσεων της θερμικής αγωγιμότητας και κυματικής διάδοσης. Η κυματική εξίσωση καθορίζει τις μετατοπίσεις του στόχου που επιβάλλονται από την εναπόθεση

ενέργειας λέιζερ, ενώ η εξίσωση αγωγής θερμότητας προβλέπει την κατανομή της θερμοκρασίας που προκαλείται από την απορρόφηση της ενέργειας του παλμικού λέιζερ στον στόχο. Το 3D μοντέλο υπολογίζει τις αλλαγές φάσης της ύλης, λαμβάνοντας υπόψη τις λανθάνουσες θερμότητες τήξης και εξάτμισης, ανάλογα με την πυκνότητα ροής της ακτινοβολίας λέιζερ. Η φωτοαποδόμηση προσομοιώνεται από την τεχνική «killing» των στοιχείων που υπερβαίνουν τη θερμοκρασία βρασμού και στη συνέχεια απενεργοποιούνται. Η εξασθένηση της ακτινοβολίας λέιζερ στην επιφάνεια-στόχο λόγω της απορρόφησης του πλάσματος λαμβάνεται επίσης υπόψη. Όσον αφορά τις συνθήκες φόρτισης, χρησιμοποιείται ως πηγή θερμότητας, η ενέργεια του λέιζερ που απορροφάται από το δείγμα και περιγράφεται από μια Γκαουσιανή κατανομή σε χρόνο και χώρο. Το Λαγκρανζιανό πλέγμα είναι τοπικά προσαρμοζόμενο ανάλογα με τις ανάγκες της προσομοίωσης. Επιπλέον, η ελαστική και πλαστική συμπεριφορά των λεπτών υμενίων ερευνάται λαμβάνοντας υπόψη, θερμοκρασιακά εξαρτώμενες καμπύλες τάσεων-παραμορφώσεων από διαφορετικά υλικά, μέχρι τη θραύση τους, στο 3D μοντέλο. Επιπλέον, το μοντέλο πεπερασμένων στοιχείων επεκτείνεται περαιτέρω, προκειμένου να προσομοιωθεί η παρουσία των επιφανειακών και των ελαττωμάτων του όγκου στο στερεό (κενά) και να μελετηθεί η μετέπειτα επιρροή τους στην παραγωγή και διάδοση των υπερηχητικών κυμάτων (επιφανειακών ακουστικών κυμάτων).

Αναφορικά με τη δυναμική συμπεριφορά της ύλης όταν αλληλεπιδρά με εξωτερικά ισχυρά ρεύματα, αναπτύχθηκε αρχικά ένα 3-D συζευγμένο μηχανικό-θερμικό μοντέλο πεπερασμένων στοιχείων, που προσομοιώνει τα αρχικά στάδια της έκρηξης ενός Z-pinch μεταλλικού χάλκινου σύρματος. Το μοντέλο λαμβάνει υπόψη τις θερμοκρασιακά εξαρτώμενες θερμικές και μηχανικές παραμέτρους μέσω της επίλυσης των εξισώσεων της θερμικής αγωγιμότητας και της κλασσικής μηχανικής. Η μηχανική εξίσωση προσδιορίζει τις μετατοπίσεις του σύρματος που επιβάλλεται από εναλλασόμενο παλμικό ρεύμα διάρκειας νανοδευτερολέπτων, ενώ η εξίσωση αγωγής θερμότητας προβλέπει την κατανομή της θερμοκρασίας. Ο όρος που λειτουργεί ως πηγή του ρυθμού παραγωγής θερμότητας είναι ο όρος της θέρμανσης Joule και χρησιμοποιείται ως συνθήκη φόρτισης, ενώ το παλμικό εναλλασσόμενο ρεύμα παρέχεται από πειράματα.

Για να αντιμετωπιστούν τα φυσικά φαινόμενα που λαμβάνουν χώρα στα αρχικά στάδια της έκρηξης του σύρματος πιο ρεαλιστικά αναπτύσσεται ένα 3D

ηλεκτρομαγνητικό-θερμικό-μηχανικό υδροδυναμικό μοντέλο βασιζόμενο στη ΜΠΣ. Μεγάλες ογκομετρικές παραμορφώσεις εξετάζονται λαμβάνοντας υπόψη την υδροδυναμική συμπεριφορά του υλικού μέσω καταστατικών εξισώσεων (Gruneisen και καταστατική σε μορφή πίνακα λαμβάνοντας υπόψη τις αλλαγές φάσης), ενώ η ελαστοπλαστική συμπεριφορά του υλικού μελετάται θεωρώντας επίσης καταστατικό μοντέλο τάσεων (Johnson-Cook). Πραγματοποιείται Λαγκρανζιανή δυναμική ανάλυση στο χρόνο, ενώ η πηγή φόρτισης της προσομοίωσης είναι παλμικό εναλλασσόμενο ρεύμα, διάρκειας νανοδευτερολέπτων το οποίο παρέχεται από πειράματα. Μελετώνται τα διαδοχικά στάδια της έκρηξης χάλκινου σύρματος Z-pinch από στερεά κατάσταση ως τη δημιουργία πλάσματος. Στη συνέχεια η διαστολή και διάδοση του πλάσματος στο χωροχρόνο διερευνάται με μαγνητοϋδροδυναμικό κώδικα ο οποίος χρησιμοποιεί ως αρχικές συνθήκες την κατανομή πυκνότητας και τις αστάθειες στην τιμή της ακτίνας από το προαναφερθέν 3D μοντέλο με τη ΜΠΣ.

Λέξεις-κλειδιά: Αριθμητική προσομοίωση, Συζευγμένα πεδία φυσικής, Μέθοδος Πεπερασμένων Στοιχείων, Αλληλεπίδραση Laser Μεταλλικού Υλικού, Εκρηγνυόμενο Σύρμα, Αλλαγή Φάσης, Πλάσμα, Μαγνητοϋδροδυναμική

"Intentionally left blank"

Acknowledgments

This thesis took part between the years 2012-2016 in the Centre of Plasma Physics and Lasers of Technological Educational Institute of Crete in collaboration with the Technical University of Crete.

I would like to thank Associate Professor Ioannis K. Nikolos for accepting me as a PhD candidate in the Technical University. I am grateful for his support and encouragement. I admire him for his scientific knowledge, kindness and ethics.

I would like to thank Professor Michael Tatarakis for accepting me as PhD candidate in his group. I am deeply grateful for his guidance, support and for providing me with financial assistance. I would like to thank him for treating me like a son a lot of times and for providing me with encouragement and optimism. I would also like to thank Professor Nektarios A. Papadogiannis for accepting me as PhD candidate. I am deeply grateful for his guidance, support, encouragement and financial assistance. I both admire them not only for their scientific knowledge, but mainly for their passion and continuous efforts to establish an International Centre of Research in Rethymno.

I would like to thank Assistant Professor Vasilios Dimitriou for his guidance in the world of finite elements. I am deeply grateful for his continuous support, advice and encouragement and for treating me like his smaller brother numerous times. I enjoyed co-working with him all these years and thank him for his friendship and understanding.

I would like to thank all the other members of the examination committee, honouring me by participating to it, and for their valuable comments and suggestions: Professor G. Stavroulakis, Associate Professor A. Delis and Associate Professor Y. Tsompanakis.

I would also like to thank Dr. Yiannis Orphanos, Dr Ioannis Fitilis and Mr. Alekos Skoulakis for carrying out the experiments in CPPL, PhD candidate Giorgos Koundourakis for his useful help with the MHD code, Stelios Petrakis for technical support and MSc graduate Manos Skarvelakis. I thank them for their support and useful suggestions.

Many many thanks to Associate Professor Makis Bakarezos and Dr. Eugene Clark for their useful suggestions and for their encouragement and many thanks to all past and new members of the CPPL group.

I thank my friends Aneta Nousia, Michael Kalogerakis for being there for me a lot of times and for their interest and also I thank my friends Panagiotis Broutas, Manthos Mathioudakis, Vaggelis Somathianos for their interest and Eirini.

The author acknowledges financial support through the Action “National Research Infrastructure for HiPER MIS 376841 (co-funded by th European Union and Hellenic National funds within the Operational Programme “Competitiveness and Entrepreneurship”. 3D MHD simulations were performed with the use of the code PLUTO.

Finally, this thesis is devoted to my father, Nikolaos. I would like to thank him and my mum Maria for all the things they provided me during this life and for the ethics they taught me. Many thanks and love goes to my sister Viki and her husband Giorgos for their support and love and an endless gratitude goes to my mum for her patience, encouragement and love.

Contents

List of Figures

List of Tables

"Intentionally left blank"

Chapter 1

1. Introduction

1.1 Phenomena of solid matter excitation

The deposition of energy in matter is always a cutting edge research field, since it leads to interesting physical processes with broad scientific interest. Some of these phenomena are still not well comprehended and establish a significant area for further research. Deposition of energy onto a solid can produce a series of thermal effects, such as heating, melting, vaporization and phase explosion as well as mechanical effects, such as material expansion and thermoelastic stresses. When the stress exceeds a certain value, the material may fracture and/or deform plastically. Moreover, effects such as ionization, plasma formation and plasma expansion may also occur in the materials for even higher energies [1]. Therefore, the study of the dynamic behaviour of materials due to energy deposition involves different scientific disciplines.

A state of matter is characterized by phase transitions a feature of major importance. A phase transition indicates a change in structure and can be recognized by an abrupt change in matter's properties. The state or phase of a given set of matter can change depending on pressure and temperature conditions, transitioning to other phases as these conditions change to favor their existence. Solid matter transitions to liquid with an increase in temperature. As heat is added it melts into a liquid at its melting point, boils into a gas at its boiling point, and if heated at higher temperature it would enter a plasma state in which the electrons are so energized that they leave their parent atoms (ionization). Heat absorbed or released as the result of a phase change is called latent heat. During a phase change, under constant pressure, there is no temperature change, thus there is no change in the kinetic energy of the particles in the material. The energy released comes from the potential energy stored in the bonds between the particles.

Another important phenomenon of matter excitation is the propensity of a material to undergo permanent deformation under load, the effect of plasticity. Plasticity is the deformation of a solid material undergoing non-reversible changes of shape in response to applied forces. Plasticity is characterized by a nonlinear relationship between stress and strain. In general, the relationship between the stress and strain that a particular material displays is known as that particular material's stress–strain curve. It is unique for each material and is found by recording the amount of deformation (strain) at distinct intervals of tensile or compressive loading (stress).

In this thesis the behavior of solid matter is investigated, when energy is transferred by either laser photonic excitation or joule heating, occurring from external strong currents. Computational models and numerical simulations are developed and, in parallel with results from optical experimental techniques, establish the frame of the study. Phase transitions, as well as plasticity effects, are taken into account for the dynamic behavior of excited matter.

Material excitation including metals, semiconductors and dielectrics, by nanosecond pulsed lasers has received considerable attention over the past decades due to its important technological applications, particularly in industry, medicine, and scientific research related to fusion [2-5]. With regard to fast photonic excitation, the dynamic behavior on metallic films-substrate systems, using ultrafast lasers with wavelengths in the visible wavelength region, is studied in this thesis. The study is based on the development of a finite element numerical model, which is validated by interferometric experimental results. The generation of secondary ultrasounds on thin-metal films-substrate systems excited by nanosecond laser pulses is also investigated. Laser-generated ultrasonic waves have diverse applications ranging from material characterization to nondestructive evaluation [6-10].

With respect to matter behaviour dynamics, governed by the interaction with external strong currents, the early time dynamics of the processes involved in the explosion of the wire may be important for the development of Magneto-Hydrodynamic (MHD) instabilities [11-16]. In this thesis, the Z-pinch target configuration [11, 13, 16] is chosen because it offers extensively studied plasma geometry over the years, with well understood plasma characteristics and dynamics

and satisfactory defined plasma instabilities. Numerical simulations are developed in order to investigate the initial stages of the matter's change from the thermoelastic to the melting and plasma regimes and are validated by experiments performed using a Z-pinch pulsed powered plasma device. Improvements in the technology of fast pulsed electrical power have re-opened interest in the field of fast, dynamic Z-pinches as X-ray sources for indirect-drive Inertial Confinement Fusion applications [17, 18].

1.2 Basic schemes of the study

From the early 60's, when the first ruby laser was made functional till nowadays, the study of laser interaction with solid materials, including laser produced plasmas, is one of the fastest growing fields of present-day physics. Lasers have the capability to accurately deliver large amounts of energy into confined regions of a material to achieve a desired response. The radiative energy delivered per unit area is called fluence and represents the energy density. However, laser-solid interaction is an interdisciplinary and complicated subject [19].

In this thesis the transfer of nanosecond pulsed energy to thin metallic film-substrates is investigated by numerical simulation and validated by experimental results. A thin film is a layer of material ranging from fractions of a nanometer (down to a monolayer) to several micrometers in thickness. Deposition process, which is the controlled synthesis of materials as thin films, is a fundamental step in many applications. A familiar example is the household mirror, which typically has a thin metal coating on the back of a sheet of glass to form a reflective interface. Advances in thin film deposition techniques during the 20th century have enabled a wide range of technological breakthroughs in areas such as magnetic recording media, electronic semiconductor devices, LEDs, antireflective optical coatings, hard coatings on cutting tools, and for energy generation (e.g. thin film solar cells and storage thin-film batteries). The thermomechanical properties of thin films are also important for applications in harsh environmental conditions. High energy irradiated chamber internal walls [20], electronic devices for space industry [21] and nuclear applications, (i.e. fusion chambers) as well as optical materials supporting high power lasers [22, 23] are typical representative examples of such environments.

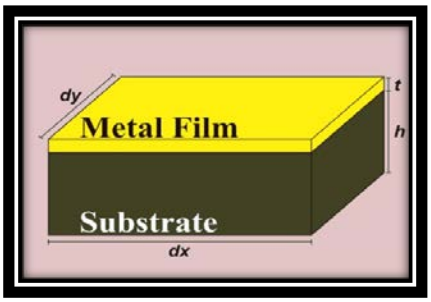

Figure 1.1 Schematic description of a thin film-substrate

During pulsed laser metallic thin-film interaction, the laser pulse deposits most of its energy on the film's surface and absorption occurs. As a consequence of the resulting heating of the surface, the thermo-mechanical properties of the film will be dynamically modified. The effectiveness of a thin film coating depends critically on its chemical properties, as well as its macroscopic mechanical characteristics, such as thickness and adhesion to the substrate. Moreover, surface acoustic waves (SAWs) are generated, and their propagation depends both on the film and substrate elastic properties, as well as on the laser pulse characteristics. A SAW is an acoustic wave traveling along the surface of a material exhibiting elasticity, with amplitude that typically decays exponentially with depth into the substrate. SAWs provide valuable elastic information in the vicinity of the surface over which the waves propagate, because the surface wave phase velocity is directly dependent on the elastic tensor of the material [24].

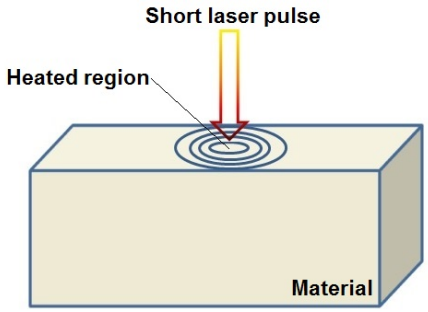

Figure 1.2 Generation of SAWs from pulsed laser irradiation

More specifically, SAWs behaviour strongly depends on the thermal diffusion, laser optical penetration, material structure and composition, as well as on parameters

of the exciting laser beam, such as power, temporal characteristics, and focusing geometry. SAWs propagation along the thin film surface is also influenced by the film thickness, as it is much smaller compared to their wavelength. Consequently, SAWs are an efficient tool for determining the mechanical and elastic properties of the film and the substrate [25, 26].

SAWs were first explained in 1885 by Lord Rayleigh, who described the surface acoustic mode of propagation [27]. Rayleigh waves, named after their discoverer, have a longitudinal and a vertical shear component that can couple with any media in contact with the surface. They are a type of surface acoustic waves that travel on solids. They can be produced in materials in many ways, such as by a localized impact or by piezo-electric transduction, and are frequently used in non-destructive testing for detecting defects. When guided in layers they are referred to as Lamb waves or Rayleigh–Lamb waves.

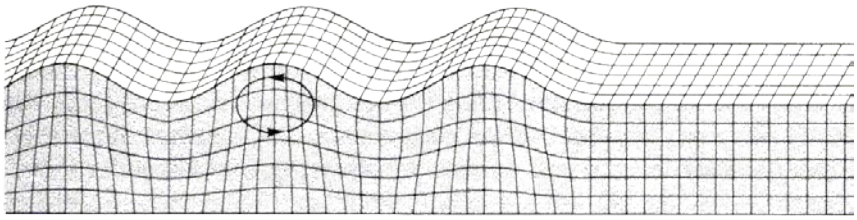

Figure 1.3 Rayleigh wave motion [28]

During the illumination of the metallic target by nanosecond laser pulses, since the thermal equilibrium between the electrons and the lattice is a process that last a few picoseconds, the electron gas is always in thermal equilibrium with the lattice. Three are the regimes of interest depending on the absorbed laser intensity on target (i.e. the absorbed laser fluence per unit time). Figure 1.4 schematically presents the regimes of the interaction, namely the thermoelastic (Figure 1.4a), the melting (Figure 1.4c) and the plasma (ablation) regime (Figure 1.4d) [10]. For lower intensities, the thermoelastic regime is dominant, where the metallic film surface driven deformation does not affect the elastic properties of the lattice and therefore of the film. Due to the absorption of the laser energy on the film, the temperature of the irradiated volume increases, which in turn causes a local thermal expansion. The localized thermal expansion generates a stress field and ultrasonic waves that propagate in the target are

generated (Figure 1.4b) [7, 29]. The laser-generated ultrasonic waves propagate out of the interaction region in all directions.

As the laser intensity increases further, the film's surface temperature reaches its melting point. As a consequence, the mechanical and thermal as well as the optical properties of the target's material change rapidly. The material is melted and transformed into its liquid phase (Figure 1.4c). For even higher laser intensities on target, the film's surface reaches its boiling point and the process of material removal from the target (ablation) begins [30-32]. This is the ablation regime of the interaction. At low laser intensities the leading edge of the laser pulse generates a vapour plume, which behaves like an optically thin medium. As a result, the rest of the laser pulse passes through the vapour plume nearly unattenuated. At higher laser intensities the temperature of the vapour plume increases and appreciable atomic excitation and ionization occurs among with the increase of the vapour density. The ionized vapour plume partly absorbs the incident laser photons leading to plasma plume formation [33, 34] (Figure 1.4d). A plasma plume (composed of electrons, ions and excited neutrals) is generated, which is characterized by the plasma properties such as the plasma temperature, density, and plasma frequency. Due to the inverse bremsstrahlung and photoionization absorption mechanisms, an appreciable part of the laser energy is absorbed in this phase of the interaction and dense plasma is formed [35, 36].

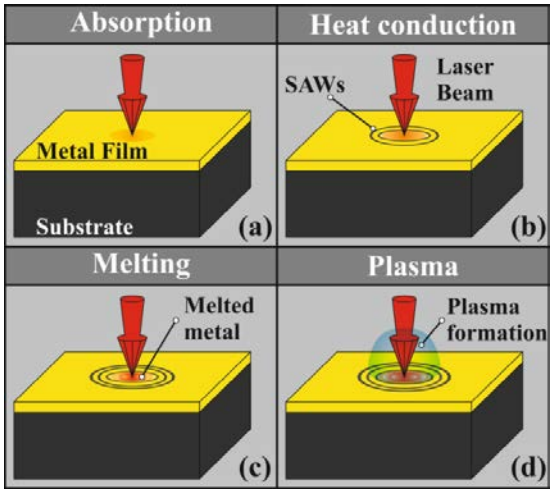

Figure 1.4 Regimes for ns laser pulse-metal film interaction: (a), (b) thermoelastic, (c) melting, and (d) plasma regimes

With respect to the study of matter behaviour dynamics, governed by the interaction with external strong currents, the simplest possible geometry is that of a single wire, the so called Z–pinch [11, 13, 37]. This is a vacuum discharge produced plasma device, which uses an electrical current to heat and convert matter into plasma state and to generate strong magnetic fields that subsequently compress it. Such plasma confinement device consists of an energy storage unit (i.e. a MARX bank), a pulse forming line and a metallic wire attached between two electrodes. Initially, the wire is heated up until it becomes a column of plasma, which then continues to drive the current along the axial direction. An azimuthal magnetic field is created along with a $\boldsymbol{J}\times\boldsymbol{B}$ force, which not only confines the plasma but may also be responsible for the appearance of MHD instabilities, such as m=0 (sausage mode instability) and m=1 (kink instability) [11, 13, 37]. The advantages of the Z-pinch are that larger volumes of plasma can be produced of very high energy density, and with greater efficiency than in laser-produced plasmas.

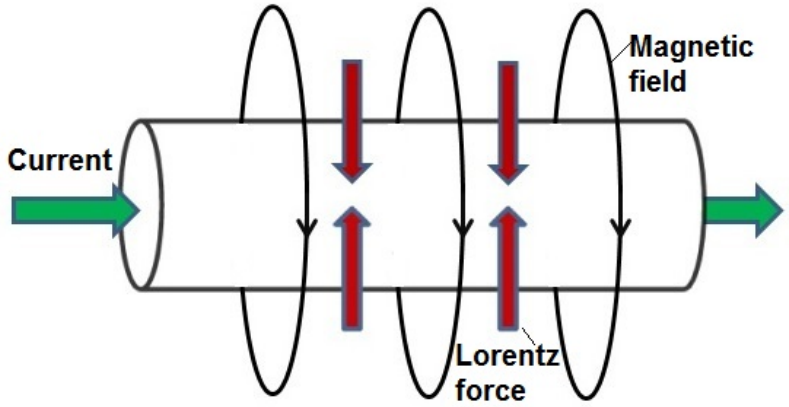

Figure 1.5 Z-pinch wire

Nowadays, the pulsed power exploding wire experiments also provide a versatile arena for studying high-energy density physics (HEDP), with applications in inertial confinement fusion [38] and laboratory astrophysics [39]. Such research is of high importance, since large-scale projects, such as NIF at the US, HiPER and LMJ in Europe, aiming at the production of fusion energy, are progressing fast.

In order to investigate the initial stages of the matter's change from thermoelastic to melting and plasma regimes, thick metallic copper wires have been used in this study. For such wires, electrical charges flow through the skin depth, which plays an

important role for the exploding dynamics. Skin depth effect is the tendency of the fast-changing current to gradually diffuse through the thickness of the conductor, resulting in current density being highest near the surface of the conductor [40]. The skin depth δ is calculated

$$\delta = \frac{1}{\sqrt{\pi f \mu \sigma}} \tag{1.1}$$

where f is the frequency of the rising current, μ is the permeability of the conductor and σ is the electrical conductivity.

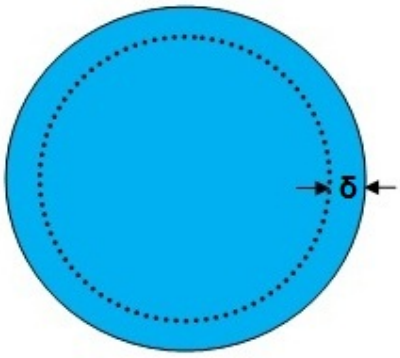

Figure 1.6 Skin depth effect

Numerical simulations, based on the Finite Element Method (FEM) and combined with Finite Volume Method (FVM) simulations, are developed to provide valuable insights for important quantitative parameters such as temperature, density and expansion rate of the exploded material from solid phase to plasma expansion. For this purpose, hydrodynamic response of the material is also taken into account. Moreover, laser probing diagnostics, such as schlieren, interferometric, and diffraction imaging techniques, have been used for the measurement of the wire's dynamics at the initial stages of the explosion. Comparison with the experimental results is performed, for the better understanding of the phenomena. The initiation of MHD instabilities in plasma and the influence of the thermoelastic regime on their creation are also investigated. In Figure 1.7 the two main instabilities that occur in a Z-pinch wire are depicted.

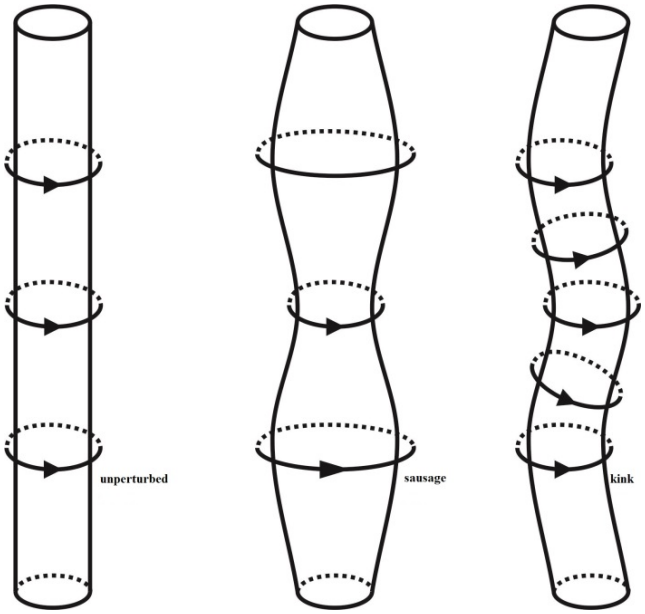

Figure 1.7 Unperturbed (left), *m*=0 (sausage), and *m*=1 (kink) instabilities of a metallic wire

1.3 Outline of the thesis

Chapters 2, 3 and 4 refer to the deposition of energy in matter via pulsed laser matter interaction, while Chapters 5, 6 and 7 refer to the deposition of energy in matter via single wire explosion. Chapter 8 refers to concluding remarks for both parts of the investigation.

More specifically, Chapters 2 and 5 contain the state of the art and literature review for pulsed laser solid matter interaction, and single wire explosion, respectively. Chapters 3 and 6 refer to the mathematical and numerical modeling of pulsed ns laser interaction with matter and of single wire explosion, respectively. The numerical results and their interpretation, as well as the comparison with experimental data, including some suggestions for future work, are presented in Chapters 4 and 7.

1.4 Publications resulted from this work

Journal articles

[1] Y. Orphanos, V. Dimitriou, **E. Kaselouris**, E Bakarezos, Nikolaos Vainos, M. Tatarakis, N. A. Papadogiannis, An integrated method for material properties characterization based on pulsed laser generated surface acoustic waves, *Microelectron. Eng.* **112**, 249-254 (2013).

[2] V. Dimitriou, **E. Kaselouris**, Y. Orphanos, E Bakarezos, Nikolaos Vainos, M. Tatarakis, N. A. Papadogiannis, Three dimensional transient behavior of thin films surface under pulsed laser excitation, *Appl. Phys. Letters* **103**, 114104 (2013).

[3] V. Dimitriou, **E. Kaselouris**, Y. Orphanos, E Bakarezos, N. Vainos, I. K. Nikolos, M. Tatarakis, N. A. Papadogiannis, The thermo-mechanical behavior of thin metal films on dielectric substrates under nanosecond laser pulse excitation above the thermoelastic regime, *Appl. Phys. A.* **118**, 739-748 (2015).

[4] **E. Kaselouris**, I.K. Nikolos, Y. Orphanos, E Bakarezos, N. A. Papadogiannis, M. Tatarakis, V. Dimitriou, A Review of simulation methods of laser matter interactions focused on nanosecond laser pulsed systems, *J. Multiscale Model.* (2015) **05**, 1330001 DOI: 10.1142/S1756973713300013.

[5] **E. Kaselouris**, I. K. Nikolos, Y. Orphanos, E Bakarezos, N. A. Papadogiannis, M. Tatarakis, V. Dimitriou, Elastoplastic study of nanosecond-pulsed laser interaction with metallic films using 3D multiphysics fem modeling, *Int. J. Damage Mech.* **25**(1), 42-55 (2016).

[6] **E. Kaselouris**, E. Skarvelakis, I. K Nikolos, G. Stavroulakis, Y. Orphanos, E. Bakarezos, N. A Papadogiannis, M. Tatarakis and Vasilios Dimitriou, Simulation of the Transient Behavior of Matter with Characteristic Geometrical Variations & Defects Irradiated by Nanosecond Laser Pulses Using FEA, *Key Engineering Materials* **665**, 157-160 (2016).

[7] **E. Kaselouris**, I. Fitilis, A. Skoulakis, G. Koundourakis, V. Dimitriou, I. K. Nikolos, E. L. Clark, M. Bakarezos, N. A. Papadogiannis and M. Tatarakis, The influence on plasma instabilities during the solid-plasma phase transition, (prepared for submission, September 2016).

Conference proceedings

[1] Ι. Ορφανός, Β. Δημητρίου, **Ε. Κασελούρης**, Σ. Μπρέζας, Ε. Μπακαρέζος, Μ. Ταταράκης, Ν. Βάινος, Ν.Α. Παπαδογιάννης, Τρισδιάστατη απεικόνιση ολικού πεδίου νανο-ακουστικών κυμάτων σε μεταλλικές και διηλεκτρικές επιφάνειες με τη χρήση παλμικών πηγών laser, *6ο Πανελλήνιο Συνέδριο Ακουστικής*, Πρακτικά ΣΣ. 120-127, ΕΚΔ: Α. Φλωρός &Α. Μνιέστρης, 8-10 Οκτωβρίου 2012, Κέρκυρα.

[2] **E. Kaselouris**, Y. Orphanos, V. Dimitriou, E. Bakarezos, N. Vainos, M. Tatarakis, N. A. Papadogiannis, 3D finite element modeling of laser-generated surface acoustic waves in film-substrate systems validated by experiments, *10th HSTAM International Congress on Mechanics*, 25-27 May 2013, Chania.

[3] **E. Kaselouris**, V. Dimitriou, I. K. Nikolos, Y. Orphanos, E. Bakarezos, N.A. Papadogiannis, M. Tatarakis, Numerical simulations for the study of matter behavior dynamics governed by the interaction with laser pulses or external strong currents, *10th HSTAM International Congress on Mechanics*, 25-27 May 2013, Chania.

[4] V. Dimitriou, **E. Kaselouris**, Y. Orphanos, E. Bakarezos, N. Vainos, I. K. Nikolos, N.A. Papadogiannis, M. Tatarakis, Matter dynamics under the interaction with laser pulses in the thermoelastic & plasma regimes, *40th EPS Conference on Plasma Physics*, Volume 1, Pages 493-496, 1-5 July 2013, Espoo Finland.

[5] **E. Kaselouris,** V.M. Dimitriou, A. Skoulakis, I. Fitilis, Y. Orphanos, I. K. Nikolos, E. Bakarezos, N. Papadogiannis, M. Tatarakis, Experimental and numerical study of the initial stages of explosion of thick single wire z-pinch, *41th EPS Conference on Plasma Physics*, 23-27 June 2014, Berlin.

[6] **E. Kaselouris**, I. K. Nikolos, Y. Orphanos, E. Bakarezos, N. Vainos, N.A. Papadogiannis, M. Tatarakis and V. Dimitriou, 3D multiphysics FEM modeling of nanosecond pulsed laser interaction with metallic films, *Joint 11th World Congress on Computational Mechanics, WCCM, and the 5th European Conference on Computational Mechanics*, Proceedings Vol II, 758-769, 20-25 July 2014, Barcelona.

[7] Ε. Τζιανάκη, Ι. Ορφανός, **Ε. Κασελούρης**, Ε. Μπακαρέζος, Β. Δημητρίου, Ν. Βάϊνος, Μ. Ταταράκης, και Ν.Α. Παπαδογιάννης, Νανοακουστικά κύματα με τη χρήση υπερβραχέων παλμών λέιζερ και οι εφαρμογές τους σε σύνθετα υλικά, *7ο Πανελλήνιο Συνέδριο Ακουστικής*, Πρακτικά ΣΣ. 270-277, 20-21 Οκτωβρίου 2014, Θεσσαλονίκη.

[8] I. Fitilis, A. Skoulakis, **E. Kaselouris**, I. K. Nikolos, E. Bakarezos, N. A. Papadogiannis, V.M. Dimitriou, M. Tatarakis, Diagnosing the initial stages from solid to plasma phase for dense plasma explosions, *Proceedings of Science*, Volume 2015, 1st *EPS Conference on Plasma Diagnostics*, 14-17 April 2015, Frascati, Italy.

[9] I. Fitilis, A. Skoulakis, **E. Kaselouris**, I. K. Nikolos, E. Bakarezos, N. A. Papadogiannis, V.M. Dimitriou, M. Tatarakis, Progress of the initial times of single wire explosion for plasma generation through numerical and experimental method, *42th EPS Conference on Plasma Physics*, 22-26 June 2015, Lisbon.

[**10**] **E. Kaselouris,** A. Skoulakis, V.M. Dimitriou, I. Fitilis, I. K. Nikolos, E. Bakarezos, N. A. Papadogiannis, M. Tatarakis, Finite Element study of the initial stages of explosion of single wire z-pinch validated by experiments, *8th GRACM International Congress on Computational Mechanics*, 12-15 July 2015, Volos.

[11] **E. Kaselouris**, E. Skarvelakis, I. K Nikolos, G. Stavroulakis, Y. Orphanos, E. Bakarezos, N. A Papadogiannis, M. Tatarakis and Vasilios Dimitriou, A FEM study on the influence of the geometric characteristics of metallic films irradiated by nanosecond laser pulses, *8th GRACM International Congress on Computational Mechanics*, 12-15 July 2015, Volos.

References

[1] J. Han and Y. Li, *Interaction between pulsed laser and materials, Laser-Applications in Science and Industry*, ed. K. Jakubczak (InTech, 2011).

[2] N. Bloembergen, From nanosecond to femtosecond science, *Reviews of modern Physics*, **71** SUPPL. 2, S283-S287 (1999).

[3] M. S. Brown and C. B. Arnold, *Fundamentals of laser-material interaction and application to multiscale surface modification, Laser Precision Microfabrication*, Vol. 135, eds. K. Sugioka, M. Meunier and A. Piqué (Springer Series in Materials Science, 2010), pp. 91-120.

[4] W. A. Eaton, V. Muñoz, S. J. Hagen, G. S. Jas, L. J. Lapidus, E. R. Henry and J. Hofrichter, Fast kinetics and mechanism in protein folding, *Annual Review of Biophysics and Biomolecular structure* **29**, 327-359 (2000).

[5] L. J. Waxer, D. N. Maywar, J. H. Kelly, T. J. Kessler, B. E. Kruschwitz, S. J. Loucks, R. L. McCrory, D. D. Meyerhofer, S. F. B. Morse, C. Stoeckl and J. D. Zuegel, High-energy petawatt capability for the omega laser, *Optics and Photonic news* **16**, 30-36 (2005).

[6] P. Cielo, F. Nadeau and M. Lamontagne, Laser generation of convergent acoustic waves for materials inspection, *Ultrasonics* **23**, 55-62 (1985).

[7] R. J. Dewhurst, C. Edwards and A. D. W. Mckie, Estimation of the thickness of thin metal sheet using laser generated ultrasound, *Appl. Phys. Lett.* **51**, 1066 (1987).

[8] J. D. Aussel and J. P. Monchalin, Precision laser-ultrasonic velocity measurement and elastic constant determination, *Ultrasonics* **27**, 165-177 (1989).

[9] C. E. Scruby and L. E. Drain, *Laser ultrasonics techniques and application*, Adam Hilger, New York (1990).

[10] S. J. Davis, C. Edwards, G. S. Taylor and S. B. Palmer, Laser-generated ultrasound: its properties, mechanism and multifarious application, *J. Phys. D: Appl. Phys.* **26**, 329–348 (1993).

[11] M. G. Haines, A review of the dense Z-pinch, *Plasma Phys. Control. Fusion* **53**, 093001 (2011).

[12] V. I. Oreshkin, et al., Wire explosion in vacuum: Simulation of a striation appearance, *Phys. Plasmas* **11**, 4771-76 (2004).

[13] D. D. Ryutov, M. S. Derzon, M. K. Matzen, The physics of fast Z pinches, *Reviews of Modern Physics*, **72(1)**, 167-223 (2000).

[14] S. V. Lebedev, F. N. Beg, S. N. Bland, J. P. Chittenden, A. E. Dangor, M. G. Haines, S. A. Pikuz and T. A. Shelkovenko, Effect of core-corona plasma structure on seeding of instabilities in wire array Z pinches, *Phys. Rev. Lett.* **85**, 98-101 (2000).

[15] M. Tatarakis et al., Optical probing of fiber z -pinch plasmas, *Phys. Plasmas* **5**, 682 (1998).

[16] M. Tatarakis, Optical probing of dense Z-pinch and laser produced plasma, PhD thesis 1997.

[17] M. K. Matzen, Pulsed-power-driven high energy density physics and inertial confinement fusion research, *Phys. Plasmas* **12**, 055503 (2005).

[18] J. H. Hammer, M. Tabak, S. C. Wilks, et al., High yield inertial confinement fusion target design for a z-pinch-driven hohlraum, *Phys. Plasmas* **6**, 2129-2136 (1999).

[19] M. Von Allmen and A. Blatter, *Laser-beam interactions with materials: Physical principles and applications* (Springer-Verlag, Berlin, 1995).

[20] A. R. Raffray, D. Haynes and F. Najmabadi, *J. Nucl. Mater.* **313**, 23 (2003).

[21] K. A. LaBel, A. H. Johnson, J. L. Barth, R. A. Reed and C. E. Barnes, *IEEE T. Nucl. Sci.* **45**, 2727 (1998).

[22] D. Garoz, R. Gonzalez-Arrabal, R. Juarez, J. Alvarez, J. Sanz, J. M. Perlado and A. Rivera, *Nucl. Fusion* **53**, 013010 (2013).

[23] R. M. Wood, *Laser-Induced Damage of Optical Materials* (Institute of Physics Publishing, Bristol & Philadelphia, 2003).

[24] D. Schneider, T. Schwarz, H-J Scheibe and M. Panzner, Non-destructive evaluation of diamond and diamond-like carbon films by laser induced surface acoustic waves, *Thin Solid Films* **295** (1997) 107-116.

[25] D. C. Hurley, V. K. Tewary and A. J. Richards, *Meas. Sci. Technol.* **12**, 1486 (2001).

[26] P. Hess, Laser diagnostics of mechanical and elastic properties of silicon and carbon films, *Appl. Surf. Sci.* **106**, 429 (1996).

[27] Lord Rayleigh, On Waves Propagated along the Plane Surface of an Elastic Solid, *Proc. London Math. Soc.* **s1-17 (1)**, 4–11 (1885).

[28] http://folk.uio.no/valeriem/spice/Frame/surfacew/

[29] C. B. Scruby, R. J. Dewhurst, D. A. Hutchins and S. B. Palmer, Quantitative studies of thermally-generated elastic waves in laser-irradiated metals, *J. Appl. Phys.* **51**, 6210-6216 (1980).

[30] X. Mao and R. E. Russo, *Appl. Phys. A* **64**, 1 (1996).

[31] R. Fang, D. Zhang, Z. Li, F. Yang, L. Li, X. Tan and M. Sun, Improved thermal model and its application in UV high-power pulsed laser ablation of metal target, *Solid State Commun.* **145**, 556 (2008).

[32] Z. Chen and A. Bogaerts, *J. Appl. Phys.* **97**, 063305 (2005).

[33] S. Amoruso, R. Bruzzese, N. Spinelli and R. Velotta, Characterization of laser-ablation plasmas, *J. Phys. B* **32**, R131 (1999).

[34] S. Amoruso, Modeling of UV pulsed-laser ablation of metallic targets, *Appl. Phys. A* **69**, 323 (1999).

[35] Ya. B. Zel'dovich and Yu. P. Raizer, *Physics of Shock Waves and High-Temperature Hydrodynamic Phenomena*, 2 vols (Academic Press, New York, 1966-67).

[36] A. V. Bulgakov and N. M. Bulgakova, Thermal model of pulsed laser ablation under the conditions of formation and heating of a radiation-absorbing plasma, *Quantum Electron.* **29**, 433 (1999).

[37] M. G. Haines, S. V. Lebedev, J. P. Chittenden, F. N. Beg, S. N. Bland and A. E. Dangor, The past, present, and future of Z pinches, *Phys. Plasmas* **7**, 1672-1680 (2000).

[38] M. K. Matzen, M. Sweeney, R. G. Adams, J. R. Asay, J. E. Bailey et al. Pulsed-power-driven high energy density physics and inertial confinement fusion research. *Phys. Plasmas* **12**, 1–16 (2005).

[39] G. A. Rochau, J. E. Bailey, R. E. Falcon, G. P. Loisel, T. Nagayama et al. ZAPP : The Z Astrophysical Plasma Properties collaboration. *Phys. Plasmas* **21**, 056308 (1–7) (2014).

[40] Jordan, Edward Conrad, *Electromagnetic Waves and Radiating Systems*, Prentice Hall, 1968.

Chapter 2

2. State of the art-Literature review of pulsed laser solid matter interaction

2.1 Light propagation in solid materials and energy absorption mechanisms

When laser radiation is incident on a solid surface, a part of it gets reflected, while the rest penetrates into the material within the laser light penetration depth and gets absorbed. Maxwell's equations describe the electromagnetic waves (laser photons) that propagate through material [1]. In the case of a plane wave propagating along the z-axis, the electric field strength *E(z,t)* can be written as

$$E(z,t) = E_0 e^{-(\omega/c)kz} e^{i(\omega/c)nz} e^{-i\omega t} \tag{2.1}$$

where E_0 is the amplitude of the field strength, n the index of refraction of the solid, k the extinction coefficient, ω the angular frequency of the wave and c is the propagation velocity of the laser light in the medium. The first exponential term describes attenuation of the wave, while the characteristics of free propagation are given by the last two terms. The intensity of an electromagnetic wave decreases over distance when passing through an absorbing medium, since it is proportional to the square of the amplitude.

The fraction of the incident power that is reflected from the surface depends on the polarization and angle of incidence θ_i of the light, as well as the index of refraction of the atmosphere n_1 and the material n_2. The reflection coefficients for the s-polarized and p-polarized components of the light can be calculated from the Fresnel equations [2]

$$R_s = \left[\frac{E_r}{E_i}\right]^2 = \left[\frac{n_1 \cos(\theta_i) - n_2 \cos(\theta_t)}{n_1 \cos(\theta_i) + n_2 \cos(\theta_t)}\right]^2 \tag{2.2}$$

$$R_p = \left[\frac{E_r}{E_i}\right]^2 = \left[\frac{n_1 \cos(\theta_t) - n_2 \cos(\theta_i)}{n_1 \cos(\theta_t) + n_2 \cos(\theta_i)}\right]^2 \quad (2.3)$$

and are related to the transmission coefficients through $T_s=1-R_s$ and $T_p=1-R_p$. For the case of normally incident light on a flat surface, the above equations reduce to [2]

$$R = R_s = R_p = \left(\frac{n_1 - n_2}{n_1 + n_2}\right)^2 \quad (2.4)$$

The reflectivity of a given material depends on the frequency of the light source through the dispersion relation of its index of refraction. In the case of normal incidence, values for reflectivity of metals in the near UV and visible spectral range are typically between 0.4 and 0.95 and between 0.9 and 0.99 for the IR, as shown for some characteristic metals in Figure 2.1 [3]. Moreover, reflectivity of a surface depends on the material, the nature of surface, the level of oxidation, temperature, wavelength, and power density of incident radiation. Reflectivity alters dramatically with the increase of the incident power density, time of exposure, and temperature. Most real life surfaces are not perfectly flat and have certain degrees of texture and roughness to them, which influence their optical behaviour [4].

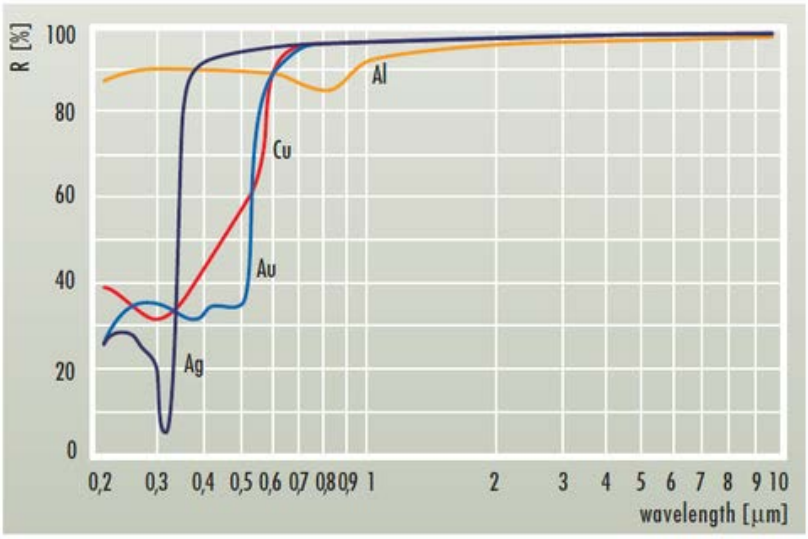

Figure 2.1 Reflectivity of common metals versus wavelength [3]

As previously mentioned, a portion *(1−R)* of the incoming laser radiation penetrates into the target surface, where *R* is the reflectivity of the solid target surface. Once inside the material, absorption causes the intensity of the light to decay with depth at a rate determined by the material's absorption coefficient *α*. According to the Beer–Lambert law [5, 6] intensity *I* decays exponentially with depth *z*

$$I(z) = (1-R)I_0 e^{-\alpha z} \tag{2.5}$$

where I_0 is the intensity just inside the surface after considering reflection loss, $\alpha = 4\pi k/\lambda_0$ is the absorption coefficient, *k* the extinction coefficient (imaginary part of the refraction index) and λ_0 is the wavelength. Different methods have been developed to experimentally determine the optical constants, *n* and *k*, with respect to light and material parameters, such as wavelength and temperature. For these constants extensive databases exist [7, 8], although they mostly refer to pure materials at room temperature with clean and smooth surface conditions. The reciprocal of the absorption coefficient is the characteristic absorption depth *δ,* the depth at which the intensity of the transmitted light drops to *1/e* of its initial value at the interface. Figure 2.2 shows optical absorption depths as a function of wavelength for a variety of metals and semiconductors [9]. An important aspect to note from Figure 2.2 is that the absorption depths are short relative to bulk material dimensions, hence the choice of a wavelength with short absorption depths allows for local modification of surface properties without altering the bulk of the material.

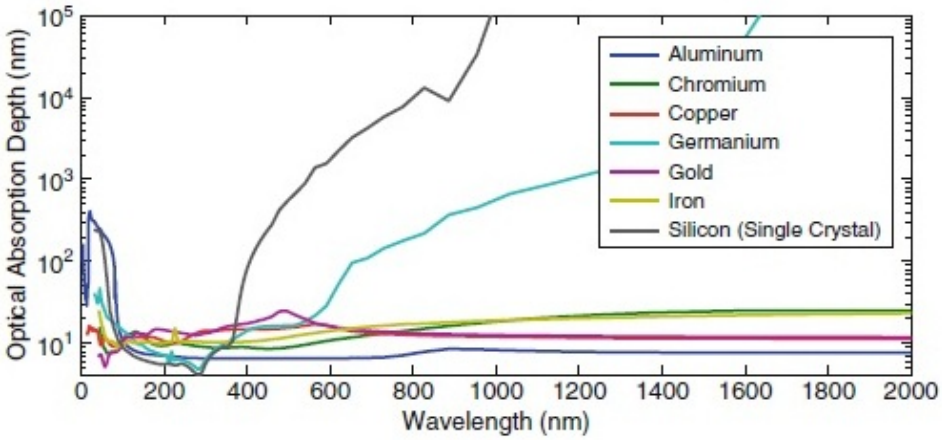

Figure 2.2 Optical absorption depths for several materials over a range of wavelengths [9]

The absorption of laser energy in a solid depends on a variety of different parameters, involving both laser parameters and the physical and chemical properties of the material. Laser parameters are the wavelength, intensity, pulse duration, spatial and temporal coherence, polarization, and angle of incidence. The intensity is a combination of the power and focal spot size of the laser beam, while the polarization of the beam is related to the orientation of the electric field in the light wave [4, 10]. The material is characterized by its chemical composition and microstructure, that is the arrangement of atoms or molecules, which determine the type of elementary excitations and the interactions between them [10], as well as its thermal and mechanical properties. The composition refers to whether we are dealing with a pure element (such as copper, iron, aluminum, etc.) or an alloy (such as brass or steel). In addition, absorption is also heavily dependent upon the surface properties of material. Regardless of the composition, light always interacts mainly with the electrons inside the metal or the alloy, since light is an electromagnetic wave and electric and magnetic fields only interact with charged matter. The atomic nuclei are so heavy that they cannot absorb light easily, therefore their direct interaction with light is neglected. Electrons are accelerated by the electric field and through various collisions among them with the other constituents of the metallic solid, energy is transferred to the lattice [11].

In a metal, atoms readily lose their valence electrons, forming positive ions. The free electrons are spread over the entire solid, which is held together firmly by electrostatic interactions between the ions and the electron cloud. When an ultrashort laser irradiates a metal free electrons absorb the laser photons through inverse Bremsstrahlung [12]. Moreover, for laser pulses of nanosecond duration, most of the absorption is due to single photon interactions.

After the absorption of laser energy into the solid target, thermalization occurs within the electron subsystem, followed by fast energy transfer to the lattice and energy losses due to the electron heat transport into the target [11, 13]. When the laser-induced excitation rate is low in comparison to the thermalization rate (typically in picosecond range of metals), the dynamics of the transient electronically excited states are not significant. The absorbed laser energy is considered to be directly transformed into heat (i.e. the laser energy is considered to absorb directly by lattice).

Such processes are called photothermal and the material response can be treated in a purely thermal way. Therefore, laser interaction with metals or semiconductors for slow laser pulse times (>=ns) is typically characterized by photothermal mechanisms. In this case electron and lattice is considered always in thermal equilibrium.

For nanosecond laser excitation and from a macroscopic perspective, the spatiotemporal evolution of the temperature field inside a material is governed by the heat equation. The heat equation is derived from the conservation of energy and Fourier's law of heat conduction, which states that the negative of the gradient of the temperature is proportional to the local heat flux. The heat equation for a coordinate system that is fixed with the laser beam, can be written as [12]

$$\rho(\mathbf{r},T)c_p(\mathbf{r},T)\frac{\partial T(\mathbf{r},t)}{\partial t}-\nabla\left[k(\mathbf{r},T)\nabla T(\mathbf{r},t)\right]+\rho(\mathbf{r},T)c_p(\mathbf{r},T)v_s\nabla T(\mathbf{r},t)=Q(\mathbf{r},t) \tag{2.6}$$

where ρ is the mass density, $\boldsymbol{r}$ is a vector of location, c_p is the specific heat at constant pressure, k is the thermal conductivity and v_s is the velocity of the target relative to the heat source. The right side incorporates the contribution of heat sources through the volumetric heating rate $Q(\mathbf{r},t)$. The left hand side describes the evolution of temperature due to heat conduction and takes also into account the convective term v_s to describe the shift in reference frame. Furthermore, the thermal properties of a uniform and isotropic metallic target are characterized by a single thermal conductivity, k and a single heat diffusivity D, with the equation $D=k/\rho c_p$.

The temperature evolution inside the material is given by the volumetric heating term $Q(\mathbf{r},t)$ as well as the boundary conditions for the particular problem. Depending on the special needs of the particular problem, heat exchanges due to convection and radiation at the surface may also be taken into account for the boundary conditions. In most cases, the laser volumetric heating term can approximately be separated into a spatial shape function $g(x,y)$ determining the beam's profile, an attenuation term $f(z)$, and a temporal shape function $q(t)$, which describes the temporal evolution of the laser pulses. Moreover, phase changes can be accounted through the term $U(\mathbf{r},t)$, i.e latent heat of melting or vaporization and consequently the term of volumetric heating has the form [12]

$$Q(\mathbf{r},t) = g(x,y)\,f(z)q(t) + U(\mathbf{r},t) \tag{2.7}$$

An analytical solution for heat equation 2.6 is quite difficult to be found, since it is a non-linear partial differential equation. The situation gets more complicated in real material systems, due to dynamic changes in material's optical, thermal and mechanical properties as a function of temperature and laser intensity. In the minority of cases the problem may be simplified and an analytical solution may be found, e.g. by incorporating laser heating through the boundary conditions for the case of surface absorption, or by setting the material properties constant, or treating the laser shape term as a delta function for the case of a tightly focused laser spot [14].

However, numerical methods are more suitable for dealing with complicated physical processes. Two basic numerical methods for solving the heat equation are the finite difference and the finite element techniques. These methods solve the equation for all internal points and have special equations for the boundaries. The numerical methods have many advantages compared to the analytical methods, due to the fact that the solution domain is divided into many smaller domains that are allowed to have different thermal conductivity, density or heat input values. This fact does not limit the choice and the form that the applied heat source may have. Moreover, temperature-dependent material thermophysical properties and real boundary conditions can be included. Consequently, a numerical analysis can include more detailed physics of the problem and, thus, reveal the effect of different phenomena on the process [15]. In the literature exists a variety of finite difference [16-18] and finite element [19-21] models for pulsed laser interaction with a solid target, which describe the heating on a macroscopic scale by considering the Fourier heat conduction equation with the laser heat as the source term. These models assume instantaneous conversion of laser radiation into heat.

Microscopically, the incident laser radiation can be considered as a source of photons. When photons impinge on a metal target surface some of them get reflected, while the rest are absorbed by the electrons in the metal conduction band. Upon absorption, the electrons get excited in a non-thermal distribution and after electron-electron interactions finally obey a thermal distribution with higher temperature. This

process happens very fast. Consequently, the hot thermal electrons interact among themselves and move inside the metal lattice. In the process, the free electrons collide with the lattice phonons, transferring energy to them. In addition, the phonons interact among themselves until equilibrium is established. The heat equation in metals implies that a complete local thermal equilibrium is reached between the electrons and phonons and this assumption is correct if the duration of the laser pulse is much longer than the characteristic time of electron-phonon relaxation time. The required time for the excited electronic states to transfer energy to phonons and thermalize depends on the specific material and specific mechanisms within the materials. For most of metals, this thermalization time is on the order of 10^{-12}-10^{-11} whereas in non-metals, there is a significantly higher variation in the absorption mechanisms and the thermalization time can be as long as 10^{-6} s [10]. For picosecond (ps) and femtosecond (fs) pulses, however, the electron-phonon equilibrium is not valid and the time evolution of the lattice and electron temperatures, T_l and T_e, is described by two coupled non-linear differential equations [11, 22]

$$C_e(T_e)\frac{\partial T_e}{\partial t} = \nabla(K_e \nabla T_e) - G(T_e - T_l) + Q(\mathbf{r}, t)$$
$$C_l(T_l)\frac{\partial T_l}{\partial t} = G(T_e - T_l) \tag{2.8}$$

where C and K are the heat capacities and thermal conductivities of the electrons and lattice, as denoted by subscripts e and l, while G is the electron-phonon coupling constant. In pure metals, energy transport by free electrons is much greater than that by lattice vibrations. Therefore, heat conductivity by the lattice is neglected. For such instances, modeling is done by considering microscopic interactions of the laser radiation with the target material (two-temperature model) [23-25].

2.2 Material response

The response of the irradiated material depends on a variety of different parameters, involving both the laser and the physical and chemical properties of the material system. For photothermal laser matter interaction and for slow laser induced excitation rates compared to the thermalization time, as already mentioned, one can

consider that the absorbed laser energy is being directly transformed into heat. In this section, focus will be placed on photothermal laser interactions, of nanosecond pulse duration, with metallic solids or films.

The response of material to the incident laser light can be categorized into thermal and mechanical effects. Thermal effects refer to melting, vaporization, boiling, and phase explosion [26], while mechanical response involves deformation and resultant stress in materials. Different thermal processes induce different mechanical responses.

2.2.1 Dynamic Response of Matter in the Thermoelastic Regime

When the irradiated laser fluences are limited below the melting threshold, a variety of temperature dependent processes are taking place within matter. The high generated temperatures can enhance diffusion rates that promote impurity doping, the reorganization of the crystal structure [27], and sintering of porous materials [28]. Selective Laser Sintering (SLS) is an additive manufacturing technique that uses pulsed laser as the power source to sinter powdered material (typically metal), aiming the laser automatically at points in space defined by a 3D model, binding the material together to create a solid structure. In addition, the localized laser heating can induce large temperature gradients, which can lead to rapid self-quenching of the material [29]. Moreover, rapid generation of large temperature gradients can induce thermal stresses and thermoelastic excitation of acoustic waves. These stresses may contribute to the mechanical response of the material, inducing secondary phenomena like work hardening, warping, or cracking [12].

When a solid sample is irradiated by a laser pulse of duration well longer than the electron–phonon energy cooling time, the absorbed energy by electrons increases the localized lattice temperature within the laser pulse duration and, consequently, causes thermal expansion of the sample within the same time interval. The creation of rapid, localized thermal expansion, releases energy in the form of propagating thermomechanical ultrasounds away in all directions from the generation area. The ability of broadband signal generation, the noncontact feature, and the relatively long propagation, make laser generated ultrasounds a reliable tool for nondestructive evaluation and materials characterization [30-32]. Moreover, laser generated

ultrasounds is a reliable tool for defect detection. Various ultrasonic waves excited in the thermoelastic regime have been studied theoretically and experimentally, i.e. longitudinal and transverse waves [33, 34], surface waves [35, 36], and Lamb waves in thin plates [37]. The characteristics of such waves depend on the optical, thermal, elastic and geometrical features of the material [38, 39], as well as on the parameters of the exciting laser pulse [39, 40].

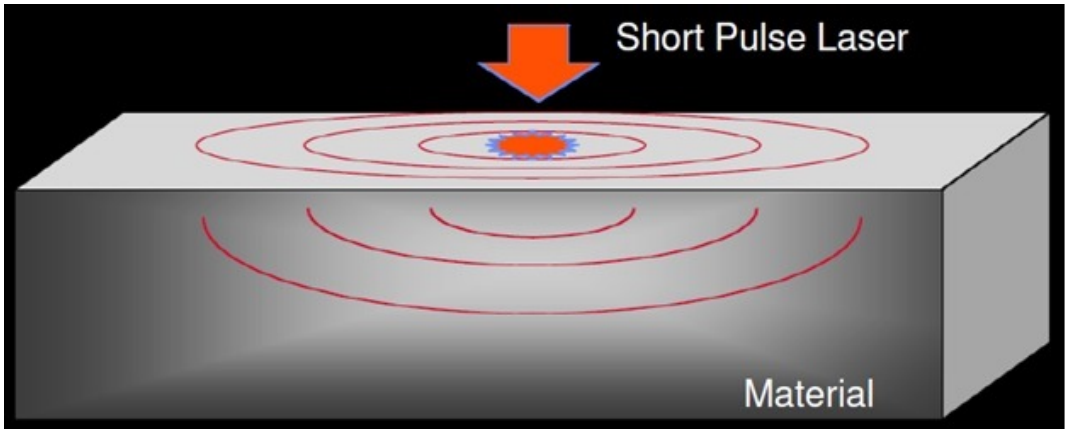

Figure 2.3 Laser generated ultrasounds

2.2.1.1 Review of modeling efforts in thermoelastic regime

The study of the thermoelastically laser-generated ultrasounds using theoretical models with analytical solutions was initiated in the early 1960s by White [41]. In this pioneering work that investigated the generation of thermoelastic waves in a material induced by a surface heat source, a 1-D elastic wave and heat diffusion equation were solved. Later, was described [42] the calculation of the surface displacement for a point radial loading of a half space with Heaviside time dependence. Scruby *et al.* [43] and Dewhurst *et al*. [44] used a Green function formalism to obtain the epicentral displacement due to a thermoelastic source. Similarly, Rose [45] considered the point source as a surface centre of expansion and obtained a formal solution again using a Green function formalism. In these theoretical models the thermal diffusion into the solid is not taken into account. In [46] the effect of thermal diffusion on the thermoelastic wave, predicting an epicenter displacement was investigated. In [33] investigated the wave generation by thermal dipoles in laser-generated ultrasound was investigated, providing a clear explanation as to how longitudinal waves are

generated. These two studies took also into account the finite spatial and temporal shape of the laser pulse. Wang and Xu [47] took into account the non-Fourier effect in heat conduction in the case of the ultrafast laser-induced ultrasonics. Zhang *et al*. [48] obtained the directivity patterns for the longitudinal wave and the transverse wave, taking into account thermal diffusion. In [37] the thermoelastic generation of longitudinal, transverse, and surface-acoustic waves in thick samples, as well as the excitation of the Rayleigh-Lamb wave modes in thin materials was inestigated, using the numerical eigenfunction expansion method.

Moreover, for the case of laser irradiating film-substrate systems, Coulette *et al*. [49] studied the transient mechanical displacement at the epicenter in two-layer plates by using a two dimensional semi-analytical model. Murray *et al*. [50] investigated the surface acoustic waves (SAWs), using a two-dimensional analytical model, based on temporal Laplace and spatial two-dimensional Fourier transformations and assuming the substrate is semi-infinite, while laser irradiation is modelled as a surface force source. In general, they concluded that the propagation of laser generated ultrasound depends not only on the properties of the coating, but also on those of the substrate.

As previously mentioned, the finite element numerical method is suitable to simulate complicated processes, especially when the material (mechanical, thermal, optical) parameters are temperature-dependent. In the literature, Kasai *et al*. [51] predicted photoacoustic signals in a brass sample by using FEM. More recently, Xu *et al*. [52-55] numerically investigated the generation and propagation of ultrasonic waves in metallic plates and film-substrate systems irradiated by pulsed laser using FEM. The 2D finite element study of Xu *et al*. for pulsed laser-generated surface acoustic wave forms in aluminum Al plates of various thicknesses, was the first that took into consideration the temperature-dependent thermal physical parameters for the material along with mechanical properties (temperature-dependent density until the melting point) and temperature-dependent optical absorptivity. In [56] a correlation between the magnitude of the residual stress in a steel block and the surface acoustic wave behavior was demonstrated by finite element modeling. Furthermore, the influence of the laser beam profile on the ultrasonic waves produced in metallic materials was investigated experimentally and numerically with FEM by Cerniglia *et al* [57].

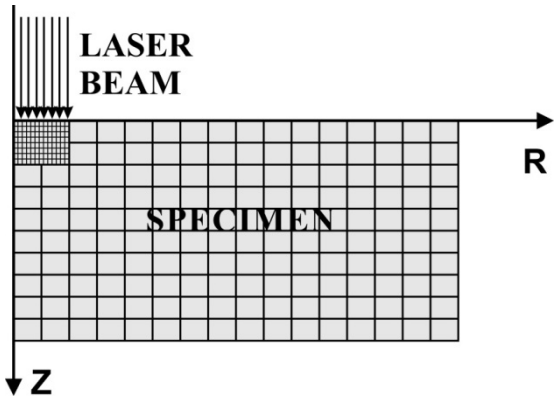

Figure 2.4 Schematic Finite element mesh diagram of the laser irradiating aluminum plate specimen based on the model of Xu et al [52]

2.2.2 Dynamic Response of Matter in the Melting Regime

When laser pulse energy increases, materials absorb more laser energy and the induced temperature exceeds the melting point. At this point the deposited laser fluence causes material melting. Fluences above the melting threshold can lead to the formation of transient pools of molten material on the surface [58, 59]. The molten phase of the material supports much higher atomic mobilities and solubilities than in the solid phase, resulting in rapid material homogenization. High self-quenching rates with high solidification front velocities can be achieved by rapid dissipation of heat into the cooler surrounding bulk material [60]. Moreover, a wide field of material modification becomes accessible upon melting, followed by rapid solidification. These phenomena can change the atomic structure of materials and realize mutual transformation between amorphous and crystalline state [12].

For temperatures higher than the melting temperature, hydrodynamic motion can reshape and redistribute material. Radial temperature gradients can develop in melt pools, causing convective flows to circulate material [60]. For most materials, the liquid's surface tension decreases with increasing temperature and the liquid is pulled from the hotter to the cooler regions (Marangoni effect) [61]. Moreover, selective laser melting is an additive manufacturing process that uses 3D CAD data as a digital information source and energy in the form of a high-power laser beam, to create three-dimensional metal parts by fusing fine metal powders together.

2.2.2.1 Review of modeling efforts in melting regime

A two-dimensional (2D) axisymmetric model of a molten pool created by a pulsed laser heat source was developed by Abderrazak *et al*. [58]. The model solves the coupled equations of laminar fluid flow (equations of continuity and momentum) and heat transfer to demonstrate the flow behavior in the pool using a FEM code. It takes into account the coupled effects of buoyancy and Marangoni forces, the dependent with temperature thermophysical variation properties and the radiation and convection heat losses. Bennett *et al*. [61] proposed a mechanism for topographical features formed during pulsed laser texturing of Ni-P magnetic disk substrates by taking into account the Marangoni effect. This perspective is investigated using Lagrangian finite element modeling for the fluid mechanics coupled with heat and mass diffusion.

O. García *et al*. [62] have investigated both experimentally and by means of a finite element simulation the a-Si local crystallization irradiated by a single nanosecond laser pulse. Different energy regimes were taken into account in order to evaluate the effect of the laser fluence on the a-Si crystallization. A Finite Element study during the heteroepitaxial growth induced by excimer laser radiation of patterned amorphous hydrogenated silicon (a-Si:H) and germanium (a-Ge:H) bi-layers deposited on a Si(100) wafer was carried out by Conde *et al*. [63, 64], using ANSYS software. In heteroepitaxy, a crystalline film grows on a crystalline substrate or film of a different material. The results were verified experimentally by an ArF (193 nm) excimer laser that provided high energy densities during short laser pulse (20 ns), provoking, at the same time, melting and solidification phenomena in the range of several tenths of nanoseconds. The set of Heat Conduction differential equations describing heat propagation were

$$\begin{aligned} \rho(T)c_p(T)\frac{\partial T(\boldsymbol{r},t)}{\partial t} &= \nabla\left[k(T)\nabla T(\boldsymbol{r},t)\right] \text{ for } T<T_{\text{melting}} \\ \frac{\partial H(T)}{\partial t} &= \nabla[k(T)\nabla T(\boldsymbol{r},t)] \text{ for } T \geq T_{\text{melting}} \end{aligned} \tag{2.9}$$

where *H(T)* is the enthalpy function that accounts for phase change. Once the melting point was reached, momentum and mass fraction equations were employed to predict the concentration profiles on both interfaces and borders of the patterned

heterostructures by means of a computational fluid dynamic code. The Boussinesq approximation was taken into account to describe the variation of the fluid density with temperature.

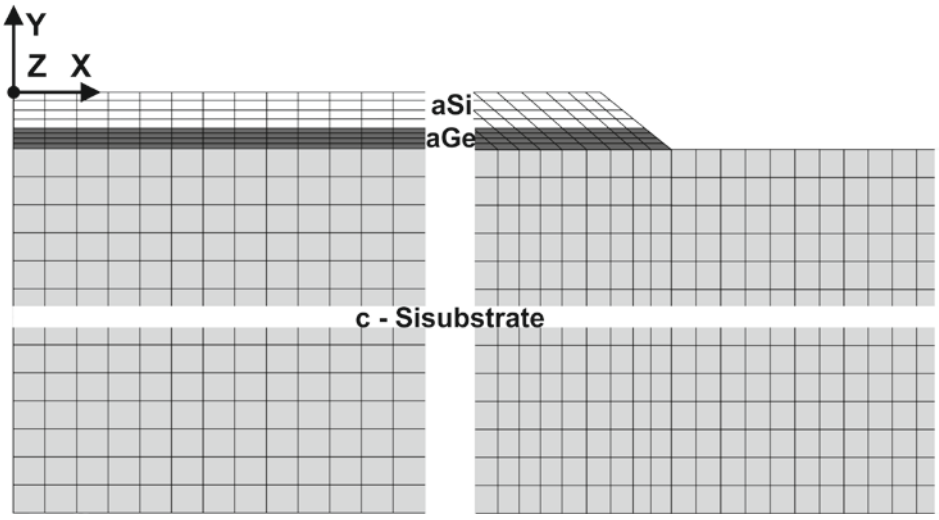

Figure 2.5 Schematic mesh of the axisymmetric finite element model of the a-Si:H(40 nm)/a-Ge:H(20 nm) bi-layers deposited on Si(100) based on the study of Conde *et al.* [64]

In general, most of the analytical models are not able to take into account the effect of the latent heat. However, finite element simulations can apply an artificially enhanced specific heat capacity in a narrow temperature interval (ΔT) close to the melting point so as to simulate the consumption of latent heat for melting or its release to simulate cooling [65]

$$c_p^* = \frac{L_m}{\Delta T} \tag{2.10}$$

2.2.3 Dynamic response of matter in the ablation regime - Plasma formation

Laser ablation is a process where macroscopic amounts of matter leave the solid, following pulsed laser excitation with laser fluence, energy density, higher than a threshold value. The required fluence in order to induce ablation depends on many factors, including the irradiated material as well as the irradiation conditions.

The laser ablation process occurs in two stages. In the first stage, laser energy is absorbed by the target, leading to a temperature increase. In this stage, the main physical processes involve heat conduction, melting, and vaporization of the target. For low laser fluence the produced vapour by the leading edge of the laser pulse behaves like a thin medium and the laser beam passes nearly unattenuated through the vapour. In the second stage, at higher laser fluence the vapour temperature is high enough to cause appreciable atomic excitation and ionization. Then the vapour begins to absorb the incident laser radiation leading to vapour breakdown and plasma formation above a certain fluence threshold. The plasma plume interacts with the incoming laser radiation, absorbing a percentage of it, thereby shielding the target surface and may further expand, depending on the fluence values [66, 67].

Plasma formation due to ablation shields the target surface by absorbing a part of incoming laser radiation. Since plasma consists of three species, electrons, ions, and neutral atoms, absorption of the radiation inside the plasma may occur by different mechanisms. Two are the dominant mechanisms by which the radiation is absorbed by the plasma. The inverse Bremsstrahlung (IB) and the photoionization (PI) processes. Absorption of photons by free electrons in the plasma is described by IB mechanism, while absorption by excited ions and neutral atoms is described by PI mechanism [66, 67].

The onset of ablation occurs above a characteristic fluence threshold. Its value depends on the absorption mechanism, particular thermo-physical material properties, material’s microstructure, morphology, possible presence of defects, and on laser parameters, such as wavelength, laser pulse energy, and pulse duration. In general, fundamental studies of the ablation process of simple one-component materials, such

as metals, allow for a better comprehension of the basic mechanisms involved in laser–solid and laser–plasma interaction. Typical threshold fluences for metals and for nanosecond laser pulses range from 1 to 10 J/cm^2 [12, 68]. In some cases and at high laser fluences, explosive-type vaporization mechanisms have been observed.

According to Kelly and Miotello [26], there are three regimes of thermal ablation: normal vaporization, normal (heterogeneous) boiling, and explosive boiling (or phase explosion). Only vaporization and explosive boiling are compatible with the time scale of nanosecond pulse duration laser. For nanosecond laser pulses, the regime of normal vaporization gives way to phase explosion with increasing laser fluence when the irradiated matter approaches the thermodynamic critical point (CP). At this point, the rate of homogeneous bubble nucleation rises and the target makes a transition from superheated liquid to an equilibrium mixture of vapor and liquid droplets.

From the above, one can assume that the modeling of the laser ablation process must take into consideration the laser heating of the target, which leads to the prediction of the target's temperature and the ablation rate, as well as the radiation absorption by plasma plume and its direct influence on the ablation rate due to radiation shielding [66].

2.2.3.1 Review of modeling efforts in ablation/plasma regime

The ablation phenomenon with nanosecond laser pulses excitation has been investigated by many researchers, using analytical and/or numerical techniques [69-77]. An energy balance criterion was used to predict the amount of ablated material by Singh *et al*. [69, 70]. According to Singh *et al*., [70], for laser interaction with plasma and the target, absorption of radiation is strong at distances very close to the target surface, where densities of the plasma species are very high. At large distances away from the target surface, the plasma is almost transparent to the incoming radiation. This is because the densities of the plasma constituents decrease as the plasma expands. This is schematically shown in Figure 2.6.

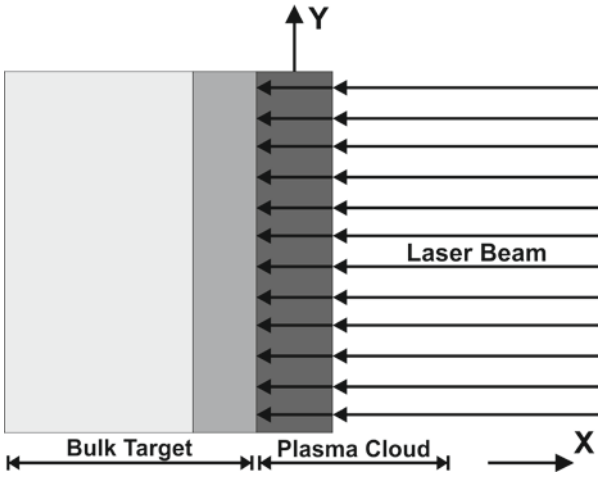

Figure 2.6 Schematic of the interaction of laser with plasma and target based on the study of Singh et al. [68]

In the literature, a large number of studies [70-72] have used the heat equation 2.6 as a governing equation of heat transfer to predict the temperature variation in the target followed by melting, vaporization, and consequently ablation. A notable theoretical study, which gives satisfactory agreement with experimental results for pulsed laser ablated mass, was carried out by Bulgakov and Bulgakova [17, 71]. According to their thermal ablation model, the time-dependent temperature distribution along the target depth *T(t,z)* follows the one-dimensional heat-flow equation

$$c_p \rho\left(\frac{\partial T}{\partial t} - u(t)\frac{\partial T}{\partial z}\right) = \frac{\partial}{\partial z} k \frac{\partial T}{\partial z} + [1 - R(T)] a_b I(t) e^{-a_b z} \tag{2.11}$$

where c_p, k and α_b are the thermal capacity, the thermal conductivity and the absorption coefficient of the target, ρ is the mass density of the target material, while $R(T_s)$ is the reflection coefficient, which is dependent on the surface temperature T_s and $u(t)$ is the surface recession velocity. The $u(t)$ value is defined under the hypothesis that the vapor pressure above the vaporized surface is estimated with the Clausius–Clapeyron equation and the flow of vaporized material from the surface follows the Hertz–Knudsen equation

$$u(t) = 0.82\frac{p_b}{\rho}\left(\frac{m}{2\pi k_b T_s}\right)^{1/2} e^{\left[\frac{L}{k_b}\left(\frac{1}{T_b}-\frac{1}{T_s}\right)\right]} \tag{2.12}$$

where m is mass of an atom, L is the latent heat of vaporization of the target material, k_b is the Boltzmann constant, and T_b is the boiling temperature under the reference pressure p_b. The parameters p_b and T_b are taken as normalization parameters and do not assume the boiling vaporization mechanism. The intensity of laser light reaching the target surface has the form:

$$I(t) = I_0(t)e^{-\Lambda(t)} = I_0(t)e^{\left[-\int_0^{\infty} a(n_p,T_p)dz\right]} \tag{2.13}$$

where $I_0(t)$ is the incident laser intensity, $\Lambda(t)$ is the total optical thickness of the plasma plume and $\alpha(n_p,T_p)$ is the plasma absorption coefficient, which depends on the plasma density, n_p, and temperature, T_p. For a low-temperature equilibrium plasma, the absorption coefficient can be written as $\alpha=\eta f(T)$, where n is density and $f(T)$ is an increasing temperature function [71]. The increase of the plasma temperature due to radiation absorption is estimated by $\Delta T=(\gamma\text{-}1)E_a/k_bN=(\gamma-1)mE_a/(k_b\Delta z\rho)$, where $\Delta z(t)$ is the ablation depth, $E_a(t)$ is the density of the laser energy absorbed by the plasma, γ is the specific heat ratio, and N is the number of vaporized particles (atoms) from a unit surface. After a series expansion of $\alpha(t)$ in terms of ΔT and restriction to the linear term it holds

$$\Lambda(t) = a\Delta z(t) + bE_{\mathrm{a}}(t) \tag{2.14}$$

The coefficients α and b, were determined by fitting the experimental and calculated data on mass removal and were the only free parameters in the model. Equation 2.11 was solved numerically by using a finite-difference scheme with second-order accuracy. The major contribution of this study is that it takes into account the plasma shielding effect (Equations 2.13 and 2.14).

Bulgakova et al. [72] have further modified Equation 2.11 by implementing the term $L_m\delta(T-T_m)$, which increases the accuracy of calculations on the liquid–solid interface giving the temperature of the melting point T_m (L_m latent heat of melting)

$$(c_p\rho + L_m\delta(T-T_m)(\frac{\partial T}{\partial t} - u(t)\frac{\partial T}{\partial z}) = \frac{\partial}{\partial z}k\frac{\partial T}{\partial z} + [1-R(T)]a_b I(t)e^{-a_b z} \quad (2.15)$$

The δ-function was approximated as

$$\delta(T-T_m,\Delta) = \frac{1}{\sqrt{2\pi}\Delta}e^{[-\frac{(T-T_m)^2}{2\Delta^2}]} \quad (2.16)$$

where Δ is in the range of 10–100 *K* depending on the temperature gradient. Furthermore, Zhang *et al*. [75, 76] developed a model of the ablation phenomenon, which also takes into account the plasma shielding effect. Radiation shielding by plasma was considered to occur due to IB and PI.

Recently, models based on FEM dealing with pulsed laser ablation have been published [78-81]. A 2D axisymmetric thermal finite element model, based on the heat-conduction equation and on the Hertz-Knudsen equation for vaporization, was developed by Oliveira and Vilar [79], in order to simulate laser ablation of solid material (TiC) irradiated by nanosecond pulsed laser source. Neglecting convective and radiative energy transport, and for a stable target (zero velocity relative to the laser source), the heat conduction is

$$\rho(T)c_p(T)\frac{\partial T(x,y,t)}{\partial t} = \nabla[k(T)\nabla T(x,y,t)] + Q(y,t) \quad (2.17)$$

The source term *Q*(y, t) represents the laser energy absorbed by the sample and is expressed as

$$Q(y,t) = I(t)\,\mathrm{e}^{-\Lambda(t)}(1-R)a_b\exp(-a_b y) \quad (2.18)$$

where *Λ(t)* is a term relating to plasma absorption, which is described by Equation 2.14. Also, the laser beam temporal profile *I(t)* was supposed to be Gaussian, while the flow of vaporized material from the surface follows the Hertz-Knudsen equation, given by Equation 2.12.

In order to simulate the ablation of the solid, if the temperature of an element was higher than the melting temperature (T_m) at the end of a particular step, melting was assumed to occur, while the latent heat of melting (L_m) was taken into account in the

calculations. Likewise, ablation was assumed to occur when the temperature of the surface elements was higher than the boiling temperature. An ablation depth *h* was calculated with an analytic solution and compared with the element thickness, Δy. If $h > \Delta y$ the element was assumed to be vaporized and the surface temperature of the remaining material was corrected in order to take into account the latent heat of vaporization. A finer mesh in the upper part of the target was used to better estimate the material removal.

A 2D axisymmetric thermal finite element model was also developed by Vasantgadkar *et al.* [80]. Its novelty was the fact that it took into account temperature dependent absorptivity and absorption coefficients (dynamic absorbance).

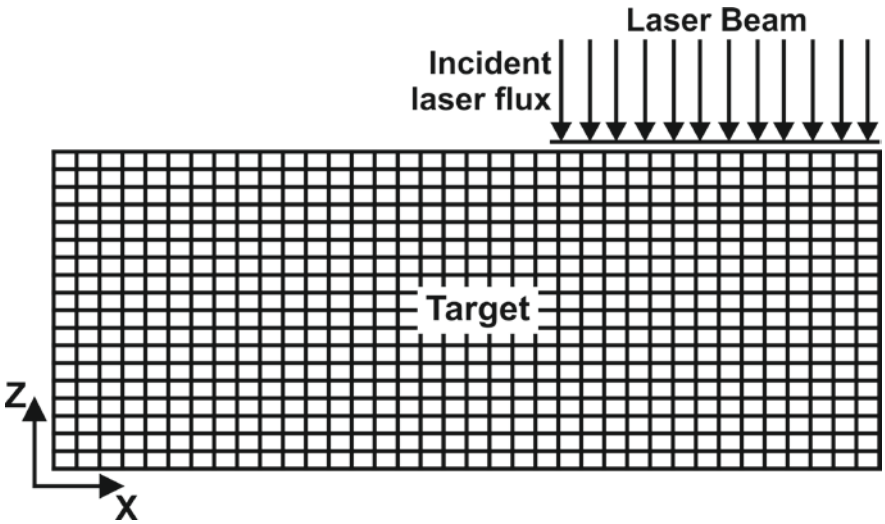

Figure 2.7 Schematic mesh of the axisymmetric finite element model, based on the study of Vasantgadkar *et al*. [80]

The same concept with the previous study, concerning the latent heat of melting and vaporization, was considered. Material removal was achieved through "killing" (capability of ANSYS software) of the elements, which were deactivated by multiplying their stiffness by a severe reduction factor, instead of using the Hertz-Knudsen equation. Plasma shielding was also considered by taking into account Equation 2.14. The coefficients α and *b* of Equation 2.14, were normally determined by fitting experimental and calculated data on mass removal.

In addition, in the literature may also be found models for pulsed laser ablation based on molecular dynamics simulation (MD) [82-84]. The application of the

classical MD method for the simulation of laser ablation of metals demands several modifications. Since electronic contribution to the thermal conductivity of a metal is dominant, the conventional MD method, where only lattice contribution is present, underestimates significantly the total thermal conductivity. This leads to nonphysical confinement of the deposited laser energy in the surface region of the irradiated target and does not allow the direct comparison between the calculated and the experimental data. This problem has been recognized in the first simulations of laser ablation of metals by Ohmura and Fukumoto [82]. MD was further modified in order to overcome this problem by the division of each computational cell into small blocks. Fourier's law is applied between the adjacent blocks to account for the heat conduction induced by free electrons [83].

Furthermore, with respect to the mechanical effects occurring in the plasma regime, the mechanical compression and the generation of surface waves is enhanced, while the shear wave amplitude reaches a maximum near the onset of plasma formation and then steadily decreases with increasing laser fluence [30, 31].

References

[1] M. Born and E. Wolf, *Principles of Optics* (Pergamon Press, Oxford, 1986).

[2] E. Hecht, *Optics*, Pearson Education Limited, 4th Edition.

[3] https://www.layertec.de/en/capabilities/coatings/metallic.

[4] D. Bergstrom, The Absorption of Laser Light by Rough Metal Surfaces, Ph.D. thesis (Lulea University of Technology, 2008).

[5] D. Basting, *Excimer Laser Technology: Laser Sources, Optics, Systems and Applications* (Lambda Physik AG, Gottingen, 2001).

[6] N. B. Dahotre and S. P. Harimkar, *Laser Fabrication and Machining of Materials* (Springer, New York, 2007).

[7] E. D. Palik, *Handbook of optical constants* (Academic Press, 1985).

[8] R. C. Weast, S. M. Selby, *CRC Handbook of Chemistry and Physics* (60th Edition, CTC Press, 1981).

[9] D. R. Lide, *CRC Handbook of Chemistry and Physics*, 82nd edn. (CRC, Boca Raton, 2001).

[10] D. Bauerle, *Laser Processing and Chemistry* (Springer, Berlin, 2000).

[11] N. A. Papadogiannis, S. D. Moustaizis and J. P. Girardeau-Montaut, *Study of electron relaxation phenomena on copper surface via non-linear ultrashort single photon photoelectric emission*, Journal of Physics D:Appl. Phys. **30**, 2389 (1997).

[12] M. S. Brown and C. B. Arnold, *Fundamentals of laser-material interaction and application to multiscale surface modification, Laser Precision Microfabrication*, Vol. 135, eds. K. Sugioka, M. Meunier and A. Pique (Springer Series in Materials Science, 2010), pp. 91-120.

[13] B. N. Chichkov, C. Momma, S. Nolte, F. von Alvensleben and A. Tunnermann, Femtosecond, picosecond and nanosecond laser ablation of solids, *Applied Physics A* **63**, 109-115 (1996).

[14] W. M. Steen and J. Mazumder, *Laser Material Processing* (4th ed. Springer-Verlag, London, 2010).

[15] W. M. Steen and J. Mazumder, *Theory, Mathematical Modelling and Simulation, Laser Material Processing* (4th ed. Springer- Verlag, London, 2010), pp. 251-294.

[16] R. F. Wood and G. E. Giles, Macroscopic theory of pulsed-laser annealing. I. Thermal transport and melting, *Phys. Rev. B* **23**, 2923-2942 (1981).

[17] A. V. Bulgakov and N. M. Bulgakova, Thermal model of pulsed laser ablation under the conditions of formation and heating of a radiation-absorbing plasma, *Quantum Electron.* **29**, 433-437 (1999).

[18] R. Fang, D. Zhang, Z. Li, F. Yang, L. Li, X. Tan and M. Sun, *Solid State Commun.* **145**, 556-560 (2008).

[19] M. R. Frewin and D. Scott, A Finite Element Model of Pulsed Laser Welding, *Weld. J.* **78**, 15-s-22-s (1999).

[20] B. Q. Xu, Z. H. Shen, J. Lu, X. W. Ni and S. Y. Zhang, Numerical simulation of laser-induced transient temperature field in film-substrate system by finite element method, *Int. J. Heat Mass Transfer* **46**, 4963-4968 (2003).

[21] W. Wu, N. G. Liang, C. H. Gan and G. Yu, Numerical investigation on laser transformation hardening with different temporal pulse shapes, *Surf. Coat. Tech.* **200**, 2686-2694 (2006).

[22] S. I. Anisimov, B. L. Kapeliovich and T. L. Perelman, Electron emission from metal surfaces exposed to ultrashort laser pulses, *Sov. Phys. JETP* **39**, 375-377 (1974).

[23] J. K. Chen and J. E. Beraun, Numerical study of ultrashort laser pulse interactions with metal films, *Numer. Heat Transfer, Part A* **40**, 1-20 (2001).

[24] T. Q. Qiu and C. L. Tien, Short-pulse laser heating on metals, *Int. J. Heat Mass Transfer* **35**, 719-726 (1992).

[25] G. D. Tsibidis, Thermal response of double-layered metal films after ultrashort pulsed laser irradiation: The role of nonthermal electron dynamics, *Appl. Phys. Lett.* **104**, 051603 (2014).

[26] A. Miotello and R. Kelly, Laser-induced phase explosion: new physical problems when a condensed phase approaches the thermodynamic critical temperature, *Appl. Phys. A* **69** (Suppl.), S67–S73 (1999).

[27] A. J. Hick, Rapid surface heat treatments-A review of laser and electron beam hardening, *Heat Treat. Met.* **10**, 3-11 (1983).

[28] D. L. Bourell, H. L.Marcus, J. W. Barlow and J. J. Beaman, Selective laser sintering of metals and ceramics, *Int. J. Powder Metall.* **28**, 369-381 (1992).

[29] C. W. Draper and J. M. Poate, Laser surface alloying, *Int. Met. Rev.* **30**, 85-108 (1985).

[30] C. E. Scruby and L. E. Drain, *Laser ultrasonics techniques and application*, (Adam Hilger, New York, 1990).

[31] S. J. Davis, C. Edwards, G. S. Taylor and S. B. Palmer, Laser-generated ultrasound: its properties, mechanism and multifarious application, *J. Phys. D: Appl. Phys.* **26**, 329–48 (1993).

[32] P. Hess, Laser diagnostics of mechanical and elastic properties of silicon and carbon film, *Appl. Surf. Sci.* **106**, 429–437 (1996).

[33] T. Sanderson, C. Ume and J. Jarzynski, Longitudinal wave generation in laser ultrasonics, *Ultrasonics* **35**, 553-561 (1998).

[34] W. Feng, D. Yang, X. Zhu, Y. Guo and W. Liao, Simulation of laser-generated longitudinal and shear ultrasonic waves in a diamond anvil cell by the finite element method, *J. Appl. Phys.* **111**, 013107 (2012).

[35] J. Huang, S. Krishnaswamy and J. D. Achenbach, Laser generation of narrow-band surface waves, *J. Acoust. Soc. Am.* **92**, 2527-2531 (1992).

[36] D. Royer and C. Chenu, Experimental and theoretical waveforms of Rayleigh waves generated by a thermoelastic laser line source, *Ultrasonics* **38**, 891-895 (2000).

[37] J. C. Cheng and S. Y. Zhang, Quantitative theory for laser-generated Lamb waves in orthotropic thin plates, *Appl. Phys. Lett.* **74**, 2087 (1999).

[38] M. Dubois, P. W. Lorraine, R. J. Filkins, T. E. Drake, K. R. Yawn and S.-Y. Chuang, Experimental verification of the effects of optical wavelength on the amplitude of laser generated ultrasound in polymer-matrix composites, *Ultrasonics* **40**, 809-812 (2002).

[39] Z. H. Shen, S. Y. Zhang and J. C. Cheng, Theoretical study on surface acoustic wave generated by a laser pulse in solids, *Anal. Sci.* **17**, 204 (2001).

[40] J. Guan, Z. Shen, X. Ni, J. Lu, J. Wang and B. Xu, Numerical simulation of the ultrasonic waves generated by ring-shaped laser illumination patterns, *Opt. Laser Technol.* **39**, 1281-1287 (2007).

[41] R. M. White, Generation of elastic waves by transient surface heating, *J. Appl. Phys.* **34**, 3559-3567 (1963).

[42] J. E. Sinclair, Epicentre solutions for point multipole sources in an elastic half-space, *J. Phys. D: Appl. Phys* **12**, 1309-1315 (1979).

[43] C. B. Scruby, R. J. Dewhurst, D. A. Hutchins and S. B. Palmer, Quantitative studies of thermally generated elastic waves in laser irradiated metals, *J. Appl. Phys.* **51**, 6210-6216 (1980).

[44] R. J. Dewhurst, D. A. Hutchins, S. B. Palmer and C. B. Scruby, Quantitative measurements of laser generated acoustic waveforms, *J. Appl. Phys.* **53**, 4064-4071 (1982).

[45] L. R. F. Rose, Point-source representation for laser-generated ultrasound, *J. Acoust. Soc. Am.* **75**, 723-732 (1984).

[46] F. A. Mcdonald, On the precursor in laser-generated ultrasound waveforms in metals, *Appl. Phys. Lett.* **56**, 230-232 (1990).

[47] X. Wang and X. Xu, Thermoelastic wave induced by pulsed laser heating, *Appl. Phys. A* **73** 107-114 (2001).

[48] P. Z. Zhang, C. F. Ying and J. Z. Shen, Directivity patterns of laser thermoelastically generated ultrasound in metal with consideration of thermal conductivity, *Ultrasonics* **35**, 233-240 (1997).

[49] R. Coulette, E. Lafond, M. H. Nadal, C. Gondard, F. Lepoutre and O. Petillon, Laser generated ultrasound applied to two-layered materials characterization: semi-analytical model and experimental validation, *Ultrasonics* **36**, 239–243 (1998).

[50] T. W. Murray, S. Krishnaswamy and J. D. Achenbach, Laser generation of ultrasound in films and coatings, *Appl. Phys. Lett.* **74**, 3561–3563 (1999).

[51] M. Kasai, S. Fukushima, Y. Gohshi and T. Sawada, A basic analysis of pulsed photoacoustic signals using the finite elements method, *J. Appl. Phys.* **64**, 972-976 (1988).

[52] B. Xu, Z. Shen, X. Ni, J. Lu and Y. Wang, Finite element model of laser-generated surface acoustic waves in coating-substrate system, *J. Appl. Phys.* **95**, 2109-2115 (2004).

[53] B. Xu, Z. Shen, X. Ni and J. Lu, Numerical simulation of laser-generated ultrasound by the finite element method, *J. Appl. Phys.* **95**, 2116-2122 (2004).

[54] B. Xu, Z. Shen, X. Ni, J. Wang, J. Guan and J. Lu, Thermal and mechanical finite element modeling of laser-generated ultrasound in coating–substrate system, *Opt. Laser Technol.* **38**, 138–145 (2006).

[55] B. Xu, Z. Shen, J. Wang, X. Ni, J. Guan and J. Lu, Thermoelastic finite element modeling of laser generation ultrasound, *J. Appl. Phys.* **99**, 033508 (2006).

[56] R. M. Sanderson and Y. C. Shen, Measurement of residual stress using laser-generated ultrasound, *Int. J. Pres. Ves. Pip.* **87**, 762-765 (2010).

[57] D. Cerniglia, A. Pantano and C. Mineo, Influence on the laser beam profile on the generation of ultrasonic waves, *Appl. Phys. A* **105**, 159-167 (2011).

[58] K. Abderrazak, W. Kriaa, W. B. Salem, H. Mhiri, G. Lepalec and M. Autric, Numerical and experimental studies of molten pool formation during an interaction of a pulse laser (Nd:YAG) with a magnesium alloy, *Opt. Laser Technol.* **41**, 470–480 (2009).

[59] E. Louvis, P. Fox and C. J. Sutcliffe, Selective laser melting of aluminium components, *J. Mater. Process. Tech.* **211**, 275-284 (2011).

[60] J. C. Ion, *Laser Processing of Engineering Materials: Principles, Procedure and Industrial Applications* (Elsevier Butterworth-Heinemann, Oxford, 2005).

[61] T. D. Bennett, D. J. Krajnovich, C. P. Grigoropoulos, P. Baumgart and A. C. Tam, Marangoni Mechanism in Pulsed Laser Texturing of Magnetic Disk Substrates, *J. Heat Transfer* **119**, 589-596 (1997).

[62] O. Garcia, J. J. Garcia-Ballesteros, D. Munoz-Martina, S. Nunez-Sanchez, M. Morales, J. Carabe, I. Torres, J. J. Gandia and C. Molpeceres, Analysis of wavelength influence on a-Si crystallization processes with nanosecond laser sources, *Appl. Surf. Sci.* **278**, 214–218 (2013).

[63] J. C. Conde, E. Martin, S. Chiussi, F. Gontad, C. Serra, and P. Gonzalez, Finite element simulation for ultraviolet excimer laser processing of patterned Si/SiGe/Si(100) heterostructures, *Appl. Phys. Lett.* **97**, 014102 (2010).

[64] J. C. Conde, E. Martin, F. Gontad, S. Chiussi, L. Fornarini and B. Leon, Numerical analysis of temperature profile and thermal-stress during excimer laser induced heteroepitaxial growth of patterned amorphous silicon and germanium bi-layers deposited on Si(100), *Thin Solid Films* **518**, 2431–2436 (2010).

[65] A. Kaplan, Metallurgy of Welding and Hardening, *The Theory of Laser Materials Processing*, Vol. 119, ed. J. M. Dowden (Springer Series in Materials Science, 2009).

[66] D. Marla, U. V. Bhandarkar and S. S. Joshi, Critical assessment of the issues in the modeling of ablation and plasma expansion processes in the pulsed laser deposition of metals, *J. Appl. Phys.* **109**, 021101 (2011).

[67] Y. B. Zeldovich and Y. P. Raizer, *Physics of Shock Waves and High Temperature Phenomena* (Academic, New York, 1966).

[68] S. Amoruso, R. Bruzzese, N. Spinelli and R. Velotta, Characterization of laser-ablation plasmas, *J. Phys. B: At. Mol. Opt. Phys.* **32**, R131–R172 (1999).

[69] R. K. Singh and J. Narayan, Pulsed-laser evaporation technique for deposition of thin films: Physics and theoretical model, *Phys. Rev. B* **41**, 8843-8859 (1990).

[70] R. K. Singh, O. W. Holland and J. Narayan, Theoretical model for deposition of superconducting thin films using pulsed laser evaporation technique, *J. Appl. Phys.* **68**, 233-247 (1990).

[71] N. M. Bulgakova and A. V. Bulgakov, Pulsed laser ablation of solids: Transition from normal vaporization to phase explosion, *Appl. Phys. A* **73**, 199-208 (2001).

[72] N. M. Bulgakova, A. V. Bulgakov and L. P. Babich, Energy balance of pulsed laser ablation: Thermal model revised, *Appl. Phys. A* **79**, 1323-1326 (2004).

[73] J. R. Ho, C. P. Grigoropoulos and J. A. C. Humphrey, Computational study of heat transfer and gas dynamics in the pulsed laser evaporation of metals, *J. Appl. Phys.* **78**, 4696-4709 (1995).

[74] S. Amoruso, Modeling of UV pulsed-laser ablation of metallic targets, *Appl. Phys. A* **69**, 323-332 (1999).

[75] D. Zhang, D. Liu, Z. Li, S. Hou, B. Yu, L. Guan, X. Tan and L. Li, A new model of pulsed laser ablation and plasma shielding, *Physica B* **362**, 82–87 (2005).

[76] L. Li, D. Zhang, Z. Li, L. Guan, X. Tan, R. Fang, D. Hu and G. Liu, The investigation of optical characteristics of metal target in high power laser ablation, *Physica B* **383**, 194-201 (2006).

[77] J. G. Lunney and R. Jordan, Pulsed laser ablation of metals, *Appl. Surf. Sci.* **127-129**, 941-946 (1998).

[78] J. C. Conde, F. Lusquinos, P. Gonzalez, J. Serra, B. Leon, L. Cultrera, D. Guido and A. Perrone, Laser ablation of silicon and copper targets. Experimental and finite elements studies, *Appl. Phys. A* **79**, 1105-1110 (2004).

[79] V. Oliveira and R. Vilar, Finite element simulation of pulsed laser ablation of titanium carbide, *Appl. Surf. Sci.* **253**, 7810-7814 (2007).

[80] N. A. Vasantgadkar, U. V. Bhandarkar, S. S. Joshi, A finite element model to predict the ablation depth in pulsed laser ablation, *Thin Solid Films* **519**, 1421-1430 (2010).

[81] H. S. Lim and J. Yoo, FEM based simulation of the pulsed laser ablation process in nanosecond fields, *J. Mech. Sci. Technol.* **25**, 1811-1816 (2011).

[82] E. Ohmura and I. Fukumoto, Molecular dynamics simulation on laser ablation of fcc metal, *Int. J. Japan Soc. Prec. Eng.* **30**, 128-133 (1996).

[83] E. Ohmura and I. Fukumoto, Modified molecular dynamics simulation on laser ablation of metal, *Int. J. Japan Soc. Prec. Eng.* **31**, 206-207 (1997).

[84] D. S. Ivanov and L. V. Zhigilei, Combined atomistic-continuum modeling of short-pulse laser melting and disintegration of metal films, *Phys. Rev. B* **68**, 064114 (2003).

Chapter 3

3. Mathematical and numerical modeling of pulsed ns laser interaction with matter

3.1 Introduction

The main regimes for high-power nanosecond pulsed laser irradiation of matter, as already mentioned, are the thermoelastic, melting, and ablation/plasma regime. In the thermoelastic regime the target surface deforms after the laser excitation without altering its elastic properties. Absorption of the laser pulse results in an increased localized temperature, which in turn causes thermal expansion and a consequent generation of a stress field and ultrasonic waves that propagate inside the target [1, 2]. For higher laser intensities the target surface temperature overcomes its melting point and the thermal and optical properties of the irradiated material change. When the target surface temperature overcomes its boiling point, ablation occurs and matter is vaporized. For incident laser intensities greater than the ablation threshold, a large amount of electrons, ions, and excited neutrals exist in the vaporized material and absorb the laser light forming plasma [3].

3.2 Mathematical modeling

Neglecting convective and radiated energy transport, the temperature distribution *T*, induced by absorption of pulsed laser radiation in a material, is given by the heat conduction equation, which can be expressed as

$$\rho C_p(T)\frac{\partial T(x,y,z,t)}{\partial t} - \nabla[k(T)\nabla T(x,y,z,t)] = Q(x,y,z,t) - L_i \tag{3.1}$$

where *x, y, z* are the space coordinates and ρ, C_p, k are the mass density, specific heat at constant pressure, and thermal conductivity of the target material, respectively. The source term *Q(x, y, z, t)* represents the laser absorbed energy by the sample per

volumetric unit and per second. When target's temperature is less than its melting point, the incident laser energy onto the surface is conducted into the solid target. For that period of time latent heat per unit volume per unit time L_i is equal to zero.

Due to the generated transient temperature elevation field and the transient temperature gradient field, the localized thermal expansion generates a stress field and ultrasonic waves that propagate in the material in all directions. For solids, the wave propagation, resulting from the thermal expansion due to the temperature elevation field, is expressed as

$$\rho \frac{\partial^2 U(x,y,z,t)}{\partial t^2} = \mu \nabla^2 U(x,y,z,t) + (\lambda + \mu)\nabla[\nabla U(x,y,z,t)] - \mathrm{a}(3\lambda + 2\mu)\nabla T(x,y,z,t) \qquad (3.2)$$

where U is the time-dependent displacement, λ and μ are the Lamé constants, and a is the thermoelastic expansion coefficient. Lamé parameters are two material-dependent quantities that arise in strain-stress relationships in continuum mechanics.

When the temperature exceeds the melting point of the material, phase change occurs and the latent heat of melting, L_m, of the material is taken into account (i=m) in Equation 3.1. In the ablation regime, when temperature exceeds the boiling point, the latent heat of melting is replaced by the latent heat of vaporization, L_v,(i=v).

3.2.1 Source term

The temporal and spatial distribution of the nanosecond pulsed laser source can be described by the functions $F(t)$ and $S(r)$, respectively [4]

$$F(t) = e^{-4\ln 2(t/t_0)^2}$$
$$S(x,y) = e^{-(x^2+y^2)/r_0^2} \qquad (3.3)$$

where t_0 is the FWHM laser pulse duration and r_0 is the FWHM beam radius on the sample surface. The source term *Q(x, y, z, t)* that represents the laser energy absorbed by the sample can be expressed as [4]

$$Q(x,y,z,t) = I_s(t)(1-R)F(t)S(x,y)a_b e^{-a_b z} \tag{3.4}$$

where $I_s(t)$ is the temporal laser irradiance at the sample, R is the optical reflectivity of the sample and α_b is the optical absorption coefficient ($1/\alpha_b$ is the optical penetration depth). The laser beam temporal profile in most of the cases is assumed to be of Gaussian type.

3.2.2 Plasma absorption parameter

For moderate laser fluences, energies delivered per unit area, the nanosecond laser pulse is usually accompanied by the formation of low temperature plasma. The temporal laser irradiance at the target surface is attenuated due to absorption in the plasma that is formed as a consequence of laser irradiance. An increase in the absorption as a consequence of plasma heating can be characterized by a single parameter, the density of the absorbed radiation energy E_a according to *Bulgakov and Bulgakova* [5]. The temporal laser irradiance is then expressed as

$$I_s(t) = I_0 e^{-\Lambda(t)} \tag{3.5}$$

where I_0 is the incident laser pulse energy per unit area per second and $\Lambda(t)$ is the optical thickness of the ablation plume which is given by the following equation [4]

$$\Lambda(t) = b\,h(t) + d\,E_a(t) \tag{3.6}$$

where h is the ablation depth and b, d, are time independent coefficients.

3.3 2-D axisymmetric modeling in the thermoelastic regime

The geometry of the physical problem of the matter response of a homogeneous, elastic, isotropic film–substrate system, when a single laser pulse interacts with the surface of the sample, is shown in Figure 3.1. The laser beam is assumed to be perpendicular to the surface.

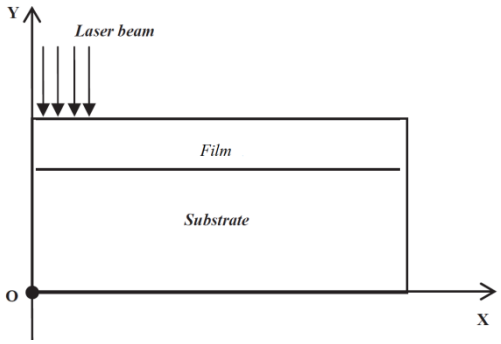

Figure 3.1 Schematic diagram for laser irradiating film-substrate system

In order to describe the previously mentioned complex multiphysics problem, finite element numerical analysis is chosen in this thesis. Finite element simulation is a convenient tool for the simulation of thermal and elastic phenomena. The FEM is a series of computerized numerical calculations using a matrix method. It is versatile due to its flexibility in modeling complicated geometries when the domain changes, when the desired precision varies over the entire domain, or when the solution lacks smoothness. Moreover it can provide substantial insights into how temperature gradients and residual stresses are developed during the laser-metal interaction, as well as information concerning time-dependent displacements at multiple locations [6-9].

Modeling methodology is initially referred to the finite element computational approach. Then, the description of the geometric topology and of the required finite elements for the mesh creation follows. Additionally, the initial boundary and loading conditions are later described, as well as the mechanical, thermal, and optical properties of the materials under study.

3.3.1 Computational approach

The classical thermal conduction equation for finite elements with the heat capacity matrix [*C*] and the conductivity matrix [*K*] can be expressed in terms of vectors, based on the finite element method:

$$[K]\{T\}+[C]\{\frac{\partial T}{\partial t}\}=\{Q\} \tag{3.7}$$

where $\{Q\}$ is the heat source vector, $\{T\}$ is the temperature vector and $\{\partial T/\partial t\}$ is the temperature rate vector. For wave propagation, ignoring damping, the governing finite element equation is

$$[M]\{\frac{\partial^2 U}{\partial t^2}\}+[S]\{U\}=\{F\} \tag{3.8}$$

where $[M]$ is the mass matrix, $[S]$ the stiffness matrix, $\{U\}$ the displacement vector, $\{\partial^2 U/\partial t^2\}$ the acceleration vector and $\{F\}$ the force vector. For thermoelasticity, the external force vector for an element is given as

$$\{F\}=\int_V [B]^T [D]\{\varepsilon_0\}\,dV \tag{3.9}$$

where $\{\varepsilon_0\}$ is the thermal strain vector, $[B]^T$ is the transpose of the derivative of the shape functions and $[D]$ is the material matrix.

3.3.2 Geometry and meshing

The solution of the matrix equations 3.8 and 3.9 is done with the use of the commercial finite element software ANSYS ver14.5. An axisymmetric analysis is initially carried out in order to reduce the computational time. The numerical simulation is performed using coupled-field thermal-structural multiphysics analysis. Both thermal and structural fields share the same 2D geometry, meshing and elements, boundary and loading conditions. With the help of a direct coupling method, a single pass solution is achieved, involving one analysis that uses a coupled-field 2D element type. PLANE 223 is the adopted 8-node solid coupled-field, 2D thermal-structural plane element to carry out the numerical process. The finite element used has eight nodes with up to four degrees of freedom per node and the analysis type of the coupled physics model is set to be transient. The choice of the element type is done so that a good relation between accuracy and computational cost can be achieved. All numerical simulations run on a 4-core Intel® Core™ i7-3820 CPU with a processor of 3.6 GHz and 32 GB RAM.

The computational model is expected to be highly demanding on computational power, due to the nature of the solution, where a highly abrupt loading over time is imposed, hence a large number of steps is needed for the time integration. Moreover,

there is a need for modeling with a number of elements as small as possible. The definition of the total number of elements highly depends on the regions of interest, as well as on the topologies with the smaller dimensions. In our case, the area of interest is the complete mass of the metal film, which has the smallest thickness; consequently it determines the minimum number of finite elements. The thickness of the film used is of the order of a fraction of a μm and the heat-affected zone is much smaller than the domain of the material, therefore a fine mesh is necessary in order to resolve temperature distribution inside the film and the irradiated region.

The dimensions that are used for the simulations correspond to real film-substrate systems used in experiments, as it will be analyzed in Chapter 4. Different metal thin film-substrate samples are simulated, produced by e-beam evaporation; 0.2 and 0.5 μm Al (aluminum) films deposited on 1 mm fused silica substrate and 0.4 μm Au (gold) films deposited on 1 mm BK7 glass substrate. The width of the films is 100 μm. A high discretization number of 10 elements per thickness is selected for the thin film and 1000 for the radial width of the film. The same values are selected for the substrate, leading to a total number of elements ranging from 20000 to 40000. The range of this number is due to different simulated thickness of the substrate for different test cases. In Figure 3.2 a schematic of the 2D axisymmetric finite element model is depicted. In all examined cases it is considered that the two different layers of material are inseparable (bonded). The same nodes are shared in the interface of the metallic film and the glass substrate (continuity of grid).

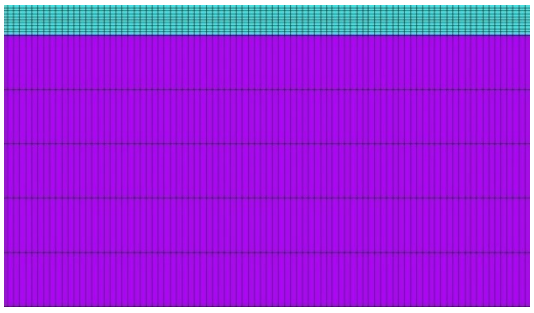

Figure 3.2 Schematic of the 2D axisymmetric finite element model

Two critical aspects for the convergence of numerical results are the temporal and spatial resolutions of the finite element model. Concerning spatial resolution, the size of the elements is chosen in a manner so that the propagating waves are spatially

resolved. Since laser-generated SAWs have high frequencies, a small element size is required to deal with such waves. In [10], it is recommended that more than 10 nodes per wavelength should be used, while in [11], the recommendation is much higher (on the order of 20 nodes per wavelength). The last recommendation can be expressed as:

$$l_e = \frac{\lambda_{\min}}{20} \tag{3.10}$$

where l_e is the element length and λ_{min} is the shortest wavelength of interest. In our case, according to experimental results that will be presented in the next Chapter, the wavelength is approximately 40 μm, therefore the element length is selected to be approximately 2 μm according to Equation 3.10. Therefore, higher accuracy for the numerical results is achieved with regard to generation and propagation of ultrasonic waves.

Moreover, the choice of an adequate integration time step is very important for the accuracy of the solution. In general, the accuracy of the model increases with smaller integration time steps. With long time steps, the high-frequency components are not resolved accurately enough. On the other hand, small time steps require increased computational time, therefore, a compromise has been found.

ANSYS [11, 12] code uses an implicit solver for the solution of Equations 3.7 and 3.8. The non-linear thermal Equation 3.7 is solved with the Newton-Raphson procedure along with a trapezoidal rule for time integration for the transient analysis. Also, the non-linear structural Equation 3.8 is solved with the Newton-Raphson procedure along Newmark time integration for transient analysis. For the Newmark time integration scheme a rule that gives accurate results is [11]

$$\Delta t = \frac{1}{20 f_{\max}} \tag{3.11}$$

where f_{max} is the highest frequency of interest. By determining the highest frequency from the available experimental results approximately equal to 50 MHz, a timestep Δt of 1 ns is small enough to model the temporal behavior of the propagation. A total time of 80 ns after excitation and 80 load-steps, resulting to a duration of 1 ns for each

load-step for the solution is considered. In Appendix A more details for the implicit solver are presented.

3.3.3 Initial and boundary conditions

Regarding initial conditions, the initial temperature of the body is assumed to be the ambient environmental temperature, while the initial mesh is considered to be non-deformed with zero initial stresses.

The boundary conditions of the model are depicted in Figure 3.3. The substrate is assumed to be clamped on its boundary for both radial and vertical directions (fixed support). Since, an axisymmetric analysis has been performed, the heat flux on left hand boundary is considered to be zero, as can be seen in Figure 3.4. The boundary conditions at r=0 (on the symmetry plane) is treated as adiabatic

$$-k\frac{\partial T}{\partial z}=0. \tag{3.12}$$

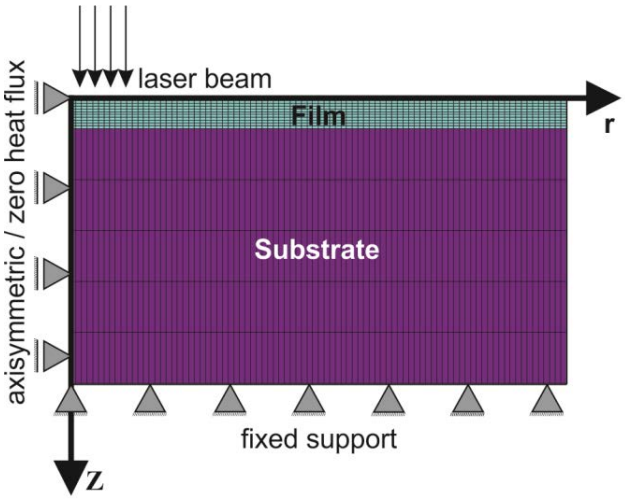

Figure 3.3 Boundary conditions of the axisymmetric FEM model

Moreover, the effect of thermal convection and heat radiation are neglected during the extremely short laser pulse, thus no heat is assumed to be flowing into or out of the boundaries of the model.

3.3.4 Loading conditions

In relation to the loading conditions of the model, a heat generation function, given by Equation 3.13, is applied to the upper part of the thin film. The heat generation source term *Q(r, z, t)* that represents the laser energy absorbed by the sample can be expressed as

$$Q(\mathrm{r},z,t) = I_s(t)(1-R)F(t)S(r)a_b e^{-a_b z} \tag{3.13}$$

where $I_s(t)$ is the temporal laser irradiance at the sample, R is the optical reflectivity of the sample, and α_b is the optical absorption coefficient. The laser beam temporal profile is assumed to be of Gaussian type. The temporal and spatial distribution of the nanosecond pulsed laser source are described by the functions $F(t)$ and $S(r)$, respectively

$$F(t) = e^{-4\ln 2(t-2t_0/t_0)^2}$$
$$S(r) = e^{-(r^2/r_0^2)} \tag{3.14}$$

where t_0 is the FWHM laser pulse duration and r_0 is the FWHM beam radius on the sample surface. The temporal Gaussian distribution *F(t)* is depicted in Figure 3.4.

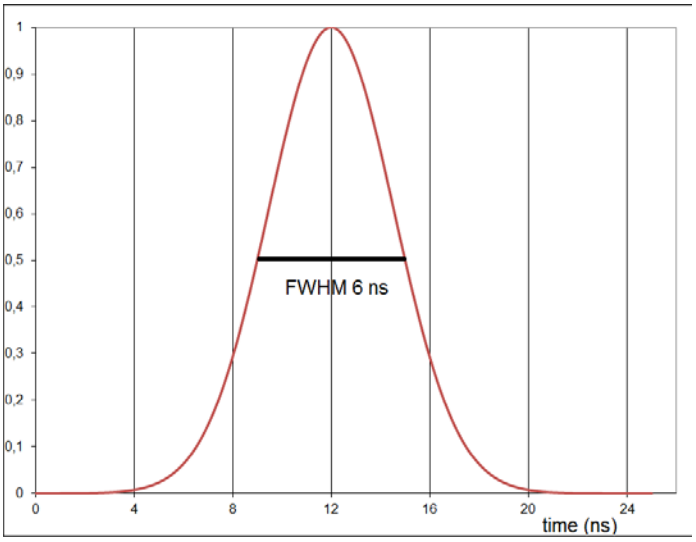

Figure 3.4 Temporal Gaussian distribution of pulsed laser source with 6 ns duration (Full Width at Half Maximum)

With respect to the laser parameters used in the simulations, the FWHM laser pulse duration t_0 is 6 ns, the FWHM beam radius of the pulsed laser spot on the sample surface, r_0, is considered to be 12.5 μm, while energy values in the range of 20-50 μJ/pulse. All these laser parameters are used in accordance with the conducted experiments utilizing the dynamic imaging interferometer technique.

3.3.5 Material properties

The material properties used in this modeling study can be categorized into optical and thermo-physical ones. Regarding the optical properties, the absorption coefficient α_b and reflectivity R are calculated from the real and imaginary part of the refraction index n and k taken from [13] using the equations

$$a_b = \frac{4\pi k}{\lambda}$$

$$R = \frac{(n-1)^2 + k^2}{(n+1)^2 + k^2} \tag{3.15}$$

where λ is the radiation wavelength with a value of 532.8 nm (value of the pulsed laser source used in the experiments). The values of the absorption coefficient, optical penetration depth and reflectivity for the different materials at 532.8 nm wavelength are summarized in Table 3.1.

Material	Absorption coefficient (m^{-1})	Optical penetration depth (m)	Reflectivity
Aluminum (Al)	151×10^{6}	6.6×10^{-9}	0.91
Fused silica (FS)	0.18	5.5	0.04
Gold (Au)	57×10^{6}	17.5×10^{-9}	0.76
Glass (BK7)	0.18	5.5	0.04

Table 3.1 Optical properties of the different materials used in this work

The values for thermo-physical properties have been adopted from existing values in [14, 15]. The material properties are divided into thermal and mechanical properties. This categorization is based on the material properties that are required for the simultaneous solution of the thermal and mechanical analysis. The thermal properties are thermal conductivity [W/m×°C] and specific heat capacity [J/kg×°C].

The properties required for the solution of the mechanical analysis are Young's Modulus [GPa], thermal expansion coefficient [1/°C], Poisson's ratio, while due to transient analysis density [kg/m^3] is also needed. Young Modulus and Poisson's ratio are related to Lamé parameters λ, μ as

$$E = \frac{\mu(3\lambda + 2\mu)}{\lambda + \mu}$$
$$\nu = \frac{\lambda}{2(\lambda + \mu)}. \tag{3.16}$$

The material properties used in the 2-D axisymmetric simulations are presented in Table 3.2.

	Density (kg/m^3)	Specific heat (J/kgK)	Thermal conductivity (W/mK)	Thermal expansion coefficient ($10^{-6}\times$1/K)	Young's modulus ($10^9\times$ Pa)	Poisson's ratio
Aluminum (Al)	2712	910	205	22.2	69	0.33
Fused silica (FS)	2200	740	1.38	0.55	73	0.17
Gold (Au)	19320	129	310	14.2	79	0.42
Glass (BK7)	2510	858	1.114	7.1	81	0.206

Table 3.2 Thermal and Mechanical Material properties

The choice of these specific materials properties and laser parameter values facilitates the direct comparison with representative experimental results, as we will see in the next Chapter.

3.4 3-D quarter symmetric modeling of thermomechanical interaction in all regimes of interest

In order to simulate the pulsed laser film-substrate interaction in thermoelastic, melting, and ablation regimes, a quarter symmetric 3D coupled thermal-structural transient model based on FEM is also developed. All numerical simulations run on a 4-core Intel® Core™ i7-3820 CPU with a processor of 3.6 GHz and 32 GB RAM. The 3D multiphysics model gives more accurate spatiotemporal numerical results in

the three dimensional space and can predict mass ablation, compared to the 2D axisymmetric model. It provides better insight to the time and space history of the surface deformation development and to the SAWs generation and propagation in all directions of the irradiated region, as well as within the volume of the material. It is capable to compute the phase changes of matter, with respect to the material properties and the experimentally used laser irradiation parameters. For this reason the matrix Equation 3.7 of thermal conductivity is formed so as to include the phase changes of matter related to temperature based criteria

$$[K]\{T\}+[C]\{\frac{\partial T}{\partial t}\}=\{Q-L_i\} \tag{3.17}$$

where L_i is the latent heat per unit volume per unit time, which equals to L_m and L_v in the melting and ablation regimes respectively. When temperature reaches the melting point L_m is taken into account in the previous equation, while L_v is taken into account when temperature exceeds the boiling point of the material. Equations 3.8 and 3.9, described in section 3.2.1, also apply here for mechanical wave propagation.

3.4.1 Computational approach, geometry and meshing

The 3D quarter symmetric finite element model simulates a homogeneous, elastic, isotropic metal film-substrate system and its transient response when a single laser pulse interacts with the metallic film for all three regimes. Both the thermal and structural fields share the same 3D geometry, meshing and elements, boundary and loading conditions. Moreover, the thermal and structural solution is computed in every time step simultaneously. Therefore a simultaneous analysis of the thermal and structural parameters, as defined by the solution of the heat conduction and wave equations, is achieved.

With the help of a direct coupling method, a single pass solution is achieved, involving one analysis that uses the coupled-field 3D element type SOLID5 of the commercial software ANSYS® 14.5. SOLID5 has eight nodes with up to six degrees of freedom per node. For this thermal structural analysis the weak field coupling is

chosen and is done by the calculation of the appropriate element matrices and load vectors occurring by the summation of the element matrices and load vectors described in Equations 3.15 and 3.8. In order to include the necessary coupling terms, the governing equation results to the matrix equation form described in Equation 3.18, where the coupled effects are accounted via load terms F-coupled: F_c and Q-coupled: Q_c. This coupling requires at least two iterations in sequence to achieve a coupled response, one for each of the applied physics.

$$\begin{bmatrix} [M] & 0 \\ 0 & 0 \end{bmatrix} \begin{Bmatrix} \{\ddot{u}\} \\ \{\ddot{T}\} \end{Bmatrix} + \begin{bmatrix} 0 & 0 \\ 0 & [C] \end{bmatrix} \begin{Bmatrix} \{\dot{u}\} \\ \{\dot{T}\} \end{Bmatrix} + \begin{bmatrix} [S] & 0 \\ 0 & [K] \end{bmatrix} \begin{Bmatrix} \{u\} \\ \{T\} \end{Bmatrix} = \begin{Bmatrix} \{F_c\} \\ \{Q_c\} \end{Bmatrix} \tag{3.18}$$

Due to the high frequencies of the laser generated SAWs and the need to resolve the temperature distribution in the film and the irradiated region, a small element size is essential to accurately simulate such effects, as likewise already described in section 3.2.2. Figure 3.5 presents technical details of the 3-D quarter symmetric finite element model. The symmetry centre is the laser's epicenter. Since the heat-affected zone is much smaller than the domain of the material, special treatment is given to the mesh of the cyclic area of the laser beam spot, at the limits of which the temperature gradients change rapidly, requiring for a locally smooth adaptive fine discretization [16]. An orthogonal fine meshed volume is generated to allow precision handling of the dynamic phase changes of matter in the centre of the irradiated target. Additionally, a second larger cyclic area encloses the irradiated zone and creates the appropriate continuum smooth space, needed for the generation and propagation of SAWs. The thickness of the metal film used is of the order of a fraction of a μm, thus 12 element divisions are used to discretize its volume in the normal direction. The whole sample is discretized to a total number of 90,000 elements. Different test cases of the model are tested with a varying thickness of the substrate.

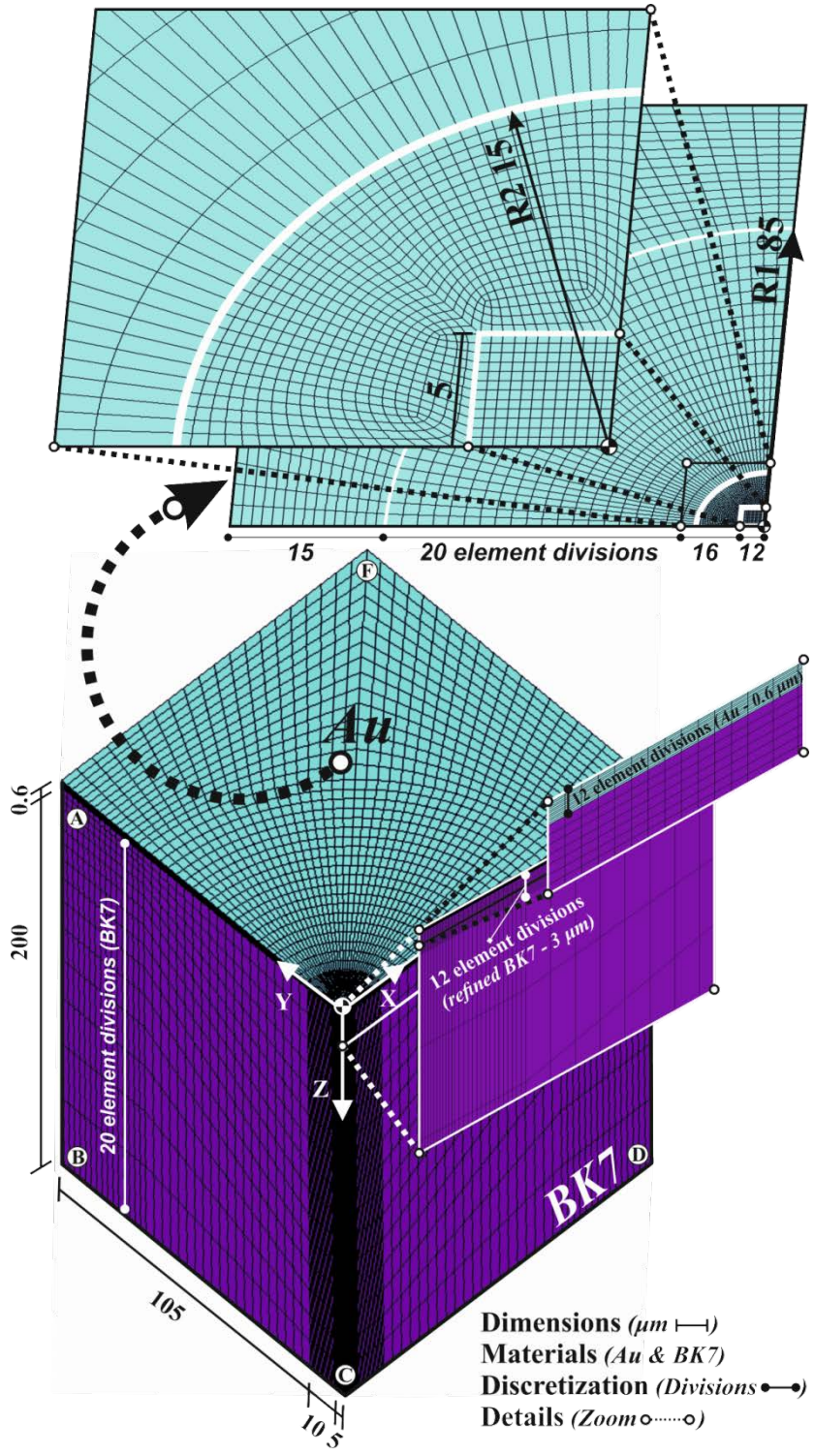

Figure 3.5 3D quarter symmetric finite element model details. As indicated in the zoomed detail of the irradiated surface (top), special treatment is given to the locally adaptive mesh of the circular area of radius R2 of the laser beam spot. A second circular area with radius R1 encloses R2 and creates the appropriate continuum smooth discretization for the generation and propagation of SAWs

The actual experimental sample is manufactured with the technique of e-beam evaporation, making the two parts bonded and so behaving as a single solid with two different material properties. This is the reason why the model treats the two parts as bonded, sharing a common surface interface, where all the finite element nodes of glass-metal on this contact interface are common.

With regard to the spatial and temporal resolutions of the finite element model Equations 3.10 and 3.11 are likewise taken into account. An implicit solver is considered and the same numerical techniques for the solution of the non-linear Equations 3.17 and 3.8 are applied, as previously described in section 3.2. The time dependent problem is solved sequentially, with an incremental time step of 1 ns over a time period of 80 ns.

3.4.2 Initial and boundary conditions

Regarding initial conditions, the initial temperature of the body is assumed to be the ambient environmental temperature, while the initial mesh is considered to be non-deformed with zero initial stresses.

The boundary conditions of the model are depicted in Figure 3.6. Symmetry displacement loads are applied to the purple sides (Figure 3.6a), where heat flux is also set to zero due to the quarter symmetry of the 3D model (Figure 3.6b). The left boundary surface of the sample is fixed in order to model the actual conditions of the experiment, while each one of the sides, where heat flux is set to zero, cannot move to one of their directions due to the quarter symmetry (Figure 3.6c).

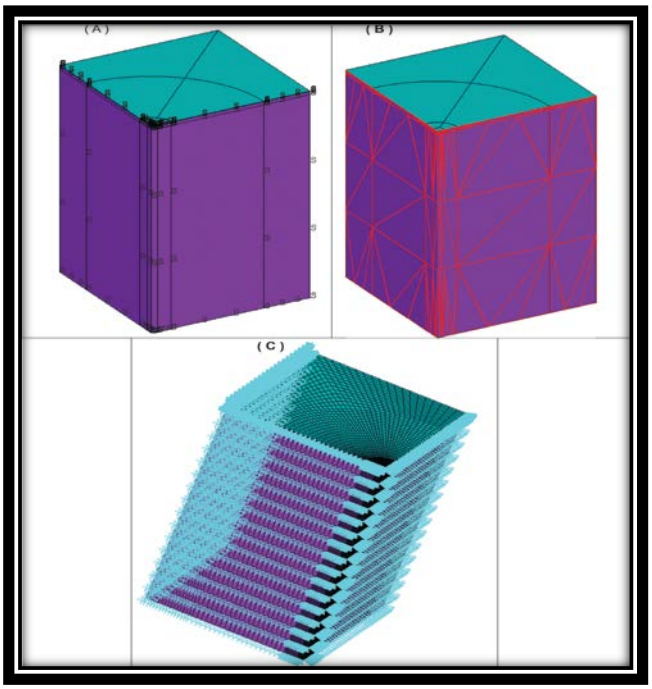

Figure 3.6 Boundary conditions of the FE model

3.4.3 Loading conditions

The energy source Q (energy per volume unit per time) is essentially the absorbed energy per unit volume per unit time and is described by the following Gaussian distribution in time and space:

$$Q(x,y,z,t) = I_0 e^{-b\,h(t)-d\,E_\alpha(t)}(1-R)e^{-4\ln 2(t/t_0)^2} e^{-(x^2+y^2)/r_0^2)} a_b e^{-a_b z} \tag{3.19}$$

where I_0 is the incident laser intensity on target, R is the optical reflectivity of the sample, α_b is the optical absorption coefficient, t_0 is the laser pulse duration at full-width at half-maximum (FWHM) and r_0 is the FWHM laser beam radius on the target. For laser intensities on target exceeding target material's ablation threshold low temperature plasma is generated on the target. This is the onset of the ablation regime, where an appreciable part of laser energy is absorbed [5, 17]. The exponential term $-bh(t)-dE_\alpha(t)$ is introduced in Equation 3.4 to describe the temporal laser irradiance, where E_a is the density of the absorbed radiation energy, h is the ablation depth, while b and d are unknown time-independent coefficients. This term equals to one for laser intensities below the ablation threshold. Coefficient b takes into account

the inverse bremsstrahlung and photoionization absorption mechanisms, as well as stimulated emission, while d modifies accordingly the density of the absorbed radiation energy [5].

With respect to the laser parameters, the FWHM of laser temporal extent, t_0, is 6 ns, while the FWHM spatial beam radius on the sample surface, r_0, is 11.5 μm as experimentally measured. For the simulation of the laser pulse loading conditions, the heat generation function is applied to the nodes of the film body.

3.4.4 Material properties

A 0.6 μm golden (Au) thin film deposited on BK7 glass substrate is used in this study. The material properties used in this modeling study can be categorized into optical and thermo-physical properties. The optical properties, of the absorption coefficient α_b and of reflectivity R are calculated from Equation 3.15, as previously mentioned, and the results can be found in Table 3.1.

For the thermo-mechanical analysis to be accurate and produce correct results the material model must provide details of the material behavior in a wide temperature range. Nevertheless, the determination of the material properties dependence on temperature requires the performance of experiments, which are considered costly and with increased level of difficulty, therefore it is difficult to find data for material properties at high temperatures.

The values for thermo-physical properties have been adopted from available data in [14, 15]. The melting point of Au is 1060 ^{o}C, its latent heat of melting L_m is 64 kJ/kg, while its latent heat of vaporization L_v is 1577 kJ/kg and the boiling point is 2856 ^{o}C. The material properties of the sample and the temperature dependent material properties of gold are given in Table 3.3.

Film-substrate material properties			Temperature dependent properties of Au		
	Au	BK7 glass	Temperature (^oC)	Thermal conductivity ($W/m\,^oC$)	Specific heat (J/kg^oC)
Density (kg/m^3)	19320	2510	27	317	129
Thermal exp. coef. ($1/^oC$)	$14.2x10^{-6}$	$7.1\ x10^{-6}$	127	311	129.5
Young's modulus (GPa)	79	81	227	304	132.3
Poisson's ratio	0.42	0.206	327	298	135.3
			527	284	135.3
			727	270	135.3
			≥927	255	135.3

Table 3.3 Material properties of the sample

3.4.5 Phase change effects and flow chart of the modeling process

The pre-processing input data are stored and loaded once at the beginning of the simulation process. The whole procedure is described in the flow chart of Figure 3.7. The computational time required for each successive time step of 1 ns, is approximately 1 h. The criterions (flags) used are strictly related to the resulting temperature fields, as shown in the decision rhombus boxes of the flow chart.

During the solution of the simulation, the output of the preceding time step becomes an input to the succeeding time step. At the end of a particular step, if the temperature of an element is higher than the melting temperature, phase change occurs. This change is taken into account in the model by considering the latent heat of melting. Therefore, the elements with a temperature exceeding the melting point are grouped and latent heat (see Equation 3.17) is subtracted at every time-step. This leads to a reduction of each element's temperature, simultaneously simulating the onset of melting. Ablation occurs when the temperature of the elements is higher than the boiling temperature. Likewise, in this case the model takes into account the phase change effect by considering the latent heat of vaporization. If the resulting temperature of an element overpasses the boiling point, a group of elements (GTv) is created. Material removal is achieved by the "killing" of the GTv. In this "killing" technique the presence of elements is deactivated by multiplying their stiffness matrix by a severe reduction factor ($\sim 1x10^{-8}$). For laser fluence higher than the ablation threshold, the attenuation of the laser irradiance at the target surface due to plasma

absorption is also taken into account [15]. The optical thickness of the ablation plume, Λ(t), is considered and Equations 3.5 and 3.6 are taken into account by the model. The coefficients *b* and *d* are evaluated by comparing the SAWs produced by the simulation with the experimental results.

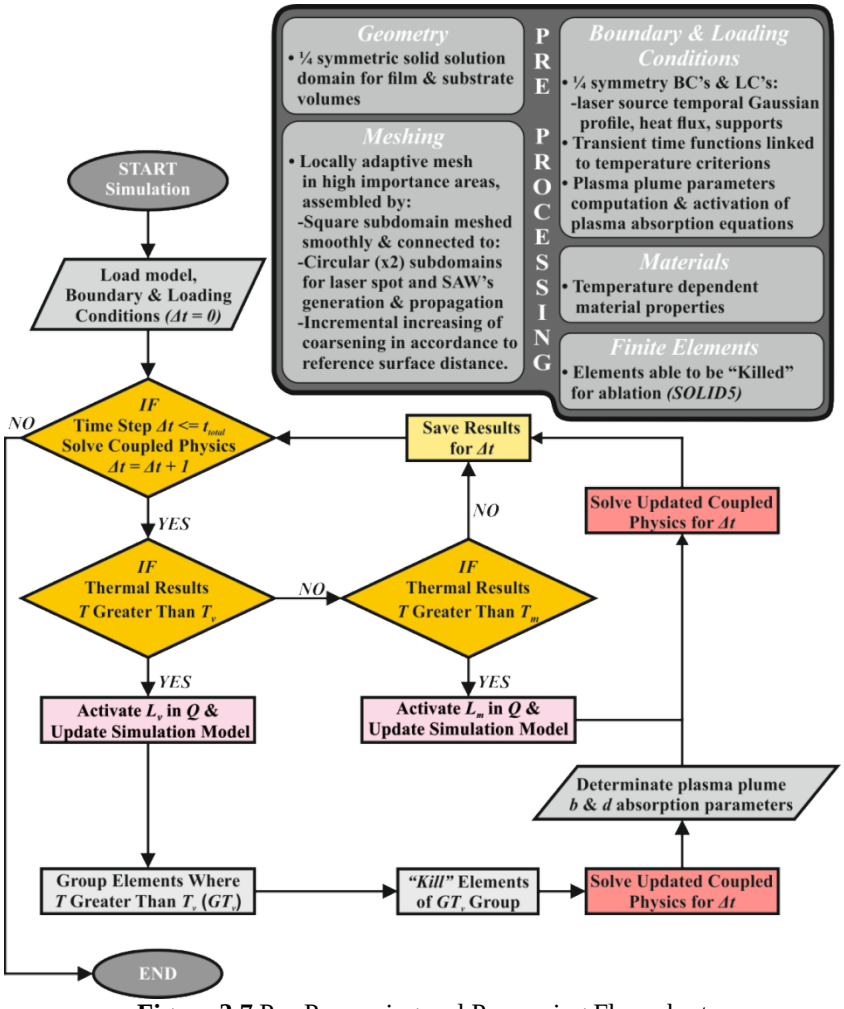

Figure 3.7 Pre-Processing and Processing Flow chart

3.4.6 3D thermomechanical modeling taking into account plasticity

Plastic deformation is observed in most materials, particularly metals, soils, rocks, concrete, foams, bone and skin. However, physical mechanisms that cause plastic deformation vary widely. At a crystalline scale, plasticity in metals is usually a consequence of dislocations. Such defects are relatively rare in most crystalline materials. In such cases, plastic crystallinity can result. In brittle materials, such as

rock, concrete, and bone, plasticity is caused predominantly by slip at microcracks. Plasticity is characterized by a nonlinear relationship between stress and strain. In Figure 3.8 a typical stress-strain curve for steel and its elasto-plastic behavior is shown.

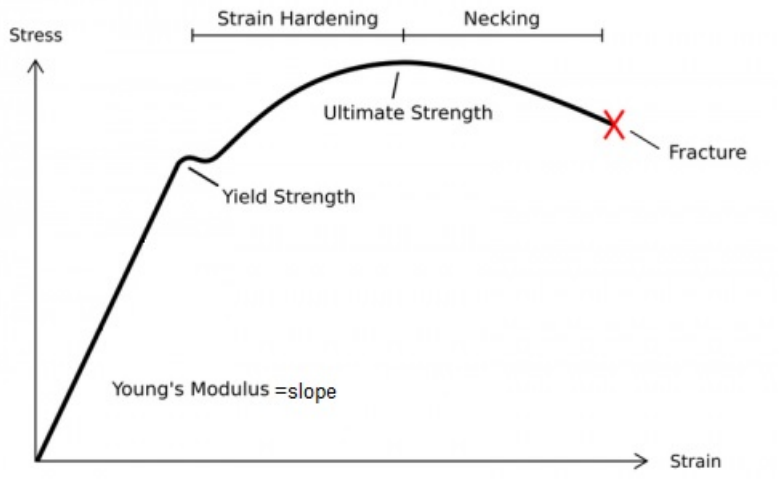

Figure 3.8 Typical stress-strain curve for steel under tensile loading

The linear portion of the curve is the elastic region and the slope is the modulus of elasticity or Young's Modulus, the ratio of the compressive stress to the longitudinal strain. If more force is applied, the material will reach its yield strength. This is known as the yield point, and after this the material will experience plastic deformation or permanent deformation. After the yield point as deformation continues, the stress increases on account of strain hardening until it reaches the ultimate tensile stress. Until this point, the cross-sectional area decreases uniformly and randomly, because of Poisson contractions. However, beyond this point a neck forms where the local cross-sectional area becomes significantly smaller than the original. The ratio of the tensile force to the true cross-sectional area at the narrowest region of the neck is called the true stress. The ratio of the tensile force to the original cross-sectional area is called the engineering stress. If the stress–strain curve is plotted in terms of true stress and true strain the stress will continue to rise until failure. Eventually the neck becomes unstable and the specimen fractures.

The 3D FE model is further modified to take into account plasticity effects in the thermoelastic and melting regimes. By taking into account temperature dependent

stress-strain curves for the mechanical properties of metallic materials the elasto-plastic mechanical behaviour of matter irradiated by laser pulses is studied. With regard to the structural behavior of the film, the material deforms elastically prior to the yield point and returns to its original shape when the applied thermal stress is removed. For developed thermal stresses that overcome the yield point the material begins to deform plastically. The irreversible plastic deformation, which occurs after yield strength, is permanent.

In order to model plasticity and define the stress–strain behavior of the metallic film, a multilinear isotropic hardening, rate-independent, elastic–plastic model (MISO) available in ANSYS is used. This model has been evaluated in the literature not only for metals but also for polymers [18]. Rate-independent plasticity is characterized by the irreversible straining that occurs in a material once a certain level of stress is reached. The plastic strains are assumed to develop instantaneously, independent of time.

This constitutive model for elastic-plastic behavior initially decomposes the total strain into elastic and plastic parts and separate constitutive models are used for each. Its essential characteristics are i) the usage of a Von Mises yield criterion that defines the material state at the transition from elastic to elastic-plastic behavior, ii) an associated flow rule that determines the increment in plastic strain from the increment in load and iii) an isotropic hardening rule that gives the evolution in the yield criterion during plastic deformation.

The Von Mises yield criterion is a scalar function, a surface in stress space. The yield criterion has the form

$$f(\boldsymbol{\sigma}) = \sigma_y \tag{3.20}$$

where $f(\boldsymbol{\sigma})$ a scalar function of Von Mises stress and σ_y the current yield stress that evolves as a function of the amount of plastic work done. Stress states inside the yield surface are given by

$$f(\boldsymbol{\sigma}) - \sigma_y < 0 \tag{3.21}$$

and result in elastic deformation. The material yields when the stress state reaches the yield surface and further loading causes plastic deformation. Plastic strains occur in a direction normal to the yield surface. Isotropic hardening, as seen in Figure 3.9, causes a uniform increase in the size of the yield surface and results in an increase in yield stress upon further loading from a state on the yield surface. The yield surface remains centered about its initial centerline and expands in size as the plastic strains develop. Stresses outside the yield surface do not exist and the plastic strain and shape of the yield surface evolve to maintain stresses either inside or on the yield surface [11].

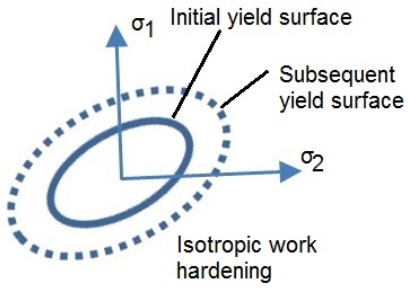

Figure 3.9 Isotropic hardening rule

Moreover, in a multilinear stress-strain curve, as seen in Figure 3.10, a Young modulus and a yield stress define the elastic part, while the rest of the curve is modelled by different pairs of stress–strain points. After the yield stress and up to the ultimate tensile strength (UTS) the curve exhibits strain hardening. For temperature-dependent curves, the current yield stress is determined by temperature interpolation of the input curves after they have been converted to stress-plastic strain curves. More details for the MISO model are presented in Appendix B.

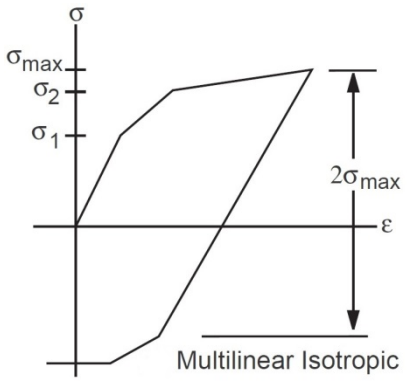

Figure 3.10 Stress-strain behavior of the multilinear isotropic model

The geometry and meshing of the thin film substrate system, as well as the boundary and loading conditions remain the same, as described in previous sections. The mechanical and thermal properties for gold, copper and aluminum, as well for the BK7 glass substrate used in the numerical simulations, are found in the literature [19-21]. These structural material properties and temperature dependent thermal properties are presented in Tables 3.4 and 3.5 respectively.

	Density (kg/m^3)	Thermal expansion coefficient ($10^{-6} \times 1/K$)	Young's modulus ($10^9 \times$ Pa)	Poisson's ratio	α_b (m^{-1}) (Palik, 1991)
Gold (Au)	19320	14.2	64.6	0.42	$57x10^6$
Copper (Cu)	8938	15.4	117	0.3406	$61x10^6$
Aluminum (Al)	2712	22.2	69	0.33	$151x10^6$
Glass BK7	2510	7.1	81	0.206	0.18

Table 3.4 Material properties at room temperature and absorption coefficient

	T_m(K)	L_m(J/Kg)	T (K)	300	400	500	600	800	1000	>1100
Au	1337	$64x10^3$	k(W/mK)	317	311	304	298	284	270	255
			C_p(J/kgK)	129	130	132	135	135	135	135
Cu	1358	$207x10^3$	k(W/mK)	401	391	385	379	366	352	339
			C_p(J/kgK)	393	398	408	417	441	480	480
Al	933	$321x10^3$	k(W/mK)	237	240	237	232	218	213	213
			C_p(J/kgK)	910	955	995	1034	1034	1034	1034

Table 3.5 Temperature dependent thermal properties of metals

Temperature dependent engineering stress-strain curves are also adopted from the literature. With respect to the gold material properties, there is a lack of stress-strain experimental values for very high temperatures, while engineering stress-strain values are considered for a specific strain rate (6×10^{-4} 1/sec) [22]. For the copper and

aluminum true stress-strains values are taken from the work of Samanta [23] for a strain rate of 1800 1/sec and 1900 1/sec respectively.

Once the material enters into the plastic regime, additional material deformation is isochoric. The plastic-flow regime has a negligible change in volume, allowing the change in length to be related to the change in area. Therefore, the engineering stress-strain (σ_e-ε_e) data can be converted into true stress-strain (σ_t-ε_t) data that are imported to ANSYS. The equations that relate engineering stress and strain to the true stress and strain of the material are valid up to the Ultimate Tensile Strength (UTS) and have the following form

$$\sigma_t = \sigma_e(1+\varepsilon_e) \tag{3.22}$$

$$\varepsilon_t = \ln(1+\varepsilon_e) \tag{3.23}$$

The true stress-strains curves used in this study are presented in Figure 3.11. After the last point in the curves, the simulation code assumes that the material is perfectly plastic. The strain will continue to increase without an increase in stress. Moreover concerning the Young modulus, temperature dependent values are taken into account for the simulation, based on the temperature dependent stress-strain curves.

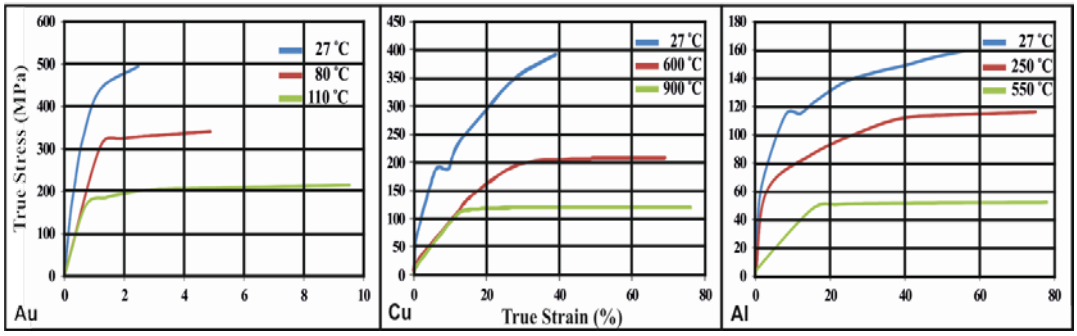

Figure 3.11 True stress-strain curves for gold, copper and aluminum [22, 23]

3.4.7 3D simulation of matter with defects irradiated with laser pulses

In this section the 3D model is further modified to take into account gap defects and the study is limited for laser fluences in the thermoelastic regime. Material defects, volume and/or surface breaking cracks, and discontinuities are a major problem mainly in the industrial sector [24, 25]. The Laser-generated ultrasound technique is particularly useful for the detection of surface defects [26]. Various finite

element numerical approaches in the literature model the propagation of ultrasounds in solids with surface cracks or defects by replacing them with a surface notch of rectangular shape for the convenience of modeling [9, 27]. This modeling approximation is also adopted here.

Different test cases of gap/defects of open and close geometry that differ in the size are tested, while their influence on the propagation of the acoustic waves is investigated, when a film-substrate system is irradiated. In Figure 3.12 the position of a characteristic volume gap of open geometry on the sample is depicted, along with its dimensions.

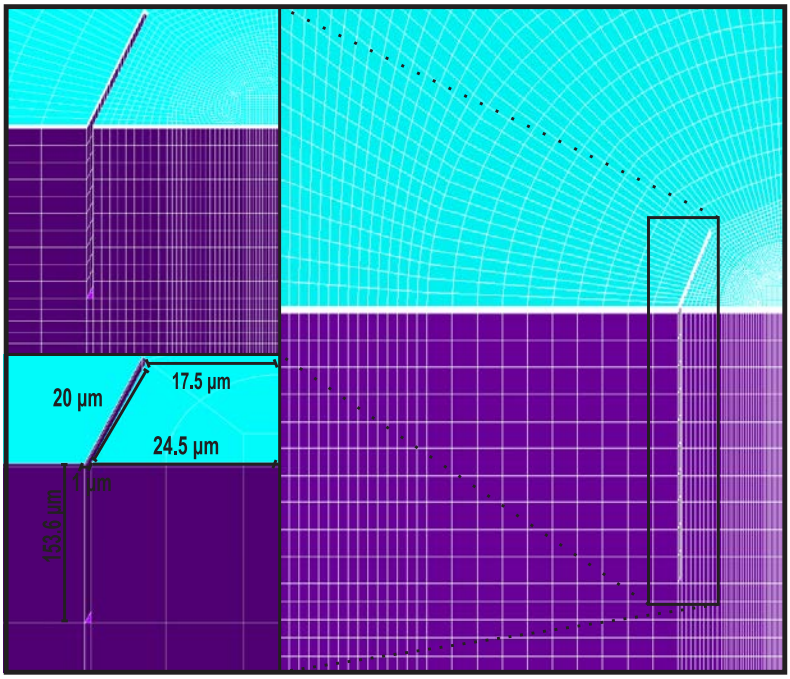

Figure 3.12 Position and dimensions of a characteristic volume gap of open geometry on the sample

The model consisted of a thin gold metal film having a thickness of 0.6 micrometers, and is supported on a thick glass substrate of 200 micron thickness. The same boundary, loading conditions as well as material properties are applied like previously described in sections 3.3.1-3.3.4.

References

[1] C. E. Scruby and L. E. Drain, *Laser ultrasonics techniques and application*, (Adam Hilger, New York, 1990).

[2] B. Sorazu, G. Thursby, B. Culshaw, F. Dong, S. G. Pierce, Y. Yang, and D. Betz, Optical generation and detection of ultrasound, *Strain* **39**, 111-114 (2003).

[3] S. Amoruso, R. Bruzzese, N. Spinelli and R. Velotta, Characterization of laser-ablation plasmas, *J. Phys. B: At. Mol. Opt. Phys.* **32**, R131–R172 (1999).

[4] J. C. Diels, W. Rudolph, Ultrashort Laser Pulse Phenomena, Second Edition (Optics and Photonics Series) 2nd Edition Academic Press.

[5] A. V. Bulgakov and N. M. Bulgakova, Thermal model of pulsed laser ablation under the conditions of formation and heating of a radiation-absorbing plasma, *Quantum Electron.* **29**, 433-437 (1999).

[6] B. Xu, Z. Shen, X. Ni, J. Lu and Y. Wang, Finite element model of laser-generated surface acoustic waves in coating-substrate system, *J. Appl. Phys.* **95**, 2109-2115 (2004).

[7] B. Xu, Z. Shen, X. Ni, J. Wang, J. Guan and J. Lu, Thermal and mechanical finite element modeling of laser-generated ultrasound in coating–substrate system, *Opt. Laser Technol.* **38**, 138–145 (2006).

[8] S. Zhou, P. Reynolds, R. Krause, T. Buma, M. O'Donnell and J. A. Hossack, Finite-Element Analysis of Material and Parameter Effects in Laser-Based Thermoelastic Ultrasound Generation, *IEEE Transactions on Ultrasonics, Ferroelectrics and Frequency Control* **51**, 1178-1186 (2004).

[9] J. Guan, Z. Shen, X. Ni, J. Wang, J. Lu and B. Xu, Numerical simulation of the reflected acoustic wave components in the near field of surface defects, *J. Phys. D: Appl. Phys.* **39**, 1237–1243 (2006).

[10] D. Alleyne and P. Cawley, A two-dimensional Fourier transform method for measurement of propagating multimode signals. *J. Acoust. Soc. Am.* **89**(3), 1159–68 (1991).

[11] ANSYS user's manual *Release 12.0* (Southpointe Canonsburg, April 2009).

[12] ANSYS Inc., *Coupled-field analysis guide, Release 12.0* (Southpointe Canonsburg, April 2009).

[13] J. Pfluger, J. Fink, W. Weber and K. P. Bohnen, in: E.D. Palik (Ed.), *Handbook of Optical Constants of Solids*, vol. II, Academic Press, 1991.

[14] http://www.engineeringtoolbox.com (last accessed May 2014)

[15] http://www.efunda.com/materials/materials_home/materials.cfm (last accessed May 2014).

[16] V. Dimitriou, A. Kanarachos and D. Koulocheris, *WSEAS Transactions on Circuits and Systems* **2**, 473 (2003).

[17] R. K. Singh and J. Narayan, Pulsed-laser evaporation technique for deposition of thin films: Physics and theoretical model, *Phys. Rev. B* **41**, 8843-8859 (1990).

[18] A. Arriaga, J. M. Lazkano, R. Pagaldai et al. Finite-element analysis of quasi-static characterisation tests in thermoplastic materials: Experimental and numerical analysis results correlation with ANSYS. *Polymer Testing* **26**, 284-305 (2007).

[19] F. P. Incropera and D. P. DeWitt, *Fundamentals of Heat and Mass Transfer*, Wiley (1986).

[20] D. R. Lide ed., *CRC Handbook of Chemistry and Physics*. Internet Version 2005, CRC Press.

[21] G. K. White and S. J. Collocott Heat Capacity of Reference Materials: Cu and W. *Journal of Physical and Chemical Reference Data* **13**, 1251-1257 (1984).

[22] N. J. Karanjgaokar, C. S. Oh, J. Lambros et al. Inelastic deformation of nanocrystalline Au thin films as a function of temperature and strain rate, *Acta Materialia* **60**, 5352–5361 (2012).

[23] S. K. Samanta, Dynamic deformation of aluminium and copper at elevated temperatures. *Journal of the Mechanics and Physics of Solids* **19**, 117-135 (1971).

[24] D. F. Cannon, K-O Edel, S. L. Grassie and K. Sawley, *Fatigue Fract. Eng. M.* **26**, 865–87 (2003).

[25] B. Dutton, A. R. Clough, M. H. Rosli and R. S. Edwards, *NDT&E International* **44**, 353–360 (2011).

[26] R. S. Edward, X. Jian and S. Dixon, *Appl. Phys. Lett.* **87**, 194104 (2005).

[27] R. J. Dewhurst, A. D. W. Mckie, and S. B. Palmer, Further evidence for two-component surface acoustic wave reflections from surface breaking slots, *Appl. Phys. Lett.* **49**, 1694 (1986).

Chapter 4

4. Numerical results and comparison with experiments

In this Chapter are presented the numerical results of the developed FE models, a description of the dynamic experimental optical technique that is used in combination with the FEM simulation and a comparison and verification of numerical with experimental results.

4.1 Numerical results

Numerical results of the 2D axisymmetric and the 3D quarter-symmetric model are here presented.

4.1.1 Results of 2D axisymmetric model

A 0.2 nm Al film deposited on a 3 μm fused silica substrate is simulated in this study. Numerical results of vertical displacement for the FEM model are presented in Figure 4.1 for Δt_1=17 ns and Δt_2=27 ns after the sample irradiation. With respect to the used laser parameters, the laser energy is 20 μJ/pulse, t_0 is 6 ns, while the radius r_0 of the pulsed laser spot on the sample surface is considered to be 12.5 μm. Figure 4.1a shows an expanded view of the vertical displacements along z-direction of the sample for the temporal moment Δt_1=17 ns. An ultrasound is created approximately 50 μm from the initial position. Similarly, Figure 4.1b shows an expanded view of the vertical displacement of the sample for the temporal moment Δt_2=27 ns. The same ultrasound has moved approximately 81 μm far from the initial position and has a propagation velocity of about 3100 m/sec. In order to examine the accuracy of the results the velocity values are compared and are in good agreement with the value C_{Al} ~$(2.96\pm0.01)\times10^3$ m/s that is estimated by the following analytic equation for the surface acoustic velocity for aluminum [1-2]

$$C = \frac{0.87 + 1.12\nu}{1+\nu}\sqrt{\frac{E}{2\rho(1+\nu)}} \tag{4.1}$$

where C is the SAW velocity, ν is the Poisson's ratio, E is the Young's modulus and ρ is the material density. The observed differences may be due to the fact that Equation 4.1 concerns the case of a homogeneous isotropic material, while the current study concerns film-substrate systems.

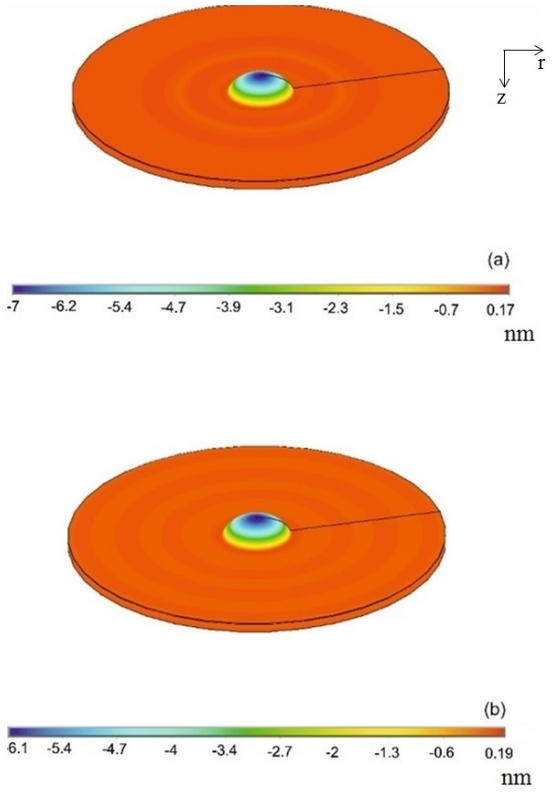

Figure 4.1 Expanded vertical displacements along r-axis for Δt_1=17 ns and Δt_2=27 ns

Moreover, for the same temporal moments Δt_1=17 ns (top) and Δt_2=27 ns (bottom) Figure 4.2 illustrates the temperature distribution of the layered structure. The maximum temperatures (^{o}C) are below the melting point of the material (660^{o}C).

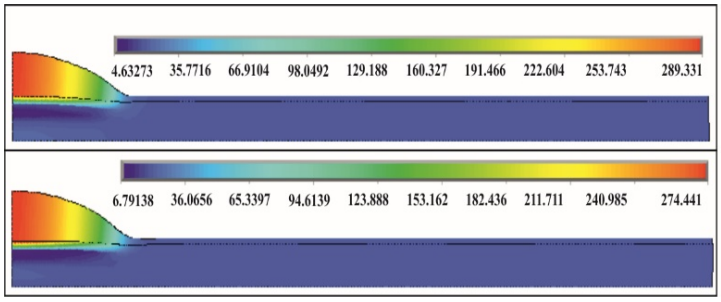

Figure 4.2 Temperature distribution of the film-substrate for Δt_1=17 ns (top) and Δt_2=27 ns (bottom)

The 2D simulations results are compared with experimental data (see section 4.3) but the displacement field is overestimated. Moreover, important information with respect to the amount of the ablated mass and the depth of the crater that is created for higher laser fluence is lost when the phenomenon is dealt with 2D simulation. Therefore, in order to simulate accurately the complex multiphysics problem of matter irradiation, in all regimes of interest, 3D numerical simulations are performed.

4.1.2 Results of 3D quarter-symmetric model

A 0.6 μm Au film deposited on 0.2 mm BK7 glass substrate is simulated in this study and is depicted in Figure 4.3. A locally adaptive fine mesh of 20160 elements in the quarter cyclic domain of radius 85μm and a total of 27360 elements in the whole volume of the Au thin film is used. The whole sample is discretized to a total number of 88920 elements. The actual thin film is produced with the method of e-beam evaporation. With respect to the laser parameters, the Full Width at Half Maximum (FWHM) of laser temporal extent, t_0, is 6 ns, while the FWHM spatial beam radius on the sample surface, r_0, is 11.5 μm, as experimentally measured. Typical values of pump laser fluences in the range of 0.1–5.0 J/cm^2 are used in order to investigate all three regimes of interest (thermoelastic, melting, ablation). Comparing the temperature values, obtained from the simulations, to the ones for the melting and boiling points of gold it is found that melting and ablation occurs for pump laser fluences of 0.34 J/cm^2 and 1.00 J/cm^2, respectively. Therefore, the thermoelastic regime is defined between 0.1 and 0.34 J/cm^2, the melting regime between 0.34 and 1.00 J/cm^2, and the ablation regime for laser fluences greater than 1.00 J/cm^2.

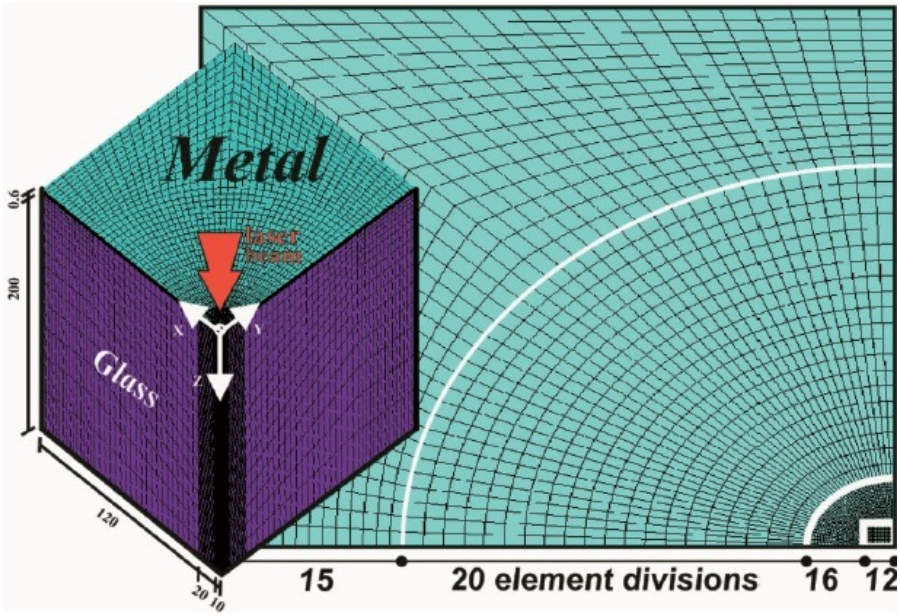

Figure 4.3 3D quartersymmetric finite element model details

In Figure 4.4 results for the temperature distribution and displacement field for laser fluence of 0.2 J/cm^2 are presented. The physical problem is restricted in the thermoelastic regime for this fluence value. The resulting temporal evolution of the bulge deformation and the corresponding temperature field (upper left sub-figures) for three temporal steps *(Δt)* are presented in Figures 4.4a, 4.4b and 4.4c. The maximum bulge deformation is 13.8 nm for the third temporal moment, while the maximum temperature approximated by the model is below the melting point and reaches the value of 953 ^{o}C. These resulting data assure the elastic deformation of the sample. In Figure 4.4d the generation and propagation of SAWs for the temporal moment of 28 ns is depicted, showing a fully symmetry formation. The displacement value of the first SAW is computed to be 0.1 nm and is found to be in a distance of 47 μm from the epicenter. The central volume of the model has been technically removed to allow a better contour color-map interpolation (without the high displacement values of the bulge) and let the SAWs propagation be clearly visible.

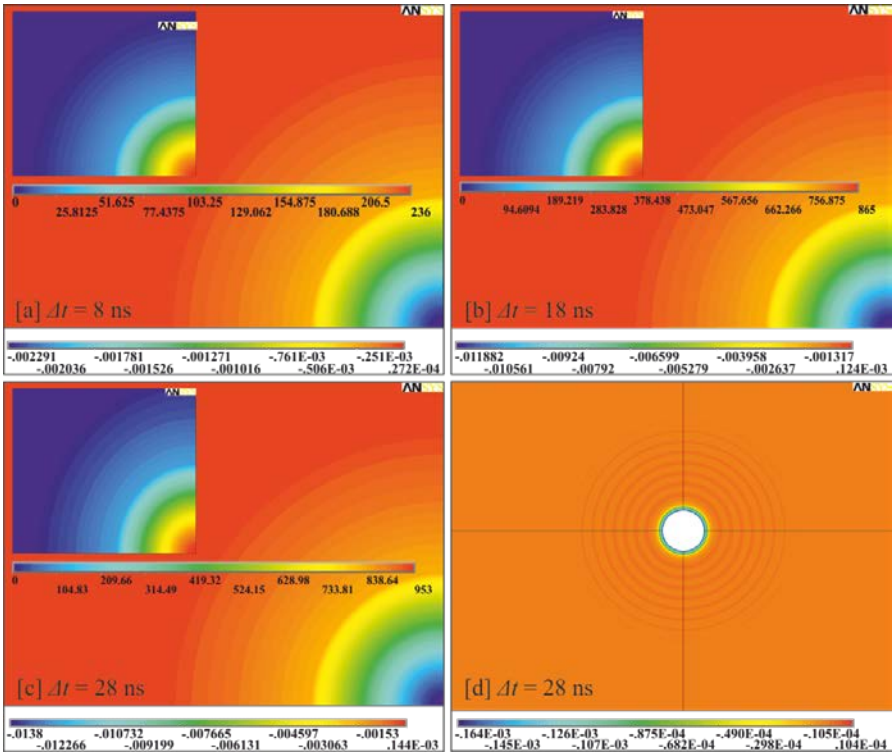

Figure 4.4 Calculated temporal (μm) and temperature (^{o}C) field evolution and SAWs propagation (μm) in the thermoelastic regime

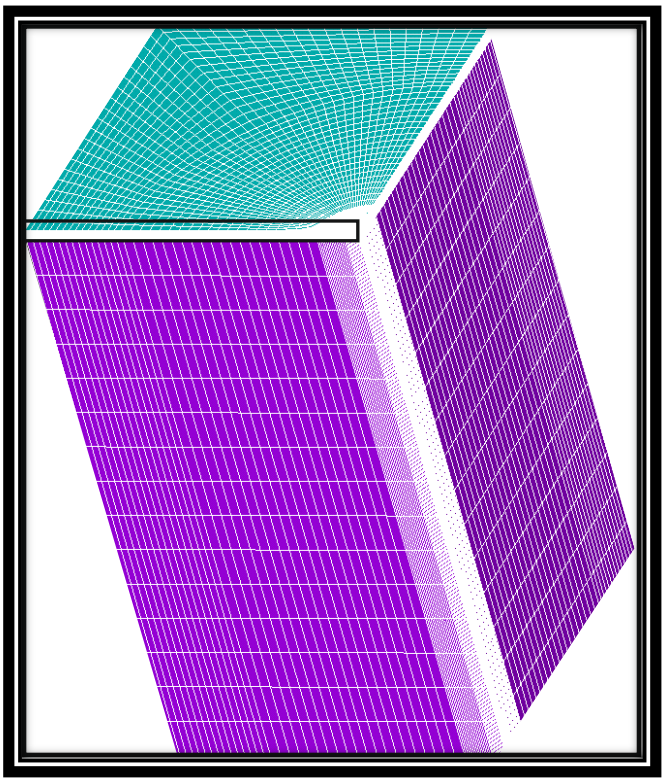

Figure 4.5 Nodes with coordinates Y, Z=0, 0≤X≤120 μm

In Figure 4.5 the boundary surface nodes of the thin film with coordinates Y, Z=0, 0≤X≤120 μm are depicted. These nodes are selected and the values of the vertical surface deformation are recorded for different temporal moments. Consequently, based on these values in Figure 4.6 graphs of surface deformation as a function of the radial distance from the laser irradiated area are presented, for laser fluences below the ablation threshold. The peak amplitude of the SAWs decreases with time, while it increases when laser fluence increases. Propagation velocities of the laser-generated SAWs are estimated. For laser fluence equal to 0.54 J/cm^2 and Δt = 17 ns, the peak amplitude of the SAW is 6 nm and is radially displaced 30 μm from the epicenter. For Δt = 33 ns the same SAW has a peak amplitude of 2.5 nm and is radially displaced 73 μm from the epicenter, resulting in a propagation velocity of ~2685 m/s.

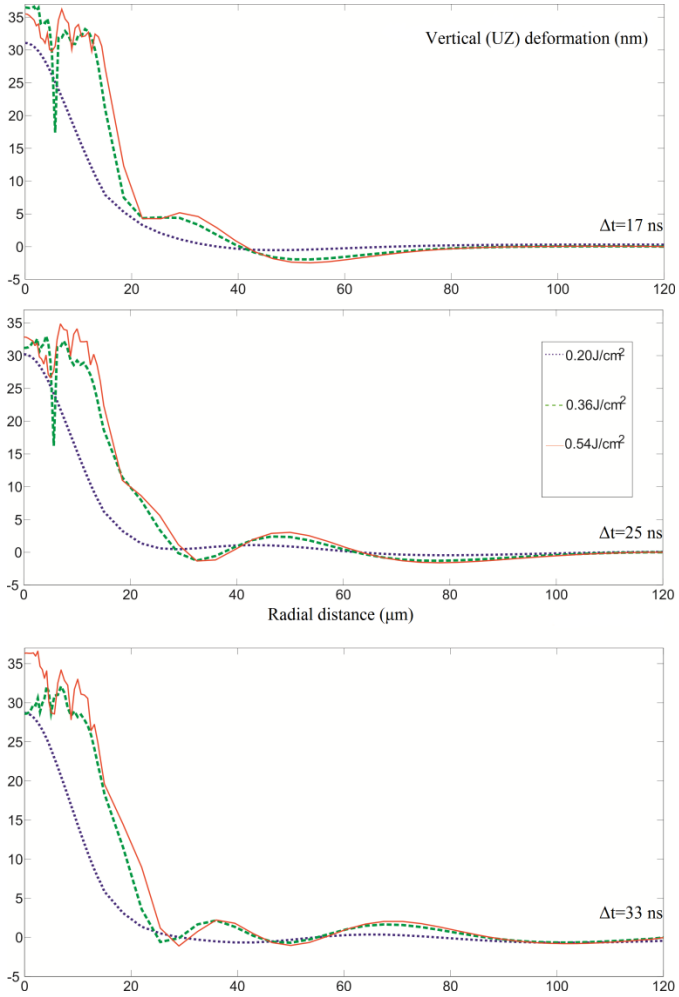

Figure 4.6 Graph of vertical surface deformation as a function of the radial distance from the laser irradiated area for three different laser fluences and for three Δt's

In Figure 4.7 graphs of surface deformation as a function of the radial distance from the laser irradiated area are presented, for laser fluences above the ablation threshold. The peak amplitude of the SAWs decreases with time, while it increases when laser fluence is increased. Additionally, the radial width of the ablated material increases. Propagation velocities of the laser-generated SAWs are estimated. For laser fluence equal to 4 J/cm^2 and Δt = 17 ns, the peak amplitude of the SAW is 12 nm and is radially displaced 39.5 μm from the epicenter. For Δt = 33 ns the same SAW has a peak amplitude of 3.5 nm and is radially displaced 81.5 μm from the epicenter, resulting in a propagation velocity of 2650 m/s.

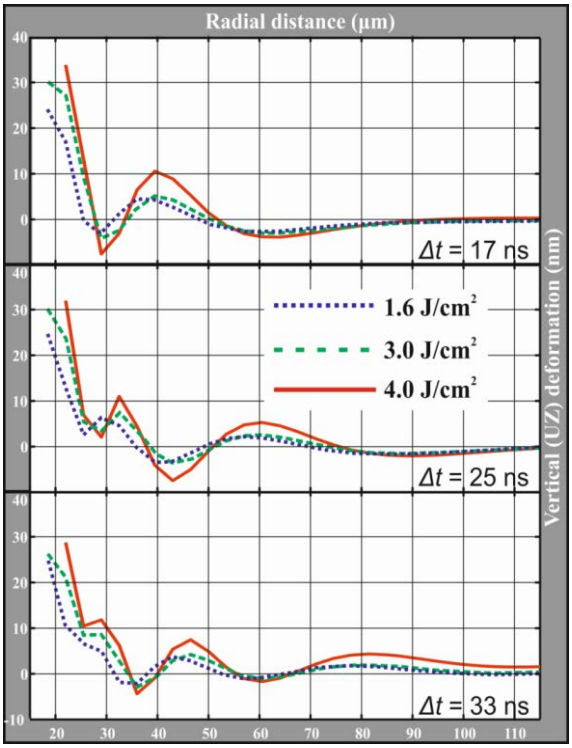

Figure 4.7 Graph of vertical surface deformation as a function of the radial distance from the laser irradiated area, for three different laser fluences and for three Δt's

In Figure 4.8 the UZ deformation, in nm, for a half-symmetric view of the model for laser fluence of 3.5 J/cm^2 and various Δt's: (a) 7 ns, (b) 10 ns, (c) 14 ns, (d) 20 ns, (e) 26 ns and (f) 32 ns, is presented. Again, the SAWs propagate outwards of the irradiated region in the form of concentric rings. For the first 9 ns the sample is elastic deformed. In Figure 4.8b the latent heat of melting is taken into account, due to the fact that the temperature exceeds the melting point of the gold. In the elastic and melting regimes (Figures 4.8(a)-(b)), a central bulge is observed, centered on the laser

irradiated region, along with the SAWs propagating outwards of the irradiated region in the form of concentric rings. In the ablation regime (Figures 4.8(c)-(f)), where material has actually been removed from the sample, a crater-type deformation with elevated edges is observed, centered around the laser irradiated region. For the temporal moment Δt=12 ns the latent heat of vaporization is taken into account, due to the fact that the temperature exceeds the boiling point of the gold and material is vaporized. In Figure 4.8c the ablated part has been removed and the first SAW is shown. Moreover, in Figure 4.8e a second SAW is created. Furthermore, in Figures 4.8(d)-(f) the propagation of the SAWs may be observed.

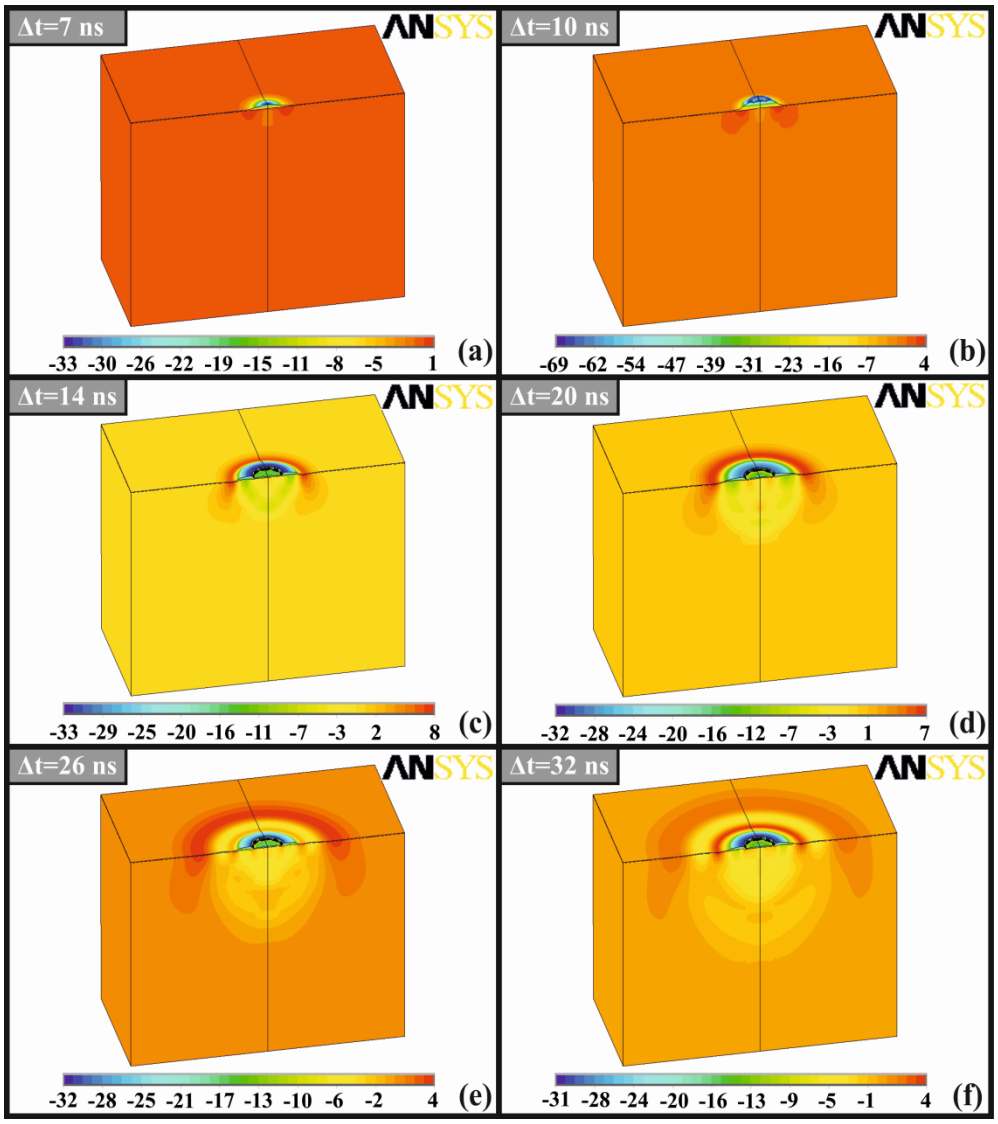

Figure 4.8 Temporal evolution of solid's deformation (UZ)

In Figure 4.9 the temperature distribution for thermoelastic, melting, and ablation regime is depicted. In the elastic regime the generation and formation of the bulge in the origin of the model occurs due to heat conduction. Temperature reaches the value of 929 ^{o}C and gradually decreases during the next timesteps. For fluence 0.8 J/cm^2 the thin Au film starts to melt at Δt=9 ns. For Δt=15 ns (Figure 4.9(e)) the effects of L_m may be observed and likewise for Δt=25 ns in Figure 4.9(f). Material removal is applied for laser fluence 2.5 J/cm^2. As shown in Figures 4.9(h) and (i), the GTv grouped elements have been killed so as to simulate the ablation process. The ablation threshold is reached in a rapid time, for Δt=9 ns after initiation of laser irradiation.

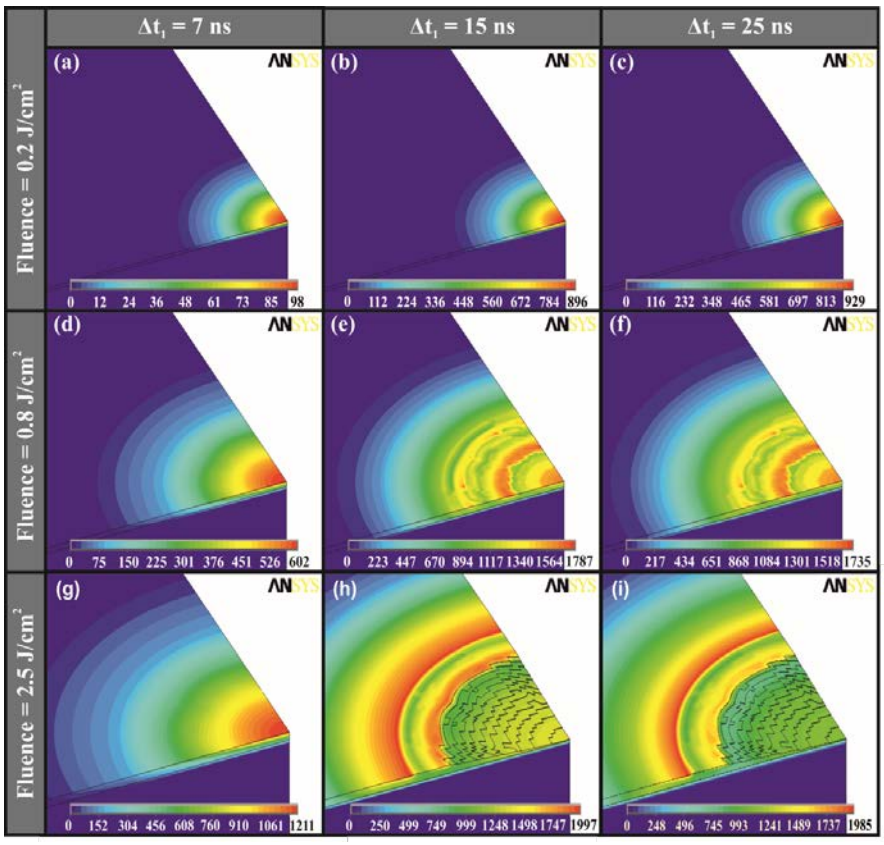

Figure 4.9 Temperature distribution of the solid sample: (a)-(c) elastic regime, (d)-(f) melting regime) and (g)-(i) ablation regime

In Figure 4.10 the vertical surface deformation obtained by the FEM model simulation for a specific distance, 50 μm away from the epicenter, is depicted in relation to time for different values of laser fluence. For increasing laser fluence it is

observed that the vertical displacement increases, as expected, and the peak deformation for both of the SAWs is reached faster in time for higher laser fluences.

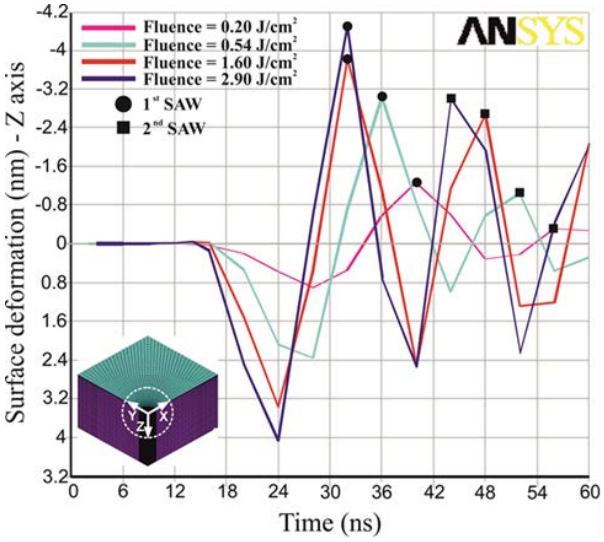

Figure 4.10 Surface deformation in relation to time

4.1.3 Results of 3D quarter-symmetric model taking into account plasticity

The research study is further expanded by taking into account the plastic properties of the materials, aiming to simulate the developed stresses and strains on the irradiated matter. Typical values of laser fluences in the range of 0.05-0.5 J/cm^2 are used to investigate regimes below and above the melting threshold, but below the ablation threshold. Simulations are performed using the expanded FEM model in order to compute the melting threshold of three metal (Gold, Copper, Aluminum) films, based on temperature criteria. The melting threshold of gold is found to be 0.34 J/cm^2 while the melting thresholds for copper and aluminum are found to be 0.3 J/cm^2 and 0.32 J/cm^2 respectively.

For laser fluence equal to 0.33 J/cm^2 and for different temporal moments the temperature and Von Mises stress distributions are depicted in Figures 4.11 to 4.13. The temperature and stress fields are shown for the gold film in Figure 4.11, while Figures 4.12 and 4.13 correspond to copper and aluminum films respectively.

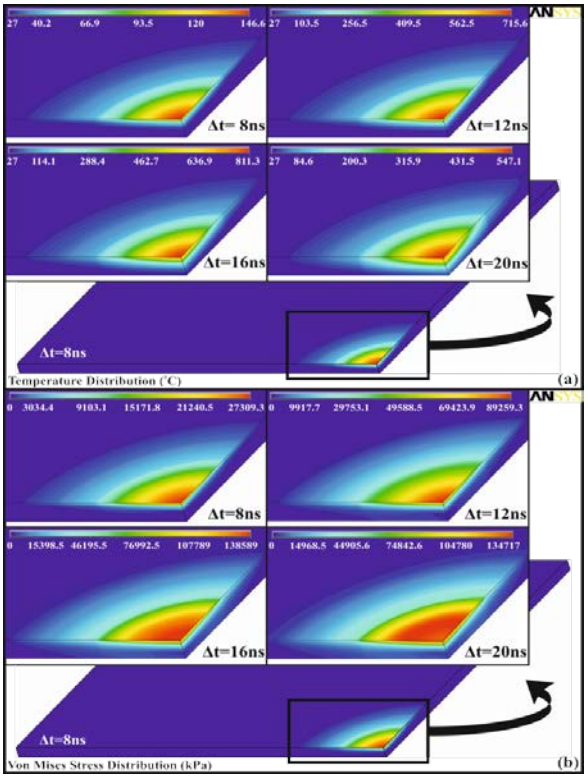

Figure 4.11 Temperature (a) and Von Mises stress (b) distributions for the gold film at four temporal moments (Δt's)

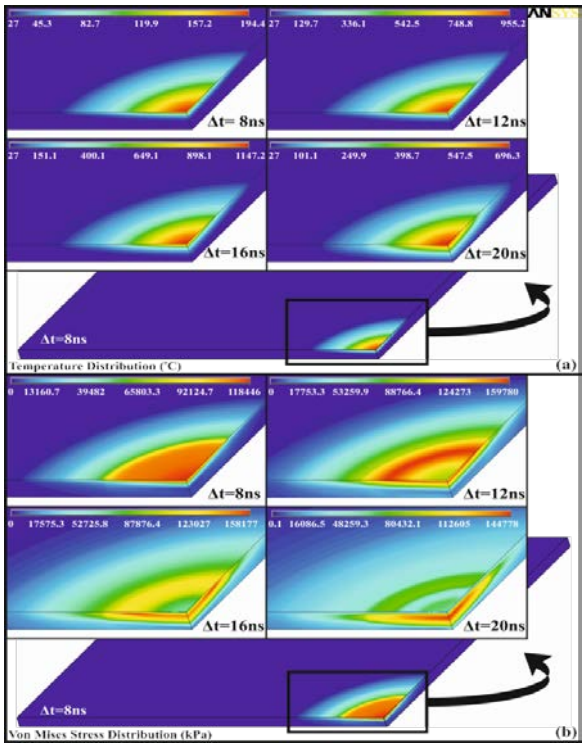

Figure 4.12 Temperature (a) and Von Mises stress (b) distributions for the copper film at four temporal moments (Δt's)

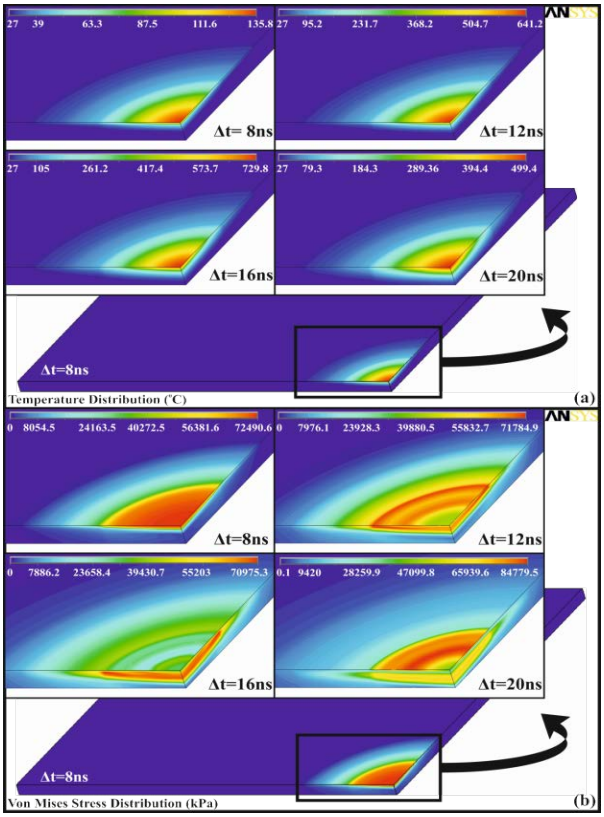

Figure 4.13 Temperature (a) and Von Mises stress (b) distributions for the aluminum film at four temporal moments (Δt's)

It is observed that the maximum temperature of the gold film is below its melting point for 16 ns after the beginning of the irradiation. Moreover, at the same temporal moment its maximum computed Von Mises stress is below the yield stress, which is approximately 150 MPa based on the stress-strain curve of gold. Therefore, no plastic strains are observed on the gold film. On the contrary, for copper and aluminum films the maximum computed temperatures at the same temporal instance (16 ns) are 1147 ^{o}C and 730 ^{o}C, respectively, in both cases higher than their melting points (which are 1085 ^{o}C and 660 ^{o}C).

With respect to the stress distribution, at the temporal moment of 12 ns the maximum Von Mises stress reaches the current yield stress of copper, which is 160 MPa. The same behavior holds for aluminum, which has a yield stress of about 72 MPa, for the same temporal moment. A stress wave is generated for temporal moment of 16 ns and later for both materials. Moreover, 16 ns after the beginning of the laser-

film interaction the maximum plastic strain for copper has a value of 22.7 $\times 10^{-3}$, while the corresponding maximum plastic strain for aluminum has a value of 22.5 $\times$ 10^{-3}.

For a half-symmetric view of the model in Figure 4.14 the UZ deformation, in nm, is presented for laser fluence of 0.4 J/cm^2 and various Δt's: (a) 20 ns, (b) 24 ns, (c) 28 ns. It can be noticed from Figure 4.6 that the 3D model provides insights to the whole solid structure. The propagation of surface acoustic waves (Rayleigh waves) that have a longitudinal and a vertical shear component, may be observed. For this laser fluence the maximum UZ displacement of the wave in the copper specimen is 1.8 nm and has a radial distance from the epicenter of 36 μm. The maximum UZ displacement of the wave in the aluminum film is 1.2 nm and is 39.5 μm away from the epicenter, while the maximum UZ displacement of the wave in the gold film is 0.9 nm and is 32.5 μm away from the epicenter.

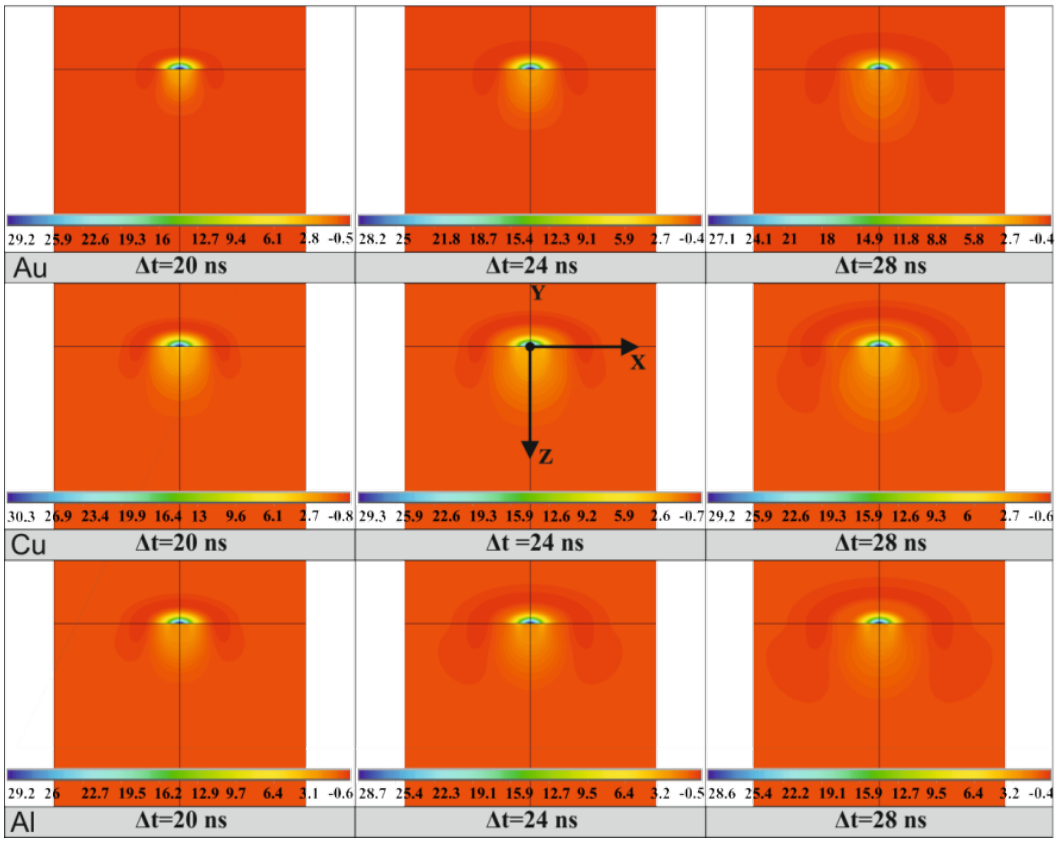

Figure 4.14 Spatiotemporal evolution for Au, Cu and Al metallic film-glass substrate deformations – UZ (nm) for laser fluence of 0.4 J/cm^2

Certain limitations are worth noting. The material models are designed to calculate problems where deformation is achieved principally by compression or tension and not by heating from external thermal sources. Also, rate independent structural material properties are considered. However, a constitutive model like Johnson-Cook [3] would be more appropriate for the simulation of matter's plastic behavior, since it takes into account strain rates that vary at high temperatures.

4.1.4 Results of 3D quarter-symmetric model with defects

A 0.6 μm Au film deposited on 0.2 mm BK7 glass substrate is simulated in this study, with different type of defects. A typical value of pump laser fluence approximately equal to 0.2 J/cm^2 is used, restricting the investigation in the thermoelastic regime. Results for the vertical displacement are presented in Figure 4.15 for a model with defects and without defects, respectively. For the first two test cases the gap of the defect has a depth of 0.6 μm, reaching the bottom of gold film. As presented in Figure 4.15(a) and (b), for a defect with open and closed geometry respectively, the FEA results show that the presence of this discontinuity has no influence to the propagation of Rayleigh surface acoustic waves. In the third test case however, where the same defect reaches the bottom of the glass (whole volume defect), a part of the Rayleigh surface acoustic waves is transmitted while the rest is reflected, as may be noticed in Figure 4.15(c). For the fourth test case, where the surface gap discontinuity has a closed geometry, only a small part of the Rayleigh surface acoustic waves is transmitted (5% of the maximum vertical displacement, Figure 4.15(d)).

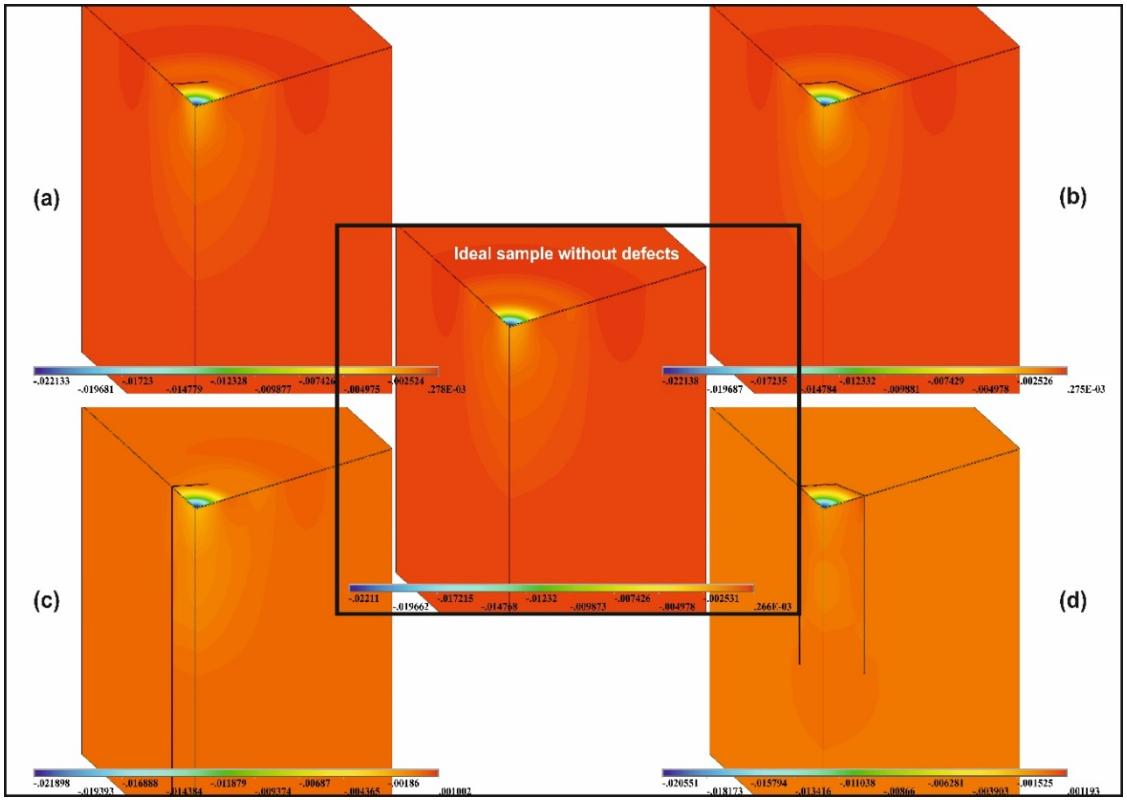

Figure 4.15 Propagation of acoustic waves in film-substrate samples with defects. Response of the original sample without defects is depicted in the middle of the figure

Results indicate that the generation and propagation of SAWs is not affected for an illuminated film-substrate system with defects reaching the bottom of the film. On the contrary, a defect exists with a depth reaching the substrate when an obtained experimental result for an irradiated thin-film substrate system indicates an ultrasound where only a part of it is transmitted.

4.2 Laser interferometric dynamic technique

For the experimental investigation of laser generated SAWs, a dynamic imaging interferometric diagnostic technique has been developed and used [4]. The target consists of a 600 nm thick metal film (Au) deposited on 1 mm thick BK7 glass substrate. A frequency-doubled (λ = 532nm) Q-switched Nd:YAG pulsed laser, having FWHM time duration of 6ns and linear horizontal polarization is used. The laser is capable of delivering laser pulses up to a maximum repetition rate of 10 Hz. The experimental dynamic imaging interferometry arrangement is shown in Figure

4.16. The Nd:YAG laser pulses are split in two beam splitters (BS1), in order to simultaneously excite the target (pump pulse) and detect the generated phenomena from the interaction (probe pulse). The pump beam is focused onto the sample using a plano-convex lens (L1) (f = 150 mm and NA = 0.085) to achieve a FWHM focal spot radius of 11.5 μm, as measured by a specialized profiling CCD camera (WinCam-D UCD12). The pump pulses are incident on the sample at an angle of ~35°. In order to investigate the laser thin film interaction at the thermoelastic, melting and ablation regimes, laser pulse energies from 0.4 μJ up to 21 μJ illuminate the target. This laser pulse energy range corresponds to pump laser fluences in the range from 0.1 J/cm^2 to 5.0 J/cm^2 or pump laser intensities in the range from 1.6×10^7 W/cm^2 to 8.3×10^8 W/cm^2. The measurements are performed at room temperature and atmospheric pressure.

The interaction region on the target and its neighborhood is imaged with the use of a high spatial and temporal resolution experimental Michelson interferometric method. As seen in Figure 4.16 in the one arm of the interferometer, the probe pulse is reflected off a stationary mirror (M4), while in its other arm the probe pulse is reflected off the excited sample surface (SA) and is collected by an objective lens system (OL) (f = 112 mm and NA = 0.09) that allows a total sample surface of 500 μm × 420 μm to be examined. A 14-bit CA-CCD camera (2452×2054 pixel sensor with 3.45 μm square pixel size / Allied Vision Pike 505B), able to identify 2^{14} greyscale divisions, is used for the recording and is synchronized to capture only in the time window, of 27 μs, in the presence of ns probe pulses. For the synchronization of the CCD camera a delay generator unit (SRS DG535) is used in order to record the probe pulses. A synchronization signal from the laser system is fed into the delay generator unit and a time-delayed triggered signal for the camera is obtained. The probe pulse is time-delayed through a variable optical delay line (VOD) up to a few tens of ns with respect to the pump pulse in order to investigate the dynamic evolution of the generated SAWs.

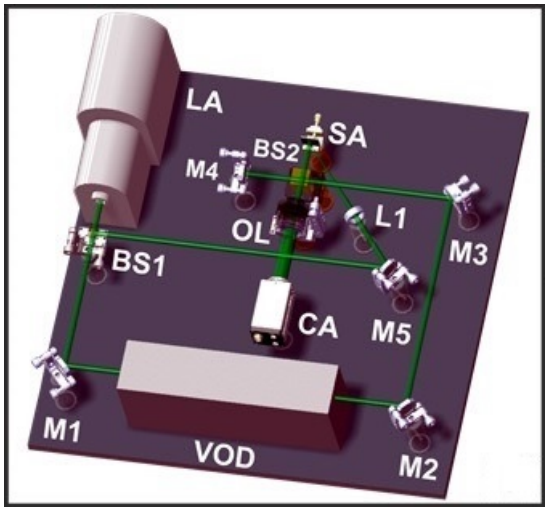

Figure 4.16 Experimental dynamic imaging interferometry set-up: LA – ns laser, BS – beam splitters, M – mirrors, VOD – variable optical delay line, L – lens, OL – objective lens system, CA – CCD camera, SA – sample [4]

With regard to the measurement procedure, in the absence of the pump pulses a first interferogram is recorded, consisting of a pre-set sinusoidal fringe pattern, with a spatial frequency f_0, the value of which depends on the relative angle between the beams of the two arms of the Michelson interferometer. The fringes in this interferogram may carry small distortions due to surface irregularities. Then, a second interferogram is recorded at a certain time delay after the illumination with a pump pulse in the presence of the induced SAWs. This procedure is the same at all time delays, while a fresh area of the sample surface is illuminated at each delay. Furthermore, interferograms are recorded after excitation to monitor any permanent damage to the sample surface.

For the analysis of the interferograms and for extraction of SAWs amplitude information, a special developed in-house algorithm using LabVIEW software is used. A Fourier transform spatial carrier frequency analysis is carried out, following the work of Takeda et al [5] and Kujawinska [6]. A 2-dimensional FFT is applied to the first and the second interferograms resulting in three distinct peaks, at DC and at around $\pm f_0$ (f_0 being the carrier spatial frequency of the fringe pattern). The DC and $-f_0$ components are discarded using a filter, and an inverse 2D FFT is then applied. This results in images where the phase, $\varphi(x,y)$, of every pixel of the interferograms is obtained and wrapped into the range of $-\pi$ to $+\pi$. The phase is then unwrapped using a

search algorithm, which traces the sign changes of the phase. Then, the phase changes are converted to the surface displacement d, with $d = \varphi\lambda/(4\pi)$, where λ is the wavelength of the laser. The basic steps of this process are graphically described in Figure 4.17 by referring to captured screenshots by using the developed software. The outcome of this process is a surface image in the absence of SAWs and a surface image in the presence of SAWs for a certain time delay. Finally, the image in the absence of SAWs is subtracted from the one in the presence of SAWs, thus the surface displacement only due to SAWs is obtained, eliminating the initial surface features before the laser pump.

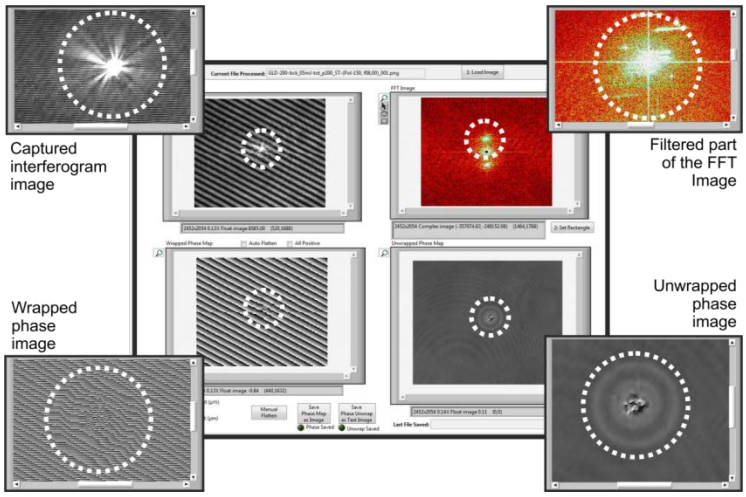

Figure 4.17 Screenshots of the interferometric data processing software. Four main steps are presented: capturing of the interferogram image, 2D FFT filtering, wrapping of the image phase and unwrapping [4]

The technique allows for a lateral resolution of ~1 μm, as experimentally determined using a standard microscopy calibration technique, which involves comparison against an appropriate calibrated test target slide. The technique also allows for an out-of-plane resolution of ~1 nm, which is estimated from the minimum irregularities obtained in the actual experiments and in areas where no SAWs exist and the background surface irregularities are subtracted. The out of plane resolution is limited by the greyscale divisions that correspond to phase differences that the system is capable to identify. The experimental method provides a 3D whole-field dynamic imaging of the interrogated surface, making it attractive for applications where a

comprehensive characterization of films containing defects, inhomogeneities, or other irregularities are needed.

In order to monitor permanent damages and to evaluate the ablation depth of the sample surface when the laser matter interaction passes into the melting and ablation regimes, a white-light interferometry method is implemented, as schematically depicted in Figure 4.18. It is also based on a Michelson interferometer layout, where the sample is placed in the stationary arm, while in the second arm a movable mirror by means of a piezoelectric transducer (PZT) is placed. A halogen lamp is used as the necessary light source, which emits a wide spectrum of light and has a small coherence length (~ 1 μm). This allows for the determination of the zero optical path difference between the two arms of the interferometer. The imaging setup for sample interrogation is kept the same (see Figure 4.16). The movement of the PZT is calibrated using a laser source having a coherence length >1 m, which offers constant fringe formation along the full PZT displacement used (~6 μm). By moving the PZT-mounted mirror, the zero optical path distance for each pixel of the recorded image can be extracted. By collecting the zero optical path difference of each pixel, a 3D map of the interrogated area of the sample surface is constructed. The whole process is fully automated using specially developed software.

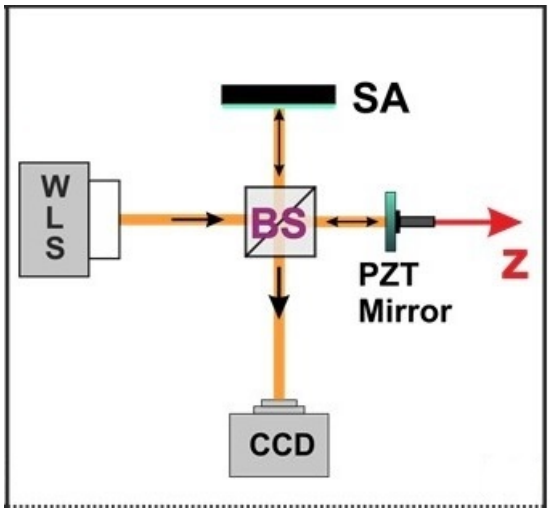

Figure 4.18 White-light interferometry setup: WLS – white light source, PZT – piezoelectric transducer [4]

4.3 Comparison and verification of numerical with experimental results

In this section 3D FEM simulation results are presented, as well as experimental results obtained by dynamic imaging interferometry and a white-light interferometric technique for the interaction dynamics emerging when nanosecond laser pulses illuminate a thin metal film on a dielectric substrate with intensities corresponding to elastic, melting, and ablation regimes. The designed experiments can monitor both the dynamic response of matter with high spatiotemporal resolution and the post-irradiation permanent modifications. The experimental results together with 3D Finite Element modeling results, implementing advanced modeling elements and schemes, can accurately treat all three regimes. This combination offers capabilities for the investigation of all three regimes, including the phase change from one regime to another, as well as permanent deformations and material ablation.

For the validation of the method the generated and experimentally measured SAWs are employed as a key tool. By experimentally investigating nm-scale SAWs, parameter values are extracted by comparing the 3D finite element model and experimental results. These experimental parameter values are obtained by investigating SAWs in a fully thermoelastic sample area far from the interaction region. Their subsequent use in the appropriately modified model allows for the detailed and accurate investigation of the interaction region in all regimes. This concept predicts accurately, in time and space, at a wide time window, the physical phenomena that take place in the interaction region for all three regimes and very good agreement between numerical and experimental results is achieved.

4.3.1 Results from direct irradiance of the film-substrate system

A 0.6 μm Au film deposited on 1 mm BK7 glass substrate is used in our study. Typical values of pump laser fluences in the range of 0.1 – 5.0 J/cm^2 are used in this work in order to investigate elastic, melting, and ablation regimes. With respect to the laser parameters, the Full Width at Half Maximum (FWHM) of laser temporal extent, t_0, is 6 ns, while the FWHM spatial beam radius on the sample surface, r_0, is 11.5 μm,

as experimentally measured. These are used along with the material properties values presented in Table 3.3.

During nanosecond laser pulse interaction with thin films the transition phase from the thermoelastic to the melting and ablation regimes, as well as the crater formation, is of great interest. The FEM simulation predicts the laser fluences where the onset of the melting and ablation regimes occurs. Comparing the temperature values, obtained from the simulations to the material's melting and boiling points, it is found that melting and ablation occurs for pump laser fluences of 0.34 J/cm^2 and 1.00 J/cm^2, respectively. The melting threshold is experimentally estimated with the interferometric technique, by comparing images of the investigated sample surface region before and after excitation, and it is found to be 0.3 J/cm^2. Moreover, using the white-light interferometric technique, the experimental observation of the film's surface before and after illumination indicates that the ablation threshold occurs at laser fluence equal to 1.1±0.2 J/cm^2, being in very good agreement with the model's predictions.

For laser fluences below the melting threshold, a central bulge is observed, centered on the laser irradiated region along with the SAWs propagating outwards of the irradiated region in the form of concentric rings. In the ablation regime, a crater-type deformation with elevated edges is observed, centered around the laser irradiated region, while material has actually been removed from the sample. Likewise, the SAWs propagate outwards of the irradiated region in the form of concentric rings. Moreover, in the thermoelastic regime the SAWs peak amplitude increases proportionally to the laser fluence. It becomes almost constant for fluences higher than the melting threshold until the onset of ablation, due to the latent heat of melting, while in the ablation regime it increases again. This behavior is in agreement with earlier studies [7].

In Figure 4.19 typical simulation (a, c, and e) and corresponding experimental (b, d, and f) results are presented, for the elastic, melting, and ablation regimes, and for various pump-probe time delay values, Δt. Values of specific surface deformation features are extracted and compared between simulations and experiments in order to investigate potential agreement. These are: the central bulge amplitude, B_d (nm), the crater elevation edge amplitude, C_d (nm), and its radial width, C_w (μm), the SAWs

amplitude, S_{di} (nm), their distance away from the centre of the irradiated region, R_i (μm) (where i = 1, 2, 3 corresponds to the number of the observed SAWs that propagate away from the centre of the irradiated region) and the optical delay Δt (ns). These values are presented in Table 4.1, cross-referenced to Figure 4.19 in order to facilitate the comparison. A very good agreement is observed between experiments and simulations, which validates the developed FEA model.

Regimes		Δt	B_d	C_d	C_w	S_{d1}	R_1	S_{d2}	R_2	S_{d3}	R_3
Elastic (Figure 4.19 a and b)	Simulation	33	24.0	-	-	1.1	55.0	-	-	-	-
	Experiment		17	-	-	1	65	-	-	-	-
Melting (Figure 4.19 c and d)	Simulation	17	34.0	-	-	3.3	47.0	-	-	-	-
	Experiment		25	-	-	3	50	-	-	-	-
Ablation (Figure 4.19 e and f)	Simulation	25	-	27	18.5	8	32.5	3.3	60	1.1	105
	Experiment		-	24	17	8	34	3	59	1	103

Table 4.1 Values of specific surface deformation features

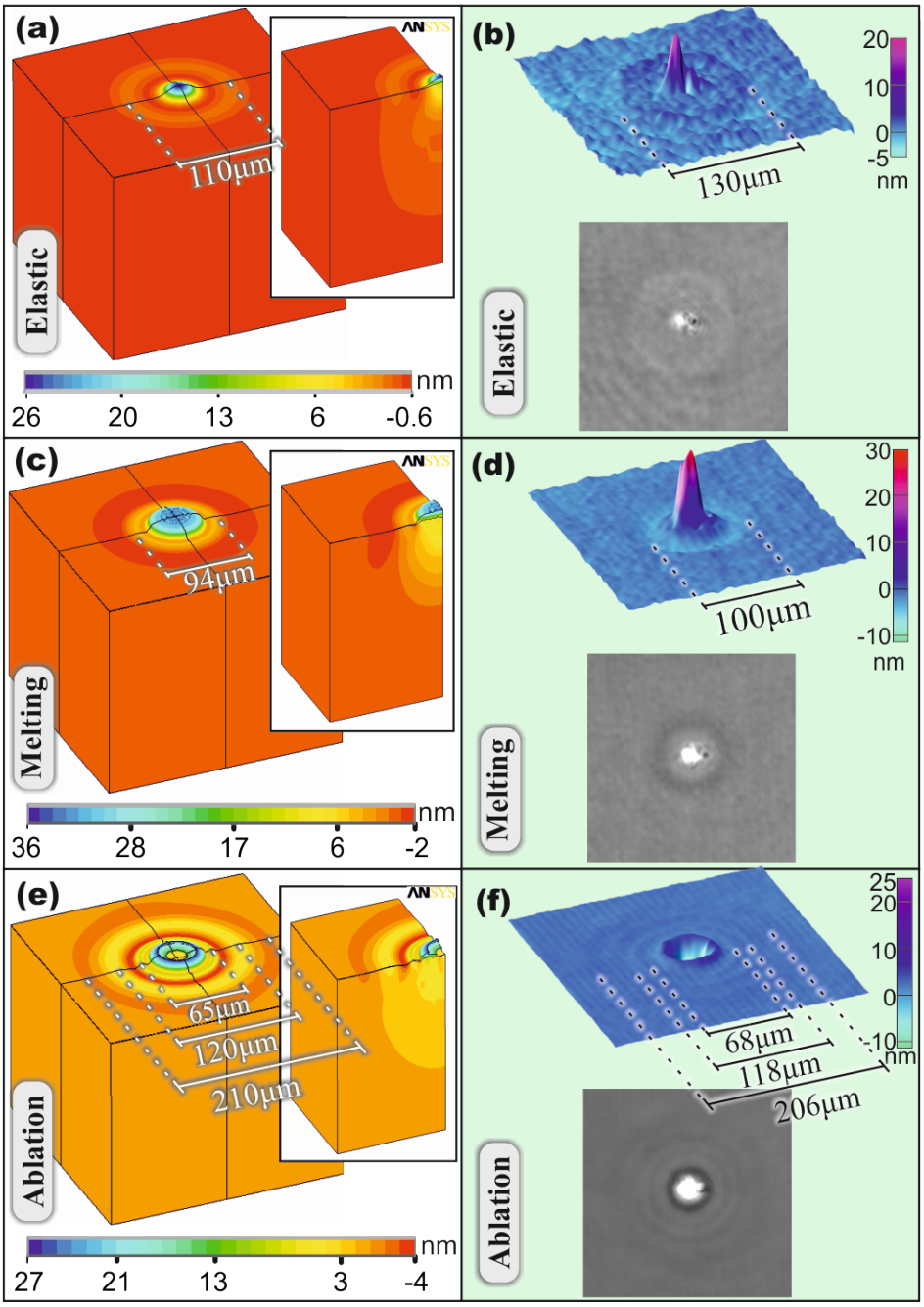

Figure 4.19 Comparison of simulated (a, c, and e) and experimentally measured (b, d, and f) laser generated spatial deformations in elastic (time delay 33 ns, laser fluence 0.20 J/cm^2), melting (time delay 17 ns, laser fluence 0.85 J/cm^2), and ablation (time delay 25 ns, laser fluence 2.90 J/cm^2) regimes. For the simulation results the insets show slices of the 3D deformations. For the experimental results 3D surface deformations (top) are extracted from the grayscale 2D images (bottom)

The temporal evolution of the laser-target interaction is important for the investigation of the transition from one phase of matter to the other. In particular, in the melting regime the temporal evolution of the melted material can be studied and the transition time from melting to ablation regime can be found. Figures 4.20, 4.21 and 4.22 present simulation as well as experimental results for laser fluences above the melting threshold. Figures 4.20, 4.21 present simulation and experimental results for time evolution of the laser-target interaction in the melting and ablation regimes respectively. Figures 4.20a and 4.20b show simulation results and experimental measurements for pulsed laser fluence of 0.54 J/cm^2 and for 17 ns after the interaction of the pump laser pulse with the target. Additionally, Figures 4.20c and 4.20d present simulation results and experimental measurements for the same fluence but 8 ns later. Figure 4.21 presents simulation and experimental results likewise for the time evolution of the laser-target interaction for laser pulse fluence of 2.9 J/cm^2, at 17 and 25 ns after the interaction of the pump laser pulse with the target. For a direct comparison between experiment and simulation, the parameters: B_d (nm) central bulge amplitude, S_{di} (nm) SAWs amplitude, R_i (μm) SAWs distance away from the center of the irradiated region, and Δt optical delay (ns), are used as previously. These parameters' values are shown in Table 4.2, cross-referenced to Figures 4.20 and 4.21. Experimental results show very good agreement with the simulation results.

Fluence (J/cm^2)		Δt	B_d	S_{d1}	R_1	S_{d2}	R_2
0.54 Figure 4.20 a & b	Simulation	17	34.0	2	32.0	-	-
	Experiment		26	1.5	37	-	-
0.54 Figure 4.20 c & d	Simulation	25	31.0	2.6	50	-	-
	Experiment		23	2	56	-	-
2.90 Figure 4.21 a & b	Simulation	17	-	2.8	43.0	-	-
	Experiment		-	2.8	42	-	-
2.90 Figure 4.21 c & d	Simulation	25	-	8.0	32.5	3.3	60.0
	Experiment		-	8	34	3	59

Table 4.2 Values of specific surface deformation features

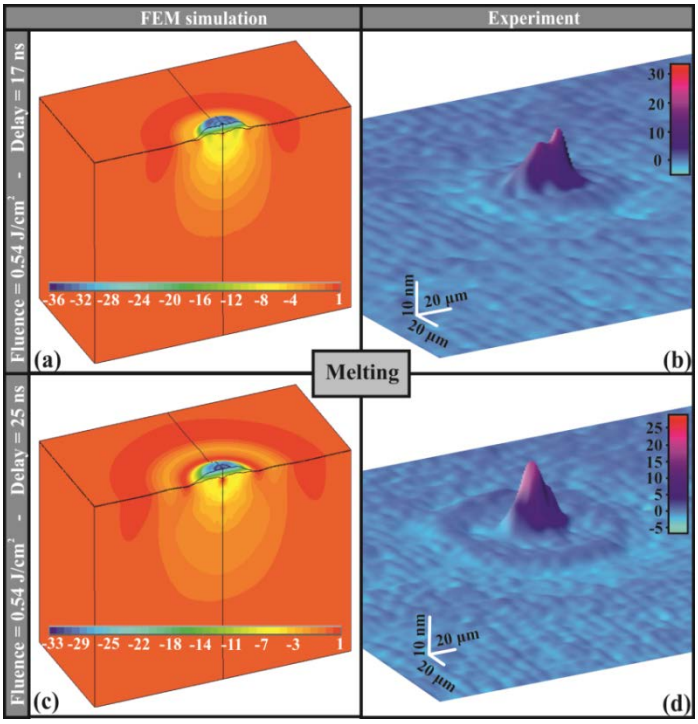

Figure 4.20 FEM simulation (a, c) and dynamic imaging interferometry experimental (b, d) displacement results for laser fluence 0.54 J/cm^2 (melting regime) and for Δt = 17 ns (a, b) and 25 ns (c, d). Color maps for both FEM simulations and experimental results are in nm, corresponding to displacements normal to the sample surface (*Z*-axis)

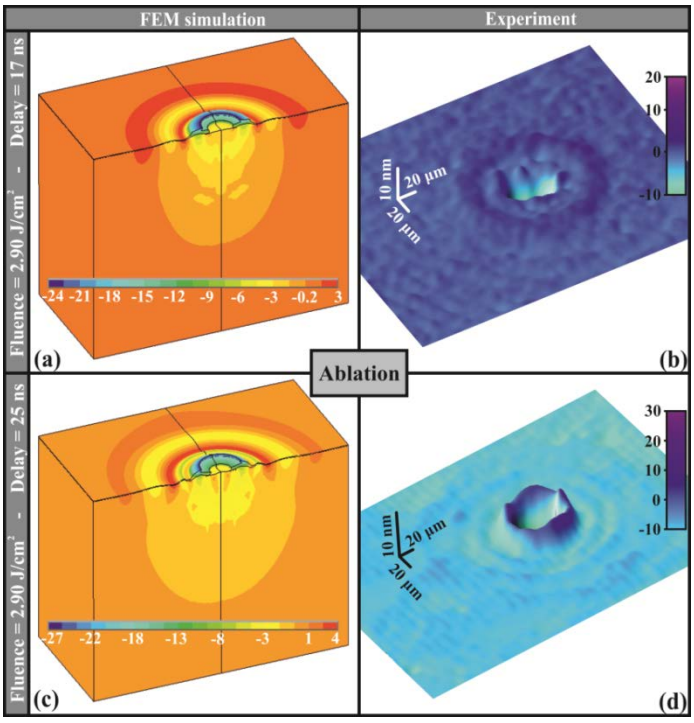

Figure 4.21 FEM simulation (a, c) and dynamic imaging interferometry experimental (b, d) displacement results for laser fluence 2.90 J/cm^2 (melting regime) and for Δt = 17 ns (a, b) and 25 ns (c, d). Color maps for both FEM simulations and experimental results are in nm, corresponding to displacements normal to the sample surface (*Z*-axis)

The comparison of the laser matter interaction in the melting and ablation regimes shows interesting features for the phase transition dynamics. As predicted by the performed experiments and simulations, the melting regime occurs from 8 ns to 10 ns after the pump laser target interaction for laser fluences above the ablation threshold. Afterwards, the ablation takes place within the next ~2 ns. This study proves the fast phase change from the melting to the ablation regime in such type nanosecond laser metallic thin film interactions.

In Figure 4.22 the displacement and the temperature distribution in relation to the radial distance is depicted at Δt=25 ns after the interaction of the pump laser pulse with the target for a) laser fluence of 0.85 J/cm^2 (in the melting regime) and (b) laser fluence 3.9 J/cm^2 (in the ablation regime). In the melting regime a centrally placed protrusion appears on the laser focal spot area, while in the ablation regime a formed crater appears at the same area. The predicted temperature distribution by the simulation is also shown. In the melting regime (Figure 4.22a), the temperature in the interaction region reaches 1700 ºC, a value between the Au melting (1064 ºC) and the boiling (2856 ºC) temperatures. With respect to the ablation regime, where the temperature exceeds the boiling value, mass removal has already occurred (Δt = 25 ns) and a crater is formed. The mass of the ablated material can be predicted, as well as the temperature distribution of the residual material, providing information for the definition of the initial conditions for potential Hydro or Magneto Hydro Dynamic (HD/MHD) numerical simulations.

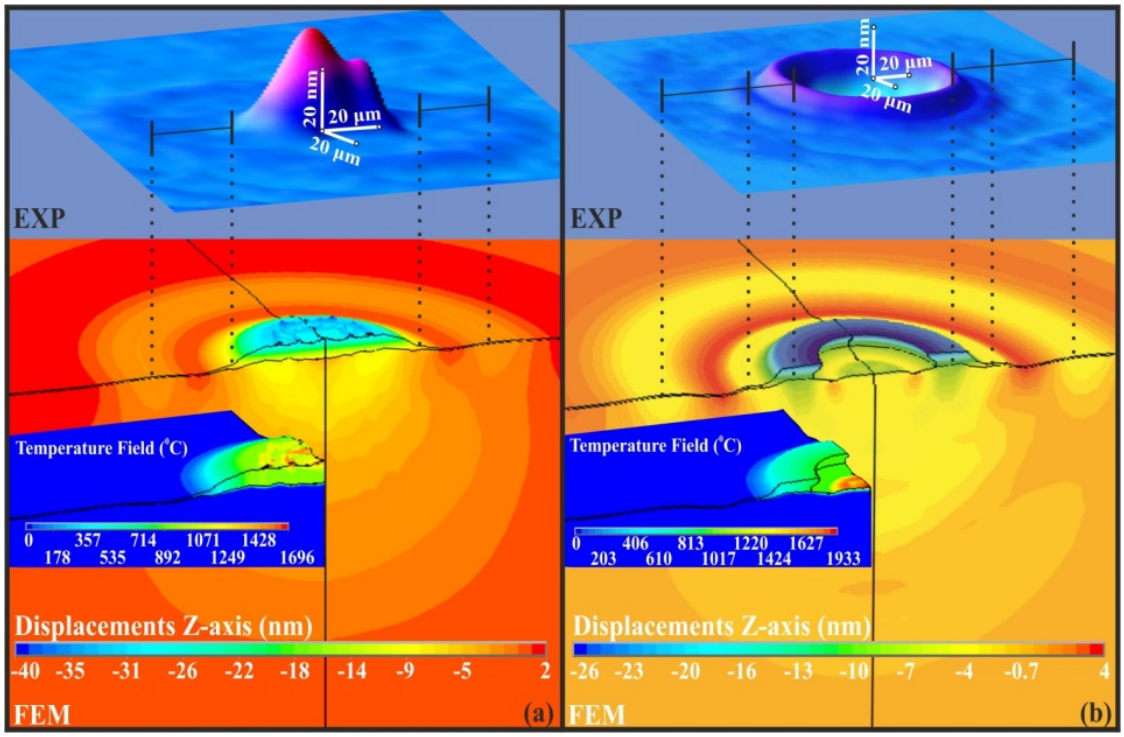

Figure 4.22 Displacement results (EXP: dynamic imaging interferometry experimental results; FEM: simulation results), for Δt=25 ns: (a) laser fluence 0.85 J/cm^2 below the ablation threshold (melting regime), and (b) laser fluence 3.9 J/cm^2 above the ablation threshold. In the lower parts (FEM results) the insets show the corresponding temperature distribution

Figure 4.23 shows simulation and experimental results for the ablation depth and the crater's radius as a function of the laser fluence. The experimental results are obtained by the white-light interferometry method described in section 4.2. The satisfactory agreement between experiment and simulation for the formation of the crater, as well as the predicted ablation depth, which occurs at times well after the laser-matter interaction period, allows for the confirmation of the FEM model's capabilities.

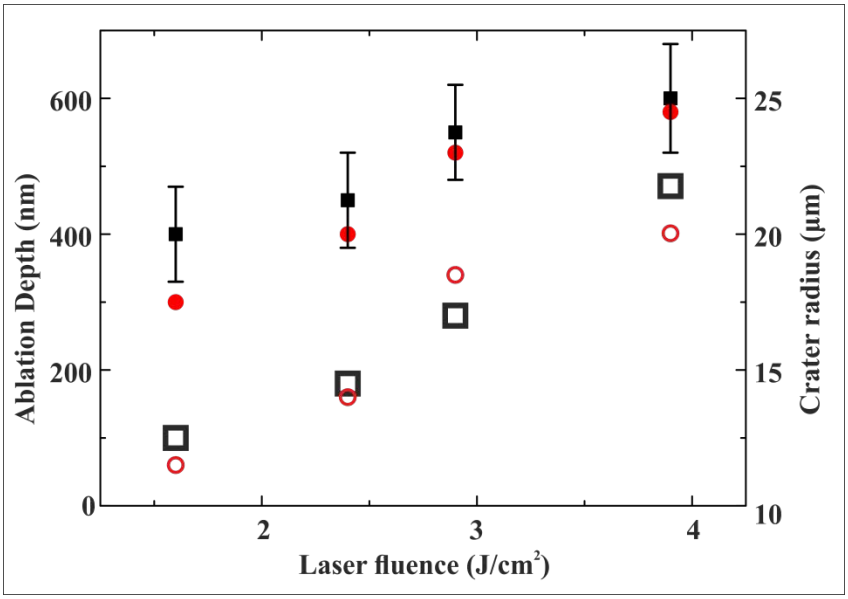

Figure 4.23 Ablation depth as a function of the pump laser fluence, theory: solid red dots, experiment: solid squares. Crater radius as a function of the pump laser fluence, theory: open red circles, experiment: open squares

To further investigate the validity of the developed model, the propagation of the SAWs has been examined for the same pump laser fluence at different time instants. More specifically, in Figure 4.24 the surface deformation is shown for a laser fluence of 2.90 J/cm^2 at two different optical time delays. This laser fluence is well above the ablation threshold, thus making easier for the generated SAWs to be experimentally monitored as they have higher amplitude. The importance of the inclusion of the optical thickness of the ablation plume, $\Lambda(t)$, is also examined. A very good agreement between simulation and experiment is observed, especially in the case where $\Lambda(t)$ is included. Based on the results, the propagation velocities of the laser-generated SAWs may also be estimated. For the first SAW (SAW1 in Figure 4.24) propagation velocity values of 1.75×10^3 m/s and 1.64×10^3 m/s are estimated by simulations and experiment, respectively, while for the second SAW (SAW2 in Figure 4.24) the corresponding values are 2.44×10^3 m/s and 2.25×10^3 m/s. The observed difference between the velocities of the first and second SAW can be attributed to the fact that SAW2 is generated by the violent conversion of the laser energy into acoustic shock wave energy, while SAW1 is generated as a secondary wave coming from the breathing of the irradiated area.

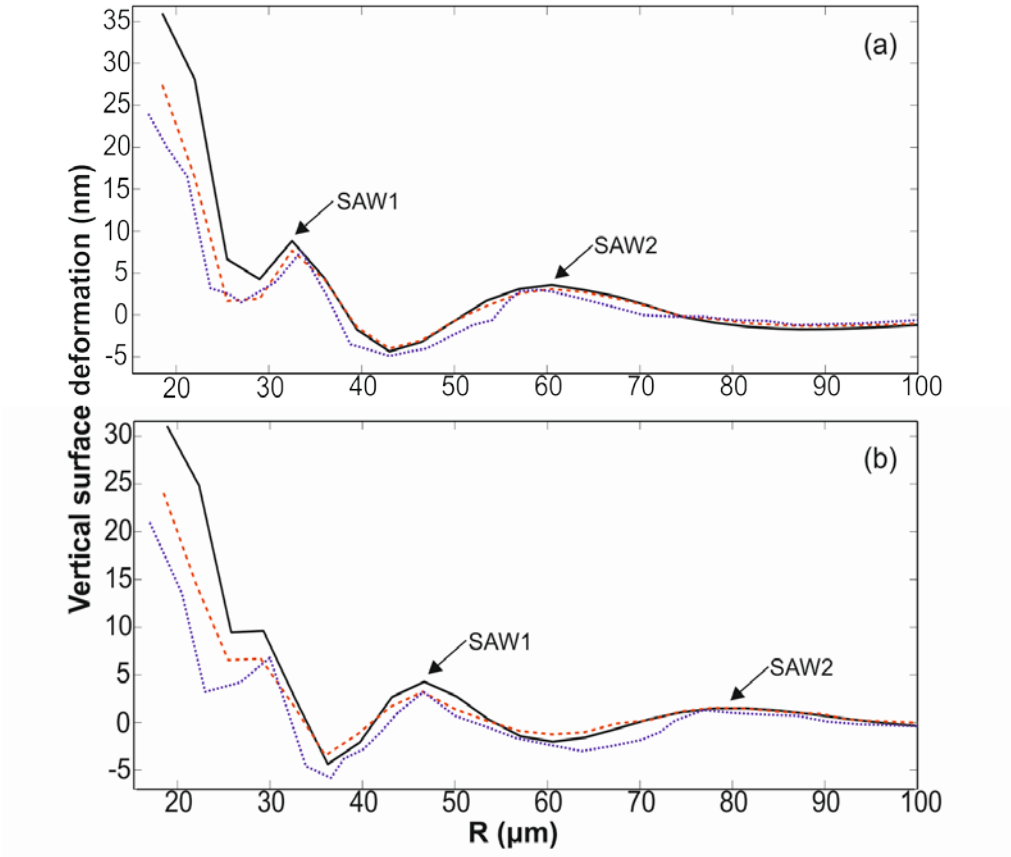

Figure 4.24 Vertical surface deformation as a function of the radial distance, *R*, away from the laser irradiated area (laser fluence 2.90 J/cm^2) for two time delays, Δt: (a) 25 ns, and (b) 33 ns. Solid line: simulations without considering $\Lambda(t)$, dashed line: simulations considering $\Lambda(t)$, dotted line: experimental results

It should be emphasized that when laser fluence is higher than the ablation threshold, the optical thickness of the ablation plume, $\Lambda(t)$, is considered and Equation 3.6 is activated and taken into account by the model. Comparison [8, 9] with the experimental results under various conditions allows for the evaluation of the values of the plasma coefficients, *b* and *d*, which are found to be 1×10^{6} and 1×10^{-4}, respectively.

Furthermore, the accurate knowledge of the temperature distribution during the phase transition, as well as the melting and the ablation depths, resulting from this research, can be used as initial data to the pure hydrodynamic [10, 11] or Monte Carlo (MC) simulations [12, 13] that investigate laser matter interactions well above the ablation threshold regime. In addition, thorough knowledge of the spatial temperature

distribution and its evolution in time during phase transitions, may contribute for the more accurate determination of the equation of state at low temperatures [14, 15] and especially for the initial time of laser-target interaction. An interesting observation of the FEM simulation is that the concentric rings that are attributed as SAWs have a skin depth that extends to several μm inside the substrate. Consequently, the generated waves are of Rayleigh type [16] and include both longitudinal and transverse motions, which decrease exponentially in amplitude within the substrate. However, this behavior cannot be monitored experimentally by the implemented method.

4.3.2 Results from irradiance of the interface substrate-film

Different simulation test cases are performed according to the incident laser energy on the substrate. The laser beam is directed on the sample so as to irradiate the metalic volume from the back, as presented in Figure 4.25. The laser beam passes through the substrate to irradiate the interface of the substrate-film. The energy absorbed by the substrate can be neglected because of the transparency of the BK7 glass.

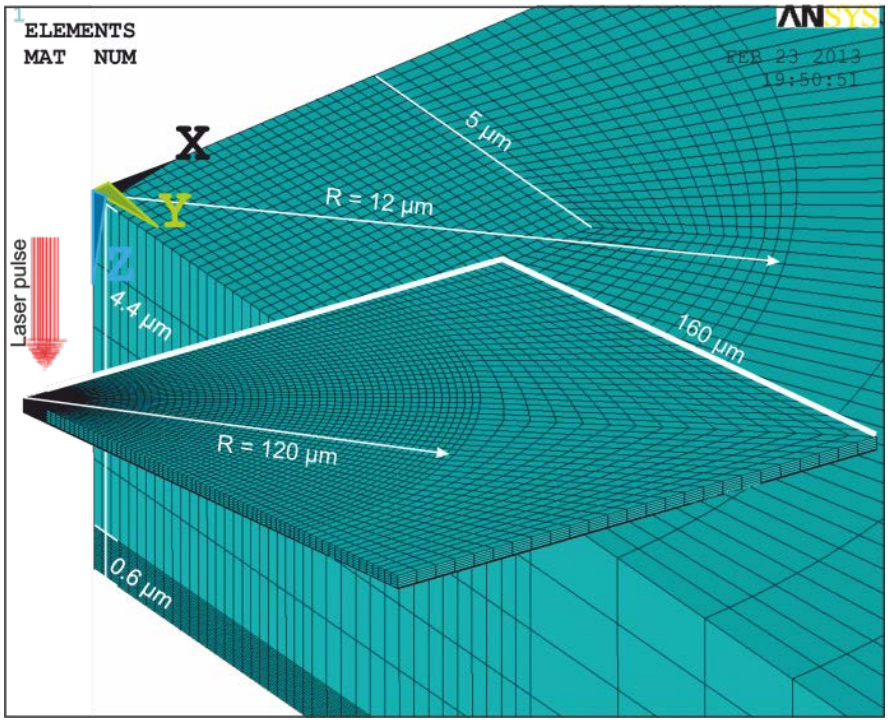

Figure 4.25 3D quarter symmetric finite element model for irradiation from the back

The laser energy per pulse had a fixed value of 100 μJ for a value of focal spot radius in a range of 10-12 μm. The first simulations are made without taking into account the optical thickness of the plasma and are compared with the experimental results for two discrete time delays. The theoretical results of the crater's walls vertical displacement and the vertical displacements of the generated SAWs are found to be ~30% higher than the experimental results.

Equations that concern absorption of the plasma plume are then introduced to the model. The incident laser fluence value exceeds the ablation threshold of gold, which is approximately 1 J/cm^2, and the numerical simulations show that gold's irradiated region reaches the boiling temperature in 6-7 ns after the irradiation, depending on the laser fluence. The whole thickness of the irradiated metal sample is ablated instantaneously in one nanosecond. For this reason the optical thickness of the plasma plume is considered to be time independent, since the ablation depth is equal to the thickness of the sample which is 0.6 μm.

The simulation results (in μm) are examined in order to determine the value of Λ for the best approximation of the experimental results by the theoretical model. This value for laser fluence of 35 J/cm^2 is approximated to be ~1.9. In Figure 4.26 experimental and theoretical results are depicted for a time delay of 28 ns after irradiation.

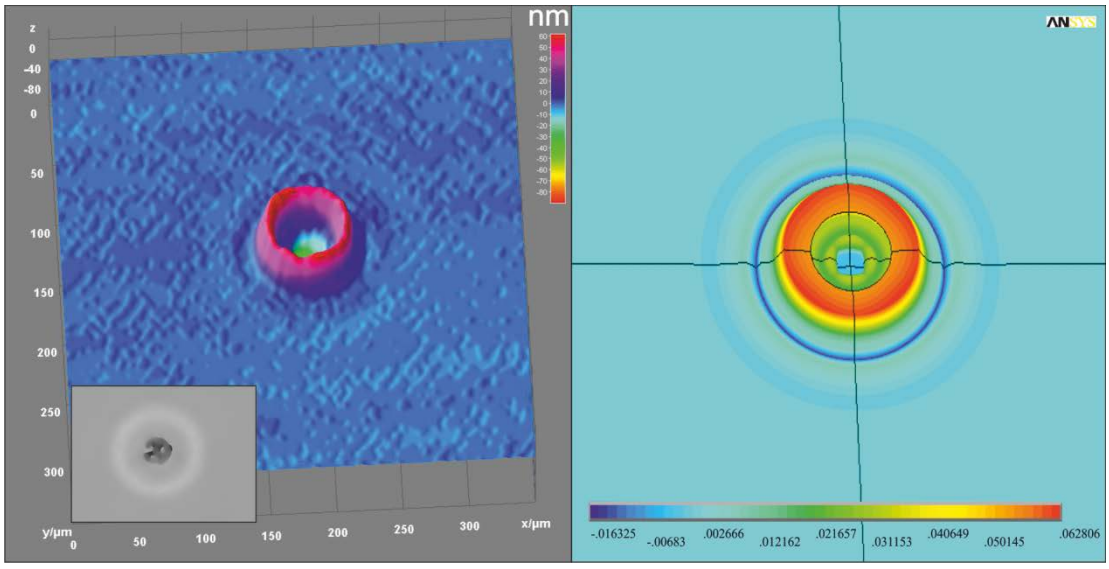

Figure 4.26 Experimental (left) and theoretical (right) data of the crater's deformation and SAWs generation for the temporal moment: Δt=28ns

The crater walls have a diameter of 40 μm for the experiment, while the numerical ones have 35 μm. Their vertical displacement is 60 nm for both experimental and numerical data. Concerning, the first SAW, it has a value of 3 nm for both experimental and numerical approaches and is observed 50 μm and 45 μm far from the epicenter for the experimental and the numerical result respectively.

References

[1] D. Schneider, T. Schwarz, H.J. Scheibe and M. Panzner, Non-destructive evaluation of diamond and diamond-like carbon films bylaser induced surface acoustic waves, *Thin Solid Films* **295**, 107–116 (1997).

[2] D. Achenbach, *Wave Propagation in Elastic Solids*, North Holland, Amsterdam, 1973.

[3] G. R. Johnson and W. H. Cook, Fracture characteristics of three metals subjected to various strains, strain rates, temperatures and pressures, *Eng. Fract. Mech*. **21**, 31-48 (1985).

[4] Y. Orphanos, Methodologies of dynamic nanoscopic material characterization using acoustic sources generated by ultrashort laser pulses, PhD thesis.

[5] M. Takeda, H. Ina and S. Kobayashi, *J. Opt. Soc. Am.* **72**, 156–160 (1982).

[6] M. Kujawinska, ‘‘Spatial phase measurement methods’’ in *Interferogram Analysis: Digital Fringe Pattern Measurement Techniques*, D. W. Robinson and G. T. Reid, Eds., Institute of Physics, Bristol, pp. 141–193, 1993.

[7] P. Hess, Laser diagnostics of mechanical and elastic properties of silicon and carbon films, *Appl. Surf. Sci.* **106**, 429 (1996).

[8] N. A. Vasantgadkar, U. V. Bhandarkar and S. S. Joshi, *Thin Solid films* **519**, 1421 (2010).

[9] V. Oliveira and R. Vilar, *Appl. Surf. Sci*. **253**, 7810 (2007).

[10] L. Balazs, R. Gijbels and A. Vertes, Expansion of laser-generated plumes near the plasma ignition threshold, *Anal. Chem.* **63**, 314 (1991).

[11] J. J. Chang and B. E. Warner, Laser-plasma interaction during visible-laser ablation of methods *Appl. Phys. Lett.* **69**, 473 (1996).

[12] T. E. Itina, A. A. Katassonov, W. Marine and M. Autric, *J. Appl. Phys.* **83**, 6050 (1998).

[13] P. Schreiner and H. M. Urbassek, Energy and angular distribution of pulsed-laser desorbed particles: the influence of a hot contribution on a cold desorbing species, *J. Phys. D* **30**, 185 (1997).

[14] W. B. Holzapfel, Equation of State for Solids under Strong Compression, *High Press. Res.* **16**, 81 (1998).

[15] G. K. Straub, J. B. Aidun, J. M. Wills, C. R. Sanchez-Castro and D. C. Wallace, *Phys. Rev. B* **50**, 5055 (1994).

[16] Lord Rayleigh, On Waves Propagated along the Plane Surface of an Elastic Solid, *Proc. London Math. Soc*. **s1-17** (1), 4–11 (1885).

Chapter 5

5. State of the art-Literature review of single wire explosion

5.1 Exploding wire

The driving of pulsed currents through single metal wires has been the subject of numerous experimental studies and theoretical analyses. When a high pulsed electric current is applied to a wire the latter explodes within fractions of a second. Depending on the magnitude of the electric current, the result of the explosion can be fluid/solid particles or plasma. The conversion of a single conducting wire from solid-density room temperature to plasma is a complex process, involving multiple phase changes from solid, to liquid, to vapor, and eventually plasma formation. Several effects may occur simultaneously, such as electromagnetic, thermal, elasto-plastic, and magnetohydrodynamic ones.

Wire explosion behavior in its initial stages is a function of several factors. These include the wire material, whether the wire is coated by an insulator or not, and the energy deposited resistively in the wire before plasma forms around the wire [1].

Exploding wires are widely used in many experimental set-ups and pulsed power systems, such as Z-pinch [2-4], high-current switches [5], copper-vapour lasers [6], and high-brightness x-ray lithography [7]. They are also used as a method of synthesis and preparation of nanopowders [8, 9] or preparation of metallic nanoparticles [10]. Among other technological applications of the electrical wire explosion are peaking of electric power in high voltage pulsed engineering [11], creation of x-ray sources for microelectronics [12], and high power sources of soft x-ray radiation in multiwire liners [13]. In this thesis, as previously mentioned, emphasis will be given in the explosion of a single wire Z-pinch from thermoelastic to plasma formation.

5.2 Z-Pinch single wire

The Z-pinch is the name of a unique class of magnetically driven or confined plasma in which a current is passed through a cylinder of plasma parallel to the axial or *z*-direction. When a large current with current density $\boldsymbol{J}$ flows in a cylindrical plasma a magnetic field $\boldsymbol{B}$ is generated. The resulting interaction of the azimuthal self-magnetic field and the axial current produces an inward radial $\boldsymbol{J}\times\boldsymbol{B}$ or magnetomotive force, which confines the plasma. This force can be employed either dynamically to collapse a hollow plasma cylinder or quasi-statically to confine the plasma through the pinch effect. The advantages of the Z-pinch are that larger volumes of plasma that can be produced of very high energy density, and with greater efficiency than in laser-produced plasmas [2].

There are many ways of forming a Z-pinch in an experiment. The earliest approach was the compressional Z-pinch to which the capillary discharge is related. The effect of walls can be removed in a gas-embedded Z-pinch, which is triggered by means of a laser or needle electrodes. For X-ray production a dynamic hollow gas-puff Z-pinch is effective, from which has evolved the wire-array Z-pinch. Moreover, the Z-pinch can be formed from a single fibre of material on the axis, which is the focus in this thesis. The fibre pinch or exploding wire Z-pinch can be made from carbon, cryogenic hydrogen or deuterium, or metal wires such as aluminum, copper, or tungsten [2].

5.3 Physics of the equilibrium pinch

In a pinch device, the magnetic force acts to confine the plasma, whereas, the plasma kinetic pressure opposes constriction of the plasma column. When these forces are balanced, an equilibrium pinch would be formed. A basic physical property of a uniform Z-Pinch in pressure balance is Bennett relation. It was first derived by Bennett [14] for charged particles streaming with a uniform axial velocity. It can be extended to cover the general case of any current density distributions in a Z-pinch under a radial pressure balance and is described by

$$\frac{\partial p}{\partial r}=-J_z B_\theta \tag{5.1}$$

The axial component of Ampère's law gives

$$\frac{1}{r}\frac{\partial}{\partial r}(rB_\theta)=\mu_0 J_z \tag{5.2}$$

and by integrating

$$B_\theta=\frac{\mu_0}{r}\int_0^r J_z r dr\ . \tag{5.3}$$

From Equation 5.1 results

$$\frac{\partial p}{\partial r}=-\mu_0\frac{J_z}{r}\int_0^r J_z r dr\ . \tag{5.4}$$

The ion line density N_i is defined by

$$N_i=\int_0^a 2\pi n_i r dr \tag{5.5}$$

where α is the plasma radius. Taking the mean electron and ion temperatures to be T_e and T_i, respectively, we can write

$$N_i k_B(ZT_e+T_i)=\int_0^a 2\pi p r dr \tag{5.6}$$

where Z is the ionic charge number and k_B is Boltzmann's constant.
Integration of Equation 5.6 gives

$$N_i k_B(ZT_e+T_i)=\pi\int_0^a pd(r)^2=[\pi pr^2]_0^a-\pi\int r^2\frac{\partial p}{\partial r}dr=\pi\mu_0\int_0^a J_r r\left[\int_0^r J_z r dr\right]dr\ . \tag{5.7}$$

For $x=\int_0^r 2\pi J_z r dr$ the previous equation becomes

$$N_i k_B(ZT_e+T_i)=\frac{\mu_0}{4\pi}\int_0^a x dx=\frac{\mu_0}{4\pi}\left[\frac{x^2}{2}\right]_0^a\ . \tag{5.8}$$

For total current defined as $I=\int_0^a 2\pi J_z r dr$ the Bennett relation has the form

$$8\pi N k_B(ZT_e+T_i)=\mu_0 I^2\ . \tag{5.9}$$

The average temperature of the equilibrium pinch can be calculated knowing only the line density and current.

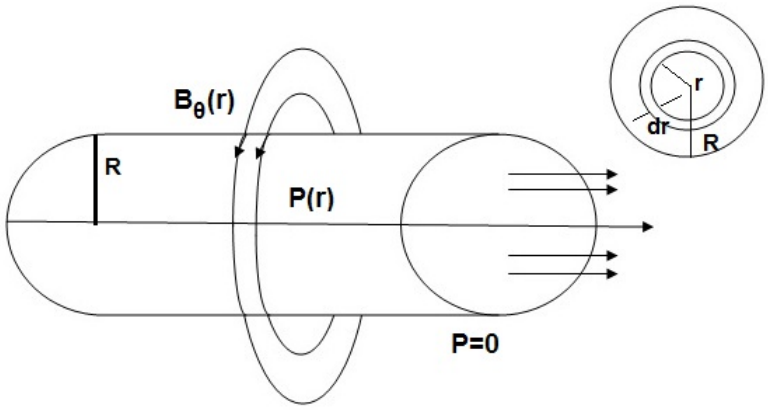

Figure 5.1 Schematic diagram of the equilibrium pinch

5.4 MHD Instabilities

The simplest model describing low frequency phenomena in plasma is the ideal single fluid magnetohydrodynamics (MHD). The plasma is treated as an electrically conducting fluid with zero resistivity. Moreover, ideal MHD theory of a single fluid neglects the Hall effect, resistivity, viscosity, thermal conduction, and assumes equal electron and ion temperatures [15]. The ideal equations for single fluid MHD are the continuity equation

$$\frac{\partial \rho}{\partial t} + \nabla(\rho \mathbf{v}) = 0 \tag{5.10}$$

the momentum equation

$$\rho(\frac{\partial}{\partial t} + \boldsymbol{v}\nabla)\boldsymbol{v} = \boldsymbol{j} \times \boldsymbol{B} - \nabla P \tag{5.11}$$

the Faraday's law

$$\frac{\partial \boldsymbol{B}}{\partial t} = -\nabla \times \boldsymbol{E} \tag{5.12}$$

Ampere's law

$$\mu_0 \boldsymbol{j} = \nabla \times \boldsymbol{B} \tag{5.13}$$

magnetic divergence constraint

$$\nabla \cdot \boldsymbol{B} = 0 \tag{5.14}$$

the ideal Ohm's law

$$\boldsymbol{E} + \boldsymbol{v} \times \boldsymbol{B} = 0 \tag{5.15}$$

and the energy equation

$$\frac{d}{dt}\left(\frac{p}{\rho^{\gamma}}\right) = 0 \tag{5.16}$$

.

A perturbation of the form [16, 17]

$$dr = \xi_0(\mathrm{r})\, \mathrm{e}^{i(m\theta + kz - \omega t)} \tag{5.17}$$

can be assumed in a cylindrical z-pinch wire, where ξ_0 is the amplitude of the plasma displacement, k is the wavenumber and m is the azimuthal mode number of the instability (equal to the azimuthal periodicity of the perturbation). The m=0 (sausage) mode consists of a series of necks (constricted regions) and bulges (expanded regions) along the pinch column, while the m=1 (kink) mode is one where the plasma column is in the form of the helix. Higher m number modes do not perturb the column on axis and appear as a twisted multistranded cable. The m=0 and m=1 modes are shown in Figure 5.2.

The m=0 instability grows as $e^{\gamma t}$ where the growth rate γ [18] is

$$\gamma = \frac{v_a}{a} \tag{5.18}$$

where α is the column radius, v_α is the Alfven velocity given by

$$v_a = \frac{B}{(\mu_o n_i m_i)^{1/2}} \tag{5.19}$$

where n_i, m_i are the ion density and ion mass respectively and B the average magnetic field ($B=\mu_0 I/2\pi\alpha$) [18].

With respect to the sausage instability, it occurs due to a wave-like perturbation. The perturbation is azimuthally symmetric about the column axis and produces crests and troughs on the surface of the plasma column. As a result, the plasma is constricted in some locations and expanded on others. Since the azimuthal magnetic field has $1/\alpha$ radial dependence, the magnitude of azimuthal magnetic field on the surface of the deformed plasma column varies. Hence, at the locations where α is smaller than its equilibrium value, the magnetic pressure exceeds the plasma kinetic pressure and forces the plasma radially inwards. The troughs will become deeper and deeper and crests higher and higher. At the final stage, when the constriction reaches the axis, the plasma column appears as a string of sausages and that is why it is termed as sausage instability [19].

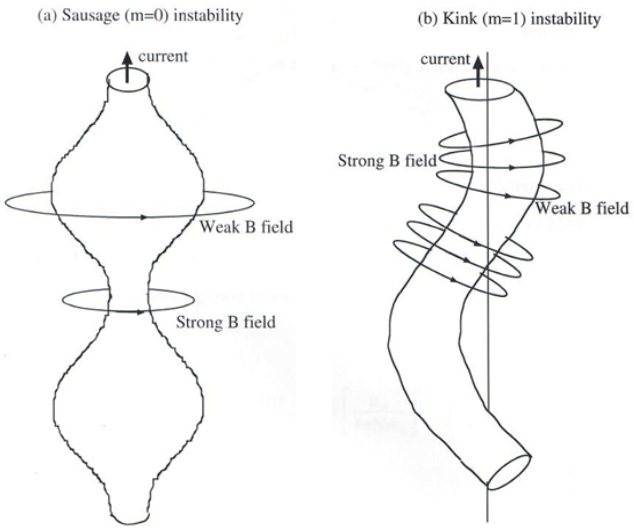

Figure 5.2 The *m*=0 (sausage) mode and the *m*=1 (kink) mode MHD instabilities in a *Z* pinch [20]

A universal diagram [21] depicted in Figure 5.3 describes the plasma regimes of a Z-pinch in pressure balance, where various theoretical models are valid. The X axis is the ion line density (*N*) and the Y axis is the product of the fourth power of the current and the pinch radius (I^4a). The MHD region is bounded by regions where finite

Larmor radius, resistive, viscous and anisotropic effects are important. Ideal MHD applies in a small region of the parameter space. An important parameter for the case of the resistive regime is the Lundquist number (*S*), which is the ratio of the timescales for convection and diffusion of the magnetic field lines through the plasma. The Lundquist number *S* can be written in terms of the current *I*, the radius a, the coulomb logarithm lnΛ and *N* the ion line density

$$S = \frac{3\mu_0 \varepsilon_0^{\,2} 2^{3/4} \mathrm{I}^4 \mathrm{a}}{64(2\pi m_e m_i)^{1/2} \ln \Lambda Z (1+Z)^{3/2} N^2} \tag{5.20}$$

where $\ln\Lambda=\ln(12\pi n_e \lambda^3_D)$, n_e the electron density and λ_D the debye length $\lambda^2_D=\varepsilon_0 k_B T_e/n_e e^2$ (T_e electron temperature, e electron charge). For a value of S<100 the pinch is considered to be stable [21, 22].

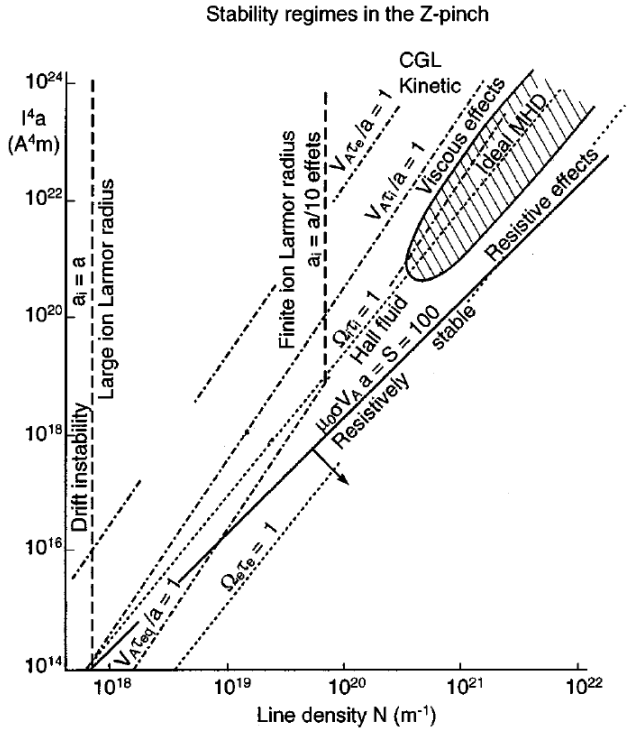

Figure 5.3 Diagram of the Z-pinch stability regimes [21]

5.5 Dynamic Response of Matter below plasma formation

In the literature [23-29] can be found studies that investigate the fragmentation of wires in the solid state. These refer to thicker wires with a diameter about 1 mm and above and lower peak currents between 0.5-10 kA.

The first experimental evidence for wire disintegration in the solid state was given by Nasilowski [23]. Nasilowski applied long, up to 20 ms duration, current pulses of 650 A to 1.5 m long, 1 mm diameter straight copper wires. The current pulses had a step-function character. The wires disintegrated into many pieces of irregular size. Since the wire disintegration occurred in the solid state, he assumed that mechanical vibrations were responsible for this. The wire ends were firmly clamped and the first breaks were observed at these clamped ends, whereas the remaining early breaks were fairly widely spaced from each other. Another important observation was an apparent waviness along the wires, which indicated that the vibrations might have had a flexural nature.

Graneau's [24] experiments in the early 1980s gave significant attention in the phenomenon of wire disintegration in the solid state. Graneau used aluminum wires of 99% purity, 1 m length and 1.2 mm diameter. He used a capacitor bank supplying under-damped current discharges of 5000–7000 A, over a period of 5–10 ms. The wire ends were free, while the current was supplied via 1 cm long air gaps. The results were similar to those of Nasilowski, as the wires broke into as many as 20–30 pieces each. Moreover, Graneau [24, 25] suggested that the fragmentation process arose from a longitudinally acting magnetic force derived from Ampere's force law.

Ternan [26] modeled the wire as an elastic string and considered stress waves in a wire with free ends induced by the Joule heating of the wire by the current, which he assumed to rise instantaneously. This model predicted the formation of standing thermal stress waves, which were of sufficient magnitude to break the wire using Graneau's experimental parameters.

Molokov and Allen [27] developed a continuum mechanics model and investigated two mechanisms for the creation of stress waves in the wire: a Lorentz force mechanism and a thermal stress mechanism arising from Joule heating. The wire was modeled as a linearly elastic solid. Inclusion of thermal effects necessitated a heat

equation with a source term arising from the Joule heating. The model used was magneto-thermo-elastic. The equations of magneto-thermo-elasticity used were

$$(\lambda+\mu)\nabla\nabla\boldsymbol{u}+\mu\nabla^2\boldsymbol{u}-a(3\lambda+2\mu)\nabla(T-T_0)+\boldsymbol{j}\times\boldsymbol{B}=\rho\ddot{\boldsymbol{u}} \tag{5.21}$$

$$k\nabla^2T=\rho c_v\dot{T}+(3\lambda+2\mu)\alpha T\nabla\dot{\boldsymbol{u}}-\sigma^{-1}\boldsymbol{j}^2 \tag{5.22}$$

$$\boldsymbol{j}=\sigma(\boldsymbol{E}+\dot{\boldsymbol{u}}\times\boldsymbol{B}) \tag{5.23}$$

$$\boldsymbol{j}=\mu_0{}^{-1}\nabla\times\boldsymbol{B} \tag{5.24}$$

$$\dot{\boldsymbol{B}}=-\nabla\times\boldsymbol{E} \tag{5.25}$$

$$\nabla\boldsymbol{B}=0 \tag{5.26}$$

where $\boldsymbol{u}$=(u,υ,w) is the displacement, $\boldsymbol{j}$ is the electric current density, $\boldsymbol{B}$ is the magnetic induction, $\boldsymbol{E}$ is the electric field, ρ and σ are the density and electrical conductivity of the metal respectively, λ and μ are the elastic constants, μ_0 is the magnetic permeability, α is the linear expansion coefficient, k is thermal diffusivity, and c_v is the specific heat. Dots denote time-derivatives. T is the temperature and T_0 is its initial value, when the wire is in a stress-free condition. These equations constitute a system of nonlinearly coupled displacement, energy, and electromagnetic equations. The wire surface is supposed to be thermally insulated. Thermal diffusion and heat generated by material deformation were neglected. A uniform-current density in the wire was considered and the current rise-time was assumed zero. The two mechanisms were examined separately. Three different wire-end conditions were studied and sought axisymmetric solutions. It has been shown that wires with free ends break due to standing stress waves, resulting mainly from longitudinal thermal expansion of the wire material due to Joule heating.

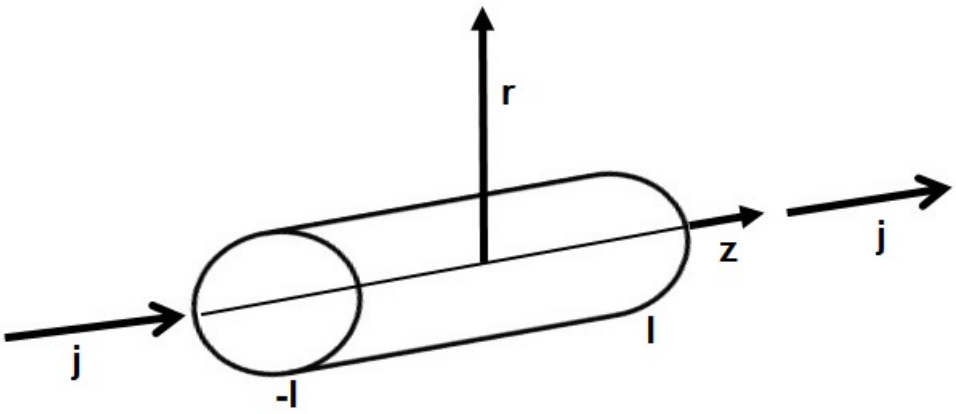

Figure 5.4 The geometry of finite-length wire and the co-ordinate system

The analysis of Molokov and Allen has been extended in [28] to include the skin effect and to study the post-fracture dynamics of wires. Despite differences in the results obtained with the inclusion of the skin effect, results supported the broad conclusions of the uniform-current model: that the largest stresses were found at the clamps for a wire with clamped ends, while the largest stresses in a wire with free ends were generated by the thermal mechanism and were located at the center of the wire. If the wire ends are clamped, buckling instability may occur [29], also as a result of thermal expansion of the wire material. It has been shown that during thermal buckling the longitudinal tensile stress may reach very high values, of the order of 100–200 MPa.

Moreover, Martynyuk [30], using the thermodynamics and kinetics of vaporization and boiling, investigated the phenomenon of explosive boiling of superheated liquid metal and showed that it constitutes a main factor in the electrical explosion of a wire. When certain conditions are satisfied, the initial point of the electrical explosion must be in the neighborhood of the boundary for thermodynamic stability of the liquid metal phase.

5.6 Dynamic Response of Matter in plasma regime

In the literature results of computer simulations [32, 37, 38] and experiments [31, 33-36] are found that assume that the fiber Z-pinch consists of two different regions: a low density hot corona plasma and a dense core during the discharge. An important

feature of the discharge in a single wire is that the wire core, at least for thick wires, may remain cold and expand very slowly. The plasma corona that surrounds the core contains only a small fraction of mass but carries almost all the current. The majority of these studies concern experiments with current >100 kA in which magnetic forces play a major role.

Aranchuk et al. [31] found that, in explosions of 20-μm-diameter copper wires, only 2–7% of the total mass was carrying the current and radiating. The rest of the mass remained cold. Corona was subject to violent unstable motions, while the core remained more or less cylindrical. The maximum current through the wire was 0.5 MA and the current rise time was approximately 100 ns. Two dimensional MHD simulations performed by Lindemuth [32] showed that the m=0 instability begins at very early times in the coronal plasma surrounding the cold pinch core. The m=0 instability leads to an enhanced fiber ablation rate.

Kalantar and Hammer [33] observed experimentally that a high-current exploding wire consists of rapidly expanding coronal plasma surrounding a slowly expanding dense core. Schlieren imaging was used to follow the coronal plasma dynamics in time from the moment of current initiation. The dense core was observed about 30 ns after the start of the current pulse using X-ray backlighting from an x pinch, driven in parallel with the exploding wire, as the X-ray source. Their work focused on 25 to 100 mm diameter Al wires driven by 100 ns FWHM, 40 ns rise time, and 100 to 350 kA/wire current pulses. Using a combination of X-ray backlighting diagnostics to study the dynamics of the dense wire core (with 10 mm spatial resolution) and optical shadowgraphy and Schlieren diagnostics to study the corona, they characterized the exploding wire behavior. A series of experiments with 100 mm diameter Al wires driven by about 100 kA peak current showed that the outer edge of the coronal plasma expanded at a rate of 2.4±0.2 cm/μs starting about 20 ns after the current pulse. By contrast, the core expanded at a rate of 0.8±0.2 cm/μs, and also appeared to begin its expansion at the same moment as the corona. They also estimated that the amount of mass in the corona was 10% or less. Their study concluded that the coronal plasma expansion rate is roughly independent of the initial wire diameter.

Fibre pinch experiments using high z-materials showed unstable behavior at early times in the discharge [34]. Z-pinch plasma was formed from carbon and aluminum

fibers, driven by a pulsed power generator delivering 100 kA with a rise time of 55 ns. It was observed that the instability appeared in the first few nanoseconds of the discharge, while for thicker fibers it appeared later in time. A thorough publication by Ruiz-Camacho et al. [35] used optical diagnostics to study the explosions of 5 to 18 mm diameter W wires and 15 mm diameter Al wires. The wires were driven by a 160 kA peak current (120 kA current for Al) having a 10–90% rise time of 65 ns. Schlieren observations showed that the coronal plasma of various diameters of tungsten wires expanded with the velocity of $(9.4\pm1.0)\times10^3$ m/s. The aluminum pinch expanded at least a factor of 2 faster. The m=0 perturbations appeared at about 8 ns for the aluminum compared with 20 ns for the tungsten pinch. The wavelength and diameter of the perturbations increased with time for both types of wires and were relatively faster for the aluminum pinch. The short wavelength perturbations (~200 μm) persisted for a longer time for larger diameter tungsten wires. Moreover, a series of fiber pinch experiments has been carried out on the MAGPIE (mega-ampere generator for plasma implosion experiments) generator (1.8 MA, 150 ns) to study the temporal evolution of the coronal plasma produced from carbon fibers [36]. Analysis of schlieren photographs, axial streak images, and gated X-ray photographs, gave the radial and axial motion of the coronal plasma. Axial wavelengths of dominant instabilities in the corona were measured to be between 0.05 and 0.2 cm.

A 2-D Eulerian resistive MHD simulation was used by Chittenden et al. [37] to explain the rapid expansion of the plasma column and the development of large non-linear scale m=0 perturbations in the plasma corona. The code models a single temperature admixture of electrons, ion species of different charge and neutral gaseous atoms. The code incorporates a corrected Thomas–Fermi model equation of state, which emulates the behavior of material in condensed phases, such as the reduction of electron pressure near solid density, which is responsible for keeping the core intact at early stages. Modified versions of Lee and More's transport coefficients, which approximate the transition from low resistivity in the solid phase to higher resistivities as the wire material heats and expands, are used. Explicit hydrodynamics on an Eulerian grid with implicit solution of magnetic and thermal diffusion was performed, while a random density perturbation of 0.1% was used to initiate

instability growth. With respect to equations used, the rate of change of mass density is given by the advective term

$$\frac{\partial \rho}{\partial t} = -\nabla(\rho \mathbf{v}) \tag{5.27}$$

The rate of change of momentum is determined by advection, the electromagnetic force, pressure gradient, and the divergence of an artificial viscosity tensor

$$\rho(\frac{\partial}{\partial t} + \boldsymbol{v} \cdot \nabla)\boldsymbol{v} = \boldsymbol{j} \times \boldsymbol{B} - \nabla P - \nabla \pi \tag{5.28}$$

while the rates of change of internal energy is determined by advection, compressional heating, thermal diffusion, Ohmic heating and ionization energy

$$\frac{\partial E}{\partial t} + \nabla(E\boldsymbol{v}) = (PI + \pi)\nabla \boldsymbol{v} - \nabla(-k\nabla T) + \eta \left|\boldsymbol{j}\right|^2 + \sum_{Z=0}^{N}(\frac{\partial \eta_z}{\partial t}\sum_{i=Z}^{N} E_{ionization(i)}) \tag{5.29}$$

.

The rate of change $\partial \eta_z / \partial t$ of the number densities of different ionization stages from neutral (Z=0) to fully stripped (Z=N) are determined by calculating the average ionic charge (Z*) from the Thomas–Fermi model and then iteratively solving the Saha equation. Also, the rate of change of magnetic field strength is given by the advection of magnetic flux ‘‘frozen’’ to the plasma and the rate of resistive diffusion of the field through the plasma

$$\frac{\partial \boldsymbol{B}}{\partial t} = \nabla \times (\boldsymbol{v} \times \boldsymbol{B}) - \nabla \times (\eta \boldsymbol{j}) \tag{5.30}$$

Figure 5.5 shows a series of mass density contour plots from a 33 μm carbon pinch simulation at 0, 10, 20, 30 and 35 ns respectively. The current waveform used in the simulation is based on that obtained using the MAGPIE generator at 60 % of full charge and approximates to a linearly rising dI/dt. After 10 ns the simulation shows that the current is flowing in a low density, highly ionized corona containing only 1 % of the fiber material. Thus, the temperature of the corona is very high and the instability involves rapidly. At later times it is observed that the instability is giving rise to the formation of necks and bulges along the length of the pinch. Moreover, the

instability wavelength increases as time progresses and at late times, only density islands exist, separated by tenuous regions.

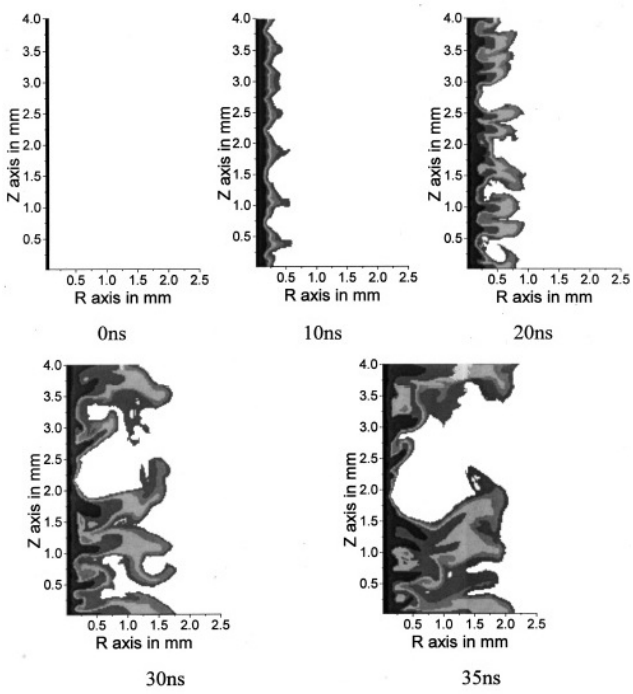

Figure 5.5 Mass density contours from a 2D Eulerian resistive MHD code simulation of a partially ionized carbon Z-pinch [37]

The time evolution of single wires from different wire arrays was simulated using ALEGRA-HEDP [38]. ALEGRA-HEDP uses an Arbitrary-Lagrangian-Eulerian (ALE) operator split algorithm to solve the resistive MHD equations, as well as thermal and radiative transport. The approach used to obtain the simulation initial conditions in this study was to start with a two-state initial condition consisting of a liquid core and a corona. The material models used for this study were ANEOS SESAME 3540 equation of state, Lee-More-Desjarlais for Tungsten conductivity, and XSN opacities for single-group radiation diffusion calculations.

Moreover, single wire experiments that used low current less than 5 kA were done in order to study the pre-pulse conditions on large wire arrays such as Sandia's Z-machine [39, 40]. Sinars et al. [40] using X-pinch X-ray backlighting investigated the explosion of 12.7 μm thick aluminum wires. The results revealed a similar behavior of the dense core to the experiments performed by Kalantar and Hammer [33]. In such type of experiments the magnetic pressure is negligible and the coronal plasma, as well as the wire core expands freely.

References

[1] D. A. Hammer and D. B. Sinars, Single-wire explosion experiments relevant to the initial stages of wire array *z* pinches, *Laser and Particle Beams* **19**, 377–391 (2001).

[2] M. G. Haines, A review of the dense *Z*-pinch, *Plasma Phys. Control. Fusion* **53**, 093001 (2011).

[3] D. D. Ryutov, M. S. Derzon and M. K. Matzen, The physics of fast Z pinches, *Reviews of Modern Physics* **72**, 167-223 (2000).

[4] M. Tatarakis, R. Aliaga-Rossel, A. E. Dangor and M. G. Haines, Optical probing of fiber z-pinch plasmas, *Phys. Plasmas* **5**, 682-91 (1998).

[5] A. I Fedorov, Prospects for increasing the energy output characteristics of a Cu laser excited by a transverse discharge, *Technical Physics* **41**, 696-700 (1996).

[6] G. Lins, Measurement of the densities of Cu and Ag vapours in a low-voltage switch using the hook method, *Journal of Physics D: Applied Physics* **45**, 205202 (2012).

[7] D. B. Sinars, S. A. Pikuz, T. A. Shelkovenko, K. M. Chandler and D.A. Hammer, High energy density physics and high resolution point projection imaging with X-pinch plasmas, *PPPS 2001 - Pulsed Power Plasma Science 2001* **1**, 341-345 (2015).

[8] Yu. A. Kotov, Electric explosion of wires as a method for preparation of nanopowders, *Journal of Nanoparticle Research* **5**, 539-550 (2003).

[9] Y.-S. Kwon, Y.-H. Jung, N. A. Yavorovsky, A.P. Illyn and J.-S Kim, Ultra-fine powder by wire explosion method, S*cripta Materialia* **44**, 2247-2251 (2001).

[10] P. Sen, J. Ghosh, A. Abdullah, P. Kumar and S. Vandana, Preparation of Cu, Ag, Fe and Al nanoparticles by the exploding wire technique, *Proceedings of the Indian Academy of Sciences: Chemical Sciences* **115**, 499-508 (2003).

[11] V. A. Burtsev, N. V. Kalinin and A. V. Luchinskii, *Electrical Explosion of Conductors and Its Applications* (Energoizdat, Moscow, 1990) p. 289.

[12] S. A. Pikuz, V. M. Romanova, T. A. Shelkovenko, D. A. Hammer, and A. Ya. Faenov, *Phys. Scr.* **51**, 517 (1995).

[13] V. V. Alexandrov, I. N. Frolov, M. V. Fedulov, E. V. Grabovsky, K. N. Mitrofanov, S. L. Nedoseev, G. M. Oleinik, and G. G. Zukakischvili, *IEEE Trans. Plasma Sci.* **30**, 559 (2002).

[14] W. H. Bennett, Magnetically Self-Focusing Streams, *Phys. Rev.* **45**, 890 (1934).

[15] J. P. Freidberg, Ideal magnetohydrodynamic theory of magnetic fusion systems, *Reviews of Modern Physics* **54**(3), 801 (1982).

[16] M. Kruskal and M. Schwarzchild, *Proceedings of the Royal Society* **A223**, 348 (1954).

[17] R. J. Tayler, *Proceedings of the Physical Society* **B70**, 31 (1957).

[18] M. Coppins, Ideal magnetohydrodynamic linear instabilities in the Z-pinch, *Plasma Physics and Controlled Fusion* **30**(3), 201 (1988).

[19] http://textlab.io/doc/2154284/pinch-effect

[20] M. Tatarakis, Optical probing of dense Z-pinch and laser produced plasma, PhD thesis 1997.

[21] M. G. Haines and M. Coppins, Universal diagram for regimes of Z-pinch stability, *Phys. Rev. Lett.* **66**(11), 1462 (1991).

[22] I. D. Culverwell and M. Coppins, The ideal MHD stability of time-dependent Z-pinch equilibria *Plasma Physics and Controlled Fusion* **31**, 1443-1449 (1989).

[23] J. Nasilovski, *Unduloids and striated disintegration of wires, Exploding Wires* vol 3, ed. W. G. Chase and H. K. Moore (New York: Plenum) 295 (1964).

[24] P. Graneau, Ampere tension in electric conductors, *IEEE Trans. Magn.* **20**, 444 (1984).

[25] P. Graneau, Wire explosions, *Phys. Lett.* A **120**, 77 (1987).

[26] J. G. Ternan, Stresses in rapidly heated conductors *Phys. Lett. A* **115**, 230 (1986).

[27] S. Molokov and J. E. Allen, The fragmentation of wires carrying electric current, *J. Phys. D: Appl. Phys.* **30**, 3131 (1997).

[28] D. P. Wall, J. E. Allen and S. Molokov, Influence of the skin effect and current risetime on the fragmentation of wires by pulsed currents, *J. Appl. Phys.* **98**, 023304 (2005).

[29] A. Lukyanov and S. Molokov, Flexural vibrations induced in thin metal wires carrying high currents, *J. Phys. D: Appl. Phys.* **34**, 1543–1552 (2001).

[30] M. M. Martynyuk, Vaporization and boiling of liquid metal in an exploding wire, *Sov. Phys. Tech. Phys.* **19**, 793-797 (1974).

[31] L. E. Aranchuk et al., *Sov. J. Plasma Phys.* **12**, 765 (1986).

[32] I. R. Lindemuth, Two-dimensional fiber ablation in the solid-deuterium z pinch, *Phys. Rev. Lett.* **65**, 179-182 (1990).

[33] D. Kalantar and D. Hammer, Observation of a stable dense core within an unstable coronal plasma in wire-initiated dense Z-pinch experiments, *Phys. Rev. Lett.* **71**, 3806–3809 (1993).

[34] F. N. Beg, A. E. Dangor, P. Lee, M. Tatarakis, S. L. Niffikeer and M. G. Haines, Optical and x-ray observations of carbon and aluminium fibre Z-pinch plasmas, *Plasma Phys. Control. Fusion* **39**, 1–25 (1997).

[35] J. Ruiz-Camacho, F. N. Beg, A. E. Dangor, M. G. Haines, E. L. Clark and I. Ross, Z-pinch discharges in aluminum and tungsten wires, *Phys. Plasmas* **6**, 2579-87 (1999).

[36] S. V. Lebedev, R. Aliaga-Rossel, J. P. Chittenden, I. H. Mitchell, A. E. Dangor, M. G. Haines and J. F. Worley, Coronal plasma behavior of the Z pinch produced from carbon and cryogenic deuterium fibers, *Phys. Plasmas* **5**, 3366-72 (1998).

[37] J. P. Chittenden, R. A. Rossel, S. V. Lebedev, I. H. Mitchell, M. Tatarakis, A. R. Ball, and M. G. Haines, Two-dimensional magneto-hydrodynamic modeling of carbon fiber Z-pinch experiments, *Phys. Plasmas* **4**, 4309 (1997).

[38] C. J. Garasi, D. E. Bliss, T. A. Mehlhorn, B. V. Oliver, A. C. Robinson and G. S. Sarkisov, Multi-dimensional high energy density physics modeling and simulation of wire array Z-pinch physics, *Phys. Plasmas* **11**, 2729-37 (2004).

[39] R. B. Spielman *et al.*, *Phys. Plasmas* **5**, 2105 (1998).

[40] D. B. Sinars *et al.*, *Phys. Plasmas* **7**, 1555 (2000).

Chapter 6

6. Mathematical and numerical modeling of exploding single wires

6.1 Introduction

Electrical wire explosion is a sharp change of the physical state of a metal as a result of intense energy release when high-density current pulses run through it. As previously mentioned, during the explosion of a single wire Z-pinch, depending on the magnitude of the electric current, several effects may occur, such as thermal, elasto-plastic, electromagnetic, and magnetohydrodynamic.

In this Chapter different modeling efforts are presented in order to simulate the complex multiphysics problem of an exploding metal wire from solid to plasma phase. In order to be able to study these effects numerically and experimentally, a relative thick copper metallic wire is selected. For the numerical simulations that will be described in the next sections, one aspect that is taken into consideration is the skin depth effect. The current density j of an alternating current (AC) in a conductor decreases exponentially from its value at the surface according to the depth d from the surface. It holds

$$j = j_0(\mathrm{t})e^{\frac{-(d)}{\delta}} \tag{6.1}$$

where $d=r_0-r$ the depth from the surface, r_0 radius of the cross section of the wire, r radius that varies and δ is called the skin depth. The skin depth is thus defined as the depth below the surface of the conductor at which the current density has fallen to *1/e* (about 0.37) of j_0. The skin depth δ can be calculated [1]

$$\delta = \frac{1}{\sqrt{\pi f \mu \sigma}} \tag{6.2}$$

where f is the frequency of the rising current, μ is the permeability of the conductor and σ is the electrical conductivity.

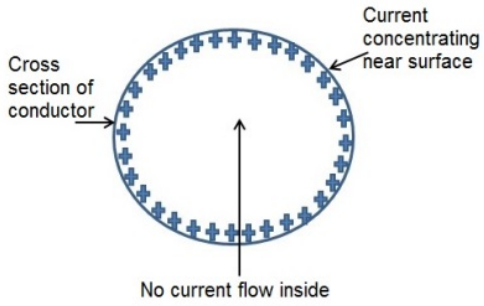

Figure 6.1 Skin depth effect

An initial attempt to model the electrical wire explosion of a Z-pinch metallic copper wire is carried out by taking into account only the thermal-structural effects (section 6.2). This numerical study is limited to elastic and melting regimes and considers a small volumetric deformation. A more accurate attempt to model the single wire explosion from solid to plasma formation is subsequently (section 6.3) carried out, where electromagnetic effects are further taken into account with the thermal-structural. Large volumetric deformation is considered by taking into account the material's hydrodynamic behavior via an equation of state, while the elastoplastic behavior is also considered by a flow stress constitutive model. Moreover, results from this study are further used in section 6.4 where magnetohydrodynamic effects are taken into account and plasma expansion and instability development is investigated.

6.2 3D Thermomechanical modeling

In order to describe the previously mentioned complex multiphysics problem, finite element numerical analysis is chosen in this thesis. A 3D coupled mechanical/thermal FEM simulation is developed using the ANSYS finite element software. All numerical simulations run on a 4-core Intel® Core™ i7-3820 CPU with a processor of 3.6 GHz and 32 GB RAM. In this preliminary simulation approach the loading term is the heat generation per volume, generated by the alternating pulsed current, the Joule heating effect. Hence, Joule heating, also known as Ohmic heating

and resistive heating, is the process by which the passage of an electric current through a conductor releases heat. In particular, when the electric current flows through a solid or liquid with finite conductivity, electric energy is converted to heat through resistive losses in the material. The heat is generated on the microscale when the conduction electrons transfer energy to the conductor's atoms through collisions.

6.2.1 Computational approach, geometry and meshing

The model conveys a simultaneous analysis of the thermal and structural parameters, as defined by the solution of the heat conduction and mechanical motion equations. The mechanical equation determines the displacements of the wire imposed by the pulsed current, while the heat conduction equation predicts the temperature distribution. Convective heat transfer as well as radiative heat transfer in the wire are neglected. As previously described in Chapter 3, matrix equations for heat conduction and mechanical motion have the form

$$[K]\{T\}+[C]\{\frac{\partial T}{\partial t}\}=\{Q-L_m\}$$

$$[M]\{\frac{\partial^2 U}{\partial t^2}\}+[S]\{U\}=\{F\} \quad (6.3),$$

where L_m is the latent heat of melting and Q is the heat generation per volume source term due to Joule heating effect.

The solution of the matrix Equations 6.3 is done using the commercial finite element software ANSYS ver. 14.5. Both thermal and structural fields share the same 3D geometry, meshing, elements, boundary, and loading conditions. With the help of a direct coupling method, a single pass solution is achieved, involving one analysis that uses a coupled-field 3D element type. Therefore, a simultaneous analysis of the thermal and structural parameters is achieved, as defined by the solution of the heat conduction and wave equations. For this thermal-structural analysis the weak field coupling is chosen, which was previously described in Chapter 3. The adopted SOLID5 element has eight nodes with up to six degrees of freedom per node.The analysis type of the coupled physics model is transient, while the choice of the

element type is done so that a good relation between accuracy and computational cost is achieved.

The dimensions that are used for the simulations correspond to real metal wires used in experiments, as will be mentioned in Chapter 7. A copper wire with a diameter of 300 μm and a length of 15.2 mm is simulated. An important aspect of the developed simulation is that the Lagrangian mesh is adaptive, depending on the simulation needs. In Figure 6.2a a schematic of the 3D finite element model is depicted. A small element size is used to accurately simulate the dynamic phase change of matter (from solid to liquid) in the region of the skin depth and resolve the temperature distribution. The skin depth of the copper wire is computed to be 30.6 μm for experimental current frequency f=4.5 MHz and copper resistivity 1.68×10^{-8}Ohm·m. For this reason, in order to accurately resolve the temperature distribution in the skin depth effect region, the element size in the radial direction is selected to be 5 μm, as can be seen in Figure 6.2b. The total number of elements, according to different mesh discretization test cases, for achieving mesh independent solution is approximately 80000.

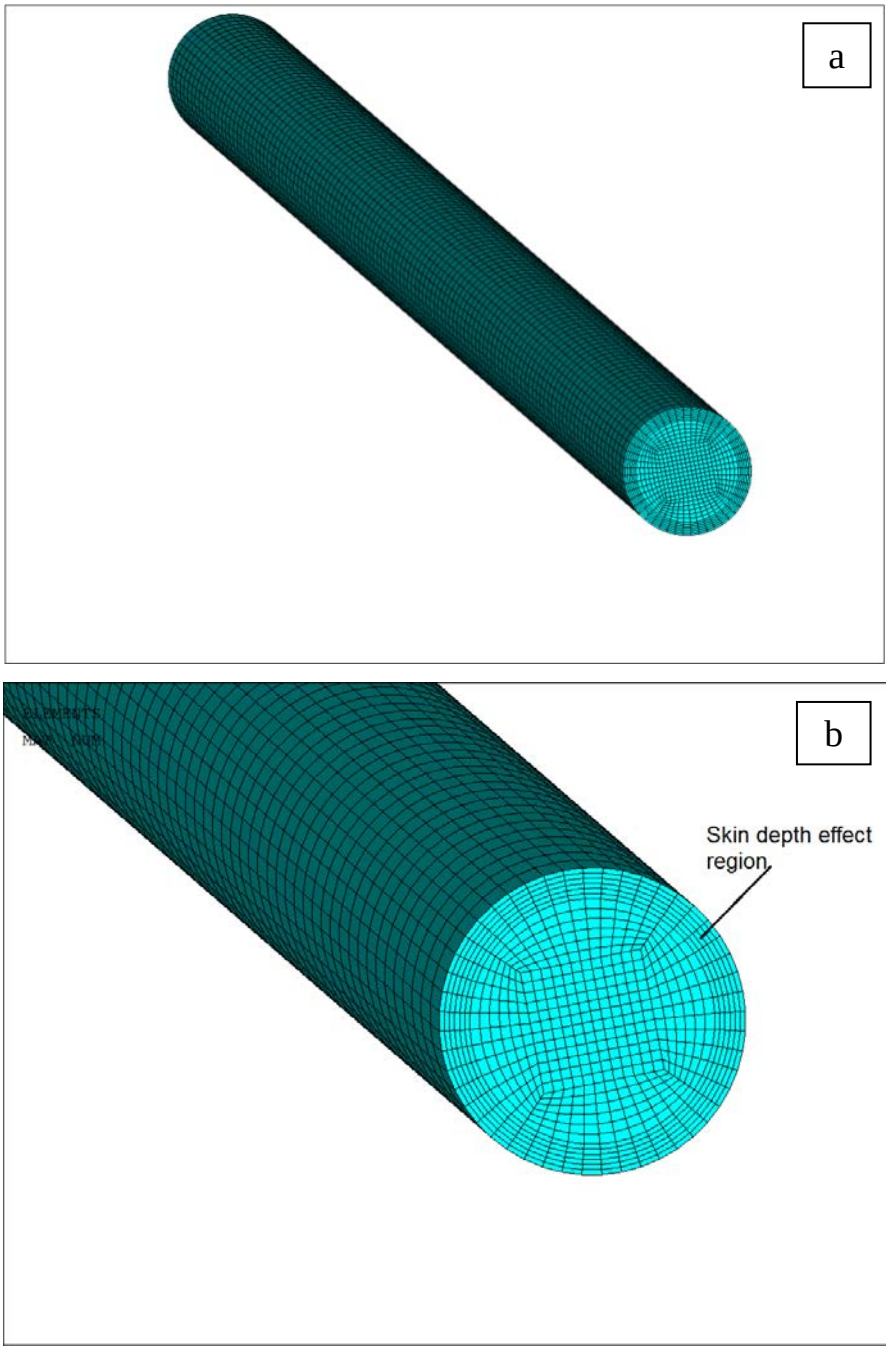

Figure 6.2 a) 3D finite element mesh of the model in ANSYS, b) Zoomed view of the cross-section

An implicit solver is considered and the same numerical techniques are used for the solution of the coupled non-linear equations 6.3, as previously described in section 3.2. The time dependent problem is solved with an incremental time step of 1 ns over a time period of 120 ns. Furthermore, at the end of each solution step, if the

temperature of an element is higher than the melting temperature, phase change occurs, by considering the latent heat of melting in the model.

6.2.2 Initial, boundary and loading conditions

Concerning the boundary conditions, the ends of the wire are fixed at environmental temperature (27 ^{o}C). The ambient initial temperature is also assumed to be 27 ^{o}C, while the wire is initially considered to be non-deformed.

In relation to the loading conditions of the model, a heat generation per unit volume function Q due to the Joule heating effect, is applied to the whole volume of the wire. The source term of the heat generation rate (W/m^3) is the Joule heating term j^2/σ, where $\boldsymbol{j}$ is the current density and σ the electrical conductivity, which is the inverse of resistivity. The analytical equation of j that takes into account the diffusion of the current is [1]

$$j(r,t) = \frac{I_{\exp}(t)\, e^{\frac{-(r-r_0)}{\delta}}}{2\pi\delta(r_0 + (e^{\frac{-r_0}{\delta}} - 1)\delta)} \tag{6.4}$$

where I_{exp} is the pulsed current as experimentally measured, δ the skin depth, r_0 the radius of the cross section of the wire, and r the varied radius. In Figure 6.3 the experimentally measured alternating pulsed current is depicted, with a peak of approximately 38 kA, 70 ns from the current start. Details about the experimental methods are provided in Chapter 7.

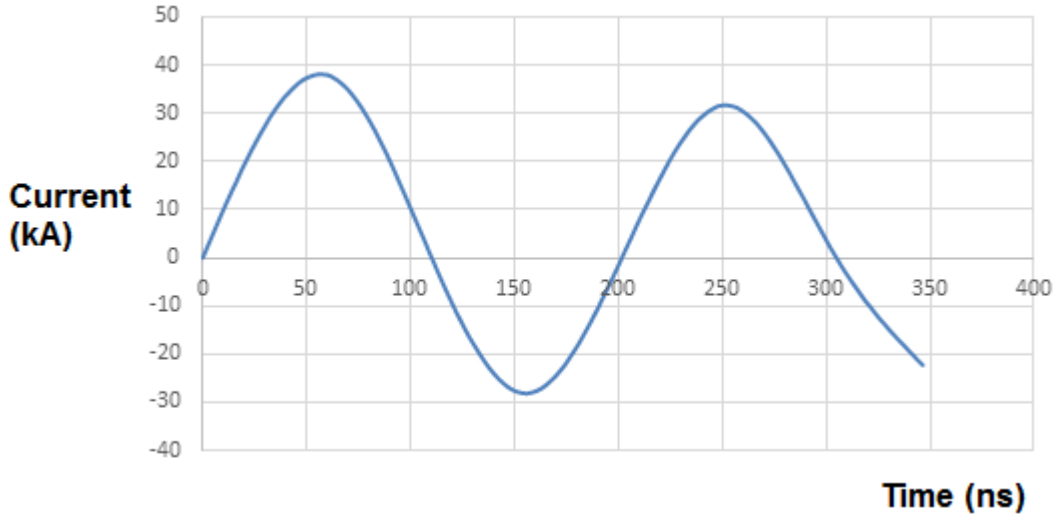

Figure 6.3 Alternating pulsed current in relation to time

With regard to the temperature dependence of resistivity r_e a linear approximation is used

$$r_e(T) = r_{e0}[1+\alpha(\mathrm{T}-\mathrm{T}_0)] \tag{6.5}$$

where α is called the temperature coefficient of resistance, T_0 is a fixed reference temperature (usually room temperature), and r_{e0} is the resistivity at temperature T_0. The parameter α is an empirical parameter fitted from measured data and has the value of 0.004 $1/^{o}$C for room temperature.

6.2.3 Material properties

The values for thermo-physical properties of copper have been adopted from existing literature values [2-5]. The temperature dependent material properties that are taken into account in this study are presented in Table 6.1. In particular, the quantities of thermal expansion, Young modulus, thermal conductivity, and specific heat of copper are considered temperature dependent until the melting point (1085 ^{o}C). Moreover, the density of copper is 8910 kg/m^3 and the latent heat of melting of copper is 207 kJ/kg.

Temperature (^oC)	Thermal conductivity (W/m ^oC)	Specific heat (J/kg ^oC)	Thermal expansion coefficient ($10^{-6}\times1/^oC$)	Young Modulus (GPa)	Poisson's ratio
27	401	385	15.4	117	0.3406
127	393	398	16.2	113	0.3406
227	386	408	16.9	111	0.3435
327	379	417	17.7	105	0.3465
427	373	425	18.5	100	0.35
527	366	432	19.3	95	0.3527
627	359	441	20.2	89	0.355
727	352	451	21	84	0.3575
827	345	464	21.9	78	0.36
927	339	480	22.8	72	0.362
≥1027	332	506	23.7	65	0.365

Table 6.1 Material properties of the wire sample [2-5]

6.3 3D coupled electromagnetic thermomechanical hydrodynamic modeling

In order to more accurately describe the complex problem of electrical wire explosion from solid to plasma formation, multiphysics finite element numerical analysis is again chosen but this time electromagnetic effects are taken into account, since their influence cannot be neglected. Moreover, for the thermomechanical response of the exploded material it is needed to take into account both the hydrodynamic behavior of the material, using a dedicated equation of state (EOS), and the deviatoric behaviour, using a dedicated strength material model. An equation of state that relates resistivity to temperature and density is also used.

The choice of the material constitutive equations, which include both strength model (deviatoric component) and equation of state (hydrodynamic component), is of major importance for high strain-rate and shock loading conditions. With respect to continuum mechanics theory, the complete stress tensor describes the material condition state. It is divided into two components: the deviatoric and the hydrostatic tensors

$$\sigma_{ij} = s_{ij} - P\delta_{ij} \tag{6.6}$$

where s_{ij} is the deviatoric stress component [6, 7]. The hydrostatic component of stress is associated to the pressure in the material, which is equal to the trace of the complete stress tensor.

$$P = -\frac{\sigma_{11} + \sigma_{22} + \sigma_{33}}{3} = -\frac{\sigma_{\kappa\kappa}}{3}. \tag{6.7}$$

The use of an EOS is omitted only when volumetric deformation is very small and

$$\left|P\right| << s_{ij}. \tag{6.8}$$

Since large volumetric deformations occur in wire explosion, the inclusion of an EOS is mandatory for the simulation [6].

6.3.1 Equation of state

An equation of State (EOS) generally expresses the relation between dependent thermodynamics variables (such as pressure P, internal energy E and entropy S) and independent ones (such as density ρ and temperature T). All these variables define the thermodynamic state of the matter. An EOS represents a set of surfaces, where it is possible to define one-dimensional paths, that identify isotherm, isobaric, isochoric, isentropic, etc. transformations. In order to obtain the entire surface a great number of paths needs to be measured.

Usually, in hydrodynamics, the internal energy is used instead of temperature as independent variable. In this case, the EOS assumes the general form which, is used in the most part of the commercial FE codes

$$P = P(\rho, E) \tag{6.9}$$

In general, the equations of state can be divided into two categories: analytical EOS, such as Gruneisen [8] and GRAY [9], and tabular EOS, such as SESAME [10, 11].

When a material is subjected to high energy deposition, impact, or deformation at high strain-rate, it suffers large changes in its thermodynamic state. At these extreme loading conditions, the material could be subjected to high-temperature and high-pressure conditions. There are cases in which a great amount of energy is deposited in a very short time (order of a few nanoseconds). Some examples are deposition of x-ray energy from the detonation of nuclear explosives, high energy particle beams deposition, laser deposition and wire explosion, which is the focus in our study. For this reason it is necessary to use a multi-phase EOS, which is able to describe a great number of all the possible states of the matter [12].

6.3.2 Strength material model

In the continuum mechanics treatment, the deviatoric component concerns phenomena that are associated with the material strength, such as plasticity and failure. In order to investigate high strain response of metallic materials and their thermo-plastic behavior, a constitutive strength material model is necessary. This model is applicable in wide range of strain, strain-rate, and temperature. Moreover, it defines the flow stress as a function of variables of interest, such as deformation, strain-rate temperature, and pressure [12].

In the literature there are many material models that keep into account strain rate and temperature influences on mechanical behavior. These models are classified to empirical, semi-empirical, and phenomenological. The empirical models have nonphysical basis, but are obtained by interpolation of experimental data, while the phenomenological models are obtained starting from the transformation in the material that occurs during a deformation process. Models such as those proposed by Johnson-Cook (J-C) [13] and Cowper-Symonds (C-S) [14] are purely empirical models and they are the most widely used. An example of semi-empirical model is the Steinberg-Cochran-Guinan-Lund (S-C-G-L) model [15], which was first developed for the description of high strain-rate behaviour and after extended to low strain-rate. A phenomenological model is the Zerilli-Armstrong (Z-A) model [16], that is obtained on the basis of the dislocation mechanics theory. The Johnson-Cook elasto-plastic model is selected for the conducted simulations in this thesis.

6.3.3 Mathematical and computational modeling

The 3D electromagnetic-thermal-structural numerical simulations are performed using the commercial FEM code LS-DYNA [5], since an electromagnetic module has been recently developed [17-19] that couples with previously developed LS-DYNA mechanical and thermal solvers. All numerical simulations run on a 4-core Intel® Core™ i7-3820 CPU with a processor at 3.6 GHz and 32 GB RAM. The electromagnetic module allows for the application of electrical currents to solid conductors to compute the associated magnetic and electrical fields and determine the induced currents. Electromagnetic Metal Forming (EMF) [20] is one of the main applications of the module. The electromagnetic fields are computed by solving the Maxwell equations in the eddy-current approximation. Eddy current solver is also called induction-diffusion solver, due to the two combined phenomena of induction and diffusion that are being solved. Induction is the property of an alternating fast rising current in a conductor to generate a current and a voltage in both the conductor itself (self-induction) or to potential nearby conductors. Self-induction in conductors is then responsible for the skin effect or current diffusion. Solution of those coupled phenomena allows for the calculation of the Lorentz force and the Joule heating energy, which are added to the mechanical and thermal solvers respectively. Moreover, Maxwell equations are solved using Finite Element Method (FEM) [21] for the solid conductors, coupled with Boundary Element Method (BEM) [22] for the surrounding air or vacuum. Both the FEM and the BEM are based on discrete differential forms (Nedelec-like elements) [23]. The investigation of the exploding conducting copper metallic wire, which is the focus of our study, involves the phenomena of self-induction (since no nearby conductors are present) and current diffusion.

6.3.3.1 Maxwell equations

The Maxwell equations solved by the solver for electromagnetism assuming a divergence free current density and no charge accumulation, have the form

$$\nabla \times \boldsymbol{E} = -\frac{\partial \boldsymbol{B}}{\partial t} \tag{6.10}$$

$$\nabla \times \boldsymbol{B} = \mu_0 \boldsymbol{j} \tag{6.11}$$

$$\nabla \cdot \boldsymbol{B} = 0 \tag{6.12}$$

$$\nabla \cdot \boldsymbol{E} = 0 \tag{6.13}$$

$$\boldsymbol{j} = \sigma \boldsymbol{E} + \boldsymbol{j}_s \tag{6.14}$$

$$\nabla \cdot \boldsymbol{j} = 0 \tag{6.15}$$

where σ is the electrical conductivity, μ_0 is the magnetic permeability of the free space, $\boldsymbol{B}$ is the magnetic flux density, $\boldsymbol{E}$ is the electric field, $\boldsymbol{j}$ is the total current density, and $\boldsymbol{j_s}$ the source current density.

The divergence equation given by Equation 6.12 allows for writing the magnetic flux density as

$$\boldsymbol{B} = \nabla \times \boldsymbol{A} \tag{6.16}$$

where $\boldsymbol{A}$ is the magnetic vector potential. Equation 6.10 then implies that the electric field is given by

$$\boldsymbol{E} = -\nabla \Phi - \frac{\partial \boldsymbol{A}}{\partial t} \tag{6.17}$$

where Φ is the electric scalar potential. Then, the Gauge condition is used

$$\nabla(\sigma \boldsymbol{A}) = 0\,, \tag{6.18}$$

which allows a separation of the vector potential from the scalar potential in the equations. Equations 6.14, 6.15, 6.17 and 6.18 give

$$\nabla(\sigma \nabla \Phi) = 0 \tag{6.19}$$

Furthermore, Equations 6.11, 6.14, 6.16 and 6.17 give

$$\sigma \frac{\partial \boldsymbol{A}}{\partial t} + \nabla \times (\frac{1}{\mu} \nabla \times \boldsymbol{A}) + \sigma \nabla \Phi = \boldsymbol{j}_s\,. \tag{6.20}$$

The last two equations constitute the system that will be solved, with $\boldsymbol{A}$ and Φ being the two unknowns of the problem.

6.3.3.2 Finite element method for conducting wires and Boundary element method for vacuum/air

Equations 6.19 and 6.20 are solved for the conducting materials with a Finite Element Method using a library called “FEMSTER”, which was developed at the Lawrence Livermore National Laboratories [24]. FEMSTER provides discrete numerical implementations of the concepts from differential forms (often referred as Nedelec elements) [25]. These include in particular the exterior derivatives of gradient, curl, and divergence, and also the div-grad, curl-curl and grad-div operators. The solver runs implicitly and more details are presented in Appendix C.

The BEM method uses an intermediate variable, the surface current. This variable is introduced on the boundary between conductor and vacuum/air, so as to produce the same magnetic field in the vacuum region as the magnetic field created by the actual volume current flowing through the conductor. An advantage of this method is that does not need a mesh in the vacuum or air that surrounds the conductor, therefore avoiding meshing problems of complicated geometries and distorted elements. Moreover, a disadvantage is the high memory requirement, as well as the longer CPU time to assemble the matrices, because full dense matrices are generated in place of the sparse FEM matrices.

6.3.3.3 Mechanical and thermal analysis and coupling with electromagnetism

LS-DYNA is a non-linear finite element hydrodynamic code capable to simulate complex phenomena that involve large deformations or large changes of density, using the appropriate strength material model and equation of state for a given problem. The equations that are solved by the mechanical solver of LS-DYNA that runs an explicit analysis, are the Cauchy momentum equation, equation of mass, and equation of energy. Details about time integration are given in Appendix C. Cauchy momentum equation has the form

$$\rho \ddot{\boldsymbol{x}}_i = \boldsymbol{\sigma}_{ij,j} + \rho \boldsymbol{f}_i \tag{6.21}$$

where $\boldsymbol{\sigma}_{ij,j}$ is one order partial derivative of Cauchy stress component $\boldsymbol{\sigma}_{ij}$ with respect to the coordinate variable in the j-th direction, $\boldsymbol{f}_i$ is the volume force vector of unit

mass (body force density), $\ddot{\boldsymbol{x}}_i$ is the acceleration vector, and ρ is the density. Conservation of mass has the form

$$\rho = V\rho_0 \tag{6.22}$$

where ρ_0 is the reference density, V the relative volume, the determinant of the strain gradient matrix

$$V = \left| \frac{\partial x_i}{\partial X_j} \right| \tag{6.23}$$

x_i is the space coordinate in the i-th direction, X_j is the matter coordinate in the j-th direction, and $\frac{\partial x_i}{\partial X_j}$ is the strain gradient with respect to X_j. Energy equation has the form

$$\dot{E} = V\boldsymbol{s}_{ij}\dot{\boldsymbol{\varepsilon}}_{ij} - (p+q)\dot{V} \tag{6.24}$$

where $\dot{\varepsilon}_{ij}$ is the strain rate tensor, $\dot{E}$ is the energy rate, and q is artificial bulk viscosity. Deviatoric stress tensor is given by

$$\boldsymbol{s}_{ij} = \boldsymbol{\sigma}_{ij} + (p+q)\delta_{ij} \tag{6.25}$$

where δ_{ij} is Kronecher symbol and the hydrodynamic pressure p is given by

$$p = -\frac{1}{3}\sigma_{kk} - q\,. \tag{6.26}$$

Details about the artificial bulk viscosity are presented in Appendix C.

With respect to the thermal solver of LS-DYNA, it runs implicitly. Based on the work of Shapiro [26], the differential equation of conduction of heat in a three-dimensional continuum is

$$\rho(x,y,z)C_\rho(\mathrm{x,y,z},T)\frac{\partial T(x,y,z,t)}{\partial t}-\nabla[k(\mathrm{x,y,z},T)\nabla T(x,y,z,t)]=Q(x,y,z,t) \quad (6.27)$$

Details about time integration of the thermal solver are presented in Appendix C.

With respect to the coupling of the electromagnetic solver with the mechanical and thermal solvers, once the electromagnetic field and the current density have been computed from the EM module, the Lorentz force $\boldsymbol{F} = \boldsymbol{j} \times \boldsymbol{B}$ is evaluated at the nodes and added to the mechanical solver, which computes the deformation of the conducting wire. The new geometry is then used to compute the evolution of the EM fields in a Lagrangian way. The electromagnetic force is added to the momentum Equation 6.21. Moreover, the joule heating power term j^2/σ is added to the thermal solver to update temperature. Temperature is used in turn in an electromagnetic equation of state to update the electromagnetic parameters, mainly the conductivity σ [27, 28]. In Figure 6.4 the interaction between the different solvers is depicted for the simulation of the exploding wire.

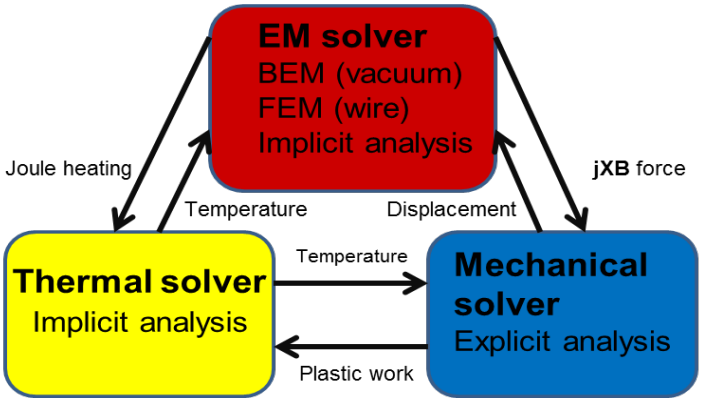

Figure 6.4 Interaction between the different solvers

6.3.4 Geometry, meshing, boundary and loading conditions

The dimensions that are used for the simulations correspond to real metal wires used in experiments, as will be mentioned in Chapter 7. A copper wire with a diameter of 300 μm and a length of 15.2 mm is simulated. Hexahedral 8-node elements with one-point integration are used. An important aspect of the developed simulation is that the Lagrangian mesh is adaptive, depending on the simulation

needs. In Figure 6.5a a schematic of the 3D finite element model is depicted, while in Figure 6.5b a close view to the cross-section is presented. A small element size is used in the radial direction in order to accurately simulate the dynamic phase change of matter (from solid to plasma formation) in the region of the skin depth and also in the core region, where large compressive stresses are observed. A small element size is also used in the vertical direction, in order to simulate the observed instabilities (see Chapter 7 for more details). The skin depth of the copper wire is computed to be 30.6 μm for experimental current frequency f=4.5 MHz and copper resistivity 1.68×10^{-8}Ohm·m. The total number of elements, according to different mesh discretization test cases, for achieving mesh independent solution is approximately 140000 (5 μm element length along radial direction and 50 μm along vertical direction), where 14000 are BEM faces (shell elements) for the wire exterior.

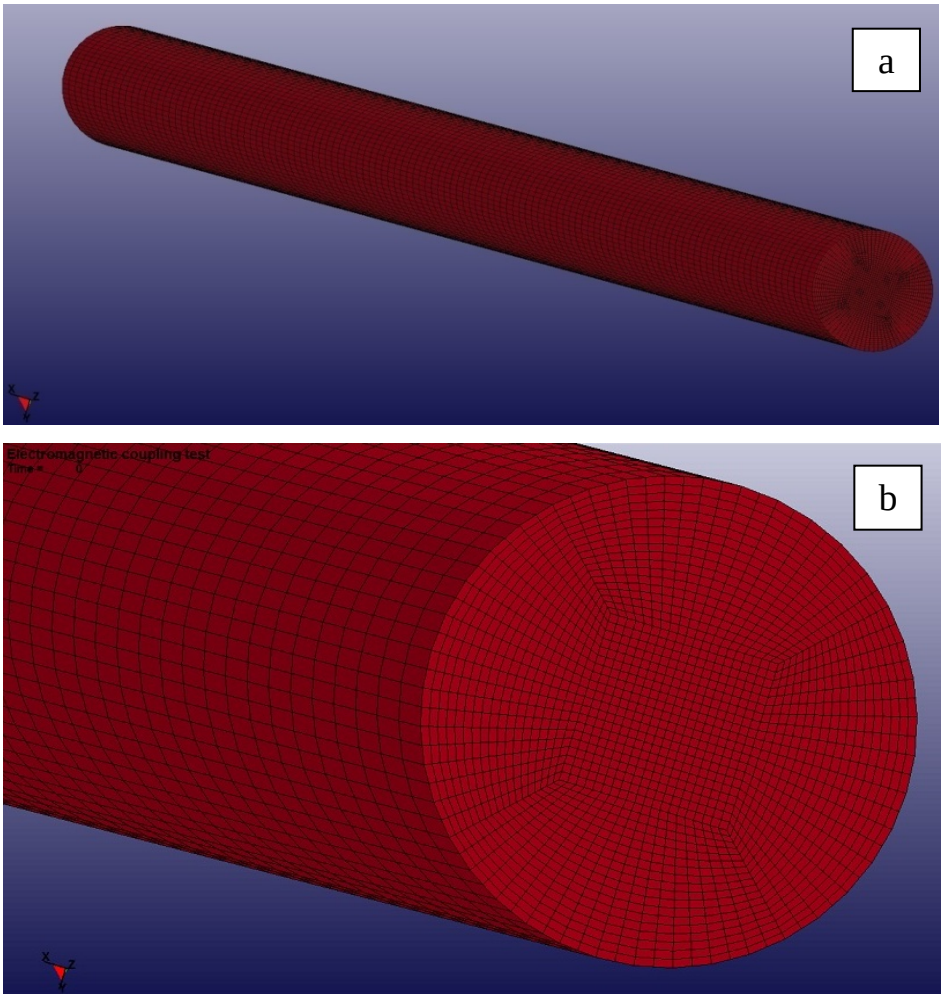

Figure 6.5 a) 3D finite element model of the wire, b) Zoomed view of the wire cross-section

With respect to the boundary conditions, the ends of the wire are fixed at constant environmental temperature, of 27 ^{o}C. The initial temperature of the simulation domain is also considered to be 27 ^{o}C, while the wire is initially considered to be non-deformed. The loading source term is the alternating current, as measured and recorded during the real experiments, with a peak of 38 kA, that was previously described in section 6.2.2. The load curve of current in relation to time is imposed to the ends of the wire. The current is considered to be oriented as going into the structural mesh from the input current segment, while it is considered to be oriented as going out of the structural mesh from the output current segment. The coupled multiphysics time-dependent problem is solved with an incremental time step of 0.1 ns for all solvers, in order to satisfy the conditions for time step control for solid elements (see Equations C.19-C.21 and C.8 on the Appendix C). The simulation runs over a time period of 200 ns.

6.3.5 Analytical Gruneisen and SESAME tabular equations of state

In LS-DYNA, as in other FEM codes, such as Autodyn [29], the implemented EOS are defined, in general, as described by Equation 6.9. The independent variables are density and internal energy, while the dependent variable is the pressure. The density can be replaced by the specific volume v, which is equal to $1/\rho$, where ρ is the density at the current temporal moment. The reference specific volume, v_0, holds for the condition in which the stress or strain state of the material is null. At zero compression or expansion, the material is in equilibrium with its ambient surrounding. It holds $v_0=1/\rho_0$, where ρ_0 is density at reference usually non-deformed state. The reference specific volume represents a unique state, with respect to which the material stress tensor is computed, so it is very critical in computing the pressure level in the material.

Additionally, the volumetric parameter $\eta=\rho/\rho_0$ assumes a value greater than one if the material is compressed ($\rho>\rho_0$), less than one if the material is expanded ($\rho<\rho_0$),and equal to one if no loads are applied to the material. Similarly, the volumetric parameter $\mu=\eta-1$ is positive if the material is being compressed and negative if the material is being expanded. Another important derived quantity used in

LS DYNA is the internal energy per unit of reference volume (e_{v0}), which relates internal energy to temperature

$$e_{vo} = \rho_0 C_v T \,. \tag{6.28}$$

The EOS of Equation 6.9 is then expressed as $P=P(\rho,E)=P(\mu,e_{v0})$. In more details, pressure in the EOS implemented in LS-DYNA is computed as the sum of two components

$$P=P_C(\mu)+P_T(\mu,e_{v0})=A(\mu)+B(\mu)e_{v0}. \tag{6.29}$$

The first term, $P_C(\mu)$, is called *cold curve* and is a function of the density. It is hypothetically evaluated along the 0 K isotherm. The second term, $P_T(\mu,e_{v0})$ expresses the dependency of pressure on both density and internal energy. In particular, the cold curve is a generic function of density, while the thermal component is again a generic function of density and it is a linear function of energy.

As already mentioned, the hydrodynamic and deviatoric behavior of the wire in this thesis is taken into account simultaneously by using an equation of state, combined with a strength material model. With regard to the equations that are used for the simulations of the exploding wire, the analytical Grüneisen equation of state is initially used [8]. The Grüneisen equation allows for extending the range of application to higher pressures and also to the liquid phase, but with limitations for expanded liquid or vapour zone. The analytical Grüneisen equation of state with cubic shock velocity-particle velocity (U_s-U_p) defines pressure for expanded materials as [6,8]

$$P = \rho_0 C_0^{\,2} \mu + (\gamma_0 + \alpha\mu)E \tag{6.30}$$

where C_0 is the sound speed, γ_0 the Grüneisen parameter that defines the effect on the atoms vibration consequent to the change in energy (or temperature), and a is the first volume correction to γ_0.

For compressed materials it has the form [6,8]

$$P = \frac{\rho_0 C_0^{\,2}\mu[1+(1-\frac{\gamma_0}{2})\mu-\frac{\alpha}{2}\mu^2]}{[1-(S_1-1)\mu]^2}+(\gamma_0+\alpha\mu)E\,. \tag{6.31}$$

For most materials, shock velocity U_s varies linearly with respect to the particle velocity U_p [30] as $U_s=C_0+S_1U_p$, where S_1 is a non-dimensional coefficient of the slope of the U_s-U_p curve.

However, due to the wide ranges both in temperature and density that have to be considered for the complete description of all the states of the matter, the SESAME tabular EOS is needed for the exploding wire simulation, since the Grüneisen equation has limitations in the expanded vapour zone. The SESAME is a library of EOS, in which the thermodynamic properties of a large number of materials are reported in the form of a table. The EOS are obtained for different types of materials, such as simple elements, compounds, metals, minerals, polymers, mixtures, etc. The EOS contained in the SESAME library are multi-phase and allow for the description of all the states of the matter: solid, liquid, gas, plasma and their transitions. Moreover, the dependent variable (i.e. pressure or internal energy) is defined as a function of the independent variables (temperature and density). In Figures 6.6 and 6.7 isotherms and isodensities from the SESAME database for copper are depicted [31-33].

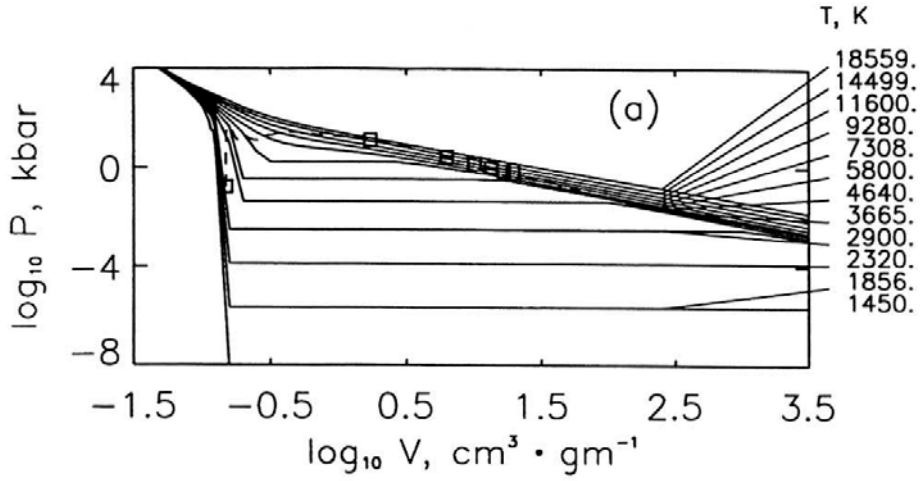

Figure 6.6 Isotherms in the P-V plane from the SESAME database for copper [30]

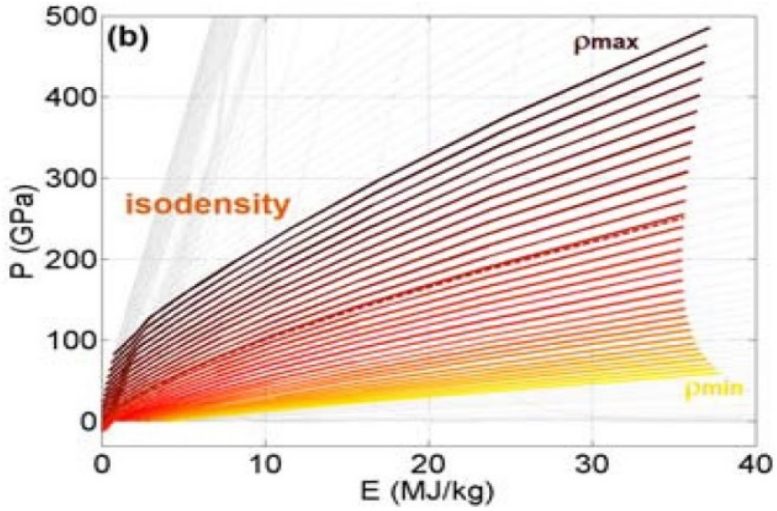

Figure 6.7 P-E plane as a function of density from the SESAME database for copper [31, 32]

However, in LS-DYNA code it is not possible to directly use a SESAME tabular equation of state. In order to deal with this problem, a polynomial user-defined EOS is implemented. A standard polynomial EOS of the following form is used to fit the tabular data

$$P = C_0 + C_1\mu + C_2\mu^2 + C_3\mu^3 + (C_4 + C_5\mu + C_6\mu^2)E \,. \tag{6.32}$$

Different solutions for the interpolation are analyzed in order to obtain the set of parameters that correspond to the best fit. The cross-section of the wire is divided into three regions, one corresponding to the skin depth and the other two based on the preliminary results of temperature and density using Grüneisen equation of state. A dedicated interpolation is done for each region of the model. Each interpolation is performed limiting the range of interest of the entire tabular data in pressure, density and energy. The purpose is to neglect in the interpolation the areas of the tabular equation of state that are physically unreachable for each model region-part. The hypothesis of linearity in *E* is not valid over all the data range; however for each part the interpolation of the tabular data with the polynomial EOS is calculated in smaller areas where the hypothesis of linearity of the pressure with energy is more reasonable.

Figure 6.8 depicts a SESAME tabular equation of state for copper [32-34], where are defined characteristic limits set for the interpolation with the polynomial EOS. A linear interpolation of the *P-E* curve is done, calculating a value of slope and

intercept. Then, the slopes are fitted by a polynomial of II order, obtaining the coefficients of the thermal part $P_T(\mu,E)$ according to Equation 6.32. In Chapter 7 further details are presented.

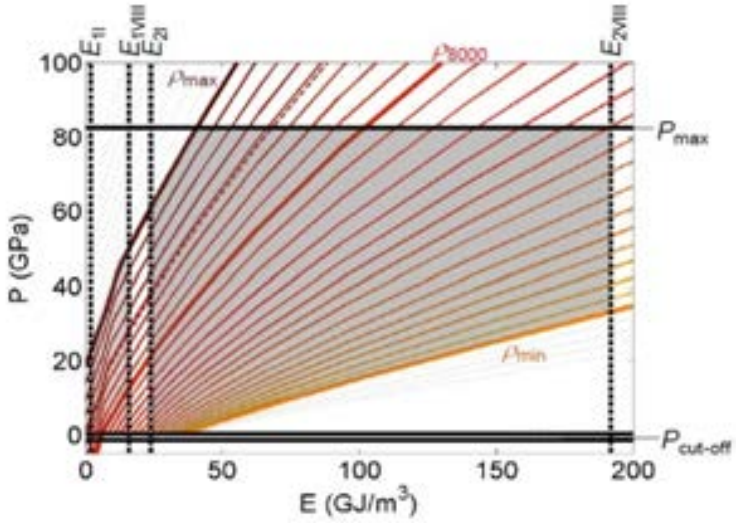

Figure 6.8 Definition of the limits set for the interpolation with the polynomial EOS [31, 32]

6.3.6 Johnson-Cook strength material model

The material model chosen for the numerical analysis is the Johnson-Cook material model. It is a purely empirical one that takes into account the effect of plastic strain, strain rate, and temperature. It can predict the mechanical behavior of the materials under different loading conditions and is one of the most used and cited in many FEM codes in the literature for many materials [13]. The model expresses the flow stress as [13]

$$\sigma_y = (A + B\bar{\varepsilon}_p^n)(1 + C\ln\frac{\dot{\bar{\varepsilon}}_p}{\dot{\bar{\varepsilon}}_0})(1 - \frac{T - T_r}{T_m - T_r})^m \tag{6.33}$$

where $\bar{\varepsilon}_p$ is the equivalent plastic strain, $\dot{\bar{\varepsilon}}_p / \dot{\bar{\varepsilon}}_0$ is the dimensionless plastic strain rate, $\dot{\bar{\varepsilon}}_0 = 1\text{s}^{-1}$ is a reference strain rate used to normalize the strain rate, A is the yield stress, B is the hardening constant, C is the strain rate sensitivity, n is the hardening exponent, m is the thermal softening exponent, T_m is the melting temperature and T_r the room temperature. The strain rate $\dot{\bar{\varepsilon}}_0$ represents the highest strain-rate for which

the strain-rate effects on the flow stress are negligible. Moreover, the equivalent plastic strain rate is expressed as [6]

$$\dot{\bar{\varepsilon}}_p = \sqrt{\frac{2}{3}\dot{\varepsilon}_{ij}^p \dot{\varepsilon}_{ij}^p} \tag{6.34}$$

where $\dot{\varepsilon}_{ij}^p$, is the plastic strain rate.

With respect to the thermal effects described by the J-C model, for temperatures above the melting point T_m the material mechanical strength goes to zero and the material behaviour can be completely described using the multi-phase equation of state. This means that the material loses its shear strength and starts to behave like a fluid.

The Johnson-Cook material model includes also a fracture model. It is selected as the damage initiation criteria, since it takes into account the nucleation, growth, and coalescence of voids in a ductile material at high strain rates. It defines the equivalent plastic strain at the onset of damage as [6]

$$\varepsilon_f = ([D_1 + D_2 \exp D_3 \frac{p}{\sigma_{VM}}][1 + D_4 \ln \frac{\dot{\varepsilon}_{pl}}{\dot{\varepsilon}_0}][1 + D_5 \frac{T - T_r}{T_m - T_r}]) \tag{6.35}$$

where D_1, D_2, D_3, D_4 and D_5 are the failure parameters and σ_{VM} the Von Mises stress. The material fracture occurs when the damage parameter

$$D = \sum \frac{\Delta \varepsilon_{pl}}{\varepsilon_f} \tag{6.36}$$

reaches the value of 1. Moreover, a pressure cut-off p_{min} is defined that limits the minimum hydrostatic pressure to the specified value $p \geq p_{min}$. If pressures more tensile than this limit are calculated, the pressure is reset to p_{min}.

Certain limitations of the model are that it neglects the influence of pressure and changes in volume on the flow stress and considers the shear modulus and the melting temperature constant [33], although they could be influenced by density. All the values of the used parameters of the J-C strength material model for the simulations are presented in section 6.3.8 for material properties.

6.3.7 Burgess resistivity equation of state

Burgess model [35] gives the electrical resistivity in relation to temperature and density for the solid and liquid phase, taking into account phase transition. Burgess EOS is coupled with the thermal solver. To check which elements are in the solid and in the liquid phase, a melting temperature is computed by [35]

$$T_m = T_{m,0}\left(\frac{V}{V_0}\right)^{-\frac{1}{3}} e^{(2\gamma_o - 1)\left(1-\frac{V}{V_0}\right)} \tag{6.37}$$

where V is the specific volume and V_0, γ_0 are the reference specific volume and reference Gruneisen value respectively. If $T<T_m$ the electrical resistivity in the solid phase has the form [35]

$$\eta_S = (C_1 + C_2 T^{C_3})\left(\frac{V}{V_0}\right)^{2\gamma-1} \tag{6.38}$$

where C_1, C_2, C_3 are fitting constants, while

$$\gamma = \gamma_0 - (\gamma_0 - \frac{1}{2})(1 - \frac{V}{V_0}) \tag{6.39}$$

.

If $T>T_m$ the electrical resistivity in the liquid phase has the form [35]

$$\eta_L = (\eta_L)_{T_m}\left(\frac{T}{T_m}\right)^{C_4} \tag{6.40}$$

where $(\eta_L)_{T_m} = ke^{0.69 L_m/T_m}(\eta_s)_{T_m}$, k and C_4 are constants and L_m is the latent heat of melting. The parameter values of the Burgess model for the simulations are presented in section 6.3.8 for material properties.

6.3.8 Material properties

The values for copper electromagnetic, thermal, and mechanical properties have been adopted from existing literature values [2-5, 33-36]. In Table 6.2 the parameter values of Cu for the Grüneisen equation of state are presented [10].

C_0 [m/s]	S_1	α	γ
3940	1.5	0.47	1.99

Table 6.2 Parameter values of Cu [10] in the Grüneisen equation of state

In Table 6.3 the parameter values for the Johnson-Cook strength material model are shown, while in Table 6.4 are given the parameters for Cu used in the Johnson–Cook failure model [33, 34].

Parameter	Value	Unit	Parameter	Value	Unit
ρ_0	8910	Kg/m^3	C	0.025	-
G	4.6×10^{10}	Pa	$\dot{\varepsilon}_0$	1.00	s^{-1}
E	1.11×10^{11}	Pa	m	1.09	-
v	0.3406	-	T_{melt}	1356	K
A	9×10^{7}	Pa	T_{room}	300	K
B	2.92×10^{8}	Pa	C_p	383	J/kg K
n	0.31	-	$P_{cut\text{-}off}$	0.001	Pa

Table 6.3 Parameters of the Johnson-Cook strength material model for Cu [33, 34]

D_1	D_2	D_3	D_4	D_5
0.54	4.84	-3.03	0.014	1.15

Table 6.4 Failure damage parameters for Cu [33, 34]

In Table 6.5 the parameter values for the Burgess EOS are presented, while in Table 6.6 values of resistivity in relation to temperature are presented for simulations test cases where the Burgess EOS is not used. However, similar results for temperature and density are obtained compared to Burgess.

Parameter	Cu
V_0 (cm^3/g)	0.112
γ_0	2
T_{m0} (eV)	0.117
L_m (kJ/mol)	0.13
C_1	-4.12e-5
C_2	0.113
C_3	1.145
C_4	0.700
k	0.964

Table 6.5 Parameter of Burgess model for Cu [35]

Temperature (K)	Electrical Resistivity 10^{-8} (Ohm m)
300	1.72
400	2.4
500	3.09
600	3.79
700	4.51
800	5.26
900	6.04
1000	6.86
1100	7.72
1200	8.62
1300	9.59
1350	19.2
1500	19.5
1650	20.5
1800	21.5
2000	22.7
2250	24.3
2500	25.9
2750	27.5
3000	29.1
3250	30.7
3500	32.4
6000 [37]	89.1

Table 6.6 Electrical resistivity in relation to temperature for Cu [3, 37]

Moreover, temperature dependent properties of thermal expansion, thermal conductivity, and specific heat, as well as the latent heat of melting are also taken into account. These values are the same and are taken from Table 6.1, while for a temperature range of 1100 ^{o}C to 2600 ^{o}C the thermal expansion coefficient is considered to have the value of 10^{-4} 1/^{o}C according to Ref. [38].

6.4 3D Magnetohydrodynamic (MHD) modeling

In order to study the plasma expansion the results of density, displacement, and velocity from the multi-physics coupled analysis with LS-DYNA, when plasma based on temperature-related criteria is formed, are given as input in the single fluid MHD code PLUTO. As already mentioned, results of computer simulations and experiments are found that assume that the fiber Z-pinch consists of two different regions: a low density hot corona plasma and a dense core that remains for a long time during the discharge. Based on these studies a two-state condition that consists of a fluid region and a plasma region is considered in PLUTO.

PLUTO is a finite-volume/finite difference, shock-capturing code designed to integrate a system of conservation laws [39, 40]

$$\frac{\partial \boldsymbol{U}}{\partial t} = -\nabla T(\boldsymbol{U}) + S(\boldsymbol{U}) \tag{6.41}$$

where $\boldsymbol{U}$ represents a set of conservative quantities, $\boldsymbol{T(U)}$ is the flux tensor and $\boldsymbol{S(U)}$ defines the source terms. An equivalent set of primitive variables $\boldsymbol{V}$ is used for assigning initial and boundary conditions.

A structured mesh approach for the solution of the system of conservation laws is adopted. Flow quantities are discretized on a logically rectangular computational grid enclosed by a boundary and augmented with guard cells or ghost points in order to implement boundary conditions on a given computational stencil. When the computational grid is generated, a domain portion is defined by the global integer variables IBEG ≤ i ≤ IEND and JBEG ≤ j ≤ JEND, see Figure 6.9. Ghost cells are added outside the local computational domain to complete the stencil at the boundaries. The global variables NX1 and NX2 define the total number of points

(boundaries excluded) such that IEND - IBEG + 1 = NX1, JEND - JBEG + 1 = NX2. The total number of zones (boundaries included) is given by the global variables NX1_TOT and NX2_TOT.

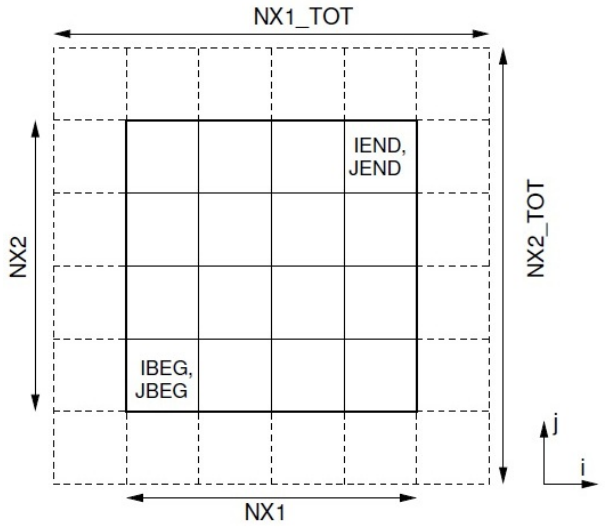

Figure 6.9 Computational grid in 2 dimensions with NX1 = NX2 = 4 and 1 ghost zone. Internal zones (solid boxed) are spanned by IBEG ≤ i ≤ IEND, JBEG ≤ j ≤ JEND. Dashed boxes represent boundary ghost zones

6.4.1 Ideal and resistive MHD equations

For the solution of ideal non-relativistic MHD equations, PLUTO solves the following system of conservation laws [41]

$$\frac{\partial}{\partial t}\begin{pmatrix} \rho \\ \boldsymbol{m} \\ E+\rho\Phi \\ \boldsymbol{B} \end{pmatrix} + \nabla\begin{pmatrix} \rho\boldsymbol{v} \\ \boldsymbol{m}\boldsymbol{v}-\boldsymbol{B}\boldsymbol{B}+Ip_t \\ (E+p_t+\rho\Phi)\boldsymbol{v}-\boldsymbol{B}(\boldsymbol{v}\boldsymbol{B}) \\ \boldsymbol{v}\boldsymbol{B}-\boldsymbol{B}\boldsymbol{v} \end{pmatrix} = \begin{pmatrix} 0 \\ -\rho\nabla\Phi+\rho\boldsymbol{g} \\ \boldsymbol{m}\boldsymbol{g} \\ 0 \end{pmatrix} \tag{6.42}$$

where ρ is the mass density, $\boldsymbol{m}=\rho\boldsymbol{v}$ is the momentum density, $\boldsymbol{v}$ is the velocity, $p_t=p+B^2/2$ is the total pressure (thermal and magnetic), $\boldsymbol{B}$ is the magnetic field, E_{IN} internal energy and E is the total energy density

$$E = \rho E_{IN} + \frac{m^2}{2\rho} + \frac{B^2}{2} \tag{6.43}$$

where an additional equation of state provides the closure $\rho E_{IN}=\rho E_{IN}(p,\rho)$. The source term on the right includes contributions from body forces and is written in terms of the (time-independent) gravitational potential Φ and the acceleration vector $\boldsymbol{g}$. Source term from body forces are neglected in our study. Moreover, it holds that

$$\nabla \cdot \boldsymbol{B} = 0, \tag{6.44}$$

while the induction equation may equivalently be written as

$$\frac{\partial \boldsymbol{B}}{\partial t} + \nabla \times \boldsymbol{E}_l = 0 \tag{6.45}$$

where $\boldsymbol{E}_l = -\boldsymbol{v} \times \boldsymbol{B}$ is the electric field.

The sets of conservative and primitive variables $\boldsymbol{U}$ and $\boldsymbol{V}$ are given by $\boldsymbol{U}= (\rho, \boldsymbol{m}, E, \boldsymbol{B})^{\mathrm{T}}$, $\boldsymbol{V}= (\rho, \boldsymbol{v}, p, \boldsymbol{B})^{\mathrm{T}}$ and the primitive form of the Equations 6.42 has the form

$$\begin{aligned}
&\frac{\partial \rho}{\partial t} + \boldsymbol{v}\nabla\rho + \rho\nabla\boldsymbol{v} = 0 \\
&\frac{\partial \boldsymbol{v}}{\partial t} + \boldsymbol{v}\nabla\boldsymbol{v} + \frac{1}{\rho}\boldsymbol{B}\times(\nabla\times\boldsymbol{B}) + \frac{1}{\rho}\nabla p = -\nabla\Phi + \boldsymbol{g} \\
&\frac{\partial p}{\partial t} + \boldsymbol{v}\nabla p + \rho c_s^2 \nabla\boldsymbol{v} = 0 \\
&\frac{\partial \boldsymbol{B}}{\partial t} + \boldsymbol{B}(\nabla\boldsymbol{v}) - (\boldsymbol{B}\nabla)\boldsymbol{v} + (\boldsymbol{v}\nabla)\boldsymbol{B} = 0
\end{aligned} \tag{6.46}$$

For resistive MHD equations magnetic field dissipation is modeled by introducing the resistivity tensor η so that the electric field is $\boldsymbol{E}_l = -\boldsymbol{v} \times \boldsymbol{B} + \eta \boldsymbol{j}$, where $\boldsymbol{j} = \nabla \times \boldsymbol{B}$ is the current density. The induction and energy equations from Equation 6.42 gain extra terms on the right hand sides

$$\begin{aligned}
&\frac{\partial \boldsymbol{B}}{\partial t} + \nabla\times(-\boldsymbol{v}\times\boldsymbol{B}) = -\nabla\times(\eta\boldsymbol{j}) \\
&\frac{\partial E}{\partial t} + \nabla[(E+p_t)\boldsymbol{v} - \boldsymbol{B}(\boldsymbol{v}\boldsymbol{B})] = -\nabla[(\eta\boldsymbol{j})\times\boldsymbol{B}]
\end{aligned} \tag{6.47}$$

.

Similarly, the primitive form of the internal energy equation modifies to

$$\frac{\partial p}{\partial t} + \boldsymbol{v}\nabla p + \rho c_s^2 \nabla \boldsymbol{v} = (\Gamma - 1)(\eta \boldsymbol{j})\boldsymbol{j} \tag{6.48}$$

where $\Gamma = c_p/c_v$ the ratio of specific heats. The resistive tensor η is assumed to be diagonal with components $\eta = diag(\eta_{x1}, \eta_{x2}, \eta_{x3})$.

6.4.2 Computational approach, geometry and meshing

Numerical integration of the conservation law, Equation 6.41, is achieved through shock-capturing schemes using the finite volume (FV) formalism where volume averages evolve in time. These methods are comprised of three steps: an interpolation routine, followed by the solution of Riemann problems at zone edges, and a final time evolution stage. With respect to interpolation that sets the spatial order of integration, piecewise Total Variation Diminishing TVD linear interpolation is applied to primitive variables. It is 2nd order accurate in space, while stencil is 3 point wide. The solver used for flux computation in our study is a Lax-Friedrichs scheme. Moreover, with respect to time evolution, second order Total Variation Diminishing Runge-Kutta is used to advance the solution from time t_n to the next step time t_{n+1} [39-41]. For more details see Appendix D.

Polar cylindrical coordinates (r, φ, z) are considered for the geometry of the problem. The half and full length of the wire (15.2 mm) is modeled for different test cases. With respect to the 3D grid creation, discretization that ranges from 4-8 μm is considered along the radial and azimuthal direction, while a discretization of 2-4 μm is considered for the vertical direction for the different investigated test cases. The whole grid domain has a number of cells that ranges from 3×10^6-12×10^6. In Figure 6.10 a characteristic grid of the whole domain is depicted, visualized using the open source software VisIt 2.10.0, which is a distributed, visualization tool for visualizing data defined on two and three dimensional structured and unstructured meshes [42]. For the simulation, the initial plasma cylindrical wire is assumed to be four times smaller than the radius of the whole domain.

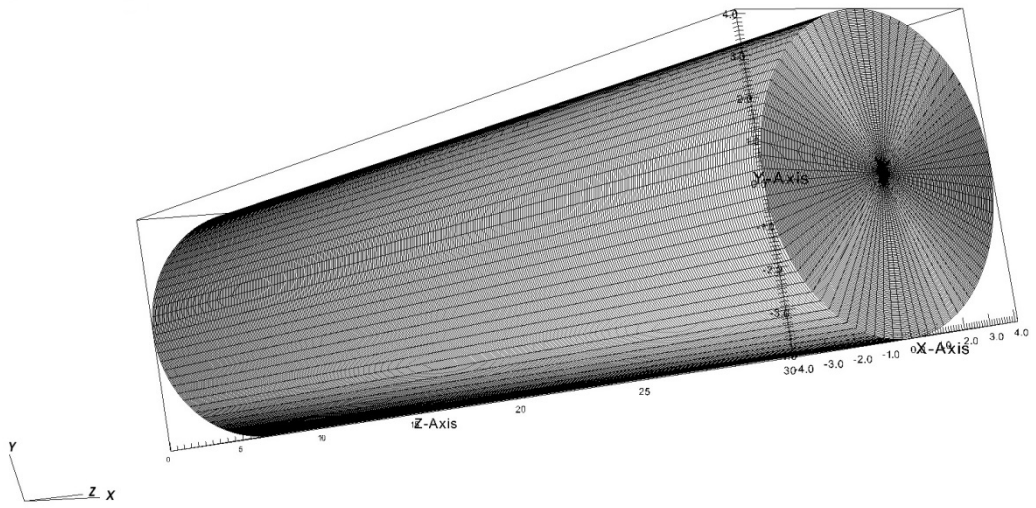

Figure 6.10 Grid of the whole domain in VisIt

6.4.3 Initial and boundary conditions

As previously mentioned, a two-state condition that consists of a fluid region and a plasma region is considered as initial approach in PLUTO. An ideal gas equation of state is considered as well as Spitzer conductivity. The data of density distribution, initial velocity when plasma is formed from LS DYNA, as well as the observed radius instabilities, that will be mentioned in detail in Chapter 7, are given as input data to PLUTO. Three regions are initially considered; a cylindrical fluid region, a cylindrical plasma region, and a cylindrical vacuum region.

For initial conditions inside the cylindrical fluid region, the initial density distribution is given from the density distribution of LS DYNA at the last time step of its solution. The same holds for the initial value of radial velocity. The initial pressure follows a parabolic distribution $P=P_0\cdot(r_1-r^2/r_0^2)$, where r_1 is the fluid radius and r_0 is the plasma plus fluid radius, while the magnitude of the magnetic field in the azimuthal direction is given by $B_\Theta=B_0\cdot r$, where r is the radius that varies. Inside the plasma region, density and pressure follow a parabolic distribution, of the form $a=a_0\cdot(1-r^2/r_0^2)$, while the initial value for radial velocity is given by LS DYNA data, and the magnitude of the magnetic field is the same with the one for the fluid region. Outside the plasma region initial pressure and velocity are considered to be zero, the magnitude of the magnetic field in the azimuthal direction is given by $B_\Theta=B_0\cdot r_0/r$,

while the density is 2-3 orders lower so that is considered as vacuum. In Figure 6.11 the magnitude of the magnetic field B_Θ is depicted.

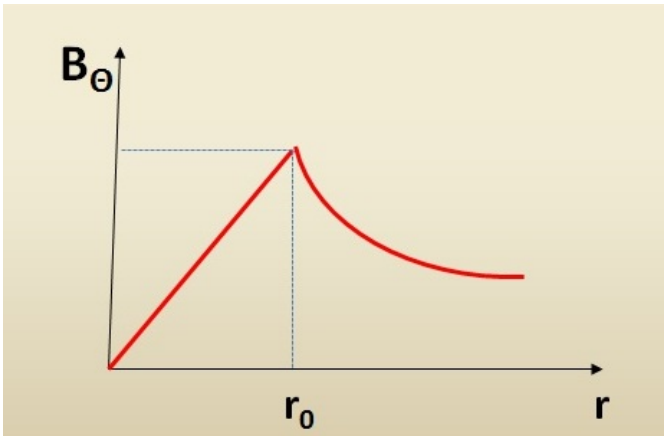

Figure 6.11 Magnitude of the magnetic field B_Θ inside and outside plasma region

Ampere's law is used to calculate the maximum magnetic field induction for radius r_0 and maximum current I_0 and it holds, $B_0 = \frac{\mu_0 I_0}{2\pi r_0}$, while the maximum Alfvèn velocity is $u_0 = \frac{B_0}{\sqrt{\mu_0 \rho_0}}$ for density ρ_0. Moreover, the characteristic time is given by $t_0 = \frac{r_0}{u_0}$. It is noteworthy that PLUTO works with dimensionless units. All quantities can be set from Gaussian units to non-dimensional PLUTO units as long as three fundamental quantities are set to be equal to unit: B_0=1.0, r_0=1.0, ρ_0=1.0.

With respect to the ideal equation of state, the ratio of specific heats $\Gamma = c_p/c_v$ of an ideal gas is constant and the internal energy E_{IN} can be written as

$$\rho E_{IN} = \frac{p}{\Gamma - 1} \tag{6.49}$$

Moreover plasma's resistivity can be estimated from Spitzer's formula [43]

$$n = \frac{\pi \cdot Z \cdot e^2 \cdot m \cdot \ln \Lambda}{(4\pi\varepsilon_0)^2 (k_b T)^{3/2}} \tag{6.50}$$

where m is the mass of an electron, $\ln\Lambda$ Coulomb's algorithm, k_b Boltzmann constant, ε_0 vacuum permittivity, e charge of electron and Z the ion charge state. However, PLUTO works with diffusivity, where $n_d=n/\mu_0$ (S.I) or $n_d=n\cdot c^2/4\pi$ (Gauss).

With regard to the boundary conditions assigned, in the physical ghost zones of the computational domain outflow conditions are specified. Assuming that q is a scalar quantity and n is the coordinate direction orthogonal to the boundary plane, zero gradient across the boundary is considered, i.e.:

$$\frac{\partial q}{\partial n}=0,\frac{\partial \mathbf{u}}{\partial n}=0,\frac{\partial \mathbf{B}}{\partial n}=0 \quad . \tag{6.51}$$

References

[1] Jordan, Edward Conrad, *Electromagnetic Waves and Radiating Systems*, Prentice Hall, 1968.

[2] A. Monnier, B. Froidurot, C. Jarrige, P. Teste and R. Meyer, A Mechanical, Electrical, Thermal Coupled-Field Simulation of a Sphere-Plane Electrical Contact, *IEEE Transactions on components and packaging technologies* **30**, 787-795 (2007).

[3] R. A. Matula, Electrical resistivity of Copper, Gold, Palladium and Silver, *J. Phys. Chem. Ref. Data* **8**, 1147 (1979).

[4] F. P. Incropera, D. P Dewitt, *Fundamentals of Heat and Mass Transfer*, Second Edition.

[5] *Handbook of Chemistry and Physics*, First Edition, CRC Press, 12 - 108.

[6] LS-DYNA Theory Manual, LSTC.

[7] L. E. Malvern, *Introduction to the Mechanics of a Continuous Medium*, Prentice Hall, Englewood Cliffs, New Jersey, 1969.

[8] K. Nagayama, *Introduction to the Gruneisen Equation of State and Shock Thermodynamics*, Kindle Edition (2011).

[9] E. B. Royce, *GRAY, a three-phase equation of state for metals*, UCRL-51121, Lawrence Livermore Laboratory, 1971.

[10] D. J. Steinberg, *Equation of State and Strength Properties of Selected Materials, Lawrence Livermore National Laboratory*, UCRL-MA-106439, (1996).

[11] K. S. Holian, *T-4 Handbook of Material Properties Data Bases*, vol: Equation of State, LA-10160-MS, 1984.

[12] M. Scapin, Shock-wave and high strain-rate phenomena in matter: modeling and applications, PhD thesis 2013.

[13] G. R. Johnson and W. H. Cook, Fracture characteristics of three metals subjected to various strains, strain rates, temperatures and pressures, *Eng. Fract. Mech.* **21**, 31-48 (1985).

[14] G. R. Cowper and P. S. Symonds, 1952, *Strain hardening and strain rate effects in the impact loading of cantilever beam*, Brown University Div of Appl. Mech. Report no 28.

[15] D. J. Steinberg and C. M. Lund, A constitutive model for strain rates from 10^{-4} to 10^{6} s^{-1}, *Journal de physique Symposium* C3 **49**, 433-440 (1988).

[16] F. J. Zerilli and R. W. Armstrong, Dislocation-mechanics-based constitutive relations for material dynamics calculations, *J. Appl. Phys.* **61**, 1816 (1987).

[17] I. Caldichoury and P. L'Eplattenier, *EM theory manual*, LSTC, Livermore, 2012.

[18] P. L'Eplattenier, G. Cook, C. Ashcraft, M. Burger, A. Shapiro, G. Daehn and M. Seith, Introduction of an Electromagnetism Module in LS-DYNA for Coupled Mechanical-Thermal-Electromagnetic Simulations, *9th International LS-DYNA Users conference*, Dearborn, Michigan, June 2005.

[19] P. L'Eplattenier, G. Cook, C. Ashcraft, M. Burger, J. Imbert and M. Worswick, Introduction of an Electromagnetism Module in LS-DYNA for Coupled Mechanical-Thermal-Electromagnetic Simulations, *Steel Research Int.* **80**, 351-358 (2009).

[20] J. Imbert and M. Worswick, Electromagnetic reduction of a pre-formed radius on AA 5754 sheet, *J. Mater. Process. Technol.* **211**, 896–908 (2011).

[21] J. Jin, *The Finite Element Method in Electromagnetics*, Wiley, 1993.

[22] J. Shen, *Computational Electromagnetics Using Boundary Elements, Advances In Modelling Eddy Currents*, *Topics in Engineering* Vol 24, Series Eds: C. A. Brebbia and J. J. Connor, Southampton and Boston: Computational Mechanics Publications, 1995.

[23] J. C. Nedelec, A New Family of Mixed Finite Elements in R3, *Num. Math*. **50**, 57-81 (1986).

[24] P. Castillo, R. Rieben and D. White: FEMSTER: An object oriented class library of discrete differential forms. In *Proceedings of the 2003 IEEE International Antennas and Propagation Symposium*, volume 2, pages 181-184, Columbus, Ohio, June 2003.

[25] Z. Ren and A. Razek: Computation of 3-D electromagnetic field using differential forms based elements and dual formulations, *International Journal of Numerical Modeling: Electronic Networks, Devices and Fields* **9**, 81-98 (1996).

[26] A. B. Shapiro, *TOPAZ3D - A Three Dimensional Finite Element Heat Transfer Code*, University of California, Lawrence Livermore National Laboratory, Report UCID-20481 (1985).

[27] G. Le Blanc, J. Petit, P. Chanal et al., Modelling the dynamic magnetothermomechanical behavior of materials using a multi-phase EOS, *7th European LS-DYNA Conference*, 2009.

[28] G. Le Blanc et al., Ramp wave compression in a copper strip line: comparison between MHD numerical simulations (LS-DYNA) and experimental results (GEPI device), *10th International LS-DYNA Conference*, Dearborn, Michigan, 8-10 June 2008.

[29] ANSYS Autodyn User Manual, Release 13.0, ANSYS Inc., 2010.

[30] F. Q. Jing, *Guide of experimental equation of state*, Beijing: Science Press; 1999.

[31] A. W. DeSilva and J. D. Katsouros, Measurement of the Electrical Conductivity of Metals in the Vicinity of the Critical Point, *International Journal of Thermophysics* **20**, 1267-1277 (1999).

[32] G. I. Kerley, *Equation of State for Copper and Lead*, KTS02-1, 2002.

[33] M. Scapin, L. Peroni and A. Dallocchio, Effects induced by LHC high energy beam in copper structures, *Journal of Nuclear Materials* **420**, 463–472 (2012).

[34] M. Scapin, L.Peroni and A. Dallocchio, Damage evaluation in metal structures subjected to high energy deposition due to particle beams, *Journal of Physics: Conference Series* **305**, 012062 (2011).

[35] T. J. Burgess, Electrical resistivity model of metals, *4th International Conference on Megagauss Magnetic-Field Generation and Related Topics*, Santa Fe, NM, USA, 1986.

[36] G. R. Gathers, Thermophysical Properties of Liquid Copper and Aluminum, *International Journal of Thermophysics* **4**, 209-226 (1983).

[37] M. P. Desjarlais, Practical Improvements to the Lee-More Conductivity Near the Metal-Insulator Transition, *Contributions to Plasma Physics* **41**, 267–270 (2001).

[38] M. Kumari and N. Dass, Temperature dependence of density and thermal expansion in some liquid metals, *Journal of Non-Crystaline Solids* **156-158**, 417-420 (1993).

[39] A. Mignone, G. Bodo, S. Massaglia, T. Matsakos, O. Tesileanu, C. Zanni and A. Ferrari, PLUTO: A Numerical code for computational Astrophysics, *Astrophysical Journal Supplement* **170**, 228-242 (2007).

[40] A. Mignone, C. Zanni, P. Tzeferacos, B.van Straalen, P. Colella and G. Bodo, *Astrophysical Journal Supplement* **198**, 7 (2012).

[41] PLUTO v. 4.1, User's guide, 2014.

[42] VisIt user's manual, October 2005.

[43] L. Spitzer and R. Haem, Transport Phenomena in a Completely Ionized Gas, *Physical Review* **89**, 977-981 (1953).

Chapter 7

7. Numerical results and comparison with experiments

In this Chapter the numerical results of the developed FE models are presented, as well as a description of the experimental optical probing techniques that is used in combination with the numerical simulations, followed by a comparison and verification of numerical with experimental results.

7.1 Numerical results

In this section, numerical results using transient coupled finite element thermal-structural and electromagnetic-thermal-structural hydrodynamic analysis are presented.

7.1.1 Thermal-structural analysis results

Figure 7.1 illustrates typical numerical simulations for the 300 μm diameter wire with a length of 15.2 mm, which demonstrates that the wire begins to melt at 86 ns from the current start. The temperature distribution predicted by the 3D FEM model is also shown for a cross-section of the wire, where it can be observed that due to the skin depth effect temperature is higher on the outer part. Moreover, in Figure 7.2 the displacement distribution along the radial direction is depicted. The maximum expansion of the wire at this time is 1.1 μm. The result of expansion agrees well with experimental results, as it can be seen in the next section.

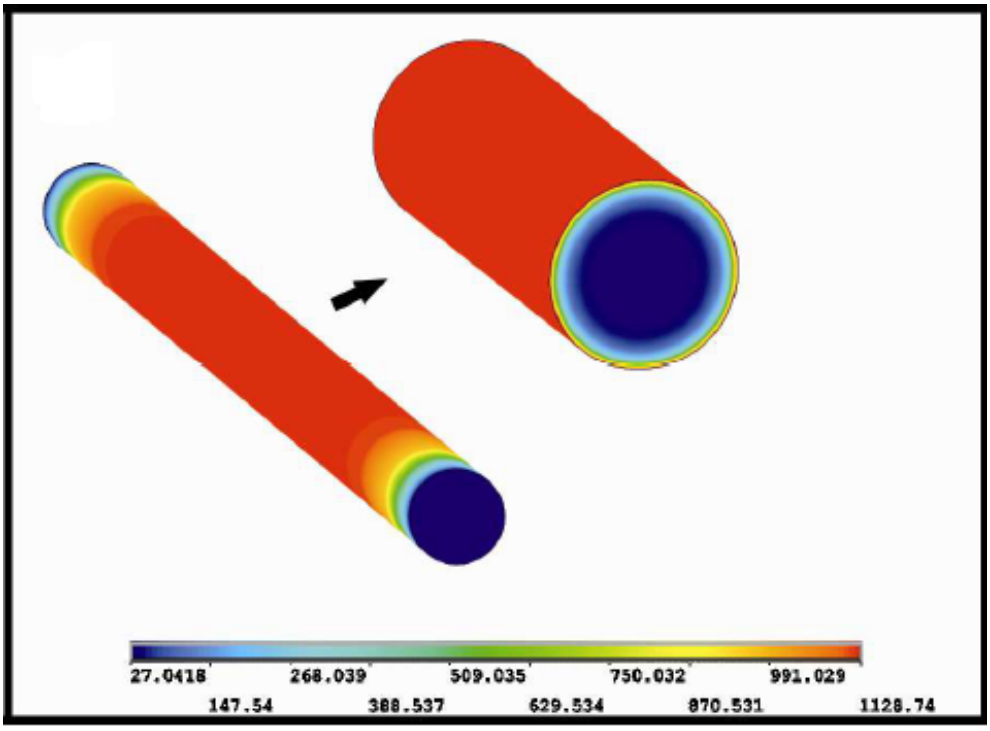

Figure 7.1 Predicted temperature distribution at 86 ns from the current start (at the right is the enlarged cross-section of the wire). The depicted chromatic scale corresponds to ^{o}C

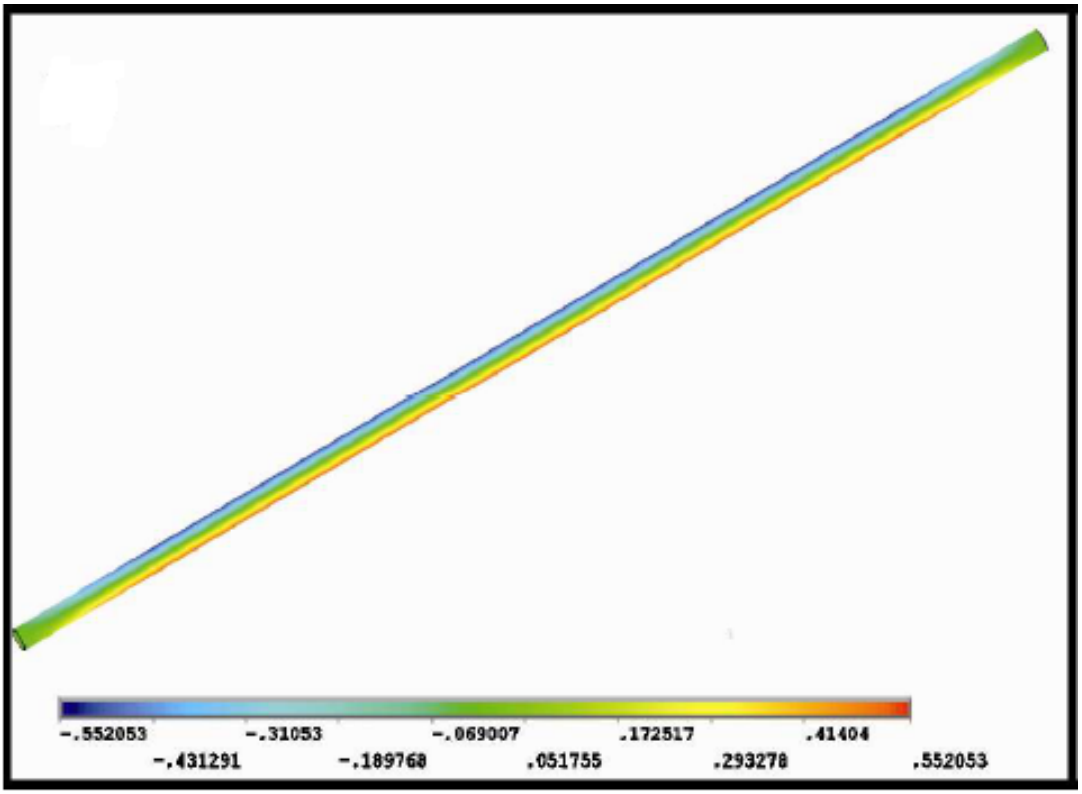

Figure 7.2 Predicted displacement distribution along the radial direction at 86 ns from the current start. The depicted chromatic scale corresponds to μm

However, due to the fact that the electromagnetic effects are not taken into account, due to the nonexistence of an EOS since the volume deformation is high and due to the need to study the elasto-plastic behavior of the material, an electromagnetic-thermal-structural-hydrodynamic analysis is carried out.

7.1.2 Electromagnetic-thermal-structural-hydrodynamic analysis results

A 15.2 mm Cu wire with radius of 0.15 mm is simulated in this transient electromagnetic-thermal-structural study. In the skin depth region, the pressure and temperature increase rapidly and the material could arrive at its melting temperature or vaporize faster than the remaining part of the wire. This part of the wire is characterized by higher temperatures and lower densities. The material response in this condition is correctly described using equation of state with higher energy limits and lower density limits. The hydrodynamic behavior of the material is more significant than the deviatoric. On the other hand, the core part of the wire is characterized by high values of plastic strain, strain-rate, lower temperatures, and higher densities. The role of the strength material model is significant here.

With regard to the chosen equations of state for the simulations, initially preliminary results are taken into account using Grüneisen equation of state for the whole volume of the wire. Next, the cross-section of the wire is divided into three regions, one corresponding to the skin depth (Region 3) and the others based on the preliminary results of temperature and density using Grüneisen equation of state (see Figure 7.3). In Region 1, where high stresses are observed and temperature change is not very high, Grüneisen equation of state is used. A dedicated interpolation is performed for regions 2 and 3 of the model. The variables' limits for temperature, density, and pressure for Regions 2 and 3 using multiphase SESAME equation of state for copper [1, 2] are set according to preliminary numerical simulations using Grüneisen equation of state. In order to obtain the correct interpolation a plot is created drawing the function $P=P(E)$ for each density calculating a value of slope. Then, the slopes are fitted by second order polynomial fitting obtaining the coefficients of the thermal part $P_T(\mu,E)$, while the curve P-μ at 5 K is interpolated to

obtain the coefficients of the cold curve $P_C(\mu)$. For region 2 the density is between 4000 and 10000 kg/m^3 and the temperature is between 5 and 20000 K [3], while for Region 3 the density is between 1000 and 10000 kg/m^3 and the temperature is between 5 and 20000 K. Therefore, each interpolation is performed limiting the range of interest of the entire tabular data in pressure, density and energy, as explained in Chapter 6. The parameters that are used for Regions 2 and 3 are summarized in Table 7.1. Johnson-Cook material model and Burgess resistivity EOS are also used.

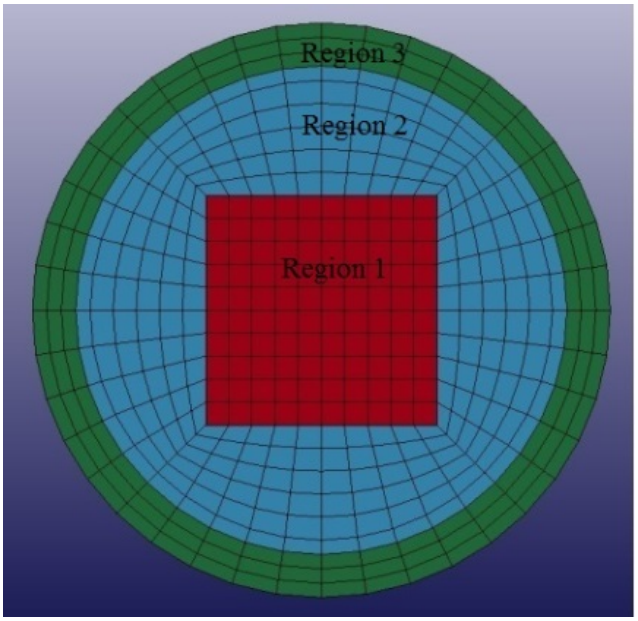

Figure 7.3 Regions of the model

Region 2	**C_0 (Pa)**	**C_1 (Pa)**	**C_2 (Pa)**	**C_3 (Pa)**	**C_4**	**C_5**	**C_6**
	-2.176×10^{8}	1.113×10^{11}	3.019×10^{11}	2.088×10^{11}	1.076	1.667	-0.039
Region 3	**C_0 (Pa)**	**C_1 (Pa)**	**C_2 (Pa)**	**C_3 (Pa)**	**C_4**	**C_5**	**C_6**
	-2.176×10^{8}	1.113×10^{11}	3.019×10^{11}	2.088×10^{11}	2	4.145	2.2

Table 7.1 Multiphase EOS parameters

In Figures 7.4-7.6 the temperature, density, and Von Mises stress distribution are illustrated for a cross-section of the wire 45, 90, 95 and 145 ns from current start respectively.

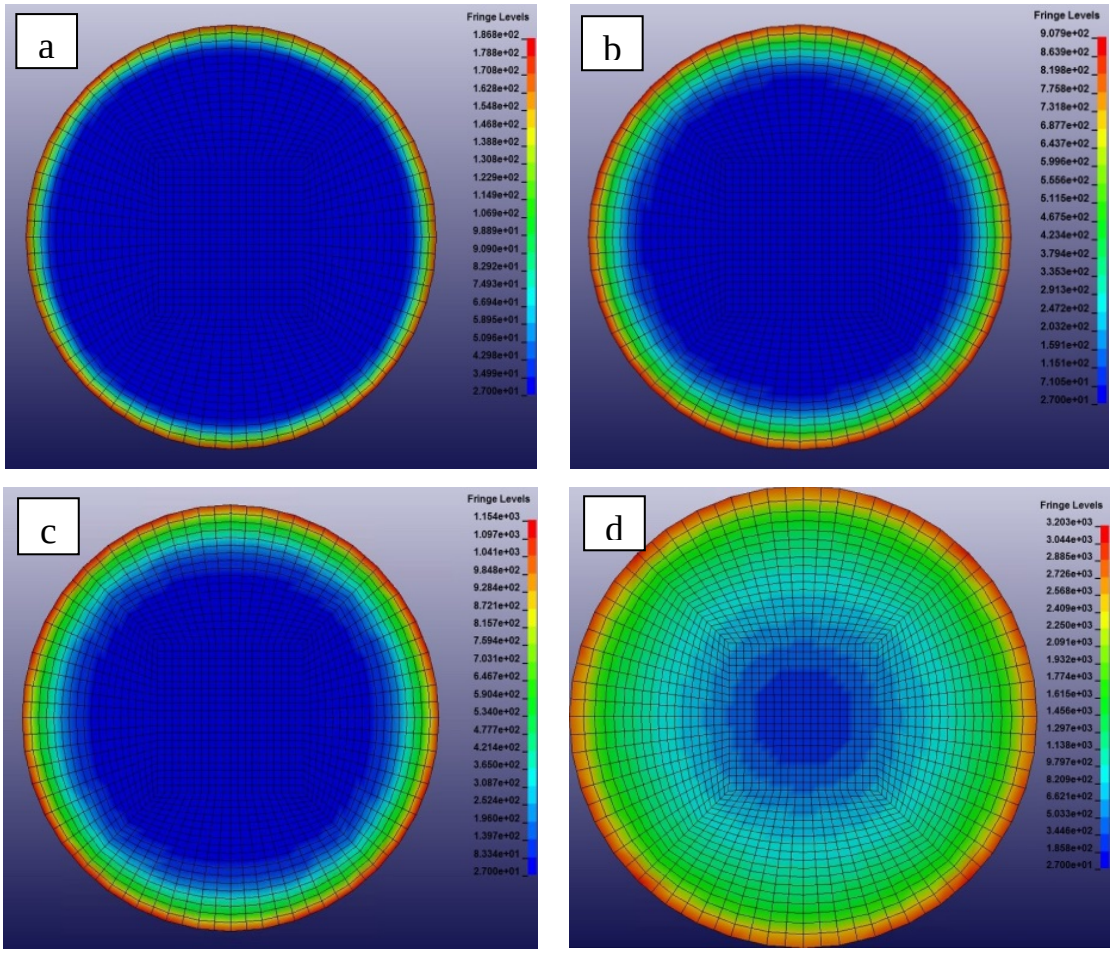

Figure 7.4 Temperature distribution (^{o}C) of a cross-section of the wire at a) 45 ns, b) 90 ns, c) 95 ns and d) 145 ns from current start

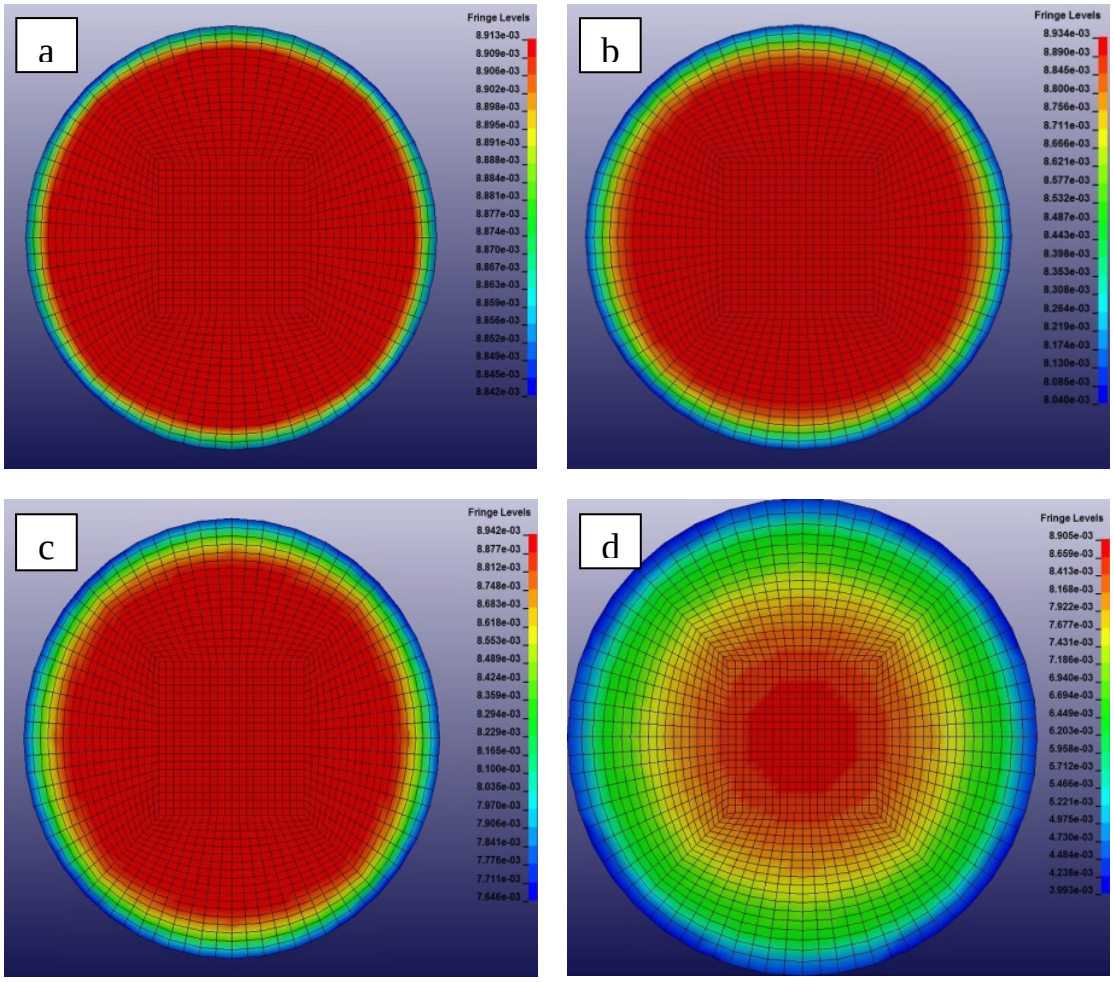

Figure 7.5 Density distribution (kg/cm^3) of a cross-section of the wire at a) 45 ns, b) 90 ns, c) 95 ns and d) 145 ns from current start

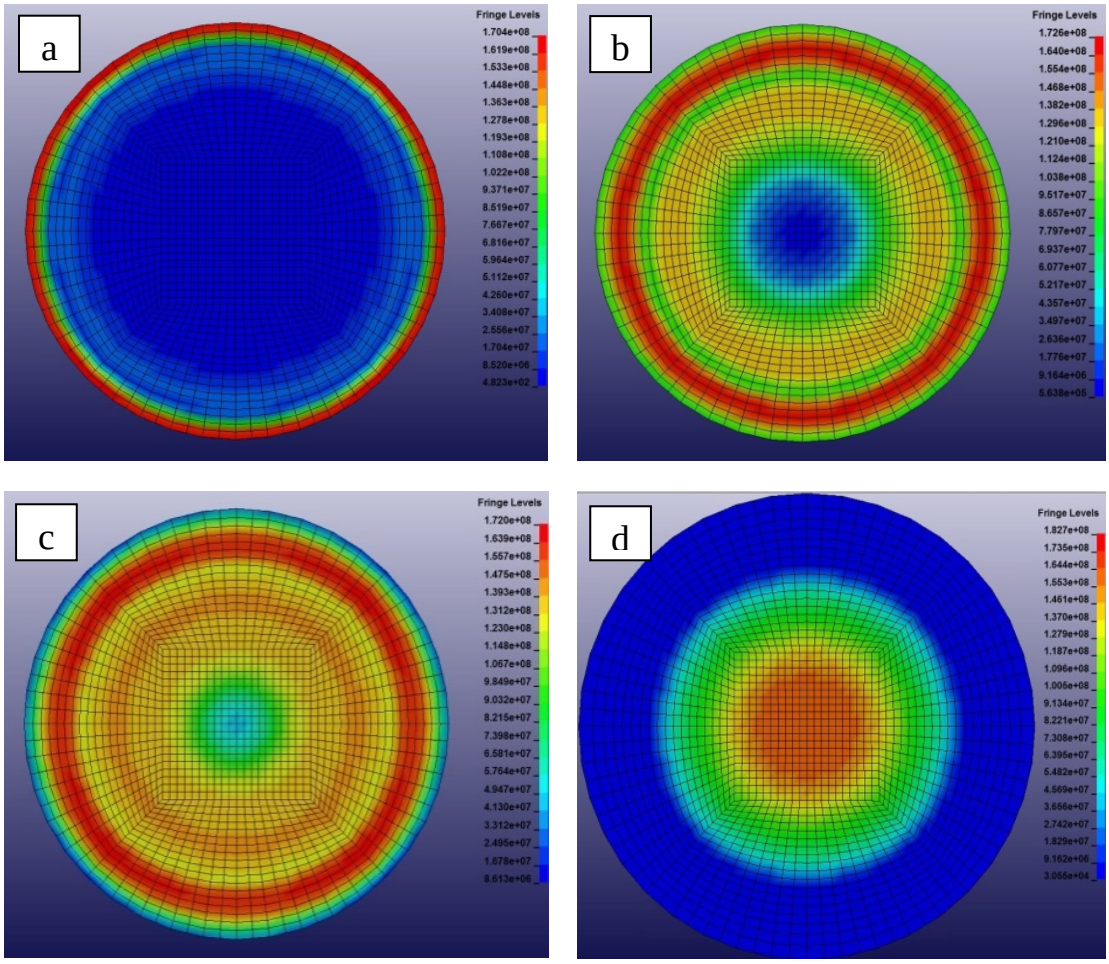

Figure 7.6 Von Mises stress (Pa) distribution of a cross-section of the wire at a) 45 ns, b) 90 ns, c) 95 ns and d) 145 ns from current start

At 45 and 90 ns the whole wire is in the thermoelastic regime, since maximum temperature is approximately 187 and 908 ^{o}C, while at 95 ns the outer part of the wire has reached temperature above the melting point (melting point of copper: 1085 ^{o}C). At 145 ns from current start the outer part of the wire has a maximum temperature of 3203 ^{o}C, higher than the boiling point of copper (boiling point of copper: 2560 ^{o}C). At 90 and 95 ns from current start compressive elastic stresses are observed with a direction towards the core of the wire. The Von Mises developed stresses increase in the central-core part of the wire, while they decrease in the outer, where the solid starts to behave like a fluid due to the increased temperatures above the melting point. Moreover, one can observe that maximum density in the core is higher than the initial

solid density (8913 Kg/m^3), due to the compression forces that act upon it, compressive stresses that react to thermal expansion and Lorentz force. At 145 ns the Von Mises stress is higher in the central-core part of the wire, while stress and density are lower in the outer part. The minimum density is 3993 kg/m^3. Moreover, in Figure 7.7 a Von Mises stress distribution is illustrated for a longitudinal cross-section of the wire, at 145 ns from current start. One can observe that the stresses are higher in the central part of the wire.

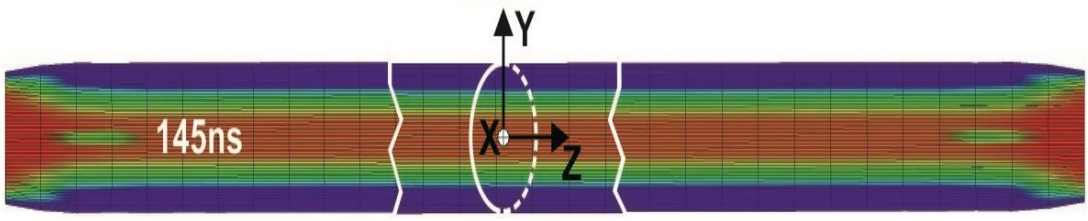

Figure 7.7 Von Mises stress distribution of a longitudinal cross section

In Figures 7.8 and 7.9 data of temperature and density time history are illustrated for different radial distances. The temperature of an element far from the core of the wire is higher than the temperature of the element closer to the core, while for the density it is lower as expected. For an element closer to the core of the wire (r=0.05 mm) one can observe that for approximately 60 ns density increases due to the existence of compressive stresses.

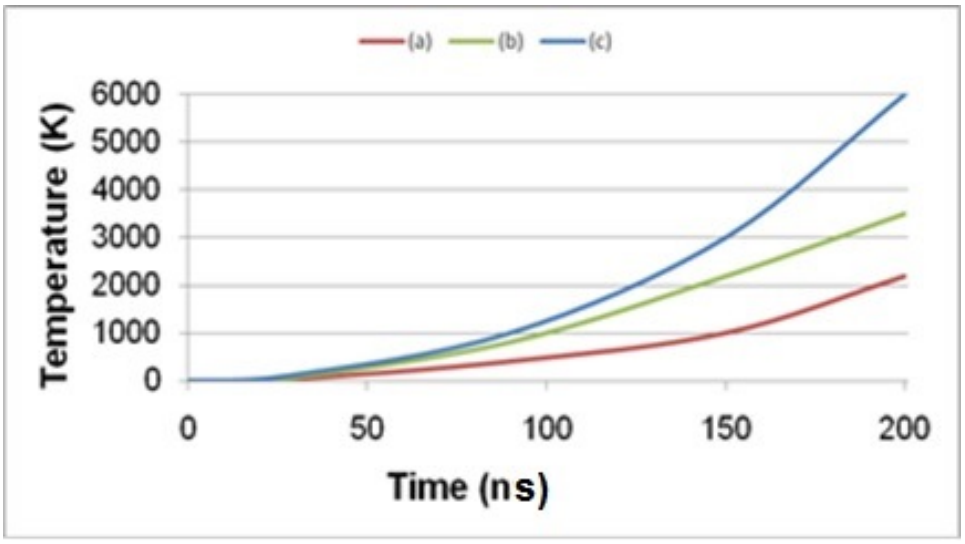

Figure 7.8 Temperature time history in three elements for different radial distances (a) r=0.05 mm; (b) r=0.1 mm; (c) r=0.15 mm

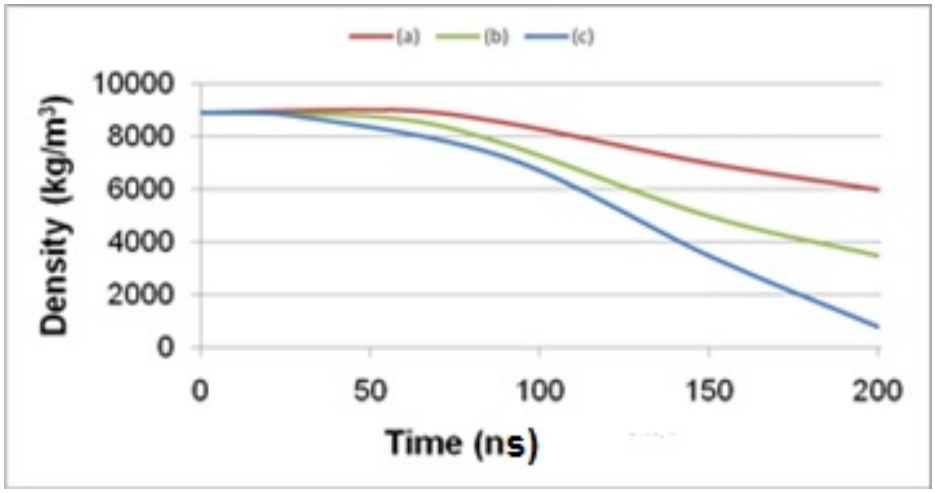

Figure 7.9 Density time history in three elements for different radial distances (a) r=0.05 mm; (b) r=0.1 mm; (c) r=0.15 mm

In Figure 7.10 the magnetic field and Lorentz force distribution for a cross-section of the wire 85 ns after current start is shown. The maximum magnetic field is approximately 8.8 T. Lorentz electromagnetic force has a maximum of 1832 N at the same temporal moment. Lorentz forces in x, y directions tend to compress the wire. Magnetic field x, y components have opposite directions than respective Lorentz force components.

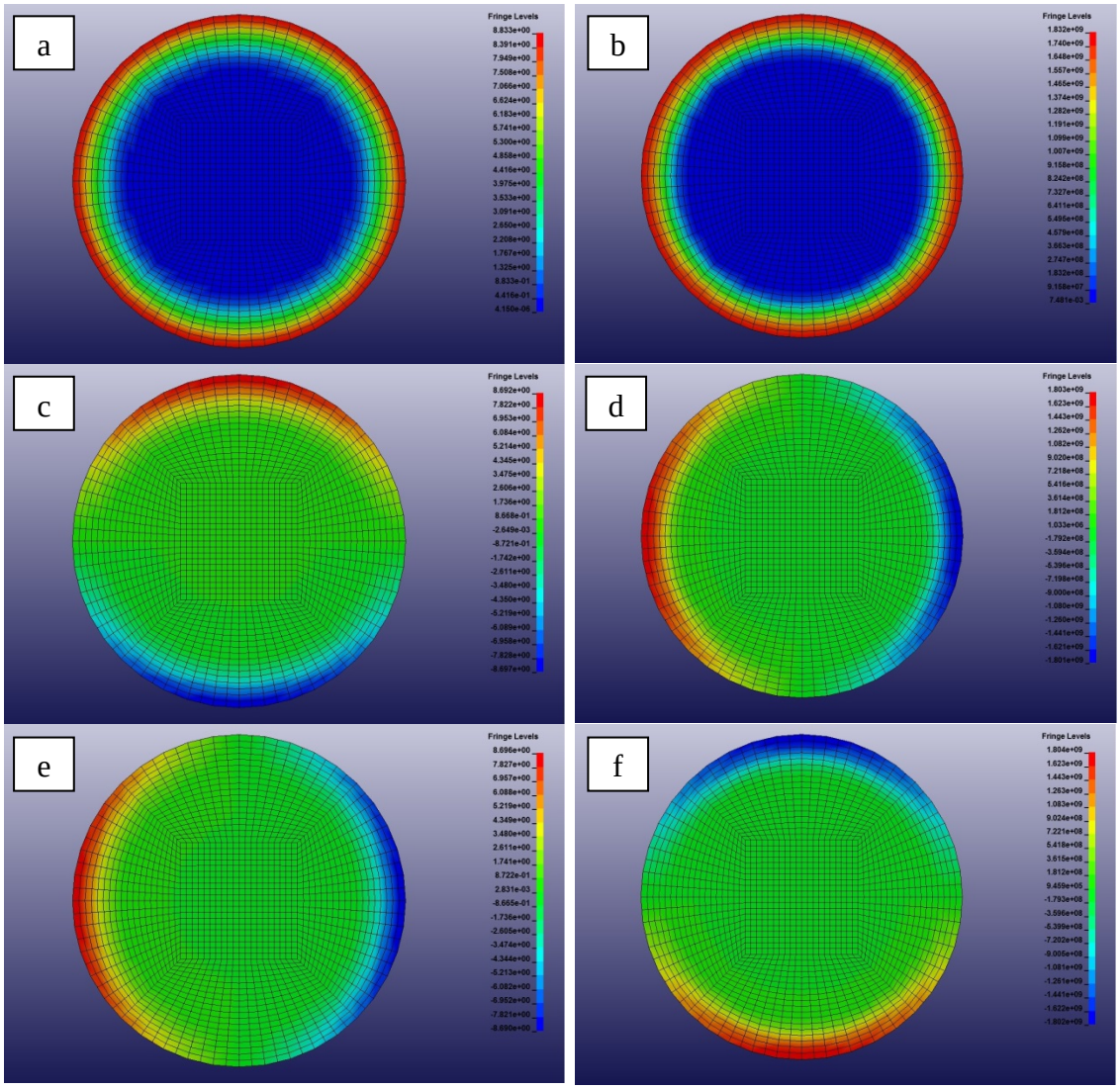

Figure 7.10 Distribution of: a) total Magnetic field B (in Tesla), c) B_x, e) B_y, b) Lorentz force (in $\times 10^{-6}$ N) d) L_x, f) L_y in a cross section of the wire 85 ns after current start in the thermoelastic regime

Furthermore, in Figure 7.11 results for stress and strain distribution are presented in a cross-section of the wire 85 ns after current start, in the thermoelastic regime.

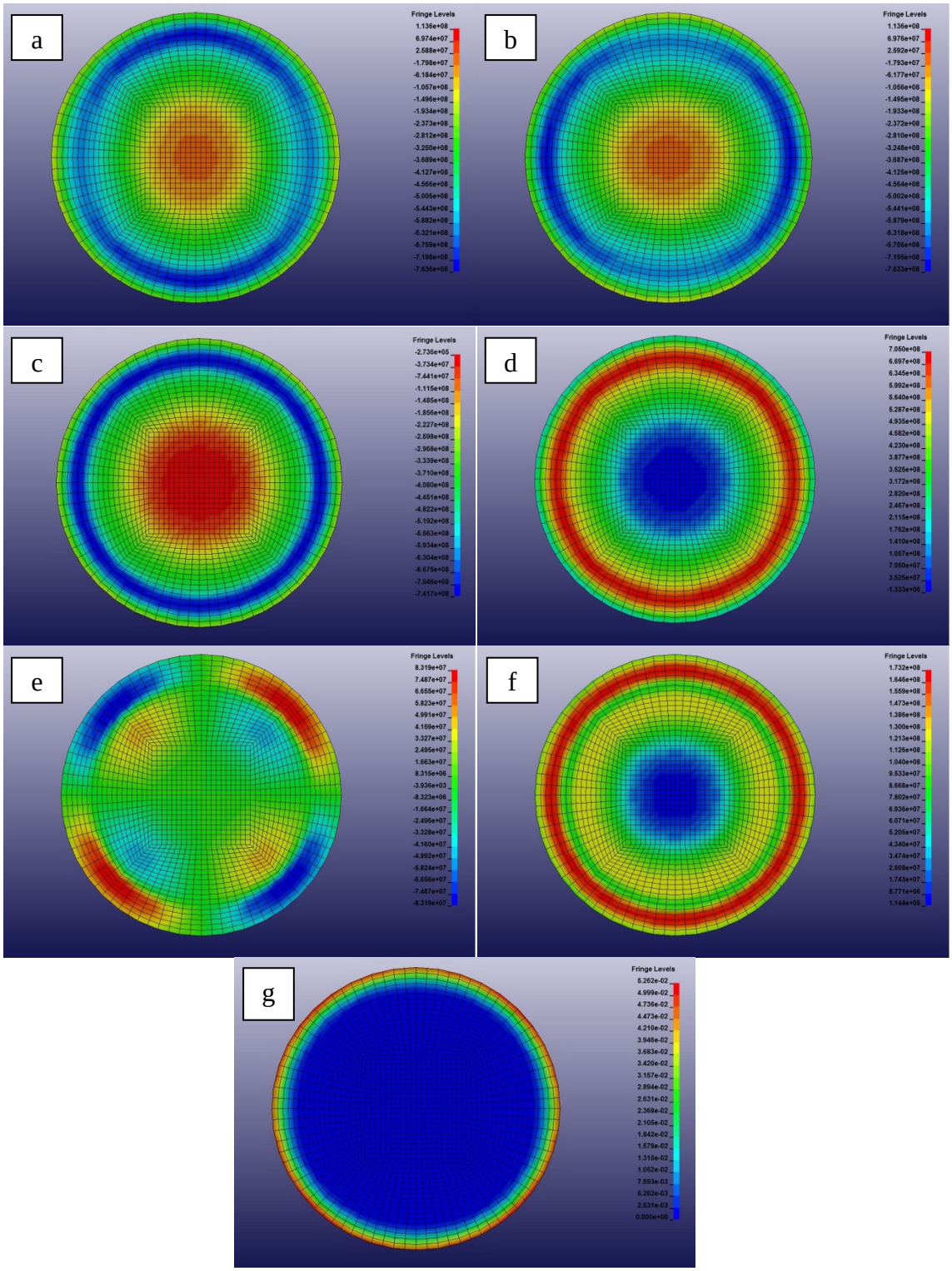

Figure 7.11 Distribution in Pa units of: a) *x*-stress, b) *y*-stress, c) *z*-stress, d) pressure, e) *xy* stress, f) Von Mises stress and g) strain non-dimensional quantity in a cross section of the wire 85 ns after current start, in the thermoelastic regime

7.2 Experimental validation methods

Laser probing diagnostics, such as shadowgraphic, schlieren, interferometric, and diffraction imaging techniques, have been used for the measurement of the wire dynamics at the initial stages of the explosion. The imaging of the Fraunhofer diffraction at the focus of a lens is employed as a method to determine the expansion of the wire at times before plasma formation [4]. Shadowgraph, schlieren, and interferometric imaging techniques are implemented in order to record the early times of the plasma formation.

Interferometry is used to determine the electron density distribution, since the refractive index is related to free electron density. The refractive index in a plasma is given by

$$\eta(r) = \left[1 - \frac{n_e}{n_c}\right]^{1/2} \tag{7.1}$$

where

$$\eta_c = \frac{\omega^2 m_e \varepsilon_0}{e^2} = 1.113 \times 10^{15} \lambda^{-2} (\mathrm{m}^{-3}) \tag{7.2}$$

is the cut-off density or critical density [5]. For $n_e < n_c$ the interferometer gives a measure of the phase difference between the beam, which has probed the plasma (main) and the reference beam. The difference in the phases between the main and reference beam can be approximated to be

$$\Delta\varphi = \frac{\omega}{2cn_c} \int n_e dl = 2.814 \times 10^{-15} \lambda \int n_e dl \,. \tag{7.3}$$

For a phase shift $\Delta\varphi = 2\pi$ the fringe shift is one. Thus, it is possible to obtain the fringe shift distribution as a function of radius. The electron density can then be evaluated by Abel inversion of the phase shift distribution [5].

Furthermore, shadowgraphy depends on the light-ray deviation, which is proportional to the refractive index gradient transverse to the beam [6].

Shadowgraphy is sensitive to the second spatial derivative of the plasma density, while the Schlieren technique is sensitive to the first derivative variations of the plasma refractive index.

Experiments are carried out using a Z-pinch pulsed powered device implemented in a mode of producing a peak current of 35 kA with a rise time (10%-90%) of 60 ns. The Z-pinch pulsed power device consists of a Marx bank of 600 J energy capacity, a water-filled pulse forming line (PFL) and a self-breaking SF6 spark-gap switch. The copper wire of 300 μm diameter and 15.2 mm length is placed in a vacuum chamber evacuated at 10^{-4} mbar. The wire is fixed by soldering it to the conical shaped copper electrodes. A V-dot probe measures the derivative of the voltage at the PFL and a Rogowski groove measures the derivative of the current passing through the wire with a fast digital oscilloscope.

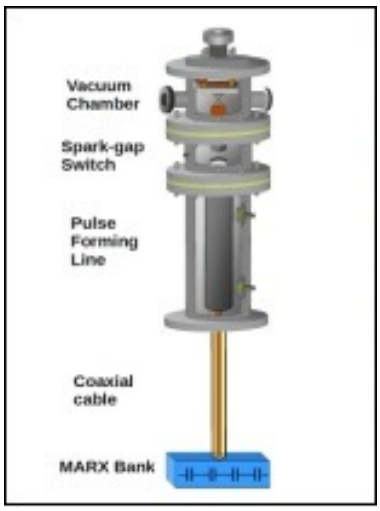

Figure 7.12 Pulsed powered Z-pinch device

The second harmonic of a SBS-compressed Nd:YAG, Q-switch laser (EKSPLA, SL312), with 150 ps pulse duration, is used for the shadowgraphic, schlieren, interferometric, and diffraction imaging laser probing techniques. This gives the ability of ns time resolved tracing of the explosion stages. In Figure 7.13 the electro-optical diagram of the experiment is presented.

A Mach-Zehnder interferometer in finite-fringe mode is developed and used for plasma density measurements. For the schlieren imaging a knife-edge is used at an orientation parallel to the wire at the focal length of the imaging lens, enabling to

distinguish the light deviation caused by plasma from that by the neutral Cu vapors [6]. The formation of coronal plasma is revealed from the bright light appeared at the same side of the wire as that the knife is placed [7]. Moreover, in Figure 7.14 the set-up for the optical laser probing techniques is presented.

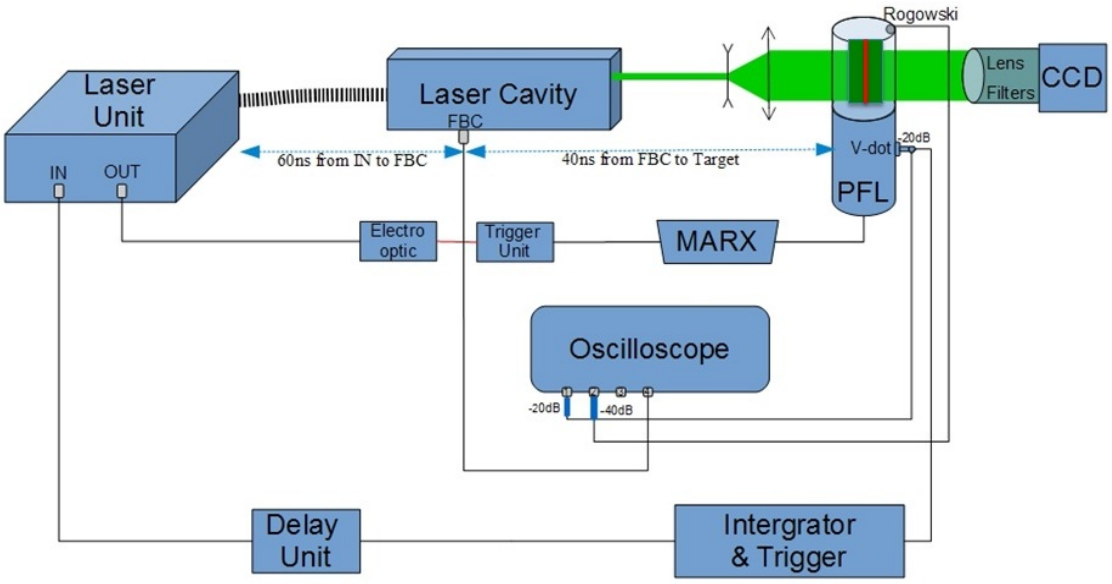

Figure 7.13 Electro-optical diagram of the experiment. Trigger signal from the laser control unit triggers the MARX bank, which provides a high voltage negative polarity output to PFL, and when it reaches the breakdown voltage of the spark-gap switch the current begins to flow through the wire to the anode

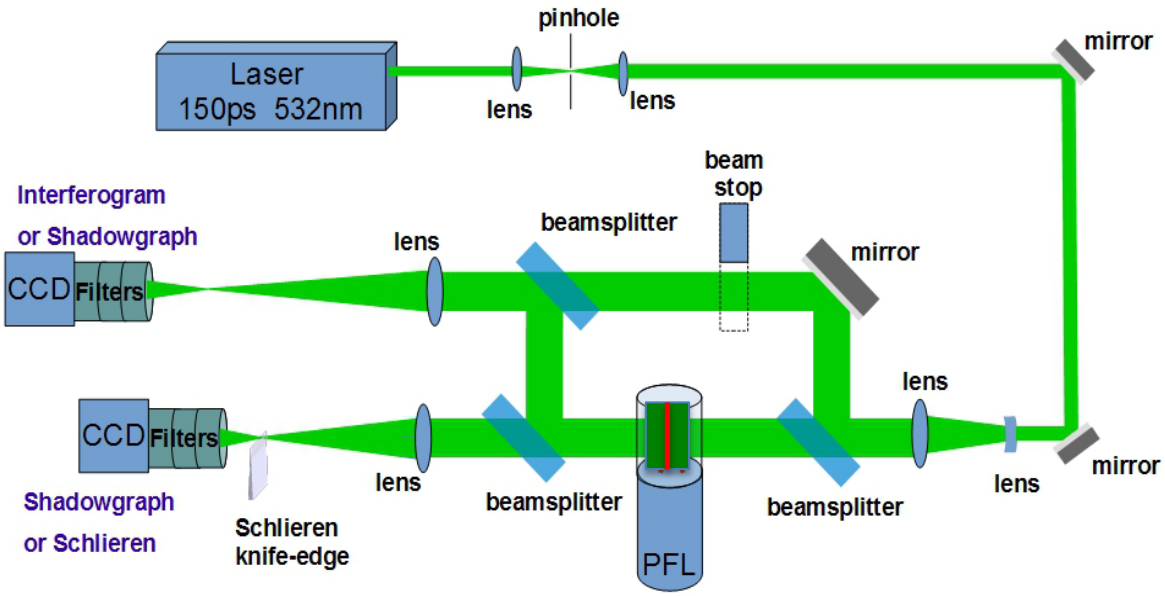

Figure 7.14 Optical laser probing techniques

7.3 Comparison and verification of simulation and experimental results

7.3.1 Comparison of numerical with experimental results before plasma creation

In order to investigate the wire diameter dynamics before plasma formation (solid or melted condition), a modified Fraunhofer diffraction method is implemented with high accuracy in measuring the wire width [4]. The fringes pattern (Fraunhofer diffraction pattern) at the focus of a lens is recorded for temporal instant predefined by the delay unit. The focal spot of the laser probe beam is shifted just out of the CCD's frame of the camera, in order to reveal the second and higher order fringes at the image. The line out of the image along the diffraction axis is used for the measurement of the wire's diameter and, consequently, the evaluation of the expansion at the time of the snapshot. The diameter is calculated by fitting a *sinc(x)* function at the line out plot along the fringes axis. Figure 7.15 illustrates the diffraction pattern of the measurement of the wire's diameter at 140 ns from the current start, just before plasma formation starts. At this time plasma has not yet been formed, as confirmed by simultaneously obtained interferogram. The measured diameter compared with the initial measurement shows an expansion of 7.4 (±0.6) μm. At that time the simulation gives an expansion of 7 (±0.2) μm, in Figure 7.16. An average radial expansion rate of 65 (±1) m/s results from experimental measurements, while a radial expansion rate of 60 m/s is computed in the simulations.

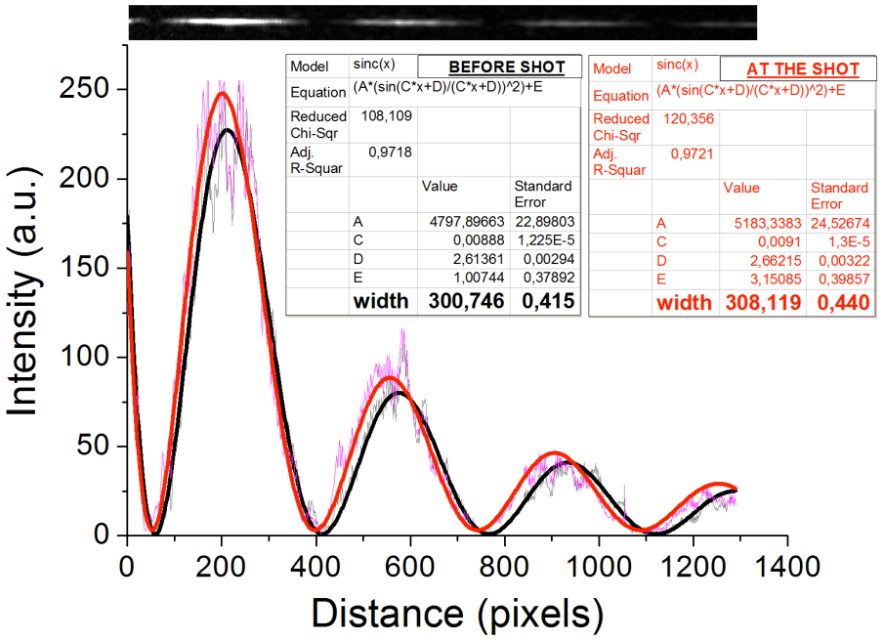

Figure 7.15 Laser probe diffraction pattern image (top) and the lineout intensity plot along the axis of the fringes (bottom) at 140 ns from the current start

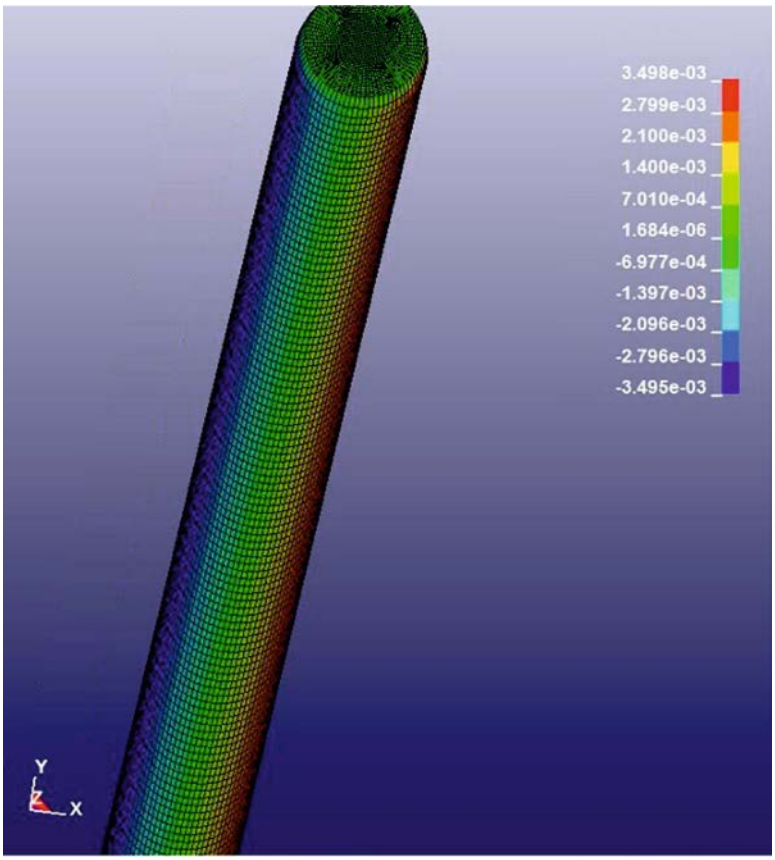

Figure 7.16 Displacement along the *x*-axis (mm) direction of the wire at 140 ns from the current start (FEM simulation)

In Figure 7.17 experimental and numerical results concerning the expansion of the wire's diameter for up to 140 ns after the current start are depicted, where satisfactory agreement is recorded. At 140 ns after initiation of the current flow the wire's maximum temperature on the outer region is 2400 ^{o}C below the copper's boiling point (2562 ^{o}C), according to FEM simulation.

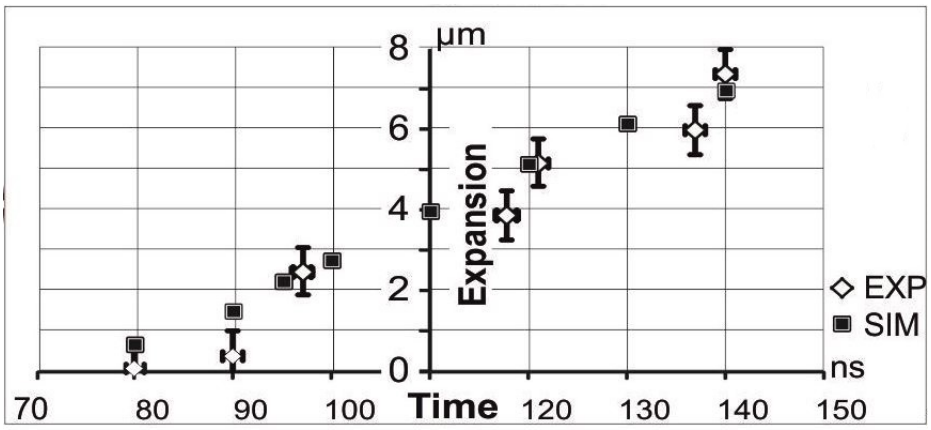

Figure 7.17 Comparison of experimental and numerical results with respect to wire's expansion

7.3.2 Comparison of numerical with experimental results in the plasma regime

In order to experimentally investigate the plasma formation at early times and to elucidate information about the initial time where the plasma formation starts, a series of shadowgraphic, schlieren, and interferometric images are taken at different times from the current start. The plasma formation time is measured to be about 200 ns±10 ns and it doesn't occur simultaneously along the wire. At a later time the corona plasma occupies all the wire's length. Figure 7.18 shows an instance of the coronal plasma at 200 ns from the current start. The upwards/downwards fringe shifts at the interferograms, as long as the left/right lighten at the schlieren images, is attributed at the plasma/vapors domination on the refractive index near the wire respectively. The coronal plasma surrounds the denser core where the probe laser beam cannot propagate, due to refraction in the steep plasma transverse density gradients. It should be pointed out here that, especially at early times, the formation of the coronal plasma can coexist with a neutral atomic gas surrounding the wire.

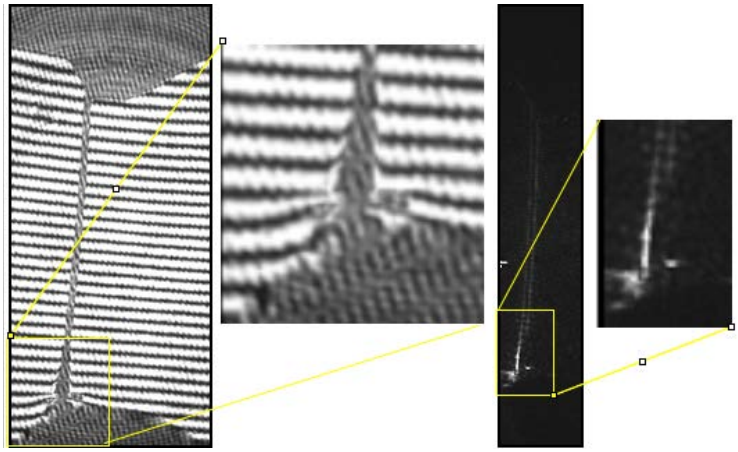

Figure 7.18 Interferograms and schlieren images from the initiation of coronal plasma forming at 200 ns

Simulation results in LS-DYNA show that a behavior similar to impulse response is observed at the ends of the wire before plasma formation in the thermoelastic regime. The imposed boundary conditions, in combination with the Joule heating phenomenon, the electromagnetic force, and the compressive stresses, are responsible for this impulse, which can be assumed as the reason for the creation of the instabilities. In more detail, the wire's ends are fixed and the wire is initially straight. The metallic material tends to expand, but the clamped ends do not allow the stress to relax. In the vertical *Z* direction of the wire, the fixed supports provide reaction forces to keep the beam at the initial length. These reaction forces result in a net compressive stress on the wire. During this initial stage, when sufficient accumulated energy in the wire (due to the joule heating effect and the electromagnetic force) is released in the form of compressive stress, elastic stress waves are induced. The wire deforms at its end and buckles owing to small disturbances, while high compressive stress converts into high tensile stresses. In Figure 7.19 this impulsive response at the end of the wire is depicted 90 ns after current start. This behavior can be further linked to experimental results, which show that plasma is formed at the bottom of the wire.

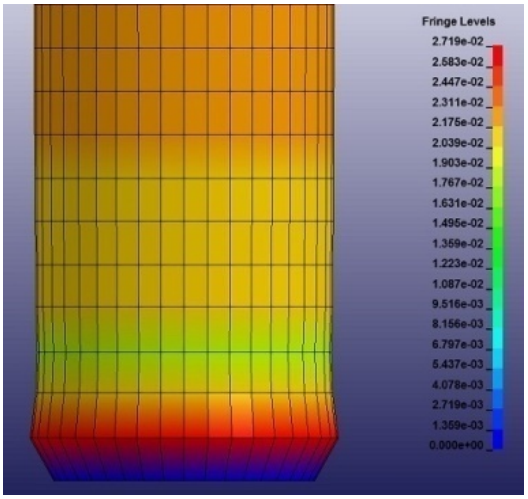

Figure 7.19 Impulsive response at the end of the wire

As the time goes by these instabilities are enhanced in amplitude but retain the same frequency until plasma formation, which is assumed, based on temperature criteria, to occur at 6000 ^{o}C 200 ns after current start [6, 7]. In Figure 7.20 the temporal evolution of observed radius instabilities along the half wire length from solid to plasma phase is illustrated. The dominant axial wavelengths of instabilities are computed to be approximately 200-250 μm. The data at 200 ns are used as input to PLUTO MHD code.

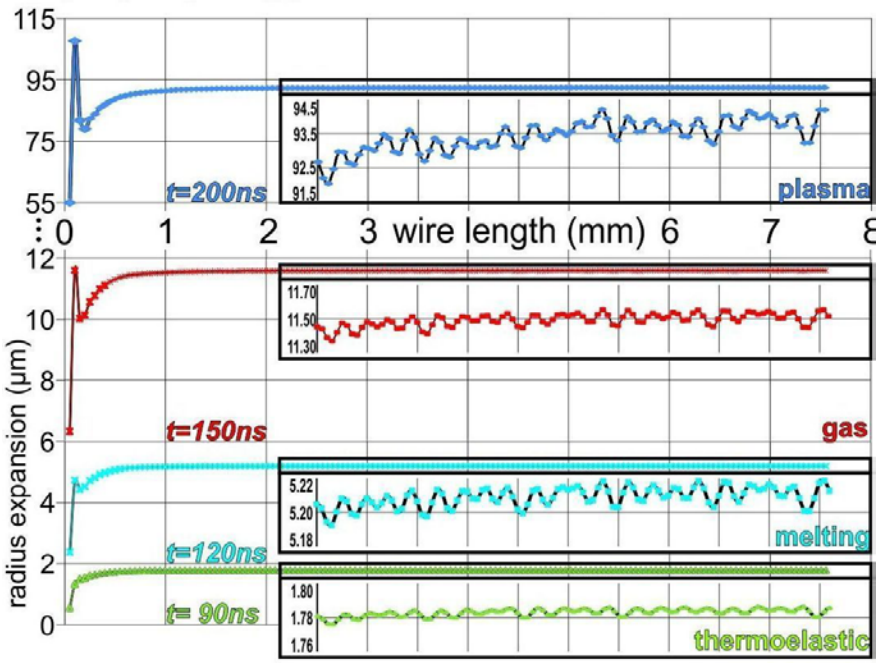

Figure 7.20 Temporal evolution of observed radius instabilities along the half wire length from solid to plasma phase

Moreover, in Figure 7.21 the deformation of the created instabilities at the end of the wire at 120 ns and 200 ns from current start is depicted. The maximum observed deformation at 200 ns is about two times higher than at 120 ns.

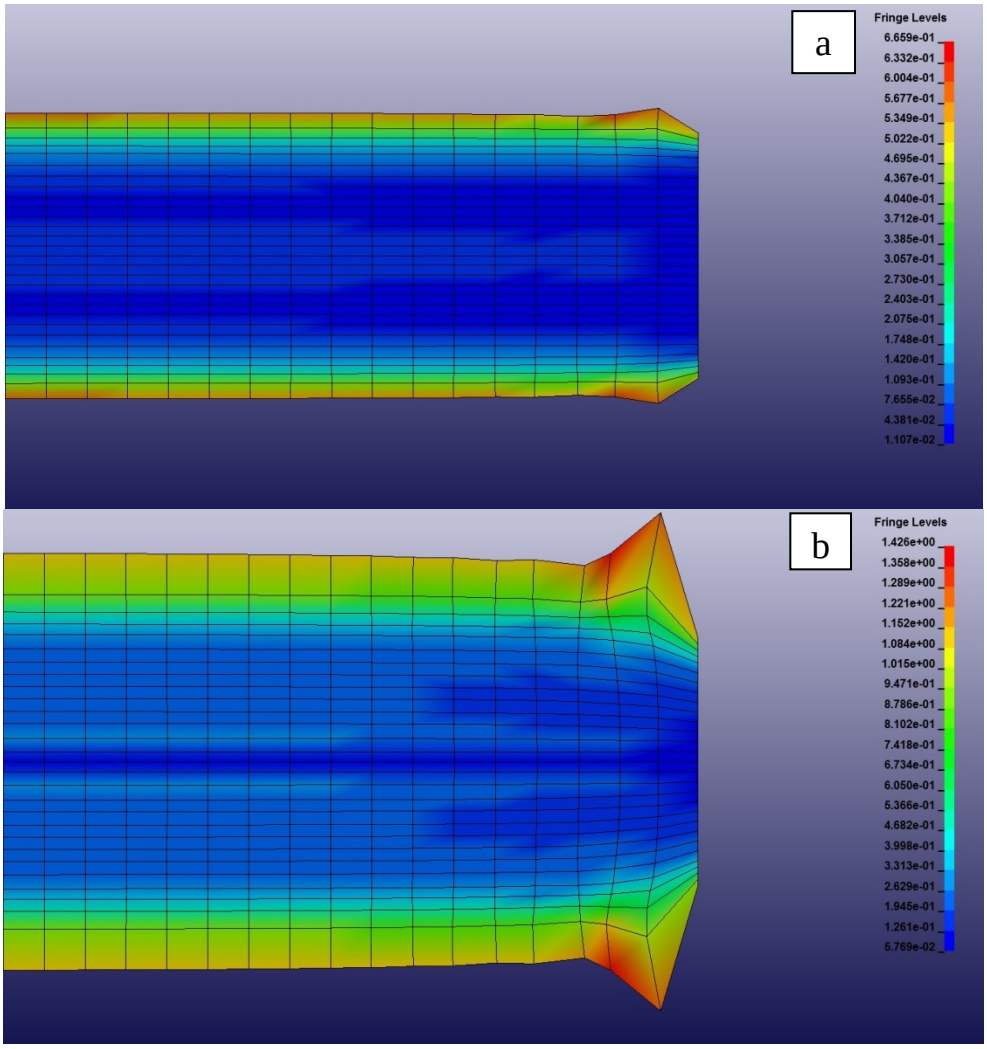

Figure 7.21 Deformation of the created instabilities at the end of the wire, at 120 ns and 200 ns from current start

In order to exclude the possibility that these instabilities are due to numerical error, a series of different test cases were carried out using different discretizations of the mesh along the vertical direction of the wire. It is concluded that for a discretization 50 μm and below the wavelength of the observed instabilities, remains the same 200-250 μm. In Figure 7.22 one can see the comparison of density distribution along a part of the wire length, for different mesh discretizations, 180 ns from current start, for external elements.

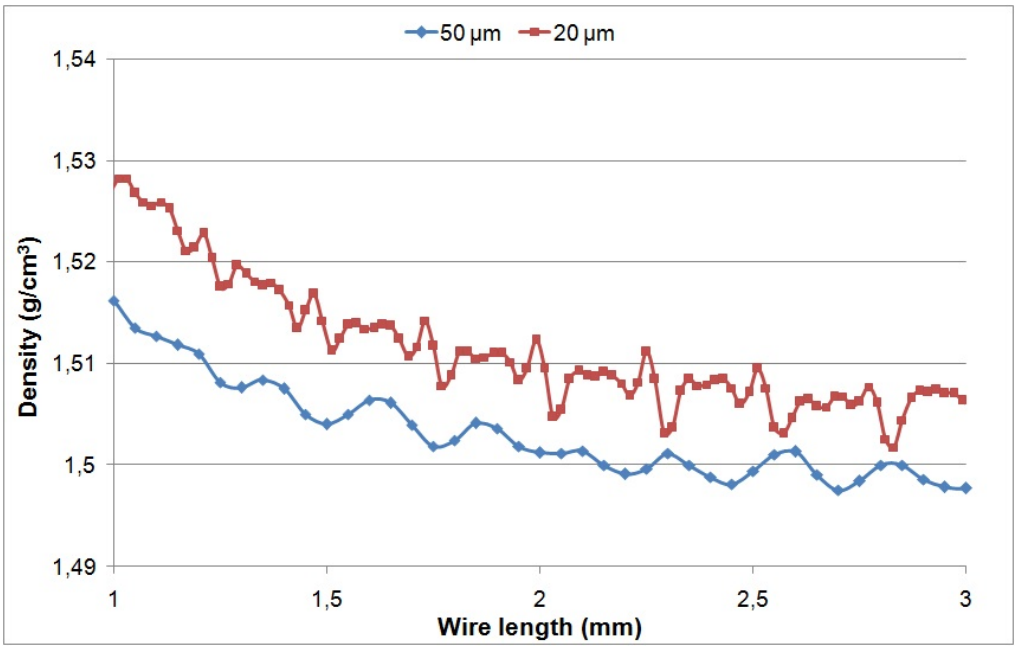

Figure 7.22 Density distribution along a part of the wire length, for different mesh discretizations, 180 ns from current start

Moreover, simulation results conclude that 10% percent of the initial total mass of the wire exceeds the temperature for plasma creation. Approximately 200 ns after the current start the radius of the wire has expanded from 150 to 245 μm. The outer part of the wire that is in plasma state, based on temperature criteria, is approximately 70 μm.

As previously mentioned in Chapter 6, a two-state condition that consists of a fluid and a plasma region is considered as initial approach in PLUTO MHD Code. An ideal gas equation of state is considered as well as Spitzer resistivity. The data of density distribution from LS DYNA at 200 ns after current start are used as input data in MHD code PLUTO. For fluid state the density distribution along radial direction is depicted in Figures 7.23 and 7.24. In PLUTO units, it is approximated by a second order polynomial equation that has the form $10.02-0.327\times(r)-13.2\times((r)^2)$, as it can be seen in Figure 7.24.

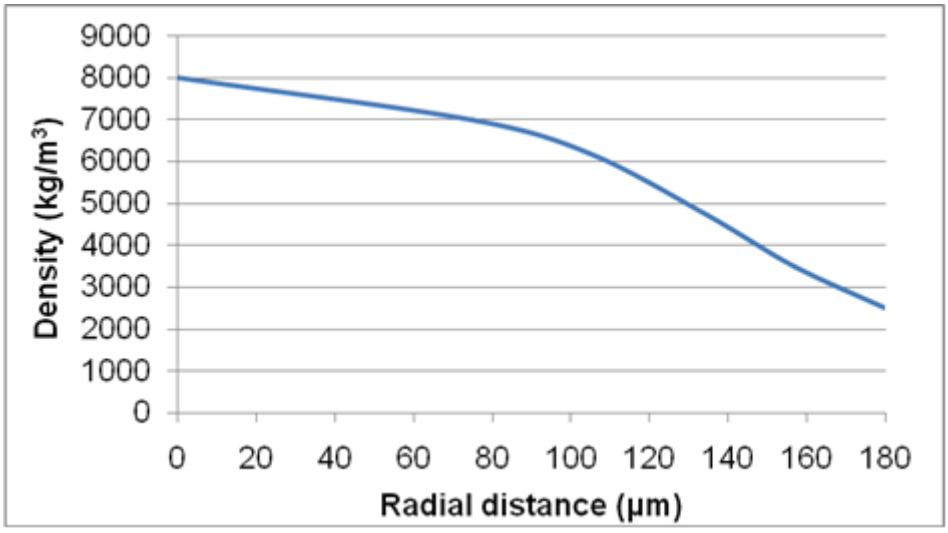

Figure 7.23 Density distribution along the radial direction 200 ns from current start from LS-DYNA

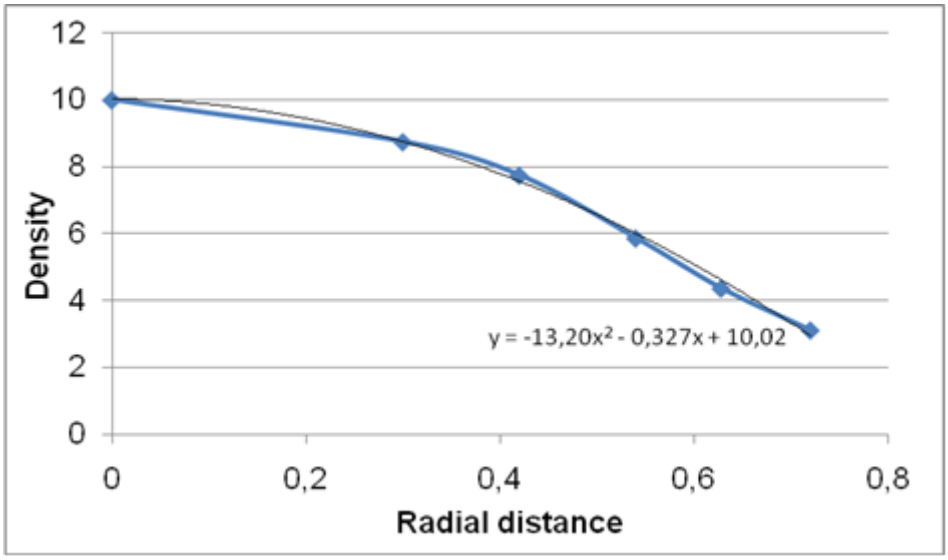

Figure 7.24 Density distribution along the radial direction in PLUTO units

The plasma corona region follows a parabolic density distribution with initial density value one order of magnitude lower i.e. ~800 kg/m^3 than the solid and has the form $\rho=\rho_0(1-r^2/r_0^2)$. The temperature of the fluid region is assumed to be 3000 ^{o}C and 6000 ^{o}C for the plasma corona [8, 9]. Moreover, the observed displacement instabilities in LS DYNA at 200 ns from current start are used as initial instabilities of the radius of the wire along the vertical direction in PLUTO and their evolution is monitored, while the MHD problem is transiently solved. A restart analysis in PLUTO is performed at every time step, with initial conditions for each step the computed values of the impulse given from liquid to gas phase from the LS DYNA

simulation. This approach allows for the accurate simulation of the original physical phenomena.

As previously mentioned in Chapter 6, PLUTO uses dimensionless units. All quantities can be set from Gaussian and S.I. units to non-dimensional Pluto units as long as we take three fundamental quantities and set them equal to unit. We set for initial conditions B_0=1.0, r_0=1.0 and ρ_0=1.0. These quantity values correspond respectively to values from LS-DYNA last solution data at 200 ns in S.I. units: 20 T for the maximum B_0 magnetic field, r_0=245 μm radius of the wire and ρ_0=800 kg/m^3 for the plasma density. Moreover, the maximum velocity of v_0=2100 m/s from LS-DYNA is also set to 1 in PLUTO units. An estimation of characteristic time t_0 is $t_0=r_0/v_0$=119 ns and every data solution step is recorded for 1.19 ns. With regard to Spitzer resistivity, it follows the expression $(\frac{\rho}{p})^{3/2}$.

Comparing the results from shadowgraphic optical experimental laser probing method and numerical simulations from the MHD code it should be pointed out that the wavelength and diameter of the perturbations of the coronal plasma increases with time. In Figure 7.25 the comparison of shadowgraphic experimental vs numerical results is depicted, at temporal moments 210 and 240 ns from current start. The axial wavelengths of instabilities in the coronal plasma 210 ns after the current start are measured to be approximately 270 μm, while the simulation computes them to be approximately 255 μm; 240 ns after the current start are measured to be approximately 600 μm, while the simulation computes them to be approximately equal to 575 μm. In Figure 7.26 the same results from numerical simulation and the shadowgraphic experimental technique are illustrated with a detailed zoomed view.

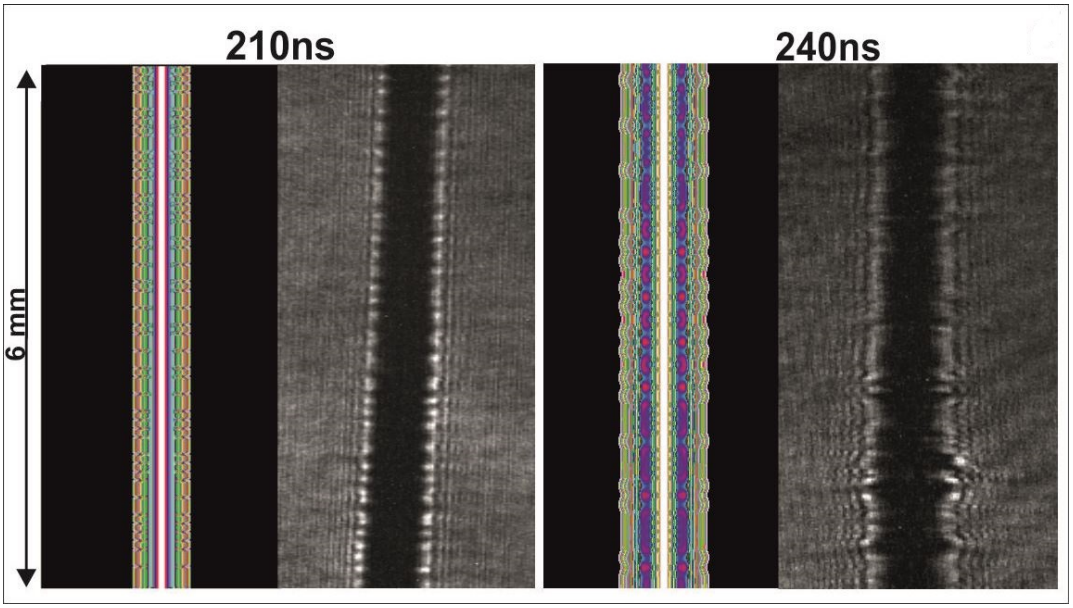

Figure 7.25 Comparison of simulation to shadowgraphic experimental results 210 and 240 ns from current start

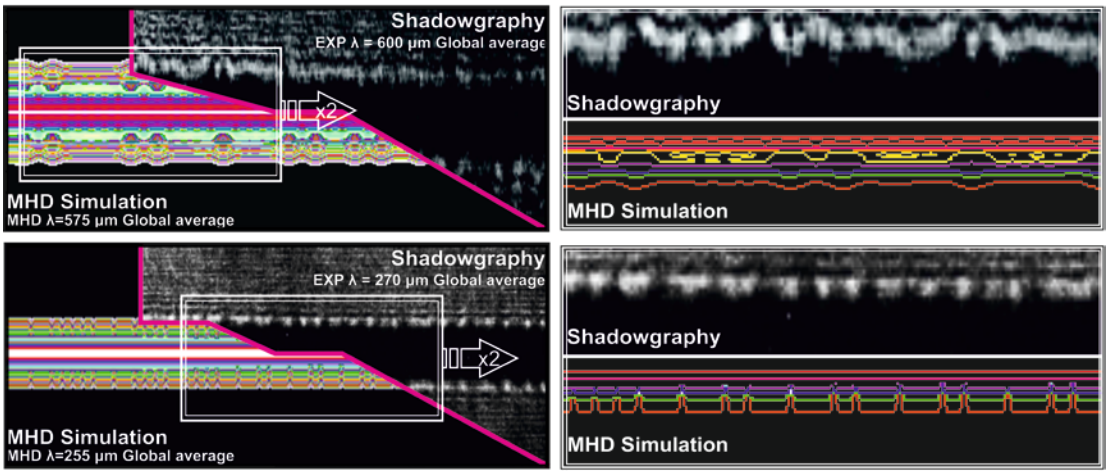

Figure 7.26 Detailed zoomed view of Figure 7.25

Quantitative comparison between experiment and simulation can be performed by calculating the value of $k\alpha$ where α is the radius of perturbations in the coronal plasma and k is the wavenumber, the spatial frequency of a wave. The instabilities are well developed at 210 ns. At 210 ns average $k\alpha$ is found to be 6.2 for the theoretical results (α=250 μm) and 5 for the shadowgraphic experimental ones (α=210 μm), while at 240 ns average $k\alpha$ is 4 for the theoretical results (α=305 μm) and 3.3 for the experimental ones (α=370 μm). It is observed very good agreement between experiment and

simulation results, indicating the success of the model used to simulate the physical problem.

Moreover, simulation shows that the amplitude of instabilities in the coronal plasma and in the core region varies. At 240 ns, there is a long wavelength and large amplitude m=0 instability in the corona plasma, while in the core region this instability shows a shorter wavelength and amplitude.

From the interferogram a maximum coronal plasma electron density of 7×10^{18} cm^{-3} at a radius of 370 μm can be calculated [5]. The Lundquist number S [8] is calculated, at 240 ns from current start, in order to know in which plasma regime the experiment belongs,

$$S = \frac{1.54\times10^{24} I^4 \mathrm{a}}{\mu^{1/2} \mathrm{Z}(1+\mathrm{Z})^{3/2} N_i^{\,2}} \tag{7.1}$$

where $\mu=m_i/m_p$, $Z=1$ the ionization state of the plasma, $I=38$ kA is the maximum current and a=370 μm is the radius of the plasma. The ion line density N_i is defined by $N_i=\int_0^{\mathrm{a}} 2\pi n_i r dr=\pi n_i \mathrm{a}$ and for $n_i=n_e=7\times10^{24}$ m^{-3} it has the value $N_i=2.84\times10^{18}$ 1/m. By taking into account the previous data, the Lundquist number is calculated to be 6.47<100. The same calculations are repeated for the simulation for a=305 μm, $n_i=n_e=3\times10^{25}$ m^{-3} and $N_i=8.62\times10^{18}$1/m and the Lundquist number is found to be 0.576<100. Therefore, the plasma is in the resistive regime of the universal stability diagram, since the Lundquist number [8] does not exceed 100.

In Figures 7.27 and 7.28 the results of both density (pseudocontours) and magnetic field (contours) are depicted at temporal instants 200 and 260 ns from current start. One can observe that the magnetic lines follow the instability evolution and may indicate the existence of Rayleigh-Taylor instability [11].

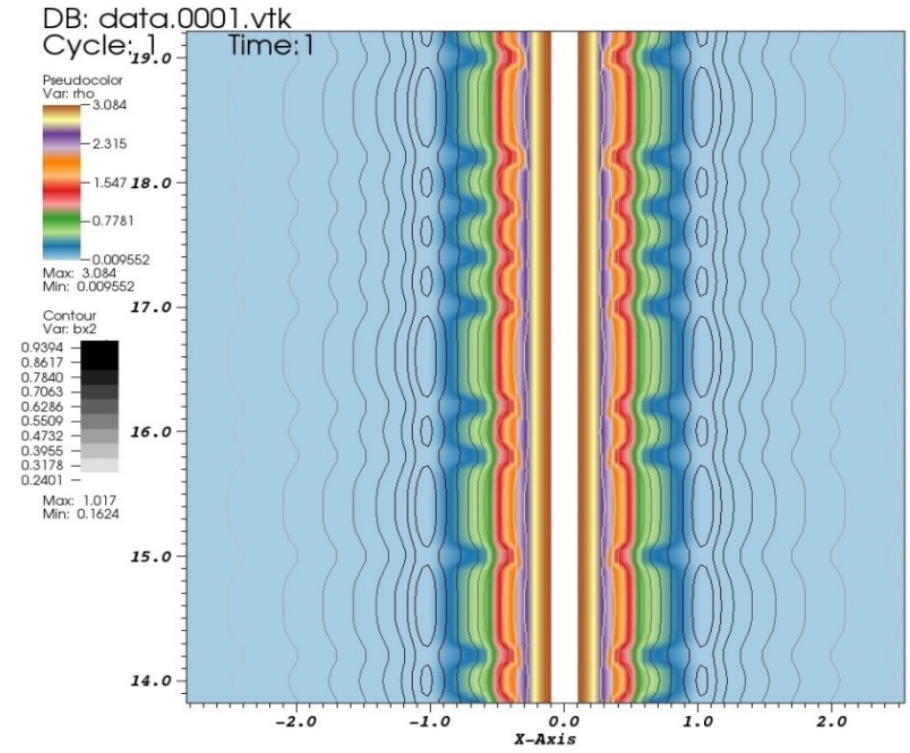

Figure 7.27 Contours of magnetic field and pseudocontours of density 200 ns from current start (initial time in PLUTO simulation)

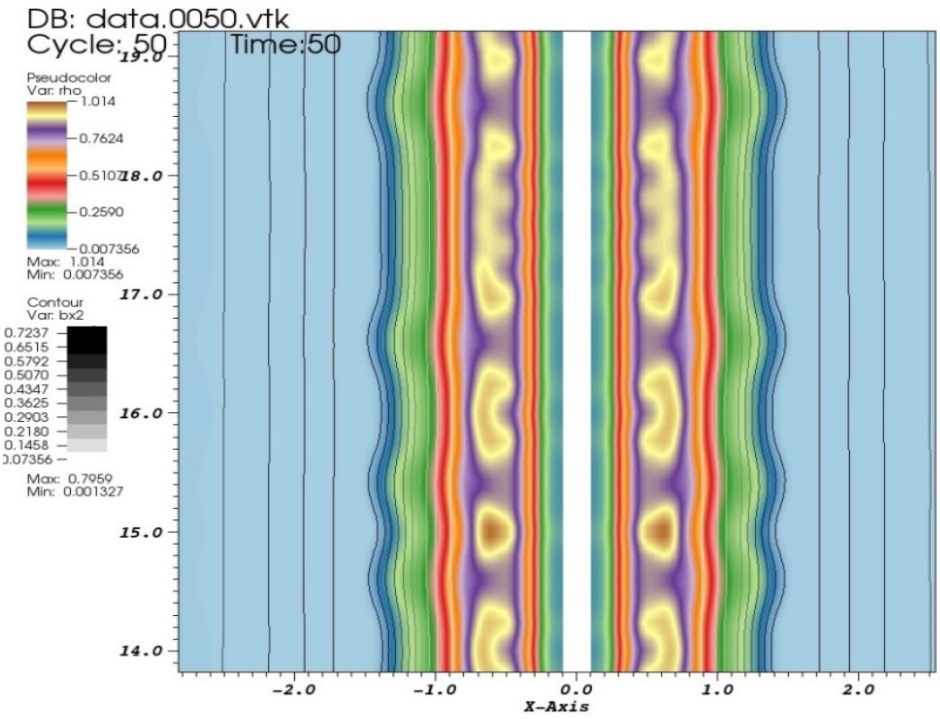

Figure 7.28 Contours of magnetic field and pseudocontours of density 260 ns from current start

References

[1] G. I. Kerley, Equation of State for Copper and Lead, KTS02-1, 2002.

[2] M. Scapin, L. Peroni and A. Dallocchio, Effects induced by LHC high energy beam in copper structures, *Journal of Nuclear Materials* **420**, 463–472 (2012).

[3] M. Scapin, L. Peroni and A. Dallocchio, Thermo-Mechanical Modelling of High Energy Particle Beam Impacts, Numerical Modeling of Materials Under Extreme Conditions, **35** of the series Advanced Structured Materials, 87-106 (2014).

[4] S. A. Khodier, Measurement of wire diameter by optical diffraction, *Opt. & Laser Technol.* **36,** 63-67 (2004).

[5] I. H. Hutchinson, *Principles of Plasma diagnostics*, Cambridge University Press (1987).

[6] R. H. Huddlestone and S. L. Leonard, *Plasma diagnostic techniques*, Academic Press, N.Y, London (1965).

[7] S. I. Tkachenko et al., Distribution of matter in current-carrying plasma and dense core of the discharge channel formed upon electrical wire explosion, *Plasma Phys. Rep.* **35**, 734-753 (2009).

[8] F. O. Borges, G. H. Cavalcanti and A. G. Trigueiros, Determination of Plasma Temperature by a Semi-Empirical Method, *Brazilian Journal of Physics* **34**, 1673-1674 (2004).

[9] M. P. Desjarlais, Practical Improvements to the Lee-More Conductivity Near the Metal-Insulator Transition, *Contrib. Plasma Phys.* **41**, 267–270 (2001).

[10] M. G. Haines and M. Coppins, *Phys. Rev. Lett.* **66**(11), 1462 (1991).

[11] D. H. Sharp, An Overview of Rayleigh-Taylor Instability, *Physica D* **12**, 3–18 (1984).

Chapter 8

8. Conclusions

The work presented in this thesis can be conceptually divided into two main parts, that both investigate the physical phenomena that occur during the deposition of energy in solid matter. The behavior of matter is investigated, when energy is transferred by laser photonic excitation, in the first part, and by Joule heating, occurring from external strong currents, in the second part. Regarding laser photonic excitation, the three dimensional spatial and temporal behavior of thin films excited by nanosecond laser pulses is investigated in the thermoelastic, melting, and ablation/plasma regimes simultaneously with a single FEM model. A main innovation of the present thesis is that it treats with a single 3D model both the generation and spatiotemporal evolution of SAWs and the transient surface deformation in all regimes of interest, accompanied and verified by experimental results, for the first time. Previous 2D studies focus on either thermal effects that cause ablation or SAWs mechanical generation but in this thesis such phenomena are simultaneously investigated. Regarding energy transfer due to joule heating occurring from external strong currents, the explosion of an initially solid metal wire with fixed ends and its intermediate phases, up to the plasma formation, via numerical simulation is investigated. An additional main innovation of the present thesis is the investigation of the whole time history of wire explosion from solid to plasma phase transition, while it points out the significant influence of the initial stages (thermoelastic & melting regimes) of a solid material to the generation and dynamics of the plasma instabilities validated by experimental results. An explanation for the initiation of sausage instabilities is also given.

Regarding the laser matter interaction, the developed FEM thermal-structural multiphysics model describes the dynamic phenomena occurring due to the laser energy concentration on metallic films. The behaviour of the material is investigated both in elastic and plastic ranges, by taking into account the material nonlinearity. It also provides insights to physical quantities like displacements, velocities, and

temperatures at any temporal step of the time solution domain. Moreover, it predicts the thermo-mechanical dynamics experimentally observed, such as the deformations in and around the irradiated region, as well as the observed phase transitions. While laser fluence values increase, the temperature is driven to higher values and the material's dynamics change, while the limits of melting and vaporizing are passed. The numerical approach is updated and the melting and vaporizing effects are taken into account in order to approximate the dynamic response of matter being in melting or ablation regime. The model can also predict the permanent characteristics that remain in the samples after being irradiated by the laser pulses (e.g. the geometry of the ablation crater).

The response of metallic film-substrate systems is studied and analyzed by the combination of the developed FEA model with a 3D whole-field imaging laser interferometric experimental technique. The developed FEM model simulates the real experiment throughout the temporal evolution for variable laser fluences. Comparisons for laser fluence ranging from 0.1 to 5 J/cm^2 have shown a very good agreement between the numerical simulation and the experimental results. The generated and experimentally measured SAWs are employed as a valuable tool for the validation of the method. By experimentally investigating nm-scale SAWs away from the interaction region, valuable parameter values can be extracted by the comparison of the 3D finite element model and the experimental results. This concept offers the capability to predict very accurately the phenomena that take place in the interaction region, for all three regimes. The experimental parameter values, obtained by investigating SAWs in a fully thermoelastic sample area far from the interaction region and their subsequent use in an appropriately modified model, allows for the detailed and accurate investigation of the interaction region in all regimes.

The comparison of the laser–matter interaction in the melting and ablation regimes shows interesting features for the phase transition dynamics. The outcome of this study proves the fast phase change from the melting to the ablation regime and offers detailed knowledge of the temperature as well as the melted and ablated mass topology and the temporal dynamics of the interaction. The accurate knowledge of the temperature distribution during the phase transition, as well as the melting and the ablation depths, resulting from this research, can be used as initial data to pure

hydrodynamic or Monte Carlo (MC) simulations that investigate laser–matter interactions well above the ablation threshold regime and is critical for a wide range of applications.

For future research a constitutive model, like Johnson and Cook, would be more appropriate for the simulation of matter's plastic behavior, since it takes into account strain rates that vary at high temperatures. Moreover, the hydrodynamic behavior of fluid material can be treated better with a use of a multiphase equation of state. Furthermore, the FEM model can be used for the prediction of high frequency surface waves in laser irradiated materials and their use for the material characterization, while it can also be further modified in order to investigate the generation of shock waves for higher laser energies. As a continuation of the presented research, the systematic use of the developed FEM model, along with the developed experimental methodologies, can contribute for the investigation in micro-scale level of a) composite materials that present anisotropies in their surface characteristics per direction (e.g. microfiber devices located in different directions), b) materials found in harsh environments (e.g. high temperatures, corrosive environment, high radiation environment). A typical example is the coatings of nuclear fission or fusion chambers, where the materials rapidly change their mechanical characteristics due both of the shock waves of nuclear reactions and of the receiving radiation.

Regarding the wire explosion, a Z-pinch target configuration is used for a proof of principle investigation for the formation and evolution of the plasma instabilities when a metallic material is used as target taking into account all the phases, from solid to plasma generation. Especially a low and slow current Z-pinch plasma geometry loaded with thick exploding metallic wires is used for this purpose. The Z-pinch target configuration is chosen because it offers extensively studied plasma geometry over the years, with well understood plasma dynamics and satisfactory defined plasma instabilities. The thick exploding wires have been chosen as a load because in connection with the low and slow rising current of the Z-pinch device and the skin depth current flow offer a convenient target configuration since all phases of matter can exist simultaneously for relatively long time (i.e., slow nanosecond process). This makes possible the effective investigation of the phase change problem and its influence on the plasma instabilities formation. Metallic wires are used, i.e.,

copper, due to the fact that it has very well investigated physical properties, established strength material behaviour as well as experimentally validated equation of states for pressure and resistivity.

A coupled transient electromagnetic-thermal-structural hydrodynamic computational model, based on FEM, is developed in order to provide key insights for important quantitative parameters, such as temperature, density, and expansion rate of the exploded material. Diffraction laser imaging technique is used for the measurement of the wire dynamics before plasma formation, as well as laser probing diagnostics, such as Schlieren, interferometry, shadowgraphy for the measurement of the wire dynamics in the plasma phase.

The FEM model predicts the initiation of instabilities in the thermoelastic regime. These are due to the imposed boundary conditions of the fixed ends and the constant temperature at the wire ends, while the dominant mechanism for their excitation is the stress dynamic behavior of the material caused by the Joule heating. The FEM multiphysics model takes into account the phase changes from solid to initiation of plasma formation based on temperature criteria. When plasma is formed the enhanced radius instabilities of the wire are taken as inputs in a resistive MHD (Magneto-Hydro-Dynamics) code and plasma expansion is investigated. Very good agreement is observed before and after the plasma regime between the numerical results and the corresponding experimental ones with regard to the expansion rate. The above proof of principle study is very important because plasma instabilities is a research topic with fundamental importance since they are unwanted for the majority of plasma applications and there is always the need for their suppression.

For future research, this study can be extended to other various plasma geometries such as multiple wire arrays for X-ray generation, laser matter interaction geometries where plasma formation could also be affected by the thermoelastic regime of the interaction. For instance, in the case of laser fusion target geometries, the thermoelastic regime of the interaction could be proven that affects the overall plasma expansion and the formation of instabilities. In addition, other materials such as insulators (i.e. carbon) should be investigated as well as different wire geometries. For these materials the Johnson-Cook model does not apply. Furthermore, a tabular equation of state should be used.

Appendix A (Implicit coupled thermal-structural analysis in ANSYS)

Thermal analysis

The representative equation for the thermal analysis using the Finite Element Method is obtained by the discretization of the energy conservation equation. Applying energy conservation to a differential control volume, the following well known equation is obtained

$$\rho c \frac{\partial T}{\partial t} + \nabla \boldsymbol{q} = Q \tag{A.1}$$

where Q is the heat generation rate per unit volume and $\boldsymbol{q}$ the heat flux vector, which is related to the thermal gradients by the conductivity matrix [K] using Fourier's law

$$\boldsymbol{q} = -[K]\nabla T \tag{A.2}$$

Neglecting convection the following boundary conditions can be considered. These cover the entire element. These are specified temperatures T^* on surface so that $T=T^*$ and specified heat flows q^* acting on the surface, so that $\boldsymbol{q}\hat{n} = -q^*$, where $\hat{n}$ is the unitary outward normal vector.

Applying the finite element discretization for the variation of the temperature field along the element, it holds that

$$T=\{N\}^{\mathrm{T}}\{T_e\} \tag{A.3},$$

where $T=T(x, y, z, t)$ is the temperature, $\{N\}=\{N(x, y, z)\}$ are element shape functions, $\{T_e\}=\{T_e(t)\}$ is the nodal temperature vector of an element. It also holds for the shape function derivative matrix [B], evaluated at the integration points, that $[B]=\{L\}\{N\}T$ where $\{L\} = \left\{ \frac{\partial}{\partial x} \ \frac{\partial}{\partial y} \ \frac{\partial}{\partial z} \right\}^{\mathrm{T}}$ vector operator. With these assumptions the following matrix equation is derived

$$[C_e]\{\dot{T}_e\} + [K_{ec}]\{T_e\} = \{Q_e^f\} + \{Q_e^g\} \tag{A.4}$$

where element specific heat capacity matrix is $[C_e] = \rho \iiint_V c[N][N]^{\mathrm{T}} dV$, element conductivity matrix is $[K_{ec}] = \iiint_V [B]^{\mathrm{T}}[D][B] dV$, $\{Q_e^f\} = \iint_s \{N\} q^* dS$ is the element mass flux vector and $\{Q_e^g\} = \iiint_V NQdV$ the element heat generation load.

The procedure employed for the temporal integration of Equation A.4 during a transient analysis is the generalized trapezoidal rule

$$\{T_{n+1}\} = \{T_n\} + (1-\theta)\Delta t\{\dot{T}_n\} + \theta\Delta t\{\dot{T}_{n+1}\} \tag{A.5}$$

where θ is a transient integration parameter, $\{T_n\}$ is a nodal temperature value at time t_n (also $\Delta t = t_{n+1} - t_n$). Substituting Equation A.5 to A.4 the result is

$$\left(\frac{1}{\theta\Delta t}[C_e] + [K_{ec}]\right)\{T_{n+1}\} = \{Q_e^f\} + \{Q_e^g\} + [C_e]\left(\frac{1}{\theta\Delta t}\{T_n\} + \frac{1-\theta}{\theta}\{\dot{T}_n\}\right) \tag{A.6}$$

This numerical scheme becomes unconditionally stable by choosing θ=1/2 (Crack-Nikolson method, second order accurate) [1].

Mechanical analysis

The derivation of the equations for the mechanical analysis starts with the stress-strain relationship

$$\{\sigma\} = [D]\{\varepsilon^{el}\} \tag{A.7}$$

where $\{\sigma\} = [\sigma_x\ \sigma_y\ \sigma_z\ \sigma_{xy}\ \sigma_{yz}\ \sigma_{xz}]^{\mathrm{T}}$ is the stress vector, $[D]$ the elasticity matrix, and $\{\varepsilon^{el}\}$ the elastic strain vector. The total strain vector is

$$\{\varepsilon\} = \{\varepsilon^{el}\} + \{\varepsilon^{th}\} = [\varepsilon_x\ \varepsilon_y\ \varepsilon_z\ \varepsilon_{xy}\ \varepsilon_{yz}\ \varepsilon_{xz}]^{\mathrm{T}} \tag{A.8}$$

while the thermal strain vector is

$$\{\varepsilon^{th}\} = \Delta T[\alpha_x\ \alpha_y\ \alpha_z\ 0\ 0\ 0]^{\mathrm{T}} \tag{A.9},$$

where α_x is the secant coefficient of thermal expansion in the x direction, and $\Delta T = (T - T_{ref})$, with T being the current nodal temperature and T_{ref} the reference temperature for stress calculation.

Moreover, the strains are related to the nodal displacements by

$$\{\varepsilon\} = [B]\{u\} \tag{A.10}$$

where $[B]$ is the strain-displacement matrix, based on the element shape functions and $\{u\}$ is the nodal displacement vector. It also holds that the displacements within the element are related to the nodal displacements by

$$\{w\} = [N]\{u\} \tag{A.11}$$

where $\{w\}$ is the vector of displacements of a general point and $[N]$ the matrix of shape functions. Using the principle of virtual work for all the internal and external sources of strain energy, taking into account the inertial effects since the analysis is transient, and by applying the finite element discretization, the following equation is obtained

$$[K_e]\{\mathrm{u}\} = [M_e]\{\ddot{u}\} + \{F^{th}\} + \{F^{ext}\} \tag{A.12}$$

where the element stiffness matrix is $[K_e] = \iiint_V [B]^{\mathrm{T}}[D][B]dV$. The element mass matrix is $[M_e] = \rho \iiint_V [\mathrm{N}]^{\mathrm{T}}[\mathrm{N}]dV$, $\{\ddot{u}\} = \dfrac{\partial^2}{\partial t^2}\{u\}$ is the acceleration vector, the element thermal load vector is $\{F^{th}\} = \iiint_V [B]^{\mathrm{T}}[D]\{\varepsilon^{th}\}dV$ and $\{F^{ext}\}$ is the element vector of potential external nodal forces. Equation A.12 represents the equilibrium equation on a one element basis.

For the solution of Equation A.12 an implicit time integration scheme, based on Newmark's algorithm, is employed during a transient analysis. The velocity and acceleration terms are given by

$$\{\ddot{u}_{t-\Delta t}\} = \frac{1}{\alpha \Delta t^2}(\{u_{t-\Delta t}\} - \{u_{t-2\Delta t}\}) - \frac{1}{\alpha \Delta t}\{\dot{u}_{t-2\Delta t}\} - (\frac{1}{2a} - 1)\{\ddot{u}_{t-2\Delta t}\}$$
$$\{\dot{u}_{t-\Delta t}\} = \{\ddot{u}_{t-2\Delta t}\} + \Delta t(1-\delta)\{\ddot{u}_{t-2\Delta t}\} + \Delta t\delta\{\ddot{u}_{t-\Delta t}\} \quad \text{(A.13)}$$

Equation A.12 is therefore converted into

$$([K_e] + \frac{1}{\alpha \Delta t^2}[M_e])\{u\}_t = \{F^{ext}\} + \{F^{th}\} + [M_e][\frac{1}{\alpha \Delta t^2}\{u\}_{t-\Delta t} + \frac{1}{\alpha \Delta t}\{\dot{u}\}_{t-\Delta t} + (\frac{1}{2a} - 1)\{\ddot{u}\}_{t-\Delta t}] \quad \text{(A.14)}$$

and, by choosing the parameters δ=1/2 and α=1/4, the scheme becomes unconditionally stable [1].

Coupling of equations

The method (for the chosen SOLID5 element) that is used to couple the matrix equations is presented at next. It is illustrated here with two types of degrees of freedom ($\{X_1\}$, $\{X_2\}$). It is called weak (load vector or sequential) coupling and the coupling in the matrix equation is shown in the most general form

$$\begin{bmatrix} [K_{11}(\{X_1\},\{X_2\})] & [0] \\ [0] & [K_{22}(\{X_1\},\{X_2\})] \end{bmatrix} \begin{Bmatrix} \{X_1\} \\ \{X_2\} \end{Bmatrix} = \begin{Bmatrix} \{F_1(\{X_1\},\{X_2\})\} \\ \{F_2(\{X_1\},\{X_2\})\} \end{Bmatrix}. \quad \text{(A.15)}$$

The coupled effect is accounted for in the dependency of $[K_{11}]$ and $\{F_1\}$ on $\{X_2\}$ as well as $[K_{22}]$ and $\{F_2\}$ on $\{X_1\}$. At least two iterations are required to achieve a coupled response.

For the thermal-structural analysis the weak coupling has the form

$$\begin{bmatrix} [M] & 0 \\ 0 & 0 \end{bmatrix} \begin{Bmatrix} \{\ddot{u}\} \\ \{\ddot{T}\} \end{Bmatrix} + \begin{bmatrix} 0 & 0 \\ 0 & [C] \end{bmatrix} \begin{Bmatrix} \{\dot{u}\} \\ \{\dot{T}\} \end{Bmatrix} + \begin{bmatrix} [S] & 0 \\ 0 & [K] \end{bmatrix} \begin{Bmatrix} \{u\} \\ \{T\} \end{Bmatrix} = \begin{Bmatrix} \{F_c\} \\ \{Q_c\} \end{Bmatrix} \quad \text{(A.16)}$$

where the coupled effects are accounted via load terms F-coupled: F_c, and Q-coupled: Q_c [2].

Newton-Raphson nonlinear solution technique

In a non-linear analysis, since the non-linear system of equations cannot be solved directly, it is necessary to use an iterative procedure. The Newton-Raphson method consists in the iterative solution of a linear approximation of the nonlinear system of equations, until a specific convergence criterion is fulfilled. The solution starts with a predictor step that is followed by the correction steps. The goal of the Newton - Raphson algorithm is to reduce the unbalanced load *R*, which in a structural system represents the out of balance load between external and internal forces, until a certain convergence tolerance is reached. The generalized nonlinear equation to solve is

$$R_{n+1}^{i} = F_{n+1}^{ext} - F_{n}^{int} = 0 \tag{A.17}.$$

Assuming u_n is the converged solution from the previous time step, then: $u_{n+1}^{0} = u_n$ and $u_n^0 = 0$. The method consists of the following loop steps until convergence [3]:

1. Compute the vector of unbalanced loads

$$\{R_{n+1}^{i}\} = \{F_{n+1}^{ext}\} - [K_i^{\mathrm{T}}]\{du_n^i\} = 0 \tag{A.18}.$$

2. Compute the Jacobian or tangent stiffness matrix $[K_i^{\mathrm{T}}]$.

3. Calculate the Newton update Δu_i^n from

$$\Delta u_n^i = \sum_{k=1}^{i} du_n^k \tag{A.19}$$

4. Add Δu_i^n to u_n in order to obtain the next approximation

$$\{u_{n+1}^{i+1}\} = \{u_n\} + \{\Delta u_n^i\} \tag{A.20}$$

When robustness and accuracy are more important, the Jacobian matrix is updated for every iteration and it constitutes a Full Newton – Raphson method. Additionally, a line search procedure non-linear optimization technique and an adaptive descent technique that switches to a stiffer matrix if convergence difficulties are encountered,

are used along with the iterative Newton – Raphson method. Moreover, the FEM system of equations is solved using a direct sparse solver.

Shape function and integration point locations of hexahedral 8-node element

In Figure A.1 the 8-node coupled field element is depicted, used for the simulations.

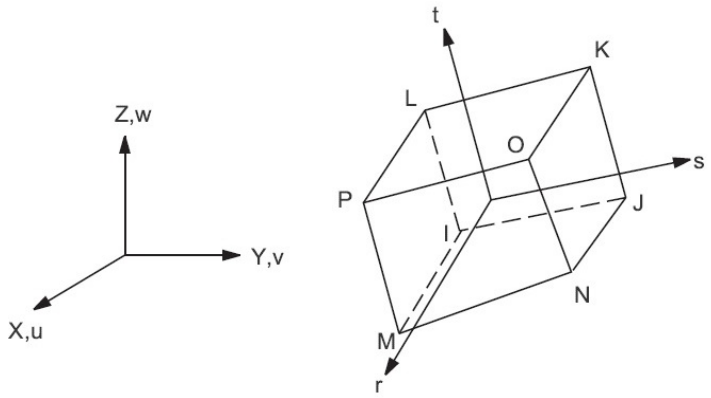

Figure A.1 Coupled-field element used for the simulations

The shape function has the form

$$u=\frac{1}{8}(u_I(1-s)(1-t)(1-r)+u_J(1+s)(1-t)(1-r)+u_K(1+s)(1+t)(1-r)+u_L(1-s)(1+t)(1-r)$$
$$+u_M(1-s)(1-t)(1+r)+u_N(1+s)(1-t)(1+r)+u_O(1+s)(1+t)(1+r)+u_P(1-s)(1+t)(1+r) \quad \text{(A.21)}$$

for u displacement in the x-direction. The same shape function form the other quantities also have, namely v, w, V_x, V_y, V_z, T (displacements in the other two directions, velocities, and temperature, respectively).

Moreover, in Figure A.2 the 2x2x2 integration point locations for the hexahedral element are depicted.

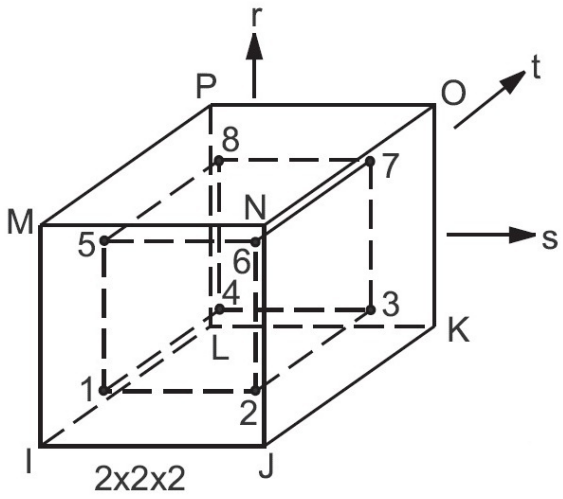

Figure A.2 Integration point locations

References

[1] ANSYS user's manual *Release 12.0* (Southpointe Canonsburg, April 2009).

[2] ANSYS Inc., *Coupled-field analysis guide, Release 12.0* (Southpointe Canonsburg, April 2009).

[3] A. S. Díaz, Thermomechanical and metallurgical modeling of laser hardening and laser cladding processes, PhD thesis March 2011.

Appendix B (Rate independent Multilinear Isotropic Hardening elastoplastic model in ANSYS)

Rate independent plasticity is characterized by the irreversible straining that occurs in a material once a certain level of stress is reached. The plastic strains are assumed to develop instantaneously, that is, independent of time. For the case of nonlinear materials the definition of elastic strain is given by [1]

$$\left\{\varepsilon^{el}\right\} = \left\{\varepsilon\right\} - \left\{\varepsilon^{th}\right\} - \left\{\varepsilon^{pl}\right\} \tag{B.1}$$

Plasticity theory provides a mathematical relationship that characterizes the elastoplastic response of materials. There are three ingredients in the rate-independent plasticity theory: the yield criterion, the flow rule and the hardening rule.

The yield criterion determines the stress level at which yielding is initiated. For multi-component stresses this is represented as a function of the individual components $f(\{\sigma\})$, which can be interpreted as an equivalent stress σ_e: $\sigma_e = f(\{\sigma\})$, where $\{\sigma\}$ is the stress vector. When the equivalent stress is equal to material yield parameter σ_y, $f(\{\sigma\})=\sigma_y$ the material will develop plastic strains. If σ_e is less than σ_y, the material is elastic and the stresses will develop according to elastic stress-strain relations. Equivalent stress can never exceed the material yield, since in this case plastic strains would develop instantaneously, hence reducing the stress to the material yield. The Von Mises yield criterion that is used for the simulations is a scalar function, a surface in stress space. It has the form

$$f(\boldsymbol{\sigma}) = \sigma_y \tag{B.2}$$

where $f(\boldsymbol{\sigma})$ a scalar function of Von Mises stress and σ_y the current yield stress that evolves as a function of the amount of plastic work done. Stress states inside the yield surface are given by

$$f(\boldsymbol{\sigma}) - \sigma_y < 0 \tag{B.3}$$

and result in elastic deformation. The material yields when the stress state reaches the yield surface and further loading causes plastic deformation.

The flow rule determines the direction of plastic straining and is given as

$$\left\{d\varepsilon^{pl}\right\} = \lambda \left\{\frac{\partial Q}{\partial \sigma}\right\} \tag{B.4}$$

where λ is the plastic multiplier (determines the amount of plastic straining), Q the function of stress termed the plastic potential (determines the direction of plastic straining). Plastic strains occur in a direction normal to the yield surface.

The hardening rule describes the changing of the yield surface with progressive yielding, so that the conditions for subsequent yielding can be established. In isotropic work hardening the yield surface remains centered about its initial centerline and expands in size as the plastic strains develop.

As previously mentioned, if the computed equivalent stress using elastic properties exceeds the material yield plastic straining occurs. Plastic strains reduce the stress state so that it satisfies the yield criterion. For the calculation of the plastic strain increment an iterative procedure takes place.

For the Multilinear Isotropic Hardening model the equivalent stress is

$$\sigma_e = \left[\frac{3}{2}\{s\}^T [M]\{s\}\right]^{1/2} \tag{B.5}$$

where $\{s\}$ is the deviatoric stress and for the matrix $[M]$ it holds

$$[\mathrm{M}] = \begin{bmatrix} 1 & 0 & 0 & 0 & 0 & 0 \\ 0 & 1 & 0 & 0 & 0 & 0 \\ 0 & 0 & 1 & 0 & 0 & 0 \\ 0 & 0 & 0 & 2 & 0 & 0 \\ 0 & 0 & 0 & 0 & 2 & 0 \\ 0 & 0 & 0 & 0 & 0 & 2 \end{bmatrix}$$

When σ_e is equal to the current yield stress σ_k the material is assumed to yield. The yield criterion is

$$F = \left[\frac{3}{2}\{s\}^T [M]\{s\}\right]^{1/2} - \sigma_k = 0 \tag{B.6}$$

For work hardening, σ_k is a function of the amount of plastic work done.

For temperature-dependent curves with the MISO option, σ_k is determined by temperature interpolation of the input curves after they have been converted to stress-plastic strain format [1].

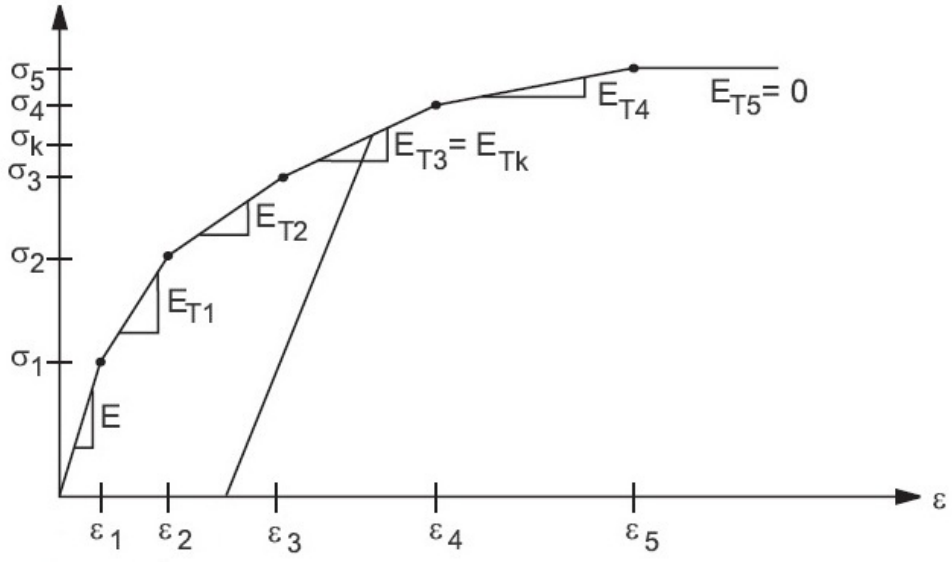

Figure B.1 Multilinear Isotropic Hardening model and σ_k determination

References

[1] ANSYS user's manual *Release 12.0* (Southpointe Canonsburg, April 2009).

Appendix C (LS-DYNA Solvers)

Electromagnetic implicit analysis

FEMSTER library provides discrete numerical implementations of the concepts from differential forms (often referred as Nedelec elements). These include in particular the exterior derivatives of gradient, curl, and divergence, and also the div-grad, curl-curl, and grad-div operators. FEMSTER provides four forms of basis functions, called 0-forms, 1-forms, 2-forms and 3-forms, defined on hexahedra. These basis functions satisfy numerical relations, such as curl(grad)=0 or div(curl)=0, which are very important for the solution of conservation laws [1, 2].

0-forms are continuous scalar basis functions that have a well-defined gradient, the gradient of a 0-form being a 1-form. At first order, the degrees of freedom associated with a 0-form are the values of the scalar field at the nodes of the mesh. These forms are used for the discretization of the scalar potential φ.

1-forms are vector basis functions with continuous tangential components but discontinuous normal components. The curl of a 1-form is a 2-form. At first order, the degrees of freedom of a 1-form are its line integrals along the edges of the mesh. They are used for the discretization of the electric field $\boldsymbol{E}$, the magnetic field $\boldsymbol{H}$ and the vector potential $\boldsymbol{A}$.

2-forms are vector basis functions with continuous normal components across elements but discontinous tangential components. The divergence of a 2-form is a 3-form. At first order, the degrees of freedom of a 2-form are its fluxes across all the facets of the mesh. They are used for the discretization of the magnetic flux density $\boldsymbol{B}$, and the current density $\boldsymbol{j}$.

Finally, the 3-forms are discontinuous scalar basis functions, which cannot be differentiated. Their degrees of freedom at first order are their integrals over the elements of the mesh.

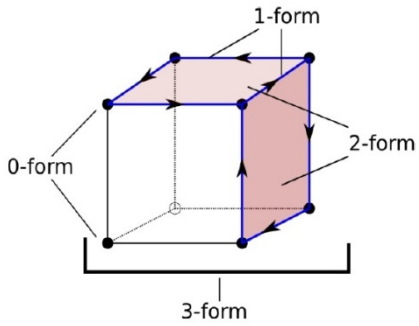

Figure C.1 l-forms on a hexahedral element

With regard to solutions of Equations 6.19 and 6.20, Equation 6.19 is projected against W^0 0-forms basis functions and Equation 6.20 against $\boldsymbol{W}^1$ 1-forms. The φ and $\boldsymbol{A}$ decompositions on respectfully W^0 and $\boldsymbol{W}^1$ give

$$\varphi = \sum \varphi_i w_i^0 \tag{C.1}$$

$$\boldsymbol{A} = \sum \alpha_i \boldsymbol{w}_i^1 \tag{C.2}$$

and after using appropriate Green's vector identities and boundary conditions they have the form

$$[S^0(\sigma)]\varphi = 0 \tag{C.3}$$

$$[M^1(\sigma)]\{\frac{d\alpha}{dt}\} + [S^1(\frac{1}{\mu})]\{\alpha\} = -[D^{01}(\sigma)]\varphi + [S]\{a\} \tag{C.4}$$

where the 0-form stiffness matrix $[S^0]$ is introduced, the 1-form mass matrix $[M^1]$, the 1-form stiffness matrix $[S^1]$ and the 0-1 form derivative matrix $[D^{01}]$. Equations C.3 and (C.4) form the FEM system, with φ and $\{\alpha\}$ being the unknowns. From this system only the outside stiffness $[S]$ matrix cannot be directly computed. The calculation of this matrix is possible through the definition of a BEM system and through the definition of an intermediate "surface current" variable $\boldsymbol{k}$ that produces the same $\boldsymbol{A}$ (and thus $\boldsymbol{B}$) in the air/vacuum as the actual volume current. The equations of the BEM system are:

$[P]\{k\}=[D]\{\alpha\}$ and $[S]\{\alpha\}=[Q_s]\{k\}+Q_d\{k\}$, where $[P],[D],[Q_s],[Q_d]$ BEM matrices.

With regard to the time integration scheme, this is done using an implicit backward Euler method

$$[[M^1(\sigma)]+dt[S^1(\frac{1}{\mu})]]\{\alpha^{t+1}\}=[M^1(\sigma)]\{\alpha^t\}-dt[D^{01}(\sigma)]\varphi^{t+1}+dt[S]\{\alpha^{t+1}\} \quad \text{(C.5)}$$

The BEM part of the right hand side $dt[S]\{\alpha^{t+1}\}$ also is implicit. It improves the stability, allowing larger time steps. It is computed by solving the BEM system equations coupled with the FEM ones in an iterative way

$$[P]\{k_{n+1}^{t+1}\}=[D]\{a_n^{t+1}\} \quad \text{(C.6)}$$

$$[[M^1(\sigma)]+dt[S^1(\frac{1}{\mu})]]\{\alpha_{n+1}^{t+1}\}=[M^1(\sigma)]\{a^t\}-dt[D^{01}(\sigma)]\{\varphi^{t+1}\}+dt[Q]\{k_{n+1}^{t+1}\} \quad \text{(C.7)}$$

until convergence on both $\{k_n^{t+1}\}$and $\{\alpha_n^{t+1}\}$. Moreover, the FEM System is solved using a direct solver, while the BEM system is solved using a pre-conditioned gradient method [3].

Time step

The time step for electromagnetic equation is based on the diffusion equation for the magnetic field, Equation 6.20. It is computed as the minimal elemental diffusion time step over the elements. For a given element, the elemental diffusion time step is given as

$$\Delta t_e=l_e^2/2D, \quad \text{(C.8)}$$

where D the diffusion coefficient $D=1/\mu_0\sigma_e$, σ_e is the element electrical conductivity, μ_0 is the permeability of free space, l_e is the minimal edge length of the element (minimal size of the element).

Mechanical explicit analysis

For a defined body, time-dependent deformation is considered, for which a point in the body initially at X_α (α=1, 2, 3) in a fixed rectangular Cartesian coordinate system

moves to a point x_i (i=1, 2, 3) in the same coordinate system. Since a Lagrangian formulation is considered, the deformation can be expressed in terms of the convected coordinates X_α and time t

$$x_i = x_i(X_a, t) \,. \tag{C.9}$$

The momentum equation is given by [4]

$$\boldsymbol{\sigma}_{ij,j} + \rho \boldsymbol{f}_i = \rho \ddot{\boldsymbol{x}}_i \tag{C.10}$$

where $\boldsymbol{\sigma}$ is the Cauchy stress, ρ is the current density, $\boldsymbol{f}$ is the body force density and $\ddot{\boldsymbol{x}}_i$ is acceleration. The comma on $\boldsymbol{\sigma}_{ij,j}$ denotes covariant differentiation. Superimposition occurs for a mesh of finite elements interconnected at nodal points on the reference configuration and it holds [4]

$$x_i(X_a, t) = x_i(X_a(\xi, \eta, \zeta), \mathrm{t}) = \sum_{j=1}^{k} N_j(\xi, \eta, \zeta)\, \mathrm{x}_i^j(t) \tag{C.11}.$$

By taking into account this consideration along with the principle of the virtual work, Equation C.10 for n elements becomes

$$\sum_{m=1}^{n} \left\{ \int_{v_m} \rho [N_m]^{\mathrm{T}} [N_m] \{a\} dv + \int_{v_m} [B_m]^{\mathrm{T}} \{\sigma\} dv - \int_{v_m} \rho [N_m]^{\mathrm{T}} \{b\} dv - \int_{\partial b_1} [N_m]^{\mathrm{T}} \{t\} dS \right\} = 0 \tag{C.12}$$

where $[N]$ is the interpolation matrix, $\{\sigma\}$ is the stress vector, $[B]$ is the strain-displacement matrix, $\{\alpha\}$ is the nodal acceleration vector, $\{b\}$ is the body force load vector and $\{t\}$ is the applied traction load.

Discretization of this problem is accomplished by means of the standard finite element procedure. After aggregation, the dynamic equilibrium equation has the form

$$[M]\{\ddot{u}\} + [C]\{\dot{u}\} + \{F_{int}\} = \{F_{ext}\} \tag{C.13}$$

where [M] is the diagonal mass matrix, $\{\ddot{u}\}$ and $\{\dot{u}\}$ the nodal acceleration and velocity vector, respectively, [C] diagonal damping matrix, $\{F_{int}\}$ the internal element force vector, while $\{F_{ext}\}$ accounts for external and body force loads. Central difference time integration (conditionally stable scheme) is used to advance to time t_{n+1}

$$\{\ddot{u}\} = [M]^{-1}[\{F_{ext}\} - \{F_{int}\} - [C]\{\dot{u}\}) \tag{C.14}$$

$$\{\dot{u}\}^{n+1/2} = \{u\}^{n-1/2} + \{\ddot{u}\}^{n}\Delta t^{n} \tag{C.15}$$

$$\{u\}^{n+1} = \{u\}^{n} + \{\dot{u}\}^{n+1/2}\Delta t^{n+1/2} \tag{C.16}$$

$$\Delta t^{n+1/2} = \frac{(\Delta t^{n} + \Delta t^{n+1})}{2} \tag{C.17}$$

Geometry is updated by adding the displacement increments to the initial geometry

$$\{x\}^{n+1} = \{x\}^{0} + \{u\}^{n+1} \tag{C.18}$$

The central difference scheme is conditionally stable. A critical time step size Δt_e is computed for solid elements from

$$\Delta t_e = \frac{L_e}{\{[Q + (Q^2 + C_d{}^2)^{1/2}]\}} \tag{C.19}$$

where Q is a function of the bulk viscosity coefficients C_0 and C_1

$$\begin{aligned} Q &= C_1 C_d + C_0 L_e \left|\dot{\varepsilon}_{kk}\right| \qquad for \quad \dot{\varepsilon}_{kk} < 0 \\ Q &= 0 \qquad\qquad\qquad\qquad for \quad \dot{\varepsilon}_{kk} \geq 0 \end{aligned} \tag{C.20}$$

where $\dot{\varepsilon}_{kk}$ the trace of the strain rate tensor and L_e the characteristic length $L_e = V_e/A_{emax}$ where V_e is the element volume, A_{emax} is the area of the largest side and C_d is the adiabatic sound speed of the material

$$C_d = \left[\left(\frac{4G}{3\rho_0} + \frac{\partial p}{\partial \rho}\right)_E + \frac{pV^2}{\rho_0}\frac{\partial p}{\partial E}\right)_\rho\Bigg]^{1/2} \tag{C.21}$$

where G is the shear modulus.

With regard to the shape function used for a mesh of 8-node hexahedron solid elements, Equation C.11 becomes

$$x_i(X_a,t) = x_i(X_a(\xi,\eta,\zeta),t) = \sum_{j=1}^{8} \varphi_j(\xi,\eta,\zeta)\, \mathrm{x}_i^j(t) \tag{C.22}$$

The shape function φ_j is defined for the 8-node hexahedron as

$$\varphi_j = \frac{1}{8}(1+\xi\xi_j)(1+\eta\eta_j)(1+\zeta\zeta_j) \tag{C.23}$$

where ξ_j, η_j, ζ_j take on their nodal values of (±1, ±1,±1) and x_i^j is the nodal coordinate of the j^{th} node in the i^{th} direction

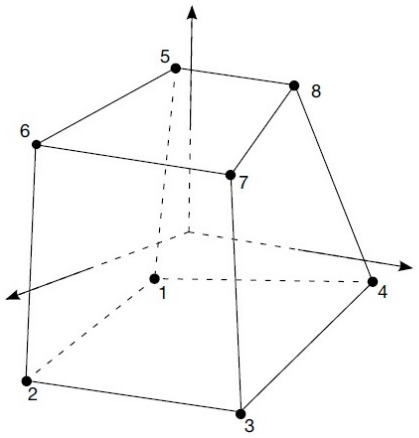

Node	ξ	η	ζ
1	-1	-1	-1
2	1	-1	-1
3	1	1	-1
4	-1	1	-1
5	-1	-1	1
6	1	-1	1
7	1	1	1
8	-1	1	1

Figure C.2 Eight node solid hexahedron element

Moreover, the 8-node hexahedral element used has one-point integration.

Artificial bulk viscosity

Bulk viscosity method is used to treat shock waves. A viscous term q is added to the pressure to smear the shock discontinuities into rapidly varying but continuous transition regions. With this method the solution is unperturbed away from a shock, the Hugoniot jump conditions remain valid across the shock transition and shocks are treated automatically [4].

The default viscosities in the LS-DYNA code have the form

$$\begin{aligned} q &= \rho l(C_0 l\dot{\varepsilon}_{kk}^2 - C_l \alpha \dot{\varepsilon}_{kk}) \quad if \quad \dot{\varepsilon}_{kk} < 0 \\ q &= 0 \qquad\qquad\qquad\qquad\quad if \quad \dot{\varepsilon}_{kk} \geq 0 \end{aligned} \tag{C.24}$$

where $\dot{\varepsilon}_{kk}$ the trace of the strain rate tensor, C_0 and C_1 are dimensionless constants with default values 1.5 and 0.06, respectively, and $l = \sqrt[3]{V}$ for volume V, and a is the local sound speed.

Thermal implicit analysis

The differential equations of conduction of heat in a three dimensional continuum are given as [4]

$$\rho c_p \frac{\partial T}{\partial t} = (k_{ij} T_{,j})_{,i} + Q \tag{C.25}$$

subject to the boundary conditions: $T=T_s$ on surface $\Gamma 1$ and $k_{ij}T_{,j}n_i+\beta T=\gamma$ on surface $\Gamma 2$, while the initial condition at t_0 is: $T_\Gamma=T_0(x_i)$ for $t=t_0$, where $T=T(x_i,t)$ temperature, $x_i=x_i(t)$ coordinates as a function of time, $\rho=\rho(x_i)$ density, $c_p=c_p(x_i,T)$ specific heat, $k_{ij}=k_{ij}(x_i,T)$ thermal conductivity, $Q=Q(x_i,T)$ internal heat generation rate per unit volume Ω, T_Γ prescribed temperature on $\Gamma 1$ and n_i normal vector to $\Gamma 2$. These equations represent the strong form of a boundary value problem to be solved for the temperature field within the solid.

Brick elements are integrated with a 2×2×2 Gauss quadrature rule, with temperature dependence of the properties accounted for at the Gauss points. Time integration is performed using a generalized trapezoidal method to be unconditionally stable for nonlinear problems [4]. Newton's method is used to satisfy equilibrium in nonlinear problems.

The finite element method provides the following equations for the numerical solution of the aforementioned equations

$$\left[\frac{C_{n+a}}{\Delta t} + \alpha H_{n+\alpha}\right]\{T_{n+1} - T_n\} = \{F_{n+\alpha} - H_{n+a}T_n\}$$

$$[C] = \sum_e [C_{ij}^e] = \sum_e \int_{\Omega^e} N_i \rho c N_j d\Omega$$
$$[H] = \sum_e [H_{ij}^e] = \sum_e \left[\int_{\Omega^e} \nabla^T N_i K \nabla N_j d\Omega + \int_{\Gamma^e} N_i \beta N_j d\Gamma \right] \tag{C.26}$$
$$[F] = \sum_e [F_i^e] = \sum_e \left[\int_{\Omega^e} N_i q_g d\Omega + \int_{\Gamma^e} N_i \gamma d\Gamma \right]$$

The parameter α is taken to be in the interval [0, 1]. It holds for different values of α

α	Method
0	forward difference; forward Euler/
1⁄2	midpoint rule; Crank-Nicolson
2⁄3	Galerkin
1	backward difference, fully implicit

References

[1] J. C. Nedelec, A New Family of Mixed Finite Elements in R3, *Num. Math*. **50**, 57-81 (1986).

[2] P. Castillo, R. Rieben and D. White: FEMSTER: An object oriented class library of discrete differential forms. In *Proceedings of the 2003 IEEE International Antennas and Propagation Symposium*, volume 2, pages 181-184, Columbus, Ohio, June 2003.

[3] I. Caldichoury and P. L'Eplattenier, *EM theory manual*, LSTC, Livermore, 2012.

[4] LS-DYNA Theory Manual, LSTC.

Appendix D (PLUTO MHD Code)

Discretization in polar coordinates

In polar cylindrical coordinates (R, φ, z) the conservative ideal MHD Equations 6.42 are discretized using the following divergence form [1]

$$
\begin{aligned}
&\frac{\partial \rho}{\partial t} + \nabla(\rho \boldsymbol{v}) = 0 \\
&\frac{\partial m_R}{\partial t} + \nabla(m_R \boldsymbol{v} - B_R \boldsymbol{B}) + \frac{\partial p_t}{\partial R} = \rho\left(g_R - \frac{\partial \Phi}{\partial R}\right) + \frac{\rho \upsilon_\varphi^2 - \mathrm{B}_\varphi^2}{R} \\
&\frac{\partial m_\varphi}{\partial t} + \nabla(m_\varphi \boldsymbol{v} - B_\varphi \boldsymbol{B}) + \frac{1}{R}\frac{\partial p_t}{\partial \varphi} = \rho\left(g_\varphi - \frac{1}{R}\frac{\partial \Phi}{\partial \varphi}\right) \\
&\frac{\partial m_z}{\partial t} + \nabla(m_z \boldsymbol{v} - B_z \boldsymbol{B}) + \frac{\partial p_t}{\partial z} = \rho\left(g_z - \frac{\partial \Phi}{\partial z}\right) \\
&\frac{\partial (E + \rho\Phi)}{\partial t} + \nabla[(E + p_t + \rho\Phi)\boldsymbol{v} - \boldsymbol{B}(\boldsymbol{v}\boldsymbol{B})] = \rho \boldsymbol{v} \boldsymbol{g} \\
&\frac{\partial B_R}{\partial t} + \frac{1}{R}\frac{\partial E_z}{\partial \varphi} - \frac{\partial E_\varphi}{\partial z} = 0 \\
&\frac{\partial B_\varphi}{\partial t} + \frac{\partial E_R}{\partial z} - \frac{\partial E_z}{\partial R} = 0 \\
&\frac{\partial B_z}{\partial t} + \frac{1}{R}\frac{\partial (R E_\varphi)}{\partial R} - \frac{1}{R}\frac{\partial E_R}{\partial \varphi} = 0
\end{aligned}
\qquad \text{(D.1)}
$$

The curvature terms are present in the radial component while the azimuthal component is discretized in angular momentum conserving form. The corresponding divergence operators are

$$
\begin{aligned}
\nabla F &= \frac{1}{R}\frac{\partial (R F_R)}{\partial R} + \frac{1}{R}\frac{\partial F_\varphi}{\partial \varphi} + \frac{\partial F_z}{\partial z} \\
\nabla^R F &= \frac{1}{R^2}\frac{\partial (R^2 F_R)}{\partial R} + \frac{1}{R}\frac{\partial F_\varphi}{\partial \varphi} + \frac{\partial F_z}{\partial z}
\end{aligned}
\qquad \text{(D.2)}
$$

In the previous equations $\boldsymbol{v}=(v_R, v_\varphi, v_z)$ and $\boldsymbol{B}=(B_R, B_\varphi, B_z)$ are the velocity and magnetic field vectors, (E_R, E_φ, E_z) are the components of the electromotive force $\boldsymbol{E}_l = -\boldsymbol{v} \times \boldsymbol{B}$, $\boldsymbol{g}$ is the body force vector and Φ is the gravitational potential.

Flow diagram of the code

Numerical integration of the conservation law (6.41) is achieved through shock-capturing schemes using the finite volume (FV) formalism, where volume averages evolve in time. Generally speaking, these methods are comprised of three steps: an interpolation routine, followed by the solution of Riemann problems at zone edges, and a final evolution stage. In PLUTO, the following sequence of steps provides the necessary infrastructure of the code.

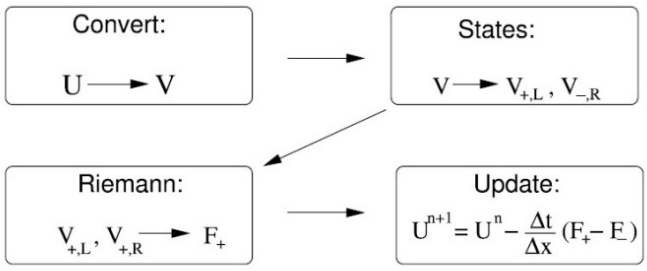

Simplified flow diagram of the reconstruct-solve-average (RSA) strategy: first, volume averages $\boldsymbol{U}$ are more conveniently mapped into primitive quantities $\boldsymbol{V}$. Left and right states $\boldsymbol{V}_{+,L}$ and $\boldsymbol{V}_{-,R}$ are constructed inside each zone by suitable variable interpolation and/or extrapolation. A Riemann problem is then solved between $\boldsymbol{V}_{+,L}$ and $\boldsymbol{V}_{+,R}$ to compute the numerical flux function $\boldsymbol{F}_+$ at cell interfaces and the solution is finally advanced in time.

Figure D.1 Flow diagram of the code strategy [1]

Riemann Solver for flux computation

The Lax-Friedrichs Rusanov flux is robust, but also the most diffusive solver. It computes the fluxes according to

$$\boldsymbol{F} = \frac{1}{2}[\, f_L + f_R - |\lambda_{\max}|(\boldsymbol{U}_R - \boldsymbol{U}_L)] \tag{D.3}$$

where $\boldsymbol{f} = \hat{\boldsymbol{e}}^d \boldsymbol{T}(\boldsymbol{U})$ is the projection of the tensor flux on the $\hat{\boldsymbol{e}}^d = (\delta_{1d}, \delta_{2d}, \delta_{3d})$ unit vector, δ_{ij} is Kronecker-Delta symbol and $|\lambda_{\max}|$ is the largest local signal velocity.

Time evolution

$\Delta t_n = t_{n+1} - t_n$ is the time increment between two consecutive steps and $\boldsymbol{L}$ denotes the discretized spatial operator on the right hand side of Equation 6.41. A second order Total Variation Diminishing, TVD, Runge Kutta (RK2) is used to advance the solution from time t_n to the next step time t_{n+1}. It holds that

$$\{U^*\} = \{U\}^n + \Delta t^n \{L\}^n$$
$$\{U\}^{n+1} = \frac{1}{2}(\{U\}^n + \{U^*\} + \Delta t^n \{L^*\}) \quad \text{(D.4)}$$

Time Step Determination

The time step Δt^n is computed using the information available from the previous integration step and it can be controlled by the Courant-Friedrichs-Lewy (CFL) number C_a. The CFL condition that is used in PLUTO for the explicit time stepping method is

$$\Delta t^n \max_{ijk}[\frac{1}{N_{\dim}}\sum_d(\frac{\lambda_d}{\Delta l_d} + \frac{2\tau_d}{\Delta l_d^2})] = C_a \le \frac{1}{N_{\dim}} \quad \text{(D.5)}$$

For a given direction d, Δl_d represents the cell physical length in that direction, λ_d provides the largest signal speed, while τ_d accounts for diffusion processes. If Δl is the cell physical length, the time step roughly scales as $\sim \Delta l$ for hyperbolic problems, but when parabolic terms are included via Super-Time-Stepping integration the time step can be much larger, being computed solely from the advection timescale (i.e. $\tau_d = 0$ in Equation D.4 above). Super-Time-Stepping (STS) is used for resistive MHD problems.

Controlling the $\nabla \boldsymbol{B} = 0$ condition (Eight-wave formulation)

In the eight-wave formalism magnetic fields have a cell-centered representation. Additional source terms are added on the right hand side of Equations 6.42

$$\frac{\partial}{\partial t}\begin{pmatrix}\rho\\ \boldsymbol{m}\\ E\\ \boldsymbol{B}\end{pmatrix} + \ldots = -\nabla\boldsymbol{B}\begin{pmatrix}0\\ \boldsymbol{B}\\ \boldsymbol{vB}\\ \boldsymbol{v}\end{pmatrix} \quad \text{(D.6)}$$

Contributions for $\nabla \boldsymbol{B}$ are taken direction by direction. The 8-wave formulation keeps $\nabla \boldsymbol{B} = 0$ only at the truncation level and not to machine accuracy.

References

[1] PLUTO v. 4.1, *User's guide*, 2014.